PARTICLE-MOLECULE INTERACTIONS FOR RADIATION AND PLASMA TREATMENT MODELS

UNIVERSIDAD AUTONOMA DE MADRID

Lilian Katryn Ellis-Gibbings

Programa de Doctorado en Física de la Materia Condensada, Nanociencia y BiofísicaInstituto de Ciencia de materiales

Facultad de Ciencia

Universidad Autonoma de Madrid

CSIC

Consejo Superior de Investigaciones Científicas

Director: Gustavo García Gómez-Tejedor

This dissertation is submitted for the degree of Doctor of Philosophy

1-June 2018

I dedicate this thesis to my family and friends, who make life worth living, and to my boss and co-workers, who do work worth doing.

There's nothing wrong with trying.

DECLARATION

This dissertation is the result of my own work and includes nothing, which is the outcome of work done in collaboration except where specifically indicated in the text. It has not been previously submitted, in part or whole, to any university of institution for any degree, diploma, or other qualification.

Signed:_____

Date:_____

Lilian Katryn Ellis-Gibbings

Madrid

ABSTRACT

Low energy collision processes are of pivotal importance in the breakdown of molecular species in several important systems. Whether the projectile is integral to the intended chemical changes, as in radiotherapy, or a byproduct whose effects are to be explored, as in plasma processing, collisions influence the outcome of the process, the byproducts produced, the radicals present and the further reactions of remaining fragmented molecular species. Understanding the fundamental processes and the individual reaction products of collisions forms a clear picture of the molecular changes occurring within a system. This understanding can direct new avenues for modelling of radiotherapy and biofuel production, both being central to the maintenance of an aging population in a world with lowered energy security and necessary resource management.

In radiotherapy, the high energy photons or ions initiate a cascade of lower energy secondary particles – particularly electrons and radicals. These produce molecular damage in radiotherapy in an indirect way, through further interactions with the surrounding cells, and thus modelling of their tracks through biological material indicates the dose deposition and range of damage propagation.

In biofuel and biodiesel production, plasma or pyrolysis are used to treat biomass and produce biodiesel. This results in low energy electrons and ions impacting biomass media, the chemical products of the conversion processes, and the waste products – determining the chemical composition of the final product. Tuning of this stage can result in higher yields of desired products.

Several experimental and theoretical techniques are available for determining the effect of collisions of electrons and positrons with individual molecules, and they are used in this work to determine the experimental electron differential cross sections of the molecule pyrimidine, the theoretical positron total and differential cross sections of the molecules nitrogen and oxygen, and the theoretical electron total and differential cross sections of the molecule furfural. Experiments to determine the energy of dissociative electron attachment resonances and their dissociated anionic products were performed on

the biofuel esters methyl acetate, methyl propionate, ethyl propionate, and butyl propionate, and the biofuel precursor furfural. After improvements were made, experimental electron energy loss profiles for furfural, argon and acetylene were collected, and the cross sections for furfural were collated with available literature data to form a collisions database ready for use in particle tracking Monte Carlo simulations. The products of electron and positron collisions include radicals, and work on a new experiment to provide data for radical-molecule collisions provided preliminary results and characterisation of the ion beam. To understand how the products of electron collisions change when the molecule is in the condensed phase, electron stimulated desorption of condensed molecules was performed on pyrimidine and pyridazine, determining, as with the dissociative electron attachment, the resonance energies and ionic products. Simulations and more complex experiments provide a link to the real world, using some of the data presented in this thesis. These include the program LEPTS, developed in Madrid for particle tracking simulations, which was used to understand how small changes in the electron energy loss input data can affect the particle energy deposition profile of real world simulations.

ACKNOWLEDGEMENTS

To acknowledge everyone who contributed to my successful completion of this thesis and the PhD it concludes would take several pages, so I will try to be brief. From a professional point of view, I would first like to thank the Marie Curie FP7 group that funded the ARGENT project and the ARGENT partners, without whom none of this would have been possible. To the 12 other ECRs of the ARGENT project - we finally did it! The staff at CSIC, where I was based, and for the most part my supervisor Gustavo García and members of the group Ali Traore, Kateryna Krupa, Alexey Verkhovtsev, Ana Lozano, Mónica Mendes and Filipe Costa are all to thank for supporting me, teaching me, putting up with me and being wonderful people to work with. Universidad de Autonoma and my thesis tutor Raúl Guantes have been very helpful. Throughout this endeavour I had the opportunity to collaborate with labs outside of CSIC, and so I thank CIEMAT, CMAM, Hospital Puerta del Hierro, Sam Eden of the Open University, León Sanche, Andrew Bass and Pierre Cloutier of Sherbrooke University, Michael Brunger and Darryl Jones of Flinders University and Sylwia Ptasinska of Notre Dame University, all for opening their doors to me and affording me space, time and expertise. External courses and industry experience were integral parts of the ARGENT project and I am very grateful for these times, and to the IT company QuantumWise for hosting me. Personally, my Mum, Dad, sisters, extended family and friends that I left back in Australia have been patient and encouraging in times of need and share in my success now - I know I will always have roots in the community back home that time and distance cannot sever. To my new friends in Spain, and across all of Europe, thank you for inviting me into your spaces and building a new family together - in particular Abby, Dolores, Ants, Sarah, and Criss. Lastly, Michal, for endless support and love, for changing things when they need to be changed, for bearing the brunt of my breakdowns, and for proofreading nearly my entire thesis - while I could have done it without you, I certainly wouldn't want to. Thank you to Kayla Friedman and Malcolm Morgan of the Centre for Sustainable Development, University of Cambridge, UK for producing the thesis template used to produce this document.

CONTENTS

LIST OF TABLES

LIST OF FIGURES

LIST OF ABBREVIATIONS AND ACRONYMS

Low Energy Particle Tracking Simulation	LEPTS
Cross Section	CS
Total Cross Section	TCS
Differential Cross Section	DCS
Integral Cross Section	ICS
Dissociative Electron Attachment	DEA
Electron Stimulated Desorption	ESD
Positron Emission Tomography	PET
Low Energy Electrons	LEE
Transient Negative Ion	TNI
Electron Energy Loss Spectra	EELS
Ion Desorption Probe	IDP
Quadrupole Mass Spectrometer	QMS
Di-Butyl Phosphate	DBP
Furan	FN
Tetrahydrofuran	TFN
Time of Flight	TOF
Microchannel Plate Detector	MCP
Independent Atom Model with Screening Corrected Additivity Rule	IAM-SCAR
Independent Atom Model with Screening Corrected Additivity Rule and Interference	IAM-SCAR+I

Di-Butyl Ether	DBE
Integral Inelastic Cross Section	IICS
First Born Approximation	FBA
Positronium	Ps
Schwinger multichannel method with psuedopotentials	SMMP
Born encounter Bethe	BEB
Dipolar Dissociation	DD
Dissociative Ionisation	DI
Integral Elastic Cross Section	IECS
Time of Flight Mass Spectrometer	TOFMS
Ultra-High Vacuum	UHV
Monolayers	ML
Rare gas solid	RGS
Pyrimidine	Pyr
Pyridazine	Pyrd
Centro de Investigaciones Energéticas, Medioambientales y Tecnológicas	CIEMAT
Consejo Superior de Investigaciones Científicas	CSIC

LIST OF EQUATIONS

LIST OF APPENDICES

1 INTRODUCTION

This thesis provides new research on the interactions between electrons, positrons and radicals, with molecules of importance to the radiobiological or renewable energy communities. It is written with a bottom-up approach, starting first with experiments of individual molecules with projectiles of low energy, including the improvement of suitable experiments, moving on to theoretical models used to provide accurate scattering data with low computational cost, followed by an investigation into condensed phase molecules and the differences therein, and lastly the culmination of the work includes an analysis of the input and output to an existing Monte Carlo particle tracking model, the Low Energy Particle Tracking Simulation (LEPTS). In going from gas phase experiments, to theory, to condensed phase experiments and finally to modelling, a clear picture of the needs and input of the scattering community and the radiotherapy and plasma industries is developed.

1.1 Motivation

To fully understand radiotherapy and plasma treatment we must start from the most basic systems and move to more complex systems from there. The collision of a single particle with a single target atom or molecule is the simplest starting point for understanding

collision processes, and experiments utilising electron collisions with molecules, examples include those being where the electron or charged molecular fragments or both are collected. To go further, this collision can be modelled theoretically, one example being taking the known atomic cross sections of interaction and using them to form molecular cross sections. To extend these simple models to low energy, adjustments to the procedure must be made. In all systems utilising radiation or plasma incident on a medium, reactive species including ions and radicals are formed, primarily by ionisation, and these proceed to react with their environment. To know the statistical outcomes of the interaction of a single radical would enable nanodosimetry modelling on a deeper scale, and so experiments colliding radical species with molecules of interest are the next most complex system. In most cases where radiotherapy or plasma treatment are commonly used, the target is not a dispersed gas but rather a liquid, solid, or combination of the two. Therefore, in order to model these examples effectively, the next most complex system to tackle is that of collisions with condensed phase material. This expands the approach past the reductive nature of single projectile-single target collisions, and explores how condensation itself can affect collision-based change. Finally, each level of complexity, from the simple collisions, to the effects of collision products, to the effects of condensation, should be understood and included in modelling procedures. In this way, an absolute understanding of the low energy processes in radiotherapy and plasma treatment can be transformed into real modelling solutions for the clinical and industrial communities.

For radiation therapy in particular it is highly important to look at the effect of the radiation and its products on biological molecules[1]. Much of the biological effect of radiation can be attributed to interactions of secondary species, be they electrons or radicals, which are produced along radiation tracks[2]. Radiobiological damage rests on the fragmentation of key molecular species within cells by these secondary species[3], additional to the direct effect of the radiation. Secondary electrons are the most abundant species, producing *via* ionisation 5×10^4 electrons per MeV of ionising radiation[4]. While an electron produced by photon ionisation has close to the initial photon energy, the

majority of secondary electrons have kinetic energy below 30 eV[5,6]. This is enough to further ionise the medium and produce large numbers of reactive species, being radicals, anions and cations. The approach of the scientific scattering community to assist clinical radiotherapists has been in the production of databases and tools to improve control of these damaging low energy processes, by a combination of experiment and theory[7]. In this way site-specific damage can be made with the least disruption to healthy tissue. The ongoing research for this project includes experimental determination of the key effects of secondary particles on important biomolecular analogues and theoretical calculations of these effects.

The simulation of positron tracks in various media is also an important field for the biomedical community[8]. Positron emission tomography[9] (PET) is the most well-known medical use of positron emitters, however positron dosimetry for ion beam therapy[10] is a growing clinical practice. It allows higher accuracy in tracking energy deposition *via* the production of positron emitters through nuclear inelastic collisions. Positrons detected in PET and ion dosimetry exhibit a wide range of initial energies, an average energy of hundreds of keV[11] up to several MeV. The positron typically emits its detectable gamma photons near the end of its transport track, and there the kinetic energy can have reduced to below 100 eV, where annihilation is more likely.

Large numbers of low energy electrons (LEEs) and radical species are also produced in plasma discharges[12]. One industry that is testing the use of plasma discharge as a treatment process is that of biofuels - either the use of biomass as a source of electricity[13–15] or biodiesel extracted from waste oils primarily for transport[16]. The production of renewable fuel sources is necessary for the continuation of the standard of living which energy-rich societies currently hold and the improvement of living standards in developing societies[17]. Biofuels can be made from the lignocellulose of crops, the most abundant non-edible plant derivative, which is a distinct advantage[18,19]. Biodiesel provides a cost effective balance between finite resources and those considered renewable, often making use of the waste products of other industries[20]. Biodiesel is an alternative of petrodiesel, and has the advantages of being made from renewable sources,

emitting fewer pollutants on burning[21], being directly safe for existing diesel engines[20], and being miscible with petrodiesel to form semi-renewable blends. If plasma is used as a treatment process in the biofuel industry then the effects of the high numbers of electrons and radical species must be clearly understood, and collision experiments represent the ideal quality of data desired in that field[22]. Many plasmas operate at low electron temperatures, often below 10 eV[12], where resonant dissociative processes exist for many molecules. Ionisation still occurs, instigated by those higher energy electrons at the edge of the Maxwellian distribution[23].

To model these systems subject to collisions with electron, positron, and radical species, Monte Carlo modelling has proven invaluable. Monte Carlo modelling procedures are capable of tracking particles in various media require accurate interaction cross section data[24]. The term cross section is a numerical probability for an event to occur with unit of area; in this case, for a collision of a specific type to occur when a projectile of particular energy interacts with a particular atomic or molecular target. This includes but is not limited to the elastic scattering, ionisation, electronic excitation, positronium formation and annihilation down to 0 eV. Some low energy electron and positron scattering databases exist for individual molecules, but the range of molecules is limited and most are individually compiled in publications such as (refs[25–28]). The energy range necessary to simulate particle transport for medical purposes crosses the region from which the First Born and Born-Oppenheimer Approximations apply (>10 keV) to energies where it fails - as such individual calculation methods tend to have regions of higher and lower accuracy. The First Born Approximation assumes that the incoming and outgoing waves of the incident particle can both be approximated by plane waves[29]. This is accurate within the Born-Oppenheimer and Fixed Nuclei approximations, where the movements of electrons and atoms in the molecule can be taken independently and if the interaction kinetic energy is high enough that the molecular atoms do not move in the time required for the incident particle to leave the system[29]. Positrons, as antiparticles, present with significant experimental difficulty in achieving high beam currents of precise energies, as such most positron experiments are restricted to particular energy ranges and spreads[30].

For particle collision calculations, resonances, positron annihilation and positronium formation present the greatest challenges to realistic interaction cross sections[31].

The Independent Atom Model is able to provide, along with the reference data available in the Livermore databases[32] developed in part from the First Born Approximation, electron-molecule scattering cross sections to reasonable accuracy above 1 keV[33]. At high energies electron scattering cross sections are widely used in place of separately calculated positron cross sections, as the polarisation potential is considered insignificant for molecules in their ground state at high impact energy. It was shown recently[34] that at energies as high as 10keV proper treatment of positron scattering introduces a difference in intensity due to the combination of signs between the polarisation potential and the static potential, being the same for electrons and opposite for positrons.

It is generally accepted that experiments in gas and condensed phase, as well as in clusters, are important for studying radiation effects and their biological outcomes. Gas-phase data on electron-pyrimidine interactions[35–39] has served to simulate electron tracks in liquid pyrimidine for comparison with liquid water[40–42], which is the preferred medium for calibrating and defining radiotherapy parameters. This comparison found a discrepancy in median electron track depth that necessitates a more accurate description of the biological medium for radiotherapy[42]. These simulations use gas phase processes as input data with some changes to account for the increased density and condensation, however dissociation processes occurring in gas and condensed phases of these tissue analogues can exhibit notable differences, such that simulations using gas phase data require realistic adjustment for the effects of condensation.

To recap, in particle-molecule scattering, several processes are important to model and understand the changes that take place along the scattering paths of particles in real world situations and those processes are the focus of this thesis. Ionising radiation produces cascades of lower energy electrons that interact with and fragment the medium through which they pass, losing energy down to their capture or thermalisation. The first of these is the probability of any interaction – the total cross section. Within this we differentiate between the cross sections for each type of interaction, nominally elastic and inelastic

scattering, the inelastic again differentiating into processes such as ionisation, electronic excitation, vibrational excitation, rotational excitation and dissociative electron attachment (DEA). Most of these processes, barring dissociative electron attachment, also have a scattering angle associated with the scattered projectile, described by the differential scattering cross sections. The energy lost during an interaction is described by the electron energy loss profile, and informs subsequent interactions of particular projectiles. Radicals produced in the target molecule by a dissociating collision interaction (DEA, most ionisations) also produce further changes in the medium and are of interest to various communities. By producing this information, it is possible to model a complete picture of a radiation event, including all secondary particles and changes inflicted to the medium. At collision energies below 10 keV the information available to the scientific community still contains large gaps in that many important molecules have not been studied, and this thesis intends to fill some of those gaps to allow for accurate radiation and plasma related modelling.

1.2 Plan

Experimental methods including electron-molecule crossed beam, electron transmission beam, dissociative electron attachment, radical-molecule cross beam, electron stimulated desorption, the theoretical method Independent Atom Model with Screening Corrected Additivity Rule and Interferences terms, IAM-SCAR+I, and the results from the modelling procedure LEPTS are used within this thesis. Their purpose is to understand the interactions at low energies (< 10 keV) between electrons, positrons and radicals with small molecules of biological or biofuel importance. Each technique adds a unique piece of information to the picture, and the results are useful not just for an understanding of scattering processes, but for practical Monte Carlo particle track modelling. Gas phase experimental and theoretical data produced in Chapters 2, 3 and 4 include cross sections and electron energy loss spectra necessary for models, as well as resonant processes and their products. These results provide comparison with low energy scattering theories and can inform the plasma treatment and radiobiological industries on the likely by-products to be accounted for. Chapter 3 also involves the development and characterisation of two

existing experiments, the electron transmission experiment and the radical-molecule crossed beam experiment. Chapter 5 investigates how interactions with condensed phase molecules exhibit important differences to gas phase interactions, something to be accounted for in particle tracking models. Finally, the interplay between the experimental or theoretical data required for LEPTS and the outputs of the LEPTS code using that data are used to inform best practice into the future in Chapter 6.

Finally, the results are summarised in the conclusions chapter, Chapter 7, where recommendations for future work are also made.

1 Introducción (Español)

Esta tesis aporta nuevas investigaciones sobre las interacciones entre electrones, positrones y radicales libres, con moléculas de importancia para las comunidades radiobiológicas o de energías renovables. El trabajo se plantea con un enfoque ascendente, comenzando con experimentos con moléculas individuales utilizando proyectiles de baja energía e incorporando importantes mejoras en los experimentos requeridos. Después se pasa a modelos teóricos utilizados para proporcionar datos precisos de probabilidades de interacción con un bajo coste computacional, seguido de una investigación de moléculas en fase condensada y las diferencias entre ambas fases. Por último, la culminación del trabajo incluye un análisis de los datos de entrada y salida de un modelo existente de seguimiento de partículas por el método de Monte Carlo, el código Simulación del Seguimiento de Partículas de Baja Energía (LEPTS). Pasando por experimentos en fase gaseosa, modelos teóricos, experimentos en fase condensada y la modelización final, se desarrolla una visión clara de las necesidades de la comunidad de la interacción de partículas cargadas con biomateriales y de las industrias de radioterapia y física de plasmas contribuyendo a la mejora de las herramientas de simulación requeridas en dichas aplicaciones

1.1 Motivación (Español)

Para entender mejor la radioterapia y el tratamiento con plasma debemos partir de los sistemas más básicos y pasar a sistemas más complejos. La colisión de una sola partícula con un solo átomo o molécula es el punto de partida más sencillo para comprender los procesos de interacción radiación-materia, como por ejemplo aquellos experimentos en los que se estudian colisiones de electrones con moléculas mediante la detección y análisis

del electrón dispersado, los fragmentos moleculares producidos o ambos. Para ir más lejos, esta colisión puede ser modelizada teóricamente, por ejemplo calculando las secciones eficaces atómicas de interacción y usándolas para formar secciones eficaces moleculares. Para extender estos modelos sencillos a bajas energías, es necesario realizar ajustes en el procedimiento. En todos los sistemas que utilizan radiación o plasma que inciden en un medio, se forman especies reactivas, incluidos fragmentos iónicos y radicales, principalmente por ionización, que reaccionan con su entorno. Conocer los resultados estadísticos de la interacción de estos radicales con las moléculas del medio permitiría aumentar el detalle de la modelización a escala nanométrica (nanodosimétria), por lo que los experimentos de colisión de radicales libres (o especies reactivas) con las moléculas de interés son el siguiente objetivo, dentro del mencionado proceso de creciente complejidad. En la mayoría de los casos en los que comúnmente se utiliza la radioterapia o el tratamiento con plasma, el blanco no es un gas disperso sino más bien un líquido, sólido o una combinación de ambos. Por lo tanto, para modelizar estos casos de manera efectiva, el siguiente problema complejo a abordar es el estudio de colisiones con materiales en fase condensada. Esto expande el enfoque más allá de la visión reduccionista de las colisiones de un solo proyectil con un solo blanco, y explora cómo el estado condensado en sí mismo puede afectar al proceso de colisión. Por último, cada nivel de complejidad, desde las simples colisiones hasta los efectos de fase condensada, pasando por los productos de colisión, deben ser comprendidos e incluidos en los métodos de modelización. De esta manera, un conocimiento completo de los procesos de baja energía en radioterapia y tratamiento con plasma puede transformarse en soluciones reales de modelización para la comunidad clínica e industrial.

En particular, para la radioterapia, es muy importante tener en cuenta el efecto de la radiación y sus productos en las moléculas biológicas[1]. Una gran parte del efecto biológico de la radiación puede atribuirse a las interacciones de especies secundarias, ya sean electrones o radicales, que se producen a lo largo de las trayectorias de la radiación[2]. El daño radiobiológico se inicia con la fragmentación de moléculas clave dentro de las células por parte de estas especies secundarias[3], además del efecto directo de la radiación.

Los electrones secundarios son las partículas más abundantes y se producen mediante ionización del orden de 5 x 10^4 electrones por MeV de radiación ionizante[4]. Mientras que un electrón producido por ionización fotónica tiene una energía cercana a la energía inicial del fotón, la mayoría de los electrones secundarios tienen una energía cinética inferior a 30 eV[5,6]. Esto es suficiente para ionizar y producir un gran número de especies reactivas, como radicales, aniones y cationes. El enfoque de la comunidad científica de colisiones / interacción de partículas cargadas con sólidos / biomoléculas para ayudar a los radioterapeutas clínicos ha sido el de la producción de bases de datos y herramientas para mejorar el control de estos procesos dañinos de baja energía, mediante una combinación de experimento y teoría[7]. De esta manera, el dañado específico del blanco (zona tumoral) puede producirse con la menor alteración posible de los tejidos sanos. La investigación en curso para este fin incluye la determinación experimental de los principales efectos de las partículas secundarias en importantes análogos biomoleculares, así como el cálculo teórico de estos efectos.

La simulación de las trayectorias de positrones en diversos medios es también un campo importante para la comunidad biomédica[8]. La tomografía por emisión de positrones[9] (PET) es la más conocida utilización de emisores de positrones en medicina. No obstante, la dosimetría de positrones para la terapia de iones[10] es una práctica clínica en crecimiento. Ésta permite una mayor precisión en el seguimiento de la deposición de energía a través de la producción de emisores de positrones mediante reacciones nucleares. Los positrones emitidos en aplicaciones PET y en dosimetría iónica exhiben un amplio margen de energías iniciales, con una energía máxima de cientos de keV[11] o incluso de hasta algunos MeV. El positrón emite sus fotones gamma de aniquilación cerca del final de su trayectoria, y allí la energía cinética puede haberse reducido a menos de 100 eV, donde la formación de positronio constituye la vía de aniquilación más probable.

En las descargas de plasma también se produce un gran número de electrones de baja energía (LEEs) y especies reactivas[12]. Una industria que está probando el uso de la descarga de plasma como tratamiento es la de los biocombustibles, ya sea utilizando la biomasa como fuente de electricidad[13–15] o el biodiésel extraído de aceites usados para el

transporte[16]. La producción de fuentes de combustible renovables es necesaria para mantener el nivel de vida actual de las sociedades ricas en energía y para mejorar el nivel de vida de las sociedades en desarrollo[17]. Los biocombustibles pueden obtenerse a partir de la lignocelulosa de los cultivos, el derivado vegetal no comestible más abundante, lo que constituye una clara ventaja[18,19]. El biodiésel proporciona un equilibrio rentable entre los recursos finitos y los considerados renovables, utilizando a veces los residuos de otras industrias[20]. El biodiésel es una alternativa al petrodiésel, y tiene la ventaja de estar hecho a partir de fuentes renovables, emitiendo menos contaminantes al quemarse[21], siendo seguro para los motores diésel existentes[20], y siendo miscible con el petrodiésel para formar mezclas semirrenovables. Ya que el plasma se utiliza como proceso de tratamiento en la industria de los biocarburantes, deben comprenderse claramente los efectos del elevado número de electrones y especies radicales, y los experimentos de colisión constituyen el procedimineto ideal para obtener los datos deseados en ese campo[22]. Muchos plasmas operan a bajas temperaturas de electrones, a menudo por debajo de 10 eV[12], donde existen numerosos procesos resonantes que conducen a la disociación molecular. En estas aplicaciones todavía se produce la ionización, provocada por los electrones de mayor energía en el borde de la distribución de Maxwell[23].

Para modelizar estos sistemas sujetos a colisiones con electrones, positrones y radicales libres, el método de Monte Carlo ha demostrado ser de una ayuda inestimable. Los procedimientos de modelización de Monte Carlo son capaces de seguir las trayectorias de partículas en diversos materiales, para lo cual requieren datos precisos de las secciones eficaces de interacción[24]. El término sección eficaz es una probabilidad numérica de que un evento ocurra. En este caso, de que ocurra una un tipo específico de colisión cuando un proyectil de energía dada interactúa con un blanco atómico o molecular particular. Esto incluye, pero no se limita a ellos, los procesos de dispersión elástica, ionización, excitación electrónica, formación de positronio y aniquilación directa hasta casi 0 eV. Existen algunas bases de datos de dispersión de electrones y positrones de baja energía para moléculas individuales, pero el rango de moléculas es limitado y la mayoría se compilan individualmente en determinadas publicaciones (refs[25–28]). El margen de

energía necesario para simular el transporte de partículas con fines médicos va desde la región de energías altas, en la que se aplican aproximaciones como la Aproximación de Born de Primer Orden y la de Born-Oppenheimer, hasta energías mucho más bajas en las que éstas fallan y requieren cálculos más sofisticados junto con resultados experimentales precisos. La Aproximación de Born de Primer Orden asume que las ondas entrantes y salientes de la partícula incidente pueden ser aproximadas por ondas planas[29] lo que simplifica notablemente los cálculos y permite la utilización de modelos de átomos independientes. En el caso de moléculas, dentro de la aproximación de Born-Oppenheimer los movimientos de electrones y núcleos atómicos pueden ser tomados independientemente, y cuando la energía cinética incidente es lo suficientemente alta como para que los núcleos no se muevan en el tiempo de interacción requerido se puede aplicar el modelo de Nucleos Fijos[29]. Los positrones, siendo antipartículas, presentan la dificultad experimental añadida del logro de corrientes suficientemente intensas de haces con una energía precisa, ya que esto implica el uso de fuentes radiactivas muy intensas junto con la eficiente utilización de materiales moderadores y complicados selectores de energía[30]. En los cálculos de colisión de partículas, las resonancias, la aniquilación de positrones y la formación de positronio representan los mayores desafíos para la obtención de secciones eficaces de interacción realistas[31].

El Modelo de Átomos Independientes puede proporcionar, junto con los datos de referencia disponibles en las bases de datos de Livermore[32] desarrolladas en parte a partir de la Primera Aproximación de Born, secciones eficaces de dispersión moleculares de electrones con una precisión razonable para energías superiores a 1 keV[33]. A energías altas, las secciones eficaces de dispersión de electrones son generalmente utilizadas en sustitución de las secciones eficaces de positrones, ya que en la primera aproximación de Born, sin considerar el potencial de polarización, la probabilidad de interacción es independiente del signo de la carga del proyectil. Recientemente se ha demostrado[34] que a energías de hasta 10keV el tratamiento adecuado de la dispersión de positrones introduce una diferencia entre sus secciones eficaces debida a la combinación de signos

entre el potencial de polarización y el potencial estático, siendo del mismo signo para los electrones y de signo contrario para los positrones.

Se acepta generalmente que los experimentos en fase gaseosa y condensada, así como en clústeres, son importantes para estudiar los efectos de la radiación y sus resultados biológicos. Los datos de la fase gaseosa sobre interacciones electrón-pirimidina[35–39] han servido para simular las trayectorias de los electrones en pirimidina líquida y para compararla con el agua líquida[40–42], que es el medio preferido para calibrar y definir los parámetros de la radioterapia. Estas simulaciones utilizan procesos de fase gaseosa como datos de entrada con algunos cambios para tener en cuenta el aumento de la densidad y la fase condensada; sin embargo, los procesos de disociación que se producen en las fases gaseosa y condensada de estos análogos de tejidos pueden presentar diferencias notables, por lo que las simulaciones que utilizan datos de fase gaseosa requieren un ajuste realista de los efectos de fase condensada.

Para recapitular, en el estudio de las interacciones de partículas con moléculas, son varios los procesos importantes que permiten modelizar y entender los cambios que tienen lugar a lo largo de las trayectorias de las partículas en situaciones realistas y esos procesos son el objeto de esta tesis. La radiación ionizante produce cascadas de electrones de baja energía que interactúan y fragmentan el material por el que pasan, perdiendo energía hasta su captura o termalización. El primero de estos parámetros es la probabilidad total de producirse cualquier interacción - la sección eficaz total. Dentro de éste diferenciamos entre las secciones eficaces para cada tipo de interacción, la dispersión nominalmente elástica e inelástica. Dentro de la inelástica, diferenciamos de nuevo procesos tales como ionización, excitación electrónica, excitación vibracional, excitación rotacional y disociación resonante por captura electrónica (dissociative electron attachment, DEA). La mayoría de estos procesos, salvo la disociación resonante por captura electrónica, también tienen un ángulo de dispersión asociado al proyectil dispersado, descrito por las secciones eficaces diferenciales. La energía perdida durante una interacción es descrita por el perfil de pérdida de energía del electrón, e informa sobre las interacciones subsiguientes de proyectiles particulares. Los radicales producidos en el blanco molecular mediante

interacciones disociativas (DEA, la mayoría de las ionizaciones) también producen cambios adicionales en el medio y son de interés para varias comunidades. Al producir esta información, es posible modelizar una imagen completa de un evento de radiación, incluyendo todas las partículas secundarias y los cambios infligidos en el medio. En las energías de colisión por debajo de 10 keV la información disponible para la comunidad científica todavía contiene grandes vacíos en que muchas moléculas importantes no han sido estudiadas, y esta tesis pretende llenar algunos de esos vacíos para permitir un modelado preciso relacionado con la radiación y el plasma.

1.2 Objetivo de la tesis (Español)

En esta tesis se utilizan métodos experimentales como el de haces cruzados de electrones y moléculas, el de haces de transmisión de electrones, el de disociación resonante por captura electrónica, el de haces cruzados de radicales y moléculas, la desorción estimulada por electrones, el método teórico del Modelo Atómico Independiente con Regla de Aditividad Corregida por Apantallamiento (Independent Atom Model with Screening Corrected Additivity Rule) y los términos de Interferencias (Interferences terms), IAM-SCAR+I, y los resultados del método/código de simulación LEPTS. Su objetivo es comprender las interacciones a bajas energías (< 10 keV) entre electrones, positrones y radicales con moléculas de interés biológico o biocombustible. Cada técnica añade una pieza única de información a la descripción, y los resultados son útiles no sólo para la comprensión de los procesos de dispersión, sino también para la modelización práctica de las trayectorias de partículas mediante el método de Monte Carlo. Los datos experimentales y teóricos de fase gaseosa producidos en los capítulos 2, 3 y 4 incluyen las secciones eficaces y los espectros de pérdida de energía de los electrones necesarios para los modelos, así como los procesos resonantes y sus productos. Estos resultados proporcionan una comparación con las teorías de dispersión de baja energía y pueden informar a las industrias de tratamiento con plasma y radiobiología sobre los posibles subproductos a tener en cuenta. El capítulo 3 también incluye el desarrollo y caracterización de dos experimentos existentes, el experimento de transmisión de electrones y el experimento de haz cruzado de radicales y moléculas. El capítulo 5

investiga cómo las interacciones con moléculas en fase condensada muestran diferencias importantes con respecto a las interacciones en fase gaseosa, algo que debe tenerse en cuenta en los modelos de seguimiento de partículas. Por último, la interrelación entre los datos experimentales y/o teóricos requeridos como dato de entrada para el código LEPTS y los resultados que éste produce empleando estos datos se utilizan para informar sobre las mejores prácticas de cara a trabajo futuro en el capítulo 6.

Por último, los resultados se resumen en el capítulo de conclusiones, capítulo 7, donde también se hacen recomendaciones para futuros trabajos.

1.3 Atoms and molecules

Each molecule investigated in this thesis is presented briefly here, to introduce them from simplest to most complex and show their relevance. The molecules are divided into three groups, being test molecules, biomolecules and biofuel molecules. In many cases the molecules are important to more than one industry, however only the aspects important to this research are shown here.

1.3.1 Test molecules

1.3.1.1 N_2 and O_2

Formation of positrons in the atmosphere can occur through nuclear reactions involving cosmic radiation with energy in excess of ~100 MeV[43]. As the two most abundant molecules in the atmosphere and both being relevant for plant and animal life on earth, N_2 and O_2 are subject to positron collisions in the atmosphere. The wealth of data already available from both experiment and theory places N_2 and O_2 as excellent molecules for comparison to new theoretical developments, as for the recent addition of interference processes to the IAM-SCAR method[44] in Chapter 4.

1.3.1.2 Argon, Ar

Noble gases were some of the first molecules studied when electron collision techniques were being developed. As such electron collision induced electronic excitations below the ionisation threshold are well known, and this atom has been used as a test electron energy loss target for the improved electron transmission experiment in Chapter 3. Argon exists in low quantities in earth's atmosphere as the third most abundant element.

1.3.1.3 Acetylene, C_2H_2

Acetylene, the smallest example of the carbon triple bond, is another well studied molecule, most recognised for its use in oxy-acetylene welding torches. Acetylene is well known to exhibit electronic excitations above the first ionisation threshold[45] and these have been studied by various methods in the past[46–48]. In Chapter 3 the electron energy loss spectra of acetylene gas is taken on the improved electron transmission apparatus.

1.3.1.4 Nitromethane, CH_3NO_2

Nitromethane, most commonly used as an explosive with greater explosive power than that of TNT[49], is well known in the electron scattering and electron transfer community as a small molecule with well-established fragmentation dynamics. Nitromethane has a large dipole moment of 3.46 D[50] and a small positive electron affinity[51] and this has made it an interesting target for electron transfer studies[52]. Data is available on electron transfer to nitromethane from collisions with neutral potassium and high energy O$^-$, as well as personal expertise of our colleagues in Lisbon with this molecule. These factors made it a good candidate for testing the fragmentation *via* electron transfer from our anion beam experiment as described in Chapter 3.

1.3.2 Biomolecules

1.3.2.1 Pyrimidine, $C_4H_4N_2$

The diazine, pyrimidine, is an experimentally convenient analogue for the DNA/RNA bases thymine, cytosine and uracil[35,38,42,53], making its fragmentation induced by LEEs an important avenue in radiobiological research. Fragmentation and damage to DNA and

other biologically critical molecules can be induced by the secondary LEEs produced during radiotherapy. At collision energies less than 20 eV much of this damage occurs *via* dissociative electron attachment (DEA, see Chapter 2)[54]. The fragmentation of DNA bases causes cross linking within the DNA chain and defects within the strands that can lead to a loss of DNA functionality[55,56] and to eventual mutagenesis[57,58].

Most prior work has considered the interactions of LEEs with gas phase diazine molecules. In the case of pyrimidine, published data includes cross sections of interaction with electrons, covering the total[59], ionisation[38,39], electronic excitation[37,60,61], vibrational excitation[62], and elastic[35,60,63] integral and differential cross sections, in the impact energy range 8 - 10 000 eV by a mixture of experimental and theoretical methods. The cationic fragmentation has been explored in the gas phase from 16 eV to 70 eV[38,64]. Electron energy loss spectra[36,40], electronic stopping power[40] and electronic state investigations[36] and assignments are available. Transient negative ions (TNIs) resonances have been investigated both experimentally[65] and theoretically[66].

Using much of this data, including those for vibrational differential cross sections provided in Chapter 2 of this thesis, García *et al.*[42] have produced a scattering database for the electron scattering community. This database is fit for use in Monte Carlo particle tracking software and details the integral and differential cross sections for interactions between electrons and pyrimidine from 0 eV to 10 000 eV, termed the 'low energy' region, and being that region below the cutoff point for traditional radiotherapy tracking software[67]. This database has been used for such modelling[42].

In Chapter 5 of this thesis is a study of the electron stimulated desorption of both anions and cations from condensed pyrimidine, important to investigate the differences between low energy collision processes between gas and condensed phase molecules.

1.3.2.2 Pyridazine, $C_4H_4N_2$

An isomer of pyrimidine, Pyridazine is also a diazine, and is a constituent of certain kinase inhibitors and presumptive radiosensitizers that are thought to act *via* their inhibition of the 'PIM1' oncogene[68,69]. While pyridazine-based kinase inhibitors have

radiosensitising properties in vivo[69], their fragmentation *via* LEE interactions and subsequent chemistry could be partly responsible for this sensitivity to radiation.

Pyridazine has received considerably less attention by the electron-molecule scattering community than pyrimidine. To date, there have been gas phase experimental and theoretical investigations of the electronic states[70–72], low lying TNI states[65,73], shape and core-excited resonances[66], electron impact induced fragmentation pathways[74] and 75 eV electron impact cationic mass spectra[75].

In Chapter 5 of this thesis is a study of the electron stimulated desorption of both anions and cations from condensed pyridazine, important to investigate the differences between low energy collision processes between gas and condensed phase molecules.

1.3.3 Biofuel molecules

1.3.3.1 Furfural, $C_5H_4O_2$

Furfural's importance to the green chemistry, agricultural, petrochemical and processing industries began in earnest early last century[76]. It is the key chemical derived from biomass lignocellulosics[19], and its applications include: oil refining; a substitute for petrochemicals; pharmaceuticals and agrochemical industrial work.

As atmospheric pressure plasma and electron beam irradiation pretreatments are already applied to biomass[77,78], it is likely that these will be used on furfural itself or in mixed media as part of the biofuel production process[79]. Additionally there is a need to provide data to expand existing electron scattering databases[80,81].

A heterocyclic aldehyde, furfural is closely related to furan. The *cis* and *trans* conformations of the aldehyde branch exist in a 20.5% to 79.5% ratio in the gas phase, though it has been shown theoretically that the differences between conformations in the various electron interaction cross sections is minimal[62].

Dissociative electron attachment to furfural has not been found in the literature, though it has been undertaken for furan and other related molecules. This low energy interaction is important for low temperature plasma physics and chemistry, where the electron

temperature may be sufficiently low to allow for a spike in this resonant dissociation process, thus affecting species concentrations. Furfural has also been posited as an analogue for the deoxyribose moiety of DNA[82], and with greater ease for vacuum collision techniques than deoxyribose itself, an investigation into this claim is of value.

To fully understand and subsequently appropriately model electron-furfural interactions, the low energy electron-molecule collisions community have collaborated internationally in producing a set of experimental and theoretical reference data. Much of the work has been published in 2015[62,83,84] and 2016[15,79,85].

Investigation of the low energy resonant electron collision process dissociative electron attachment to furfural is presented in Chapter 2. Using the IAM-SCAR+I method and the literature experimental and calculated data from literature for various scattering processes a functional database for the LEPTS program was produced and presented in Chapter 4. This was then utilised to investigate the effect of the inner shell ionisation processes within the LEPTS program in Chapter 6.

1.3.3.2 Esters

Biodiesel is most often produced from a fuel source (algae, cooking oil, feedstock oils) *via* transesterification to form esters and glycerol from triglycerides[20]. Several methods of transesterification are available and have been reviewed in literature[86]. Common transesterification reactions leave undesired products, such as excess glycerol, catalysts, and free fatty acids which contaminate the biodiesel and disrupt diesel engines[20]. Their reduction has been the aim of scientists and engineers for some time through mostly chemical innovation[87–90]. One method published in 2016[16] investigated the successful use of corona discharge plasma technology to facilitate the transesterification reaction of waste cooking oil. Cubas *et al.*[16] managed to produce biodiesel esters without the coproduct glycerol or the use of catalysts. Improvement of this method could lead to production of biodiesel that more easily fits with the strict quality control in place for Europe and the USA[20]. This study is likely to be one of many involving plasma to produce biodiesel.

Alkyl esters are used directly as biodiesels and are miscible with petrodiesel for producing blended fuels[20]. Methanol is the most commonly used alcohol reactant to produce ester biodiesels[20]. This choice is clear when considering that in the United States methanol is cheaper than ethanol, its nearest cost competitor[86]. There are countries where the production of ethanol is less expensive than methanol, such as Brazil, where the ethyl ester biodiesels are more cost effective[20]. Ethanol has been used in biodiesel production in the United States as a test for the future, were it to become financially viable[20,91].

To better understand how the corona discharge method[16] of transesterification may affect the final biodiesel composition, the products of low energy electron (such as those found in plasmas) induced DEA of biodiesel esters is of importance. As biodiesel is also produced more and more by algae which must undergo cell disruption in order for successful transesterification to take place[13], a pretreatment using plasma, already used for producing bioethanol from algae[92], is a likely candidate.

Commercial biodiesel tends to be produced from long chain fatty acids, resulting in, for methyl esters, $CH_3O(O)C$-R where R is a long alkane chain. These long chain esters provide experimental difficulties[93], often with very low vapour pressures. Four smaller, simpler analogue esters have been chosen as recommended in literature[94] and studied by dissociative electron attachment in Chapter 2. They are each introduced here.

1.3.3.2.1 Methyl acetate, $C_3H_6O_2$

As mentioned methanol is the alcohol most commonly used in the production of ester biodiesels, due to its low cost. Methyl acetate is an easy to use model biodiesel and instrumental in understanding the basic nature of biodiesel DEA. A previous DEA study to this molecule by Pariat and Allan[95] also serves to validate the results presented in Chapter 2, where they recorded the yields of 8 fragment anions in the electron energy range 0-12 eV. Pariat and Allan[95] studied the dissociation processes, particularly those below 5 eV, and indicated that a combination of fast, single fragmentation processes and complex rearrangements including proton transfer and intermediate complexes are present.

1.3.3.2.2 Methyl propionate, $C_4H_8O_2$

In order to differentiate between anion species produced from the alcohol and acid groups of the esters, methyl propionate can provide information on the methyl group. This molecule was briefly mentioned in the Pariat and Allan paper, where they predicted and detected the CH_3CCO^- fragment through a complex rearrangement process similar to $HCCO^-$ in methyl acetate. No other DEA studies were found in literature.

1.3.3.2.3 Ethyl propionate, $C_5H_{10}O_2$

Studies of ethanol-based esters are equally important, as they constitute the second most popular ester for biodiesel worldwide, and the most popular in countries where the production of ethanol is cheaper than that of methanol. Ethyl propionate is chosen with the same carboxylic acid group as the previous molecule to differentiate between those DEA structures present due to the alcohol and those of the carboxylic group. In DEA literature this molecule is only found to be mentioned in the same paper as the previous 2 molecules, that by Pariat and Allan[95], where they again predict the same fragment, CH_3CCO^-, as for methyl propionate.

1.3.3.2.4 Butyl propionate, $C_7H_{14}O_2$

To complete the study, a higher chain length alcohol is used, that of butyl propionate. Biofuels using butyl alcohol are less common, however they have been studied in the past in relation to production techniques[89]. Being formed again from a propanoic acid, this addition enables further examination of the effect of alcohol chain length on DEA. It provides a systematic comparison rather than a completely practical one, with the aim to define common traits between ester types. No prior DEA studies of butyl propionate were found.

2 LOW KINETIC ENERGY ELECTRON COLLISION GAS PHASE EXPERIMENTS

This chapter focuses on two very low energy electron scattering phenomena – vibrational excitation and dissociative electron attachment (DEA). Experimental determination of vibrational cross sections (CS) and fragmentation pathways *via* DEA require particular techniques, specialising in unique energy ranges. To isolate targeted processes and reduce analytical complications these experiments use gas phase molecules. This represents the simplest interaction model of scattering processes.

The experiments described here are a crossed beam differential cross section device used to measure the vibrational DCS of the 6 membered ring pyrimidine, and a quadrupole mass spectrometry experiment used to measure the anionic products of DEA resonances for various short chain biodiesel esters and the biofuel precursor furfural. These molecules have been introduced in Chapter 1 and their importance as analogues of biological molecules or biofuels is outlined there. Each experiment, its value and relevant theoretical

aspects, the results produced, analysis, and conclusions are presented in turn, followed by brief comments.

With these experimental measurements of low energy processes, the author adds to the particle scattering database for pyrimidine used for scattering models. Moreover, some of the first results on DEA anion production are provided for a number of biodiesel esters and a study of the effects of chain length on DEA. In addition, to the author's best knowledge, the first DEA anion study of the molecule furfural is presented, including comments on its use as a deoxyribose analogue and the effects of plasma processing.

2.1 Vibrational differential cross sections

The vibrational Differential Cross Sections (DCS) of the molecule pyrimidine at low electron impact energy (15 eV) were investigated at Flinders University of South Australia, under the guidance of Professor Michael Brunger and Dr Darryl Jones. This work stands in addition to further studies on pyrimidine, presented in Chapters 5 and 6 for condensed phase electron stimulated desorption and evaluation of particle tracking Monte Carlo modelling. The work has since been published in Jones *et al.*[96] as part of investigations performed at the same facility to provide differential and integral vibrational cross sections for pyrimidine between 15 and 50 eV electron impact energy. This set of vibrational cross sections were subsequently used for particle track models in the work of Fuss *et al.*[42], in which the author of this thesis is a contributing author, to compare the particle track depth in a pure pyrimidine medium to a pure water medium. There it was found that electron tracks extend further in pyrimidine than in pure water, suggesting pure water may not be the best substitute for biological tissue. Following are the details of pyrimidine and theory of differential cross sections DCS, the experiment, results and conclusions.

2.1.1 Introduction and Theory
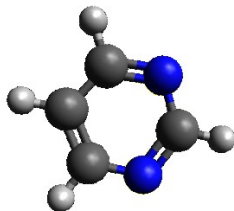
Figure 1 Pyrimidine structure[97] C$_4$H$_4$N$_2$. Grey: C, Blue: N, White: H

Pyrimidine (Figure 1), introduced in Chapter 1, has long been used as an analogue of the RNA/DNA bases thymine, cytosine and uracil, containing the same 6 member diazine ring[42] and being more technically simple to introduce into vacuum experiments due to its liquid state and relatively high vapour pressure at room temperature. Studying the effects of low energy electrons on DNA analogues is of interest to the radiobiological community, and further comments on this are found in Chapter 1. The experimental determination of scattering cross sections is still necessary at low energies where the current scattering theories are either not applicable (as in the case of the Born approximation[29]), or necessitate large amounts of computing power (as in the case of the Convergent Close Coupling[98] and R-Matrix[99] calculations).

Vibrational DCS refers to the probability that an electron-molecule collision of known kinetic energy will result in excitation of a certain (or several, or any) vibrational mode of a molecule and scattering of the electron to a certain angle θ. The integral vibrational cross section is obtained by the integration of the DCS over the full angular range and is the probability that the vibrational mode will be excited by a collision at a particular kinetic energy. The relationship between the ICS and DCS is shown in Equation (1), where σ = cross section, E_0 = electron impact energy in eV, Ω = solid angle, and θ = scattering angle.

$$\sigma(E_0) = 2\pi \int_0^\pi \frac{d\sigma}{d\Omega}(E_0, \theta) sin\theta d\theta \qquad \text{(01)}$$

DCS are used in particle tracking models to provide information on the radial spread of the primary and secondary particles following scattering events[67]. In this work, DCS for

vibrational bands of pyrimidine have been determined at 15 eV collision kinetic energy *via* the use of a crossed beam electron-molecule collision experiment, built and housed at Flinders University.

2.1.2 Experimental Set-up

The experiment has been described in detail in the past[100]. Briefly it is composed of two hemispherical energy analysers, the first to collimate and select the energy of the electrons produced from a tungsten wire filament, ensuring an electron energy resolution of 60 meV. The second analyser is used to discriminate the energy of the scattered electrons as they are guided to the channel electron multiplier serving as the detector after the collision region. The collision region is formed by the intersection of the well-collimated electron beam and the effusive molecular beam emitting from a leak-valve controlled outlet with an opening near to the collision region. The detection analyser is housed in a rotating frame, allowing detection of scattered electrons from 15° to 90° (0° being the forward scattered direction, inseparable from the unscattered beam for the procedure used here). Electron flux is measured by use of a Faraday cup and was typically 2-5 nA. The chamber pressure during measurements was kept at $\sim 5 \times 10^{-6}$ Torr to ensure single collision conditions. The pyrimidine sample was purchased from Sigma-Aldrich with a stated purity of >98.9 % and several freeze-pump-thaw cycles were performed to eliminate dissolved gases.

2.1.3 Analysis procedure

To obtain the DCS the electron energy loss spectra (EELS) are analysed for a series of scattering angles. EELS are produced by detecting the intensity of scattered electrons over a range of their kinetic energies, from the elastically scattered at the initial energy to those losing energy to inelastic collisions. In this case, the maximum energy loss detected is 1 eV, as the excitation of the vibrational bands studied all require less than 1 eV in energy transfer. An example of an EELS spectra of pyrimidine is shown in Figure 2, where the elastic scattering peak is dominant, followed by several smaller peaks assigned to the vibrational excitation bands of pyrimidine, according to the work of Levesque *et al.*[101].

Their peak positions are: Band I, 0.12 and 0.27 eV, Band II, 0.38 eV, Band III, 0.50 eV, and Band IV, 0.73 eV. These bands are then fitted with Gaussian distributions for deconvolution (with Band I requiring two Gaussians for appropriate fitting), separating the contribution of individual or closely grouped vibrational excitations for individual analyses. To determine a relative cross section for each band the deconvoluted excitations are compared to the elastic scattering peak, according to Equation (02), relating the ratio of peak areas (R) to the ratio of the cross sections. The procedure is repeated for each angle of interest, and each measurement consists of the average of multiple scans to reduce the possibilities for error.

$$R_i(E_0, \theta) = \frac{\sigma_i(E_0, \theta)}{\sigma_0(E_0, \theta)}$$

(02)

Following this procedure the relative DCS are normalised to known absolute elastic DCS from literature[35], resulting in the absolute vibrational DCS for pyrimidine. Integration according to Equation (01) provides the integral cross section for each vibrational band, and of course their sum, for the impact energy used.

Errors on the final DCS measurements are in the range $22 - 72\%$ and arise from the scattering intensity measurement, the analyser transmission calibration, the deconvolution process, and those errors in the elastic DCS used to normalise the vibrational DCS (taken directly from the publication[35]).
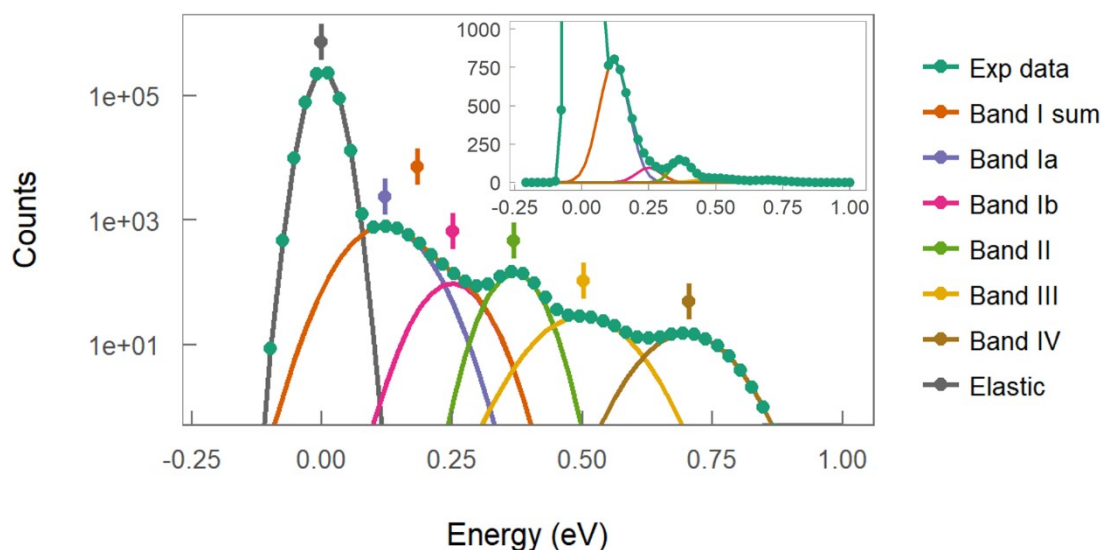
Figure 2 Standard electron energy loss (up to 1 eV) of pyrimidine, showing the fitting procedure for the elastic peak and four identified vibrational bands. Band I is a composite of two neighbouring Gaussians. The same vibrational excitation EELS is shown inset in linear scale for clarity.

2.1.4 Results and discussion

Electron energy loss spectra were measured for pyrimidine at 15 eV electron impact energy in 10° angle intervals for angles 20° - 90°. The analysis procedure described in the previous section was applied to each measurement, resulting in the calculation of vibrational DCS at each angle specified for the four bands identified. These results are presented in Table 1 and Figure 3.

The angular distribution of the vibrational cross section is quasi-isotropic, with a dip in all values at 60°, more pronounced for bands III and IV, which also exhibit a rise at 40° (Figure 3). This behaviour is reminiscent of other ring molecules studied by the same group – in THF[102,103], α-tetrahydrofurfuryl alcohol[104] and phenol[105,106].

The Flinders University group also measured pyrimidine DCS in the same apparatus[96] for 20, 30 and 50 eV. The DCS measured at 15 eV are slightly higher in value in comparison to these results, as is expected with increasing impact energy. They are also the least

peaked in the forward direction, again as expected, however band I exhibits the same flat character for all energies studied.
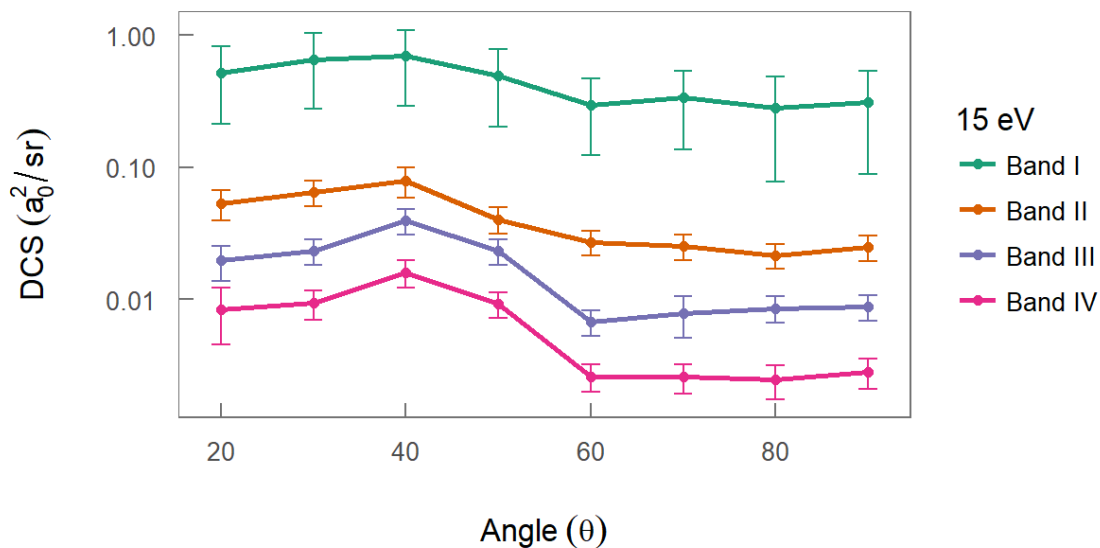
Figure 3 Summary of absolute DCS values in a_0^2 for vibrational bands I-IV at 15 eV impact energy, including errors as described in the text.

Another vibrational study of pyrimidine was that of Levesque *et al.*[101], from which the band assignments have been made. Their study of cold, condensed pyrimidine included assignment of known vibrational energy levels, from Raman and infrared spectroscopy, to the peaks seen in their electron energy loss spectra. The structures seen in our spectra are thus assigned the vibrational modes in the following table as defined by Levesque *et al.*[101].

Table 1 Differential cross sections (a_0^2/sr) for electron impact excitation at 15 eV of each identified vibrational band for pyrimidine. The integral cross sections (ICS, a_0^2) are also contained at the foot of the table. See text for further details. Errors are expressed in absolute units.

Angle (deg)	Band I		Band II		Band III		Band IV	
	DCS	error	DCS	error	DCS	error	DCS	error
20	0.5177	0.3035	0.0535	0.0137	0.0196	0.0057	0.0083	0.00378
30	0.6534	0.3785	0.0649	0.0145	0.0232	0.0052	0.0093	0.00235
40	0.6927	0.4035	0.0789	0.0199	0.0392	0.0086	0.016	0.00371
50	0.4928	0.291	0.0403	0.009	0.0233	0.0051	0.0092	0.00207
60	0.2974	0.1746	0.0271	0.0058	0.0067	0.0014	0.0026	0.0006
70	0.3371	0.2017	0.0251	0.0054	0.0078	0.0027	0.0025	0.00064
80	0.2813	0.2035	0.0216	0.0046	0.0085	0.0018	0.0024	0.00071
90	0.3103	0.221	0.0249	0.0054	0.0087	0.0018	0.0028	0.00071
ICS	5.8493	4.3316	0.5035	0.2321	0.1928	0.0857	0.0682	0.0307

The ICS determined by Levesque et al.[101] at their highest electron energy, 12 eV, can be compared to those presented here for 15 eV. By summing the appropriate bands they detected in the higher resolution condensed phase apparatus, an ICS of 2.16×10^{-17} cm^2 is compared to the value of 16.38×10^{-17} cm^2 of the ICS for Band I at 15 eV. The comparison for Band II is simply between the last band studied in the condensed phase, giving an ICS of 0.35×10^{-17} cm^2, compared to the value obtained here for Band II at 15 eV of 1.41×10^{-17} cm^2. In both cases the gas phase measurement is significantly higher that the condensed phase, by $7 \times$ and $4 \times$ for Bands I and II respectively. This effect of reduced ICS in the condensed phase has been seen previously[107], and is not likely to be simply due to the lower electron impact energy.

Table 2 Assignment of vibrational modes to the definable vibrational bands according to previous studies on pyrimidine[101].

Band #	Peak position (eV)	Peak width (eV)	Assignment[101]
I	0.12 0.27	0.14 0.10	ν_{6b}, ν_{6a}, ν_4, ν_{11}, ν_1, ν_{17a}, ν_5, ν_{10b}, ν_{19a}, ν_{19b}, ν_{12}, ν_{15}, ν_{14}, ν_3, ν_{18b}, ν_{9a}, ν_{8a}, ν_{8b} modes
II	0.38	0.09	ν_{CH}−stretching modes (ν_{7b}, ν_{13}, ν_{20a}, ν_2)
III	0.50	0.16	Various combination modes
IV	0.73	0.15	2x ν_{CH}−stretching modes

2.1.5 Conclusion

Vibrational DCS were measured for pyrimidine, a DNA/RNA base analogue, at 15 eV electron impact energy and 8 angles between 20° and 90°. Four distinct vibrational bands were identified, and the DCS and ICS calculated for each. The final ICS values for each band are in absolute values, and in decreasing order: Band I (1638 ± 1213 ×10^{-19} cm^2) >> Band II (141 ± 65 ×10^{-19} cm^2) > Band II (54 ± 24 ×10^{-19} cm^2) > Band IV (19.1 ± 8.6 ×10^{-19} cm^2). The DCS profile with respect to scattering angle appears quasi-isotropic, with a drop in intensity at 60°. Comparison to a previous study on condensed pyrimidine found that the gas phase values for Band I and Band II are 7 × and 4 × higher than the condensed phase values respectively, for similar impact energy. These experimentally determined values provide accurate DCS and ICS for particle track modelling, of use to the radiobiological community.

2.2 Dissociative electron attachment

Dissociative electron attachment (DEA) experiments were performed at the Radiation Laboratory of Notre Dame University, South Bend, USA, under the guidance of

Associate Professor Sylwia Ptasińska and Dr. Michał Ryszka. The molecules methyl acetate, methyl propionate, ethyl propionate, butyl propionate and furfural were investigated in the electron impact energy range of 0 - 15 eV and anion yields collected.

2.2.1 Introduction and theory

Fragmentation of molecules can be considered as either a positive or negative outcome, depending on the application. For biodiesel and biofuels, which can be treated with plasmas, an understanding of the molecular fragmentation caused by the free electrons in the plasma is beneficial to understanding both the process and the final product.

DEA is a process whereby an incoming electron attaches resonantly to a molecule, forming a transient negative ion (TNI), followed by dissociation into one anion and one or several neutral fragments. A thorough description of the process is available in the book "Molecule Interactions and their Applications" edited by L Christophorou[29], and the next few paragraphs provide a brief explanation for the reader.

While TNI are abundant for complex molecules, decay *via* dissociation is less common. This process is greatly affected by the details of the molecular structure, dipoles of the molecule and the medium surrounding these short-lived anions. Gas and condensed phase DEA processes often differ, and while the gas phase process is explored within this chapter, Chapter 5 explores condensed phase DEA processes that lead to electron stimulated desorption.

Most commonly seen for impact electron energies below 15 eV, TNIs that result in DEA are short-lived states, with lifetimes between 10^{-14} and 10^{-12} seconds. Autodetachment, a competing process where the TNI decays *via* release of the attached electron, is often faster. There are several types of TNIs that influence the energy at which a DEA resonance can be detected. Shape resonances occur when the interaction between the incoming electron and the neutral ground state molecule forms an attractive potential with a centrifugal barrier – the electron is trapped by the shape of this potential, hence the name. Shape resonances tend to occur between 0-4 eV and are most often subject to autodetachment. Core excited shape resonances are similar to shape resonances except

that the potential well is formed between an excited electronic state of the molecule and the incoming electron, and again the electron is trapped by the 'shape' of this interaction/resonance. Shape resonances lie energetically above the parent molecule state. Feshbach resonances, the second basic type of TNI, lie energetically below the parent molecule state, and are trapped either by coupling between vibrational modes of the molecule and the incoming electron (vibrational Feshbach resonances) or by exciting the target molecule and being trapped by the subsequently less well screened positive field of the target nuclei (core-excited Feshbach resonance).

DEA only occurs when the electron kinetic energy matches that of the resonance, at low energies near and below the ionisation threshold. Low energy electrons are most abundant in modern processes involving plasmas and ionising radiation. Plasmas generally have an electron temperature between 1-10 eV[12], and so it is likely that the resonant processes explored here are open for excitation under plasma conditions. DEA is also an important process near the end of electron tracks in radiotherapy[108], and the cascade of secondary electrons can continue to damage a medium below its ionisation threshold[109].

Biodiesel esters and the biofuel precursor furfural were studied in this section as both can be subject to low temperature plasmas during preparation and pretreatment[16,83]. All molecules studied have been introduced in detail in the Chapter 1 of this thesis, and only the relevant information will be presented here. The experimental details for all targets were the same. The biodiesel esters are presented first, examined in detail with relation to each other and relevant literature. The results for furfural follow and are compared to literature of similar molecules. Furfural is featured further in this thesis in Chapters 4 and 6, where a cross section database is developed for particle track modelling, and the results of simulations using that database explored.

2.2.2 Experimental Set-up

The DEA experiment was custom built at Notre Dame Radiation Laboratory. It utilises a Hiden Analytical Ion Desorption Probe (IDP) and Quadrupole Mass Spectrometer (QMS) under ultra-high vacuum conditions (base pressure around 1×10^9 mbar), and has been

described in detail elsewhere[110]. In brief, vaporised target molecules are introduced into the ion source of the Hiden probe, where they collide with low energy electrons produced *via* thermal emission from an oxide coated iridium filament. The pressure in the chamber was kept constant throughout each measurement, ranging between 5.0 and 9.4×10^{-6} mbar.

The mass resolution was 1 m/z over the entire mass range of 0.4 – 300 m/z, and as such fine details between similar mass fragments such as CN and C_2H_2 (26.02 and 26.04 amu respectively) are not distinguishable. The electron energy resolution is that of the filament, 0.5 eV. These detractions to resolution are countered by the high flux available, resulting in detection of low cross section DEA products not seen in higher resolution experiments in literature.

To reduce contaminant signals, the vacuum chamber and gas lines were baked up to 373 K prior to experiments for a minimum of 30 hours, until the degassing pressure in the chamber had reduced. Each liquid target sample underwent several freeze-pump-thaw cycles to eliminate dissolved gases, and the ionisation mass spectra of each sample checked against that from the NIST chemistry webbook database[111] for purity.

To detect anions formed by DEA, first a preliminary mass scan was taken for each energy from 0 – 15 eV in steps of 0.5 eV. The anion masses that were detected therein are subsequently studied individually, with energy scans for each mass of interest (0 – 15 eV, 0.1 eV steps, 1s dwell time). The corresponding spectrum is termed an 'anion yield' as it shows the count rate of that anion as a response to the change in electron energy. Background measurements of the interaction chamber with no gas present are subtracted from the anion yield readings to guard against contaminant readings. A 'resonance energy' here describes the location of the local maxima, the onset of a peak being difficult to define due to the varied shape and intensities of individual resonances[95]. A resonance is considered relatively strong if it displays a maximum count rate above 50 counts/second, moderate between 5 and 50 counts/second, and weak below 5 counts/second. All scans were controlled by the MASsoft version 7 Professional software

from Hiden. The electron energy scale was calibrated using the O^- peak signals from DEA to CO_2 *via* the 4.4 eV[112] and 8.2 eV[113] resonances.

It should be noted that the kinetic energy of the anion plays a part in its ion detection efficiency[114]. As the kinetic energy distribution of fragments is unknown in this case, the role this plays both in the intensity of count rates and the detection of ions seen in this apparatus is little known.

2.2.3 Biodiesel Esters

The anion profiles of all detected anions below 15 eV were recorded for each of the esters studied. The esters can be divided either by their alcohol or carboxylic acid constituent. The alcohols fall into two groups - those formed from methyl alcohol (methyl acetate and methyl propionate) and those formed from higher chain length alcohols (ethyl and butyl propionate respectively). Methyl based esters are the most common for biodiesel, ethyl based esters are also popular, and a butyl ester is included to expand the study. The carboxylic acids used to form these esters are also in two groups, that of the acetate (methyl acetate) and the propionates (methyl, ethyl and butyl propionates). Common anion yield profile shapes, along with the peak energy of resonances and a comparison to relevant literature, are presented for each group. Patterns that can be attributed to esters generally and to either the alcohol or carboxylic acid group are compared.

2.2.3.1 Methyl alcohol esters

Methyl Acetate, $C_3H_6O_2$, mass = 74.1 g.mol^{-1}
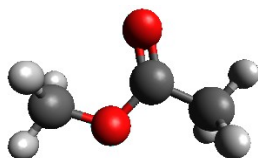
Figure 4 3D structure[97] of methyl acetate

Table 3 Methyl Acetate high intensity anion resonance energies, given by maxima locations. [D] indicates dominant peak. * indicates a shoulder. All energy values have error of ± 0.25 eV.

	CH_3^- (15 m/z)	O^- (16 m/z)	CH_3O^- (31 m/z)	C_2HO^- (41 m/z)	$C_2H_3O^-$ (43 m/z)	$C_3H_5O_2^-$ (73 m/z)
Peak 1	1.2 eV	2.75 eV*	3.25 eV	3.7 eV	7.45 eV[D]	2.75 eV[D]
Peak 2	5.9 eV*	6.25 eV[D]	7.7 eV[D]	7.85 eV*	8.75 eV	7.75 eV
Peak 3	7.55 eV[D]	9.55 eV*	9.95 eV	9.85 eV[D]		
Peak 4	9.15 eV	11.95 eV*				

The highest number of strong fragmentation resonances were found for methyl acetate, the smallest ester studied. These are for the anions with detected mass/charge ratio of 15, 16, 31, 41, 43, and 73 m/z, being assigned to CH_3^-, O^-, CH_3O^-, C_2HO^-, $C_2H_3O^-$, and $C_3H_5O_2^-$, respectively. A note on the detection of O^-, which is very often confounded in vacuum experiments with the signal from DEA to trace water. The resonance energies for the detection of O^- from water are 7.0, 9.0 and 11.8 eV[115], which can conceivably account for the resonances at 9.55 and 11.95 eV, and part of the dominant broad peak at 6.25 eV when considering the energy width of the electron beam is 0.5 eV. In fact, mass 16 m/z was detected for the three other esters studied and in those cases the spectra were easily assigned to that of water. As the dominant peak is 0.75 eV away from the expected resonance for water, and this peak is in this case nearly an order of magnitude higher in count rates and broader than those seen in the other esters, the 16 m/z signal is assigned as a mixture of O^- from water and O^- from methyl acetate, with the energy of the methyl acetate O^- peak being near 6 eV by Gaussian deconvolution of the larger peak. Peak energies are seen in Table 3. CH_3O^- and $C_2H_3O^-$ both represent the fracture of the ester bond between the alkoxyl oxygen and the acyl carbon, with the electron residing on the alkoxyl group in the first case and acyl group in the second. $C_3H_5O_2^-$ is the loss of a single hydrogen, and CH_3^- a methyl anion from one of the molecule ends, possibly the acetate

as the yield function does not match that of the same fragment for methyl propionate reported below.

Moderate and weak intensity anion signals were seen for the masses shown in Table 4 below along with the possible chemical formula.

Table 4 Moderate and *weakly* detected masses for methyl acetate. Reference indicates assignment from literature.

Mass	14 m/z	17 m/z	28 m/z	29 m/z	58 m/z	59 m/z	71 m/z
Anion assigned	CH_2^-	OH^-	CO^-, $C_2H_4^-$	CHO^- [95]	$C_2H_2O_2^-$ [95]	$C_2H_3O_2^-$	$C_3H_3O_2^-$

Methyl Propionate, $C_4H_8O_2$, mass = 88.1 g.mol^{-1}
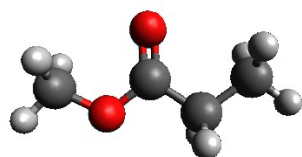
Figure 5 3D structure[97] of methyl propionate

Two strong anion resonances present themselves in the methyl propionate anion yields, those of CH_3O^- (31 m/z) and $C_3H_3O^-$ (55 m/z). The locations of their resonances are presented in Table 5. As for 31 and 43 m/z in methyl acetate, these can be assigned to cleaving of the O-C ester bond with the electron finally residing on the alkoxyl (31 m/z) or acyl (55 m/z) fragments respectively, however in this case the acyl anion endures an additional loss of two hydrogens.

Eleven moderate strength and four weak anion masses were detected in the moderate strength region for methyl propionate, seen in Table 6.

Table 5 Methyl Propionate high intensity anion resonance energies, given by maxima locations. D indicates dominant peak. * indicates is a shoulder. All energy values have error of ± 0.25 eV.

	CH_3O^- (31 m/z)	$C_3H_3O^-$ (55 m/z)
Peak 1	3.0 eV	8.4 eV
Peak 2	7.2 eV*	
Peak 3	9.0 eV^D	

Table 6 Moderate and *weakly* detected masses for methyl propionate.

Mass	15 m/z	17 m/z	25 m/z	27 m/z	29 m/z	57 m/z	58 m/z	59 m/z
Anion assigned	CH_3^-	OH^-	C_2H^-	$C_2H_3^-$	CHO^-	$C_3H_5O^-$, $C_2HO_2^-$	$C_2H_2O_2^-$	$C_3H_7O^-$, $C_2H_3O_2^-$
Mass	73 m/z	87 m/z	*14 m/z*	*24 m/z*	*41 m/z*	*85 m/z*		
Anion assigned	$C_3H_5O_2^-$	$C_4H_7O_2^-$	*CH_2^-*	*C_2^-*	*C_2HO^-*	*$C_4H_5O_2^-$*		

Methyl ester DEA

Methyl acetate and methyl propionate show similar anionic fragments as well as similar fragmentation patterns and resonances, depicted in Figure 6. 31, 58 and 59 m/z are detected for both compounds, and of these 31 m/z is a strong resonance for both. It represents cleavage of the ester bond, producing an anion of CH_3O^- (the alcohol). For 31 m/z, methyl acetate displays 3 strong resonance peaks, as seen in Figure 6A, with peak energies of 3.25, 7.7 and 9.95 eV, whereas methyl propionate displays two low intensity resonances at 3.0 and 7.2 eV and a strong resonance at 9.0 eV, depicted in Figure 6B.

Masses 58 and 59 m/z are also present for both methyl esters and it is likely that they both arise from the methyl group. This indicates structures of $C_2H_2O_2^-$ and $C_2H_3O_2^-$ where the bond between the acyl carbon and the adjacent propionate carbon is severed ($CH_3OC(O)$-

R), followed by loss of a single hydrogen atom in the case of 58 m/z. Neither ester presents with strong resonances, however 58 m/z for both esters and 59 m/z for methyl propionate present with the same double peak structure indicated in Figure 6C.

Other common yield structures are present for methyl ester anions. Most spectra exhibit a dominant peak between 7 and 10 eV. For methyl acetate many spectra show a dominant resonance around the 7.5 eV mark, whereas methyl propionate more readily produced dominant resonances between 8 and 9 eV, such as in Figure 6B. When the resonant peak is near 7.5 eV (14, 15, 17, 29, 32, 43, 58, and 71 m/z for methyl acetate, 29, 57, 58, 59, and 85 m/z for methyl propionate) the yield functions exhibit the double peak structure shown in Figure 6C, with a shoulder 1-2 eV higher than the initial peak. Exceptionally, a dominant peak between 1 and 4 eV exists for masses 14, 28 and 73 m/z for methyl acetate and 25 and 87 m/z for methyl propionate, shown for 73 m/z in Figure 6D. Methyl propionate displayed a generally lower count rate compared to methyl acetate and fewer detectable smaller secondary or shoulder resonances.
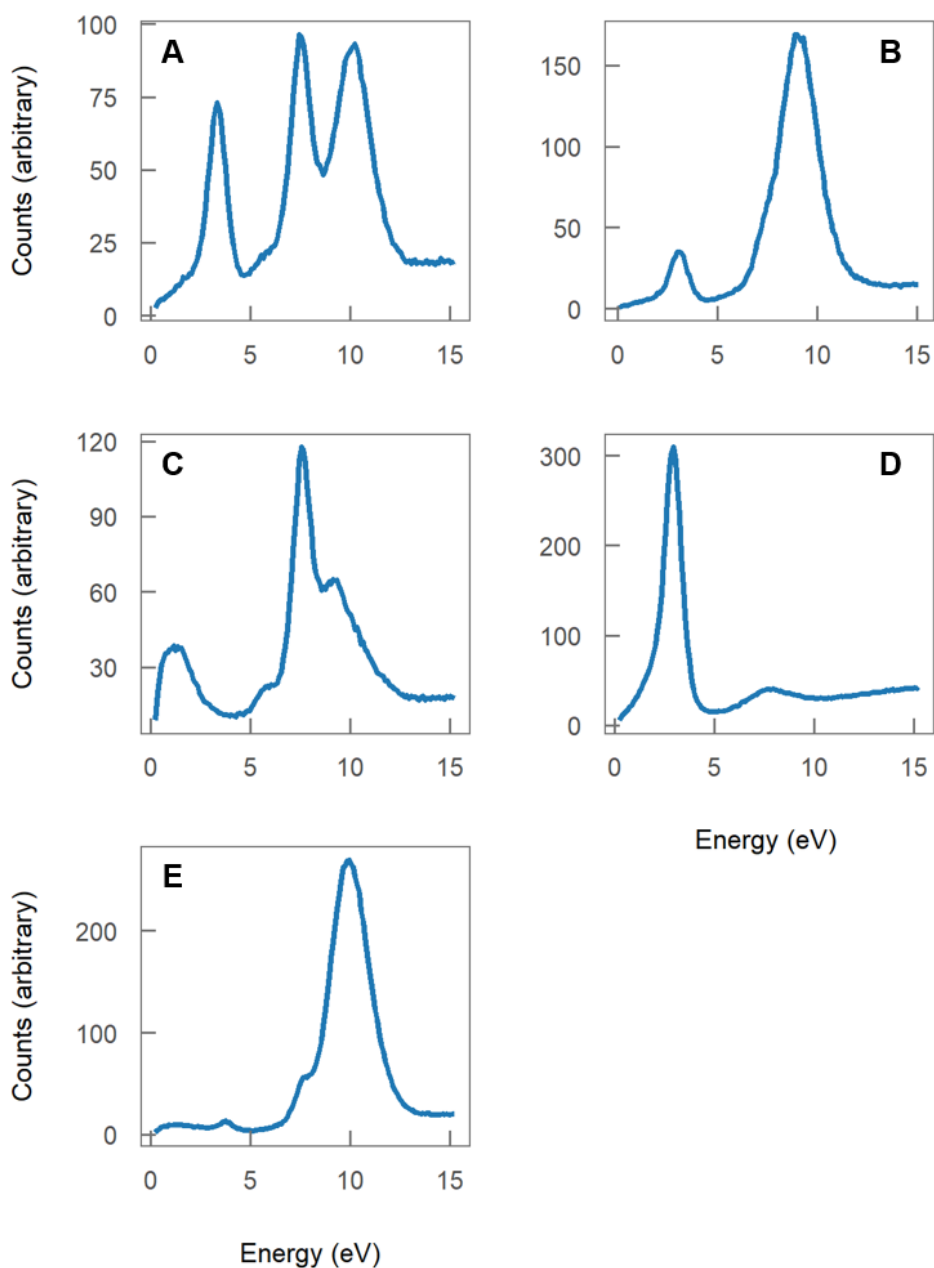
Figure 6 Methyl acetate and methyl propionate common yield function shapes, further details in text. A: Unique 3 peak structure only seen for methyl acetate in anion 31 m/z B: High energy peak structure seen commonly near 7.5 eV in methyl acetate and 9 eV in methyl propionate, including non-dominant low energy peak structure. C: Double peak structure. D: Dominant low energy peak structure. E. example of single high energy peak with shoulders.

Comparison to literature

DEA to methyl acetate has been studied previously by Pariat and Allan[95] with an additional small discussion of the DEA to methyl propionate. They identified 7 individual anions from the DEA to methyl acetate, all of which are identified in the results presented above. These 7 anions include all strong anion peaks presented above barring 16 m/z, as well as masses 29 and 58 m/z (CHO^- and $C_2H_2O_2^-$), which show only weak count rates in this work. This variation can likely be attributed to the mass sensitivity and transmission efficiency of each apparatus.

Resonances are seen in this study and the Pariat and Allan paper between 3-4 eV and 7-8 eV, while a resonance at 5-6 eV seen in the literature for several fragments was only seen for mass 15 m/z here. Higher energy resonances, or rising count rates above the ionisation limit of 10.25 eV[111] indicating dipolar dissociation, were seen in the literature and confirmed by the data here.

Below 5 eV, for the anions $C_3H_5O_2^-$, CH_3O^- and C_2HO^-, (73, 31, 41 m/z) resonance peaks were reported[95] at 3.05, 3.50 and 4.00 eV respectively. These are ~ 0.35 eV higher than the values found in this study of 2.75, 3.25 and 3.7 eV respectively, close to the overlap of the respective experimental uncertainties (this work: ± 0.25 eV, Pariat and Allan: ± 0.075 eV). A π^* resonance known to exist at 2.1 eV is likely responsible for these detected DEA signals. Otherwise Pariat and Allan attributed resonances near 5-6 eV to core excited resonances and those around 7.6 eV to Feshbach resonances of low lying Rydberg states.

Pariat and Allan also undertook a discussion of the dissociation mechanisms likely for the DEA resonances below 5 eV. They deduced that the loss of a single hydrogen atom (mass 73 m/z) is attributable to the rapid breaking of the C-H moiety due to a π^* resonance, and that the CH_3O^- anion is also produced in a rapid process involving the breaking of a simple bond without intermediary states. The C_2HO^- anion is attributed to a more complex fragmentation process from the acetyl acid group, the possible mechanisms of which are discussed in detail in their paper.

The same article briefly discusses DEA fragmentation of both methyl and ethyl propionate[95]. They predict and confirm the formation of the 55 m/z fragment $C_3H_3O^-$ at 4 eV based upon their examination of possible reaction pathways for methyl acetate. This anion is one of the two strong resonances detected for methyl propionate. They show the intensity of the 4 eV resonance to be very low, at least two orders of magnitude lower than the dominant peak at 8.4 eV, and it is not convincingly detected in this work. No other relevant literature was found for this molecule.

2.2.3.2 Ethyl and Butyl alcohol esters

Ethyl Propionate, $C_5H_{10}O_2$, mass = 102.1 g.mol^{-1}
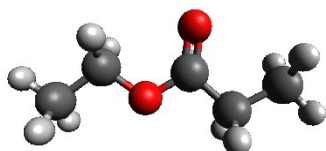
Figure 7 3D structure[97] of ethyl propionate

For ethyl propionate, 5 anions showed strong dissociation resonances; these are the fragments C_2H^-, $C_2H_3O^-$ (or $C_3H_7^-$), $C_2H_5O^-$, $C_3H_3O^-$ and $C_3H_5O_2^-$ with masses 25, 43, 45, 55 and 73 m/z respectively. The formation of the 25, 43 and 55 m/z detected masses requires significant rearrangement of the molecule, and the movement (removal or addition) of at least 2 hydrogens in all considered fragmentation patterns for the minimum number of bond cleavages. 45 and 73 m/z can be formed through the simple cleavage of a single C-O or C-C bond without further rearrangement.

The peak energy for resonances for the five strong anion yields are presented in Table 7.

Table 7 Ethyl Propionate high intensity anion resonance energies, given by maxima locations. D indicates dominant peak. * indicates a shoulder. All energy values have error of ± 0.25 eV.

	C_2H^-	$C_2H_3O^-$ or $C_3H_7^-$	$C_2H_5O^-$	$C_3H_3O^-$	$C_3H_5O_2^-$
	(25 m/z)	(43 m/z)	(45 m/z)	(55 m/z)	(73 m/z)
Peak 1	1.45 eV^D	7.45 eV*	3.0	8.65	2.6
Peak 2	9.95 eV	9.25 eV^D	9.0		9.15

Many lower strength resonances are detected. These are shown in Table 8.

Table 8 Moderate and *weakly* detected masses for ethyl propionate

Mass	14 m/z	15 m/z	17 m/z	24 m/z	27 m/z	41 m/z	46 m/z	57 m/z
Anion assigned	CH_2^-	CH_3^-	OH^-	C_2^-	$C_2H_3^-$	C_2HO^-	$CH_2O_2^-$	$C_3H_5O^-$, $C_2HO_2^-$
Mass	74 m/z	101 m/z	*29 m/z*	*44 m/z*	*71 m/z*	*72 m/z*		
Anion assigned	$C_3H_6O_2^-$	$C_5H_9O_2^-$	*CHO^-*	*CO_2^-, $C_2H_4O^-$*	*$C_3H_3O_2^-$*	*$C_3H_4O_2^-$*		

Butyl Propionate, $C_7H_{14}O_2$, mass = 130.2 g.mol^{-1}
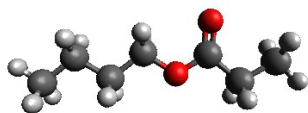
Figure 8 3D structure[97] of butyl propionate.

Contrary to ethyl propionate, only two anions show strong resonance count rates for butyl propionate, being masses 55 and 73 m/z, corresponding to anions $C_4H_7^-$ or $C_3H_3O^-$ and $C_3H_5O_2^-$ or $C_4H_9O^-$ respectively. 73 m/z, the stronger of the two, can arise from several

simple bond cleavages: $C_3H_5O_2^-$ is easily formed through the cleavage of the bond between the butane and ester O, R-OC(O)R$^-$, and $C_4H_9O^-$ through the fragmentation of the ester bond $^-$RO-C(O)R, with the electron residing with the alkoxyl. For 55 m/z, $C_4H_7^-$ can be formed from the butane chain only with the loss of two additional hydrogens, and $C_3H_3O^-$ can be formed through cleaving the ester bond RO-C(O)R$^-$, the electron residing on the acyl, again with the loss of two additional hydrogens. The peak energy for resonances for the two strong anion yields are presented in the following table.

Table 9 Butyl Propionate high intensity anion resonance energies, given by peak maxima locations. ^{D} indicates dominant peak. All energy values have error of $\pm$ 0.25 eV.

	$C_4H_7^-$ or $C_3H_3O^-$ (55 m/z)	$C_3H_5O_2^-$ or $C_4H_9O^-$ (73 m/z)
Peak 1	8.5 eV	2.6 eV
Peak 2		8.5 eV^D

A wealth of moderate and weak count rate resonances is also detected for butyl propionate, seen in Table 10. Many of these are attributable to more than one anion structure, due to the large size of the molecule. Of interest is the highest mass anion detected, 130.2 m/z, with very weak count rates, indicating the parent anion.

Table 10 Moderate and *weakly* detected masses for butyl propionate.

Mass	17 m/z	25 m/z	57 m/z	71 m/z	99 m/z	129.2 m/z	14 m/z	15 m/z
Anion assigned	OH^-	C_2H^-	$C_4H_9^-$, $C_3H_5O^-$, $C_2HO_2^-$	$C_3H_3O_2^-$, $C_4H_7O^-$	$C_5H_7O_2^-$, $C_6H_{11}O^-$	$C_7H_{13}O_2^-$	CH_2^-	CH_3^-
Mass	29 m/z	41 m/z	43 m/z	45 m/z	86 m/z	100 m/z	101 m/z	111 m/z
Anion assigned	$C_2H_5^-$, CHO^-	C_2HO^-	$C_2H_3O^-$, $C_3H_7^-$	$C_2H_5O^-$, CHO_2^-	$C_4H_6O_2^-$, $C_5H_{10}O^-$	$C_5H_8O_2^-$	$C_5H_9O_2^-$	$C_6H_7O_2^-$, $C_7H_{11}O^-$
Mass	127 m/z	130.2 m/z						
Anion Assigned	$C_7H_{11}O_2^-$	$C_7H_{14}O_2^-$						

Ethyl and propyl ester DEA

In the DEA of ethyl propionate and butyl propionate, most anion yield functions have a dominant peak between 7.5 and 9.7 eV, shown in Figure 9B by mass 55. Some of these same spectra exhibit a weaker low energy peak between 1 and 3 eV. The double peak structure presents itself, though with lower count rates and less clear features than in the anion yields for the methyl esters. The dominant peak appears at 7.4 - 7.6 eV followed by a shoulder 1 eV higher, an example of which is shown in Figure 9C. This structure is present for the anions with masses 15, 57, 71, 72 m/z for ethyl propionate and 57, 86, 99, and 100 m/z for butyl propionate. An inversion of the dominant peak is seen in 43 m/z in ethyl acetate and 71 m/z in butyl propionate, also shown in Figure 9C. A common yield function with two distinct and near equal intensity peaks, the first between 2.5 and 3.0 eV and the second between 7.3 and 9.1 eV, as shown in Figure 9A, is seen for masses 45, 46, 73 and 74 m/z in ethyl propionate and 45, 73, 101, 129.2 and 130.2 m/z in butyl propionate. This is not seen in the methyl esters. C_2H^- (25 m/z) shows again a unique

spectrum compared to the others, with the dominant peak at the low energy of 1.45 and for ethyl propionate a weak structure at 9.95 eV, as shown in Figure 9D. Masses 29 m/z in ethyl propionate and 17 and 41 m/z in butyl propionate exhibit this same resonance shape, though at very weak count rates. Several anion yields display an increasing character above the ionisation energy, which could be attributed to dipolar dissociation[29], arising from excitation of the molecule to an unstable state. An example is given in Figure 9E and this behaviour is seen for masses 14, 15, 17 and 101 m/z in ethyl propionate and 14, 15, 17, 129.2 and 130.2 m/z in butyl propionate. A high energy peak is also exhibited by masses 14, 17, 29, and 41 m/z.

In the methyl esters a common anion was the alkoxyl cleaved at the ester bond, resulting in a mass of fragment 31 m/z. The equivalent bond cleavage in ethyl propionate would result in a fragment of mass 45 m/z and structure $C_2H_5O^-$. This is detected, with resonances at 3.0 and 9.0 eV, matching perfectly with methyl propionate, although in this case both resonances are strong in character. The equivalent ester bond fracture for butyl propionate would result in the anion of mass 73 m/z and structure $C_4H_9O^-$. However, assignment of this mass is complicated as it can indicate $C_4H_9O^-$ or $C_3H_3O_2^-$ and this will be discussed in relation to relevant literature in following sections. The resonances for mass 73 m/z in butyl propionate appear at 2.6 and 8.5 eV, lower in energy than for the other esters.

Methyl esters also produced anions with masses 58 and 59 m/z, indicating the CH3OC(O)-R bond was fragmented. Equivalent bond breaking is seen for ethyl propionate at 72 and 73 m/z and for butyl propionate, though very weakly, at 100 and 101 m/z. These spectra all show the same double peak structure except for ethyl propionate at 73 m/z, as in Figure 9A, which exhibits two strong resonances at 2.6 and 9.15 eV.
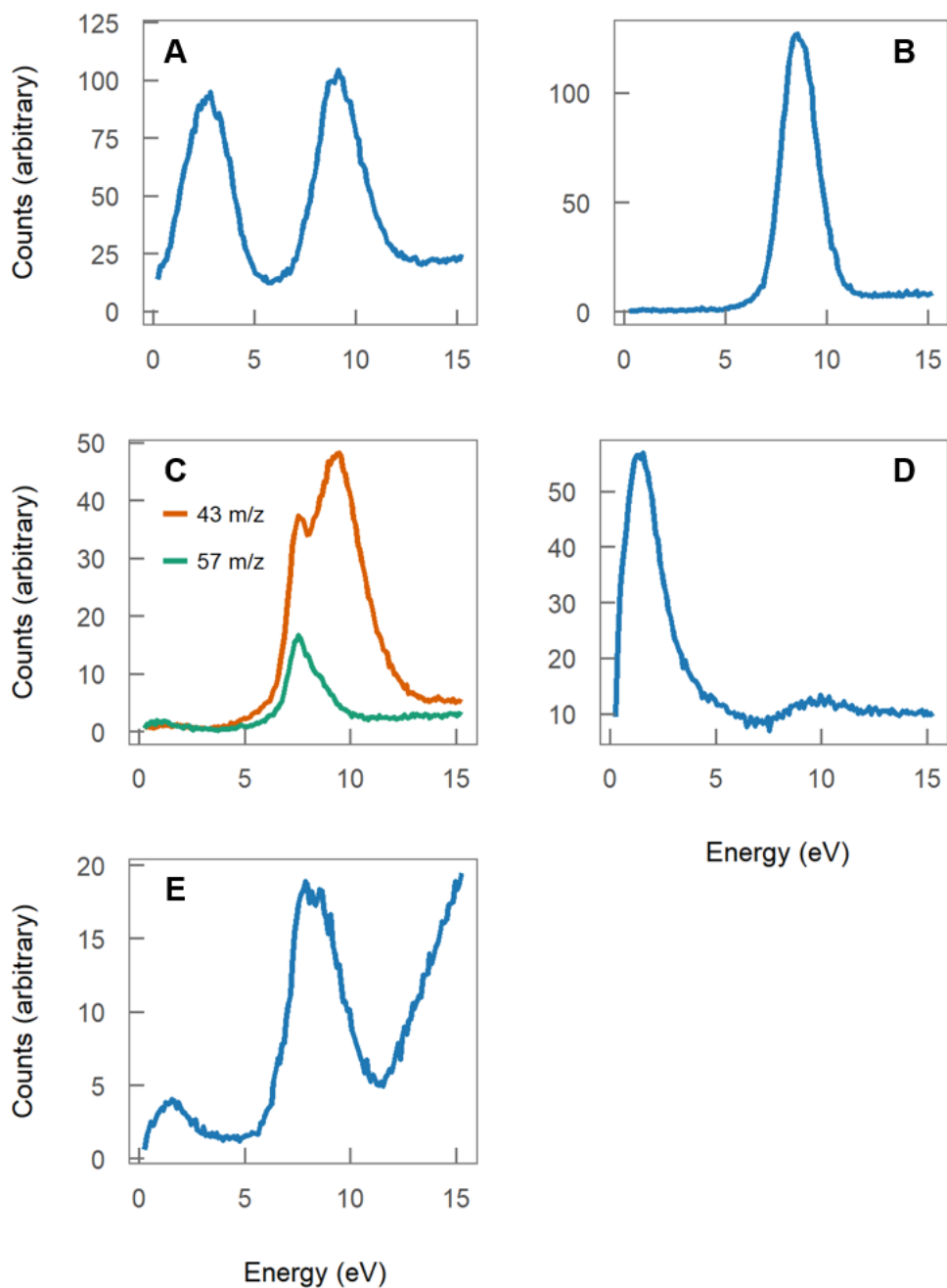
Figure 9 Ethyl propionate and butyl propionate common yield function shapes, further details in text. A: Two peak structure. B: High energy dominant peak. C: Double peak structure and inversion. D. 25 m/z exhibiting one of the only yield spectra with a low energy dominant peak at 1.45 eV. D: High energy increasing anion yield as evidence for possible dipolar dissociation.

Comparison to literature

Ethyl propionate displays a resonance for the anion $C_3H_3O^-$ at 55 m/z (Figure 9E), as predicted and experimentally confirmed by Pariat and Allan[95] for both methyl and ethyl propionate, however as with methyl propionate in this work the resonance at 4 eV is not clearly apparent and the spectrum is dominated by the higher energy peak.

The bond dissociation energies, enthalpies of formation and reaction paths for decomposition of ethyl propionate were studied by El-Nahas *et al.*[94] in 2007. These could be used for further theoretical tests of the feasibility of fragment assignment, as the kinetic energy of the projectile electron must be higher than the bond dissociation energy (determined from the enthalpies of formation) minus the electron affinity of the anion and the combined final kinetic energies of the fragments[116]. From their calculations, the lowest energy dissociation path in ethyl propionate is the $RO-CH_2CH_3$ bond with a low barrier height of 210 kJ/mol (2.176 eV), and the dominant reaction channel is the formation of ethene (C_2H_2) through this dissociation. By plain dissociation of this bond, anions of either mass 29 or 73 m/z would be detected, and mass 73 m/z is indeed strongly detected, being the third most dominant anion with resonance peaks at 2.6 and 9.15 eV. For the formation of ethene masses 26 or 74 m/z would be detected, and these do not show strong signals.

In the absence, to the author's knowledge, of DEA, electron attachment or transmission, enthalpy of formation or bond dissociation energy literature available for butyl propionate, the results presented here represent the first such measurements.

2.2.3.3 Other trends between esters

The differences between chain length in the base alcohol used for esters have been studied above, however the chain length of the carboxylic acid also deserves attention. This allows for differentiation between anions formed from the ester molecules. Additionally several anions are present for all four of the molecules studied, and several cleavage patterns remain the same across each molecule as well. These can be interpreted as general ester DEA patterns. These comparisons are explored in the following paragraphs.

Propanoic acid esters

Three of the esters studied were propanoic acid esters, i.e. $ROC(O)CH_2CH_2CH_3$. Similarities between the propanoic esters studied include the strong resonance 55 m/z, the moderate resonances 25 and 57 m/z, and the weak resonance 56 m/z.

55 m/z is assigned to $C_3H_3O^-$ in methyl and ethyl propionate, formed by the cleaving of the ester $RO\text{-}C(O)R^-$ bond followed by the loss of two hydrogens. In butyl propionate, 55 m/z can equally be assigned to $C_4H_7^-$ through cleaving the butyl-oxygen $R^-\text{-}OC(O)R$ bond and removing two hydrogens. The breaking of this particular bond was seen in a previous study with di-butyl ether[117]; however the anion detected was OR^- and neither that study nor one on di-butyl phosphate[118] reported a fragment at mass 55 m/z. This lends evidence to all three instances of a 55 m/z anion being from the $C_3H_3O^-$ propionate group, further demonstrated by all three resonances residing near 8.5 eV. The equivalent DEA in methyl acetate would present as anion mass 41 m/z, which appears as a strong resonance at 9.95 eV with additional lower energy shoulders – thus the decrease in acid chain length increased the resonance energy for the dominant peak for this fragmentation.

The presence of a moderate resonance in all three propanoic esters at 57 m/z is thus assigned to the pure cleavage of the O-C ester bond without the double hydrogen abstraction seen in 55 m/z. These masses display the same yield shape across each propanoic ester – that of the double peak featuring the sharp resonance at 7.5 eV and the higher energy shoulder at 1-1.5 eV higher energy. This shape is displayed best in Figure 6C. The equivalent bond breaking in methyl acetate results in the fragment 43 m/z, which shows the same double peak structure and is a strongly detected resonance.

The remaining mass detected for only the three propanoic esters is 25 m/z, C_2H^-, and this is also the only anion detected that exhibits a dominant resonance near 1.5 eV. This low appearance energy is unusual considering the complicated processes that must occur to remove the additional four hydrogens from the C_2H_5 end group. All three spectra also show a very low intensity broad resonance between 9.5 and 10.5 eV, however the count rate is near zero.

Of the other anions, masses 14 m/z (CH_2^-) is the same shape for the propionate esters spectra yet differs for the acetate. 14 m/z has a peak at 8.5-9 eV for the propionates and this resonance is raised to 11 eV for methyl acetate.

Across all esters

Several anion masses were detected for all four of the studied biofuel esters, those being 14, 15, 17, 29, 41, and 73 m/z. The low mass species are easy to assign, being the loss of carbon end groups (14, 15 m/z), and OH^- (17 m/z), and only showing strong resonance signals for methyl acetate and masses 15 m/z.

Mass 29 m/z is attributable to CHO^- for methyl acetate and propionate and to $C_2H_5^-$ for ethyl propionate and butyl propionate, in accordance with their resonance structures, being the double peak structure for the first case and a low and high energy peak at 1.5 and 8.5 eV for the second.

Mass 41 m/z is assigned to fragment $C(O)CH^-$ for all molecules requiring several bond breaks and a hydrogen abstraction. All four molecules exhibit a high-energy resonance for this mass, at 9.6 eV for methyl propionate, ethyl propionate and butyl propionate, and at 9.95 eV for methyl acetate (Figure 6E). As the formation of C_2HO^- from methyl acetate can be performed with a C-O bond break and 2 hydrogen abstractions, the bond strengths involved are expected to be different from those involved in the propionate fragmentations, as for ethyl propionate[94].

Mass 73 m/z consists of a strong resonance yield for methyl acetate, ethyl propionate and butyl propionate and a moderate strength yield for methyl propionate. 73 m/z corresponds to $C_3H_5O_2^-$, easily attributed to $R-OC(O)C_2H_5^-$ in the propionate esters, and in the case of butyl propionate can also be $C_4H_9O^-$, but is unable to be reliably assigned. The spectra are similar across all molecules, each consisting of two peaks, one between 2.0 and 2.7 eV, the other between 7.75 and 9.7 eV (methyl acetate: 7.75 eV, methyl propionate: 9.7 eV, ethyl propionate: 9.15 eV, butyl propionate: 8.5 eV). If this fragment is attributable to the propionate group, then the consistent decrease in resonance energy as the alcohol chain length rises in the propionate esters is of note.

The loss of a single hydrogen from any of the esters results from a dominant low energy peak at 2.6 - 2.9 eV and a broad low intensity resonance at 7.4 - 7.8 eV, as seen in Figure 6D.

2.2.3.4 Conclusion

In general, the esters studied dissociate with low anion yields into a widely varied range of fragments, some from cleavage of a single bond, others from a more complex fragmentation that must include several steps. In some cases, these steps are also seen in the anion yields, as for masses 57, 56 and 55 m/z ($C_3H_5O^-$, $C_3H_4O^-$ and $C_3H_3O^-$) for the three propionate esters. Common resonance shapes are seen across all esters. The double peak structure, with a dominant peak at ~7.5 eV and an additional broad shoulder 1 to 1.5 eV higher in energy is the most common. Next, the two peak structure, where a low energy peak near 3 eV precedes a (usually dominant) peak between 7.5 and 9 eV. A single clear resonance between 7.5 and 10 eV is also common. Finally, some fragments show a continually rising character above approximately 10 eV, which can be attributed to dipolar dissociation. Several resonances appear as shoulders and insignificant peaks at low (3-4 eV) or high (7-10 eV) energy. Only the CH_3O^- anion at 31 m/z for methyl acetate shows three strong resonances, at energies 3.25, 7.7 and 9.95 eV.

The differing carbon chain lengths for either the alcohol or acid component of the ester affect the shape and energy of resonances seen and disrupt the formation of some fragmentation patterns. Cleavage of the RO-C(O)R ester bond is the clearest example for these differences. In cases when the electron resides with the alkoxy group (RO$^-$-C(O)R), the anion yield spectra between the two methyl alcohol esters differ, but are similar between methyl propionate and ethyl propionate, indicating the length of the acid chain is more relevant than the alcohol chain here. When the electron resides with the acyl group following ester bond cleavage (RO-C(O)R$^-$), all molecules, regardless of chain lengths, show a double peak structure with the dominant peak near 7.5 eV and a shoulder 1-1.5 eV higher. A stronger resonance occurs for the more complex anion (acyl-2H)$^-$ anion. In this case, all propionate esters have resonances at 8.5 eV as well as additional resonances. However, decreasing the carboxylic chain length as in methyl acetate increased the energy

of the dominant resonance to 9.95 eV. Mass 73 m/z, when detected from propionate based esters, shows a decrease in peak energy with respect to the increase in length of the alcohol chain, decreasing from 9.7 to 8.5 eV from butyl through methyl propionate. This can be easily assigned to R-OC(O)$C_2H_3^-$ in methyl and ethyl propionate, though may arise from $C_4H_9O^-$-C(O)R in butyl propionate.

The varied fragments produced by all esters may present a problem for plasma processing in biofuel production, as an electron temperature near 3 or 8 eV would be sure to fragment the desired ester product molecules into reactive anion states. With the low intensities of anions detected the cross sections for these interactions will likely also be low and thus the number of molecules fragmented will not be in the majority. The effect of the most common fragments on the chemistry of the biofuel mixture should still be investigated to ensure that further chemical products are not harmful for diesel engines, as with the current unwanted biofuel production by-products of free fatty acids[20]. In some cases DEA resonances in the liquid phase are quenched[119], and DEA studies to clusters or cold condensed molecules could be instrumental in investigating any influence of this effect.

2.2.4 Furfural
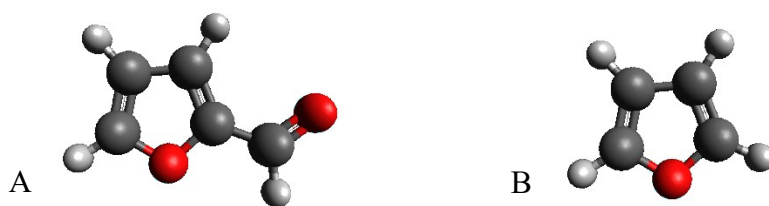
Figure 10 Furfural molecule structure[97] (A), $C_5H_4O_2$, mass 96 amu, and furan molecule structure[97] (B), C_4H_4O, mass 68 amu

Furfural (Figure 10A), introduced in more detail in Chapter 1, is important for both the biofuels and the biomedical research communities. Furfural shows strong fragmentation compared to the biofuel esters studied in this chapter, with the strongest fragment yield of 16 m/z having a count rate nearly 5 times greater than that of the strongest fragment of

the esters, mass 73 m/z for methyl acetate. While the experiments undertaken here do not allow for cross section determination, a strong fragment anion yield is a good indication of a high cross section for that resonance or resonances. It is known that high fragmentation cross sections can lead to high concentrations of radical and anionic species during irradiation processes, sometimes forming complex chemical byproducts[109]. Used in higher energy collision studies as a simple analogue of the deoxyribose molecular constituent of DNA[82] as with furan (Figure 10B), high fragmentation of furfural in the gas phase implies that this constituent could be vulnerable in a cellular environment[82]. The use of furfural as a DNA constituent analogue will be discussed here. As both a desired product for industry and an inhibitor of the biomass conversion processes[120], a better understanding of the breakdown of furfural itself in the presence of atmospheric pressure plasma is important. As such it has taken the interest of the international scattering community, with several publications[83,82,120,62,15,79,85,84] leading to an accumulation of cross sectional data appropriate for use in Monte Carlo modelling. This database is collated, refined and extrapolated in Chapter 4 and analysis of modelling using this database is presented in Chapter 6.

Electron-furfural collisions have been investigated here for electron energies of 0-15 eV and the anion yields analysed. The results are presented in a similar pattern to those of the biodiesel esters above, consisting of an analysis and assignation of the anion masses detected, an exploration of the common resonance patterns and their peak energy groupings, followed by suggested fragmentation patterns, a comparison to appropriate literature and the conclusions to be drawn from the work.

2.2.4.1 Results and Analysis

All non-isotopic anions detected, their DEA resonance energies, their assigned chemical formulas and their shape are included in Table 11. Of the fragment anions detected in the experimental study, those with masses of 16, 25 and 41 m/z showed the strongest signals, with 67, 49, 17, 51 and 65 m/z also displaying strong and clear resonances.

Other fragment anions with lower detection intensities have m/z of: 39, 50, 66, 69, 77, 79 and 95. Signals for 68 m/z and 52 m/z were detected, however further analysis of the shape and intensity proved these to be isotopic signals from the 67 m/z and 51 m/z fragments, i.e. $^{12}C_3^{13}CH_3O^-$ and $^{12}C_3^{13}CH_3^-$. The character of the individual yield spectrum, and the proposed molecular formula of the detected anions are presented in Table 11. Those energies for which the number is followed by an asterisk had yields higher than 100 cts.s^{-1} at the maxima and are as such deemed to have a relatively "strong" yield signal.

The anion yield functions have 3 common characteristic shapes, represented in Figure 11, with the fragments that share each shape identified in Table 11. Single peak fragment resonance maxima all fall between 7.5 and 8.9 eV incident electron kinetic energies. Apart from the exceptions to follow, if an anion yield has double peak structure, the higher energy also falls between 7.5 and 8.9 eV and the lower energy peak is less intense, falling between 4.6 and 5.4 eV. The ratio between the high and low peaks, from their maximum counts per second, varies from 1.8 × for 39 m/z to 11.9 × for 66 m/z. Inverted double peak structure indicates an inversion in the order of intensity – in these rare cases the lower energy resonance has a higher count rate. This behaviour is only seen in the two anion species pictured in Figure 11B and Figure 11D, 67 m/z and 95 m/z, with resonances also isolated from the previous cases. The peak groupings can be seen most clearly in Figure 12.

Table 11 Anion fragments detected from DEA of furfural

m/z	Resonance E, eV ± 0.25 (*strong yield)	Single S, Double D or Inverted Double ID structure	Anion molecular formula
16	8.7*	S	O^-
17	8.3*	S	OH^-
25	8.3*	S	C_2H^-
39	5.4 8.1	D	$C_3H_3^-$
41	5.3 8.4*	D	C_2OH^-
49	8.2*	S	C_4H^-
50	7.8	S	$C_4H_2^-$
51	4.8 7.7*	D	$C_4H_3^-$
53	5.2 8.5	D	C_3OH^-
65	8.6*	S	C_4HO^-
66	4.8 8.9	D	$C_4H_2O^-$
67	4.6* 6.6	ID	$C_4H_3O^-$
69	5.2 8.1	D	$C_3HO_2^-$
77	8.2	S	C_5HO^-
79	7.5	S	$C_5H_3O^-$
95	3.8 7.5	ID	$C_5H_3O_2^-$ == $[FURF-H]^-$

Figure 11 Furfural common yield function shapes, further details in text. A: Single peak spectrum (16 m/z). B: Inverted double structure (67 m/z). C: Double peak shape (41 m/z). D: Inverted double structure (95 m/z)

Three types of fragmentation patterns can occur – those that cleave some or part of the functional aldehyde group, those that fracture the ring in some way, and those that do both. Through mass analysis the constituents of the anion are easily determined, owing to the low number of constituent atoms in furfural. The anion fragment with 67 m/z is assigned at least in part to the cleaving of the entire aldehyde group (COH), to be discussed in regard to furan DEA in Section 2.2.4.2 below. Of interest is the shape of this

resonance profile (Figure 11B). Unlike other anions, where each resonance is clearly defined with a Gaussian shape, the profile of 67 m/z appears to have a broad low intensity feature spanning from near 1.5 eV to 9.5 eV, coupled with two sharply peaked resonances at 4.6 eV and 6.6 eV. As seen in Figure 12, no other anion shows a resonance near 6.6 eV. The lower energy resonance, at 4.6 eV, is the strongest of the resonances in that region, indicating that this fragmentation pattern (possibly the cleaving of the aldehyde in its entirety with the electron residing on the ring) is favourable over ring breakage in the low energy region. This strong lower energy resonance supports the analysis that at low energies, cleaving the aldehyde from the molecule is more favourable than breaking the ring structure. All remaining strong resonances, including ring fragmentation, reside between 7.5 and 9.5 eV.
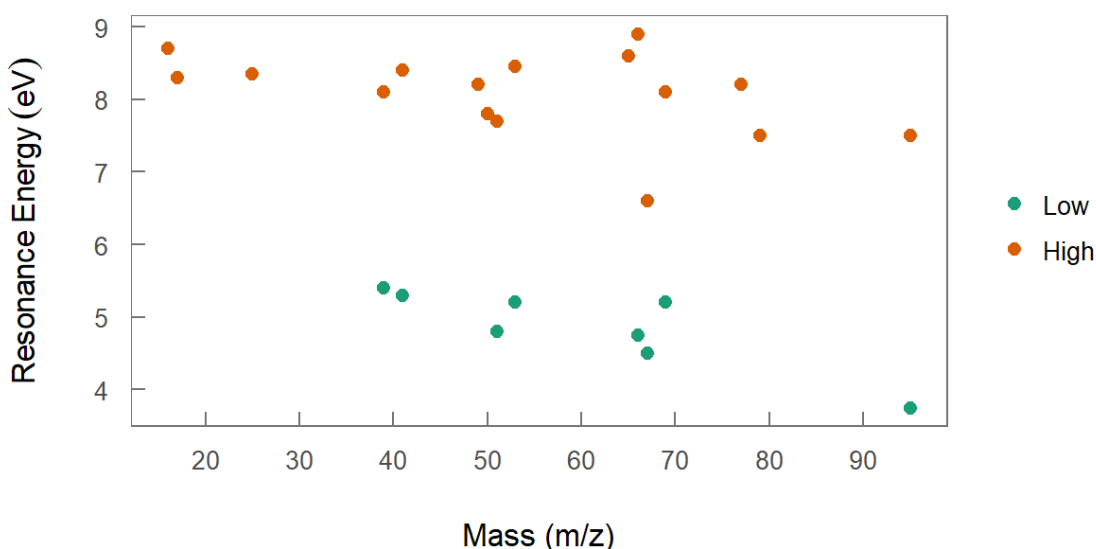
Figure 12 The resonances seen in DEA to furfural tend to be grouped into two energy ranges, those between 4.5 and 5.5 eV, and those between 7.5 and 8.9 eV. Some outliers for 95 m/z and 67 m/z are discussed in the text.

The most intensely detected anion in high energy grouping is oxygen (16 m/z), which can originate from either the aldehyde or the ring functional group, however the second highest yield, with a resonance at 8.3 eV, is the anion C_2H (25 m/z) which can only form
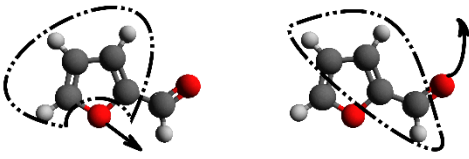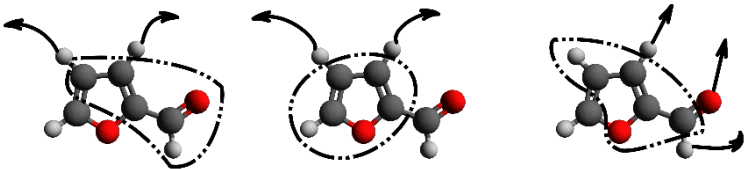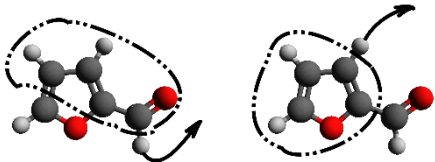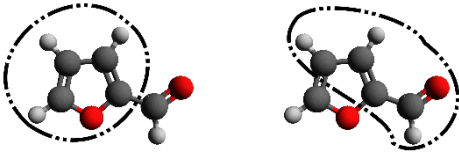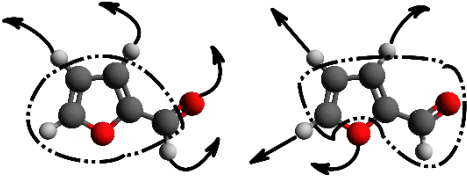
through breakage of the ring structure. Aside from anions with 16, 17, 67, and 95 m/z, all other high intensity anions require the breakdown of the ring structure.

The fragmentation resonances detected each lead to the formation of a single anion and one or several neutral components, though the anion could have several constitutional isomers. Several of the simplest fragmentation pathways have been identified for each anion. The highest intensity anions and those anions that present odd findings are shown in Table 12.

As can be seen, fragmentation pathways for 16, 41, and 67m/z can be formed with 1-2 bond cleavages, while other fragments seem to arise through more complicated processes involving at least 3 bond cleavages and the rearrangement or abstraction of hydrogen from the anion (17, 25, 49, 50, 51, 65, 66 and 77 m/z). Of these, 77 m/z is the most unusual, requiring the loss of 3 hydrogen atoms and an oxygen atom to produce the anion detected in the experiment. 77 m/z presents as a weak, though not the weakest signal, indicating this complex dissociation is not a dominant channel. While count rates do not compare analytically, though they can indicate weaker and stronger resonance cross sections. Note that in Table 12, when the molecule undergoes H loss an H atom has been chosen from the molecule at random – without a theoretical assessment or further experimentation using deuterated molecules, the location of the H-loss is unknowable.

Table 12 Possible fragmentation pathways for those fragments presenting either a strong yield or potentially complex fragmentation, determined by constituent groupings with the least rearrangement. Those atoms encircled or cupped by the dash-dot line form the proposed anion. Arrows indicate individual cleaved atoms, direction is arbitrary, hydrogen loss is designated randomly and not to be taken as the true location of the lost H atom.

Anion m/z	Chemical formula	Proposed cleavage pathways
16	O$^-$	
17	OH$^-$	
25	C$_2$H$^-$	
41	C$_2$OH$^-$	
49	C$_4$H$^-$	
50	C$_4$H$_2$$^-$	

Lilian K. Ellis-Gibbings - June 2018

51	C$_4$H$_3^-$	
65	C$_4$HO$^-$	
66	C$_4$H$_2$O$^-$	
67	C$_4$H$_3$O$^-$	
77	C$_5$OH$^-$	

2.2.4.2 Comparisons to literature

Furan (FN, Figure 10), as the base ring for furfural, is presumably the most likely molecule to exhibit similar DEA resonance behaviour. DEA of FN was studied along with tetrahydrofuran (THF) and fructose by Sulzer *et al.* in 2006[121], in a crossed beam high resolution experiment utilising a time of flight mass spectrometer. One aim of their study sought to determine the viability of using THF and FN as simple substitutes for the deoxyribose sugar in DNA, the furan based sugar that has shown important electron attachment processes in the past[122]. As they found significant differences between the DEA spectra of both FN and THF to fructose, their conclusion was that in this energy

range, neither are relevant analogues to this important structure in the DNA helix. Our results for furfural also differ significantly to those for fructose, confirming the assessment that the simple FN species in their various forms do not function well as deoxyribose analogues at low electron impact energies and the furan-based sugar itself should be used.

A comparison between furfural and FN (in Sulzer *et al.*[121]) is of interest to determine how small molecular changes (the addition of an aldehyde in this case) can affect DEA results. All 5 of the fragments seen in FN are also seen in the furfural anion yields, which can indicate that they form from the same dissociation pathways of the FN ring, not the aldehyde group. The published FN spectra all exhibit the same shape with two distinct resonances with similar energies – a strong resonance around 6 eV and a broad weak resonance around 10.5 eV, differing from the energies commonly seen in furfural of 5 eV and 8 eV.

One relevant comparison is that of the 67 m/z fragments seen in both experiments, from the [FN-H]$^-$ fragment and the (most likely) [furfural-aldehyde]$^-$ fragments respectively. For furfural a small resonance peak overlaid on a larger feature can be seen at 6.6 eV (see Figure 11B), close to that seen for FN at 6 eV. If these fragments in fact come from the same electron attachment resonance, it indicates that the H lost in FN is from the 1st or 4th ring carbon (clockwise from oxygen, these being equivalent in symmetrical FN) and that this bond is a weak point for both the C-H bond in FN and the C-C bond in furfural. Additionally, the small peak seen in the [FN-H]$^-$ yield between 3.5 and 4 eV corresponds to the largest peak for [furfural-aldehyde]$^-$ at 4.6 eV.

Furfural could have up to 3 π^* shape resonances, due to the additional double bond (C=O) found in the aldehyde group. These 3 low-lying resonances were theoretically investigated by da Costa *et al.*[15]. They estimated (*via* an empirical scaling of the shape resonances they had obtained theoretically) the vertical attachment energies of the 3 lowest lying π^* states to be $\pi^*_1 = -0.053$ eV (-0.063 eV), $\pi^*_2 = 1.97$ eV (1.89 eV), and $\pi^*_3 = 3.32$ eV (3.44 eV) for the cis (trans) isomers, respectively. Of the detected resonance features, 95 m/z has a clear sharp resonance at 3.8 eV, and the onset for the 4.6 eV

resonance of the 67 m/z anion begins at 3.2 eV, either of which could be assigned to either the π^*_2 or π^*_3 states above, considering the 0.5 eV energy resolution of any energy barriers that may be in place.

As with all gas phase experiments, there are limitations when applying this data to condensed phase situations, as with the use of plasma on biofuel precursors such as furfural, however a combination of gas and condensed phase studies are important for unravelling the complexities of low temperature plasma kinetics and other commercial uses. For further information on the products and likelihood of one fragment pathway over another, quantum chemical calculations could be performed as in Ryszka *et al.*[116], determining both the optimised structure, the expected change in enthalpy and the electron affinity of the anion group. To make the presented data applicable for the scattering community, a set of R-matrix calculations[99] for TNI cross sections could be performed and the TNI resonances produced by that calculation compared to the energies of the resonances detected here.

2.2.4.3 Conclusion

In conclusion, furfural shows strong fragmentation when compared to the biofuel esters in terms of count rates, and has a broad range of 16 anion masses detected. The 6 strongest fragments arise from anions 16 m/z (O^-), 17 m/z (OH^-), 25 m/z (C_2H^-), 41 m/z (C_2HO^-), 49 m/z (C_4H^-) involving a rearrangement of at least 2 hydrogens, and 67 m/z ($C_4H_3O^-$) likely *via* the loss of the aldehyde group. Of these, 25, 41, 49 and 67 m/z are seen in a previously reported DEA study of furan[121], though only 67 m/z have matching resonance energies. Most fragments have either a single clear resonance in the 7.5 – 8.9 eV electron energy region, or this resonance plus a lower intensity resonance at a lower energy, between 4.5 and 5.5 eV. The fragments at 95 and 67 m/z show resonance onsets that could be related to the π^* states calculated in literature, and both have an inversion of the intensity of their two resonances as compared with the norm. Due to the strong fragmentation in furfural around 7.5-8.5 eV, care should be taken during low temperature plasma treatment to avoid an electron temperature resulting in high numbers of electrons with these energies. As with FN and THF, the furfural DEA spectra differ significantly

from previously studied sugars and as such furfural is not recommended as a DNA deoxyribose sugar ring analogue, despite its advantages as a safe and cost effective liquid sample. Further work on furfural is found in Chapters 3 and 5 of this thesis, to select an appropriate cross section database for modelling, and implementing that database to investigate the effect of fine adjustments to the electron energy loss spectra in Monte Carlo models.

2.3 General Comments

Low energy gas phase collision studies provide valuable information on fragmentation and collision dynamics, not easily contributed by theory. The results in this chapter indicate that electrons with energy below the ionisation energy produce a diverse range of reactive fragmentation species (as with the biodiesel esters and furfural), they can have significant effects on their vibrational state (as with pyrimidine). Pyrimidine was shown to have higher vibrational DCS and ICS for 15 eV electron impact in the gas phase compared to condensed phase, and when compared to literature values at slightly higher energy. These results add to a database on the scattering dynamics of biologically important molecules for use in Monte Carlo particle tracking codes such as LEPTS. The esters studied show the DEA fragmentation of biodiesel esters of varying chain lengths, including the two most common in biodiesel production, methyl and ethyl alcohol esters. They exhibit weak to moderate strength anion yields, however each of the four esters produced a great variety of anions (13 – 21 individual masses detected per molecule), which are all capable of undergoing unwanted chemical interactions with their surroundings. As such, use of plasma pretreatment or processing will need to be carefully monitored for unwanted byproducts. In contrast, the furfural molecule showed more intense DEA count rates for 16 anion types. This in turn indicates that the use of plasma in processes where furfural is either the desired product or the undesired by-product should be carefully controlled to avoid the two major resonance ranges between 4.5 - 5.5 and 7.5 - 8.9 eV.

3 GAS PHASE EXPERIMENTAL DEVELOPMENT

Data relevant to the particle scattering community are not always measurable with current experimental apparatus[52] or provided by theory[123]. Two areas where theory is not able to produce the required data accurately are the electron energy loss spectra (EELS), and the dissociation of products of radical anion collisions with biomolecules. Experimental EELS are required by the LEPTS Monte Carlo particle tracking model (although theoretical formalisms have been derived for other codes[124]), and anion-biomolecule collisions serve to emulate the nanodosimetric action of radicals produced by radiotherapy, known to produce much of the damage to cells[54]. Experimental data on either of these processes are available for few targets. To fill this gap in the knowledge two experiments have been developed at CSIC, Madrid, and the author performed modifications, developments and characterisation of their function. The experiments described are a transmission gas cell experiment and a negative ion crossed beam experiment. These are used to measure electron energy loss spectra and to measure the fragmentation of molecules due to electron transfer from radical species, respectively. EELS of argon, acetylene and furfural, and preliminary results from O⁻-nitromethane

collisions and with a focus on experimental low energy ion beam improvement are presented. Each experiment is described in turn, along with any modifications or developments performed and tested, results collected and the analysis of results.

3.1 Electron transmission experiment development and electron energy loss spectra

3.1.1 Introduction to EELS

To accurately describe scattering processes in Monte Carlo models, a numerical profile of the energy lost by the projectile electron in all collision types is necessary. This is best provided by experiment, as the energy lost and intensity depends on the vibrational and electronic excitation levels, the ionisation limit, the appearance of any resonances, and their respective cross sections[29]. EELS are used directly in the Monte Carlo code LEPTS[67] to inform the kinetic energy lost by the projectile (this process is explained further in Chapter 6), and arise from experiment in the majority.

The non-resonant processes that can be detected *via* electron energy loss in this experiment include electronic excitation and ionisation. Vibrational excitations occur at energies and intensities too low to be detected and with levels too close in energy to be distinguished, however electronic excitations appear as peaks, often with Gaussian character and frequently overlapping. Ionisation, being available at the continuum of states above a threshold, appears as a double log decay (having linear character in a log-log plot). Excitation structures above the ionisation threshold are also seen in some molecules and are named 'pre-ionising' or 'auto-ionising' states[125].

EELS are produced by crossed beam and transmission electron spectroscopy, and in this thesis an electron transmission experiment was modified, improved and subsequently produced EELS for three targets. These were argon, acetylene and furfural, chosen to test the apparatus and for use in scattering models at moderate to high energy. The original experiment exhibited periodic issues with the electron source and the alignment of the equipment. Several modifications were made to avoid these issues and the final form of

the experiment is shown in detail in Figure 20, including a new electron gun and optics setup and a new frame to hold the original gas cell in exact alignment.

3.1.2 Original Experimental Set-up

The transmission beam experiment as it was inherited was described in the thesis of M. Fuss[126] and Figure 13 shows the original layout. The entire apparatus is housed in a high vacuum system with a base pressure below 10^{-6} mbar achieved through differential pumping. Electrons are produced by a tungsten wire filament *via* thermionic emission and extracted by electric fields into a beam, its direction controlled by two sets of parallel electrostatic plates and the focus by lensing electrodes. The beam passes through a gas cell of fixed length and variable target gas pressure, and those electrons that are unscattered or scatter only in the forward direction are guided to the entrance of a hemispherical energy analyser by another set of parallel electrostatic plates and focusing and retarding electrodes, before being detected by a channeltron-type detector. The gas sample is introduced to the collision chamber *via* a Varian leak valve, and the pressure detected by an MKS 627B capacitance manometer – this pressure is kept below 0.02 mbar to avoid multiple collision conditions.

The experiment collects EELS for small scattering angles by using the final parallel electrostatic plates in Figure 13 (3) to deflect the electron beam, so that the majority of unscattered electrons do not enter the hemispherical analyser. The only electrons able to enter the analyser are those which have undergone elastic or inelastic scattering to small angles (stated as 0-15° by Fuss[126]). To capture the energy loss spectra from excitation and ionisation processes the acceptance energy of the analyser is decreased in a constant fashion from slightly above the initial electron collision energy down to approximately 100 eV below this energy, collecting the scattered electrons.
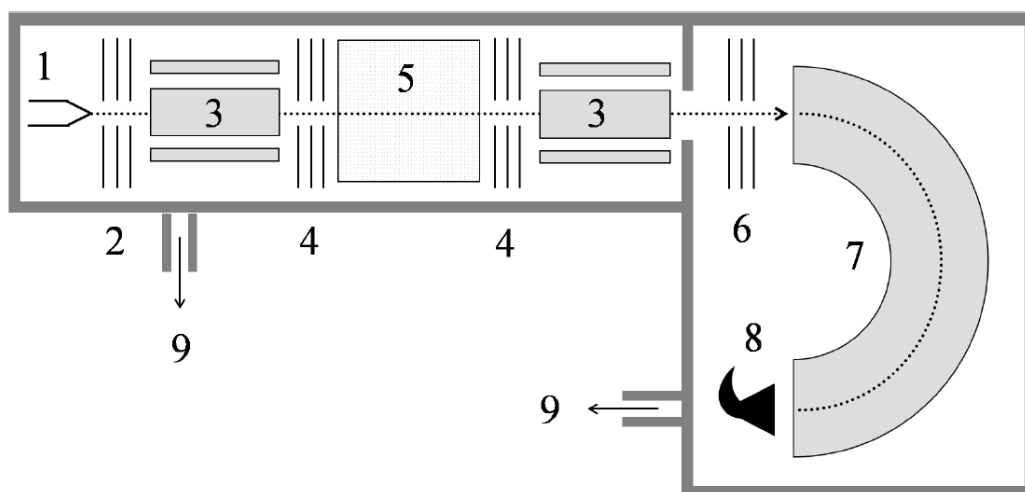
Figure 13 The electron transmission experiment, in its original condition. Image reproduced from Chapter 1.2 of the doctoral thesis of M Fuss[126]. 1: Electron emitting filament. 2: Extraction and accelerating electrodes. 3: Quadrupole electrostatic plates for beam deflection 4. Decelerating and accelerating lenses for beam focussing. 5: Collision chamber. 6: Retarding potential analyser. 7: Hemispherical electrostatic energy analyser. 8: Channel electron multiplier. 9: Turbomolecular vacuum pumps.

The experiment is functional for the 100 - 10 000 eV initial electron kinetic energy range. At these high energies the DCS for all processes are significantly forward peaked[29] and as such losses of electrons scattered beyond the acceptance angle are stated as ≤ 5 %[126]. The electron energy resolution is that of thermionic emission, 0.5 eV, and the resolution of the analyser adds to this, resulting in an overall energy resolution ≤ 2 eV. This energy resolution is suitable for identifying electronic excitations and ionisation curves but is not capable of producing vibrational EELS. Energy calibration of the electron analyser scale is achieved through analysis of the average number of channels between peaks of known electron energy with no gas in the system. The 'zero' for each EELS is the elastic scattering peak – momentum transfer lost through elastic scattering is too small to be detected in this set-up and so this is equivalent to the initial kinetic energy.

3.1.3 Adjustments to experiment

The issues with filament wear and electron beam alignment necessitated improvements to the apparatus. The additions to the experiment were machined to the author's designs by the on-site mechanical workshop (CSIC, Madrid), and installed by the author. Parts were re-used and scavenged where possible. Electrical separation of pieces requiring applied voltages is achieved using either Teflon or machinable glass ceramic (MACOR®) separating shields, also machined by the on-site mechanical workshop. Ceramic was preferable for all cases expected to be exposed to the electron beam or high intensity scattered electrons, as Teflon is not suitable for high temperature work. New pieces are non-magnetic stainless steel or aluminium.

3.1.3.1 Electron collision region

Much of the alignment problem was due to instability of the original design, where the gas cell was held in place only by the two Teflon tubes used as the gas inlet and outlet. The tubes screwed to the gas cell itself allowing freedom of rotation and therefore requiring much time and effort to align, and at risk of dislodgement due to vibrations. In the new design, shown in Figure 14, the gas cell is held in place by solid steel struts screwed into a modified CF100-CF40 adapter flange, hence the alignment is fixed to the experiment. The original 3-piece collision chamber is used and the same Teflon tubes screw into their respective holes to introduce the gas and read the pressure. The beam focussing lenses seen after the collision chamber in the original design have been replaced with electrostatic deflecting plates in x and y, seen in Figure 14 as small cubes near the left hand side of the apparatus.
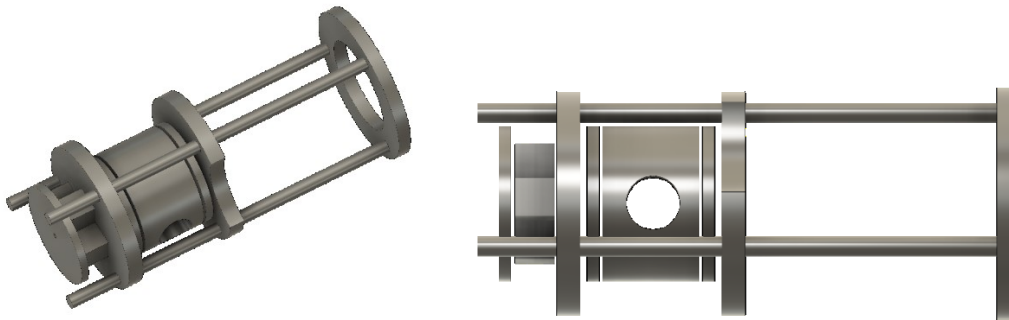
Figure 14 New design of gas cell apparatus to avoid beam alignment issues. Left exhibits the 'cubes' used for beam deflection after the collision chamber, the three struts for stability and the cut-out made to the central structural electrode to enable passage of wires. Right exhibits the holes in the central cylinder that forms the collision chamber, where gas enters and the pressure is read.

Electron beam
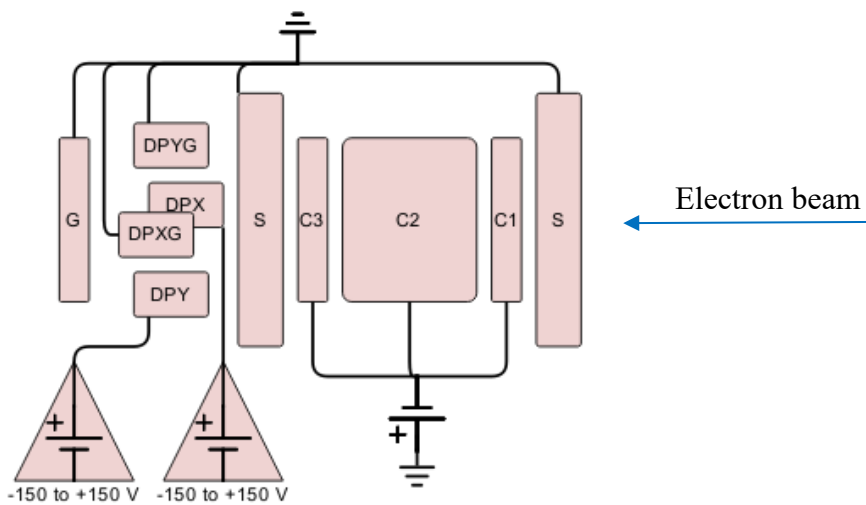
Figure 15 Circuit diagram of the collision chamber setup. Collision chamber (C1, C2, C3) and deflecting plates (DPX, DPY) connect to external DC power supplies. Structural discs (S), deflecting plates (DPXG, DPYG) and final grounded electrode (G) are all grounded.

Lilian K. Ellis-Gibbings - June 2018

The two large discs shown in Figure 14 are held in place by adjustable screws that allow the entire collision chamber system to slide along the struts, to align perfectly with the gas inlet tubes. This direct contact means they are electrically grounded, as are two of the deflecting 'cubes' and the final exit electrode seen on the left hand side of the apparatus. These ensure that the kinetic energy of the electrons is always with respect to ground as they enter and exit the collision chamber, whereas the voltage applied to the collision chamber itself can be used to artificially lower the collision energy. These details can be seen in the circuit diagram in Figure 15. The power supplies used to electrostatically bias the collision chamber and deflecting plate elements were built at the Centro de Investigaciones Energéticas, Medioambientales y Tecnológicas (www.ciemat.es, Madrid, Spain) for this purpose.

The dimension of all the pieces are shown in Figure 16. New pieces were machined according to these designs by the technical support staff at CSIC and installed by the author.
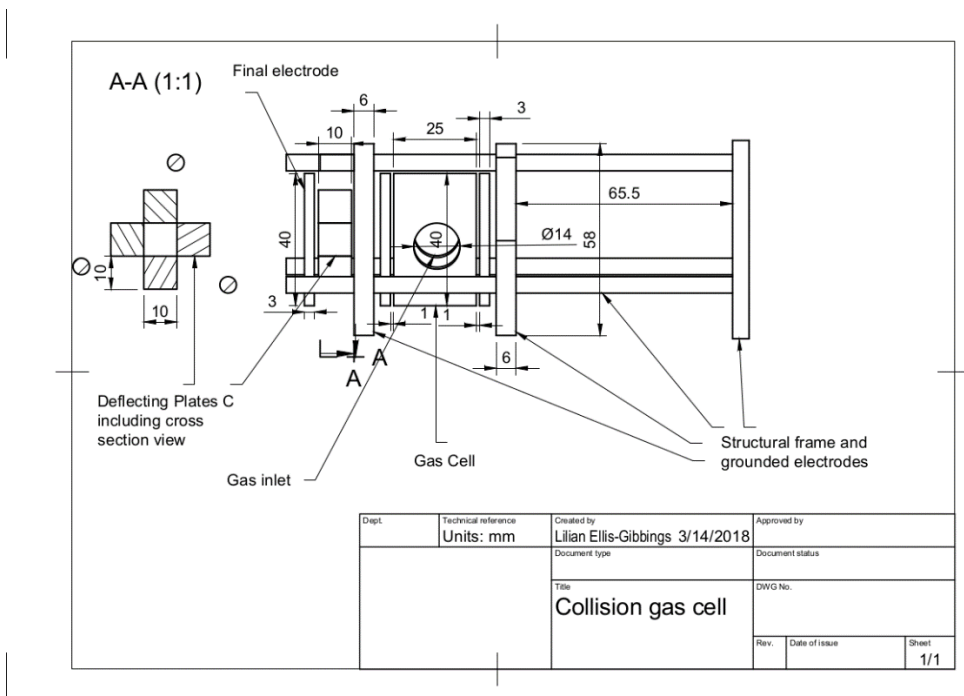
Figure 16 Dimensions of new electron collision chamber installed in electron transmission experiment. All annotations in mm.

3.1.3.2 Electron gun and beam optics

Regular filament fractures and unstable current fluctuations, such as those found in the original apparatus, are often due to high background pressure in the filament region and the adsorption of the target molecule onto the filament itself, where burnt chemical buildup inhibits regular electron emission. Separating the electron gun further from the collision region and, in the best case, differentially pumping the electron gun region, are appropriate measures to counter these issues.

The new design, pictured in Figure 17, increased the distance from the gas cell to at least 65 mm with the electron gun installed on the opposite side of a blank QF flange with an aperture of 2 mm for the passage of the electrons. In this way, the pressure in the region of the filament is kept constant during measurements, reducing filament wear and pressure related current fluctuations. To control the electron beam, an existing 3-element electrostatic Einzel lens made of 3 cylinders, and two sets of deflecting plates for dimensions x and y were installed in the additional space.
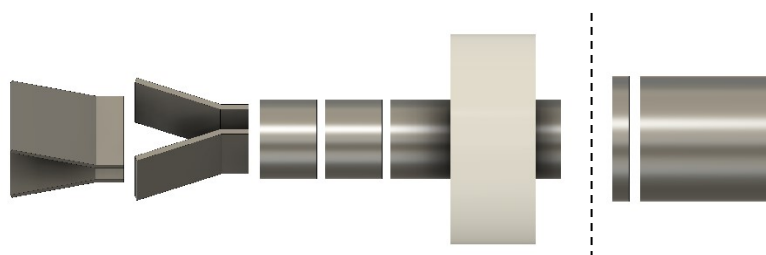
Figure 17 New design for electron gun and newly installed electron beam optics. Dashed line indicates the divide between the electron production and collision chambers.

The white disk in Figure 17 is a Teflon housing machined to seat the electron optics into the CF40 to QF40 adapter flange that holds the electron optics. A solid QF centring ring with a 2 mm aperture separates the electron gun chamber from the interaction chamber, indicated by the dashed line in Figure 17 and enabling differential pumping between the two regions. The gap between the electron extractor and the first element of the Einzel lens is adjustable by the placement of the Teflon housing in the CF40 nipple. The

electronic setup for the electron gun and optics are shown in Figure 18. The variable power supplies for electrically biasing the lens and deflecting plate elements were built at CIEMAT for this purpose, and the two power supplies that make up the filament and kinetic energy system are both from Bertran. Repeller (R) and extractor (E) (Figure 18) are electrically biased with the same circuit as the filament (F), to enable gentle electron extraction, with a potential difference of approx. 2 V above the voltage applied to the filament by the accelerating power supply unit. Additionally, the repeller has been machined such that the filament sits within a cone shaped aperture with the larger exit facing the extractor, similar to a Pierce electrode. The Einzel lens L2 and deflecting plates DPX and DPY each have a variable -150 to +150 V power supply. All other pieces are physically grounded with a common earth point. The dimensions for the pieces are annotated in Figure 19. The setup is approximately 150 mm in length and is stable in standard vacuum equipment of inner diameter 40 mm.
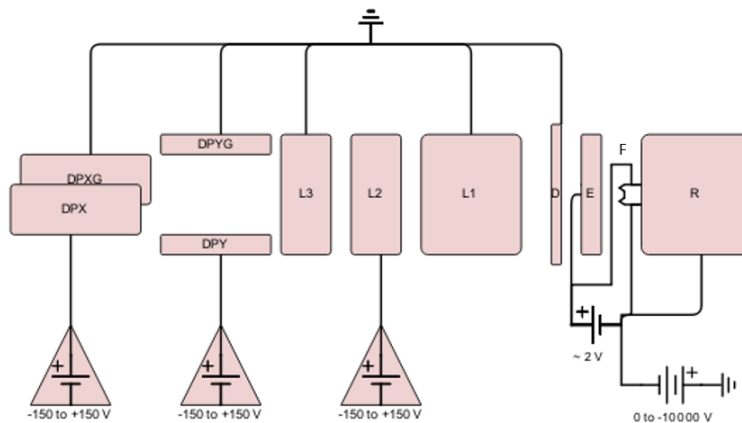
Figure 18 Circuit diagram for the electron gun and optics setup. Repeller (R), Filament (F), Extractor (E), Einzel lens (L2), deflecting plate (DPY) and deflecting plate (DPX) connect to DC power supplies. All other pieces (Einzel lens L1 and L2, deflecting plates DPYG and DPXG, differential pumping divider D) are grounded.
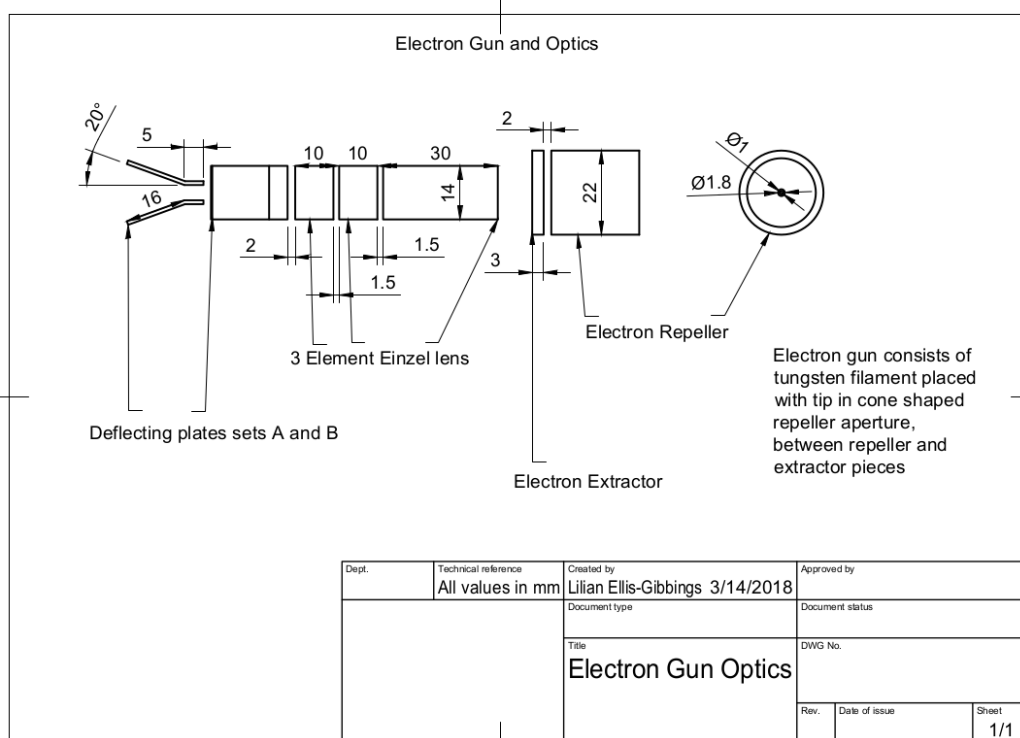
Figure 19 Electron gun and beam optics design schematics. All dimensions in mm. The cross section of the electron repeller is additionally shown and its cone shaped aperture has the larger diameter facing the electron extractor.

3.1.3.3 Final set-up

The electron gun and its optics fit into the structural frame *via* the Teflon piece as shown in Figure 20 (left). The freedom to adjust both the position of the electron optics *via* the Teflon tube and the collision chamber *via* the screw clamps enable flexibility when aligning with the gas inlets and adjusting for electron beam intensity. The electrons pass from right to left and following their exit from the last aperture then enter the parallel electrostatic plates, retarding potential analyser, hemispherical energy selector and channeltron-type detector of the original experiment.

Lilian K. Ellis-Gibbings - June 2018
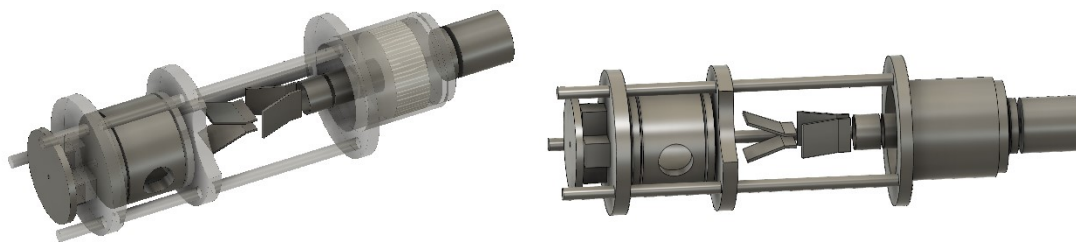
Figure 20 Left: Indicating the attachment procedure of the electron optics to the frame of the collision chamber *via* a tightly fitted Teflon cylinder. Right: Final configuration of the new electron gun, electron beam optics, and collisions chamber for the electron transmission experiment.

3.1.4 Results

With the greater stability and control provided by the new set-up, EELS were measured for three targets: Argon, acetylene and furfural. Peak assignment was possible (within the energy resolution) for all prominent peaks in argon and acetylene, and those below the ionisation threshold for furfural. No literature on the autoionising states of furfural above the ionisation threshold could be found.

Argon

Argon EELS were measured for energies ranging from 0.4 keV to 2 keV and found to differ little across this energy range. A summed and normalised spectrum is shown for 1 keV electron impact energy in Figure 21.

Excitations of four electronic levels between 11.5 and 12 eV were previously investigated by crossed beam electron scattering[127], assigned to various $3p^54s$ spin states. Due to the broad energy resolution (< 2 eV) these individual states are not distinguishable in the EELS shown here, however the excitation is still clearly visible as a single peak with a maximum at 11.7 eV (scatter point 1 in Figure 21). Further excitation states are expected at ~ 13 eV and ~ 14 eV (scatter points 2 and 3 in Figure 21), based on threshold energy electron transmission studies[128] – they suggest these states are excitations of 4p or 3d orbital electrons. At this high energy, no clear excitation occurs at 13 eV, however the 14

eV excitation is observed as the second highly visible peak in the Argon EELS with a maximum at 14.2 eV. This excitation is expected to be a combination of the two states $3p^5(^2P_{3/2})5s^2$ at 14.05 eV and $3p^5(^2P_{1/2})5s^2$ at 14.21 eV seen in the study of Brunt *et al.*[129]. Brunt *et al.* also identified metastable electron excitations at 14.54 and 14.82 eV (scatter point 4 in Figure 21), which they did not attempt to identify, and which may be responsible for the high count rates at energy losses preceding the ionisation energy of 15.76 eV (green line in Figure 21).
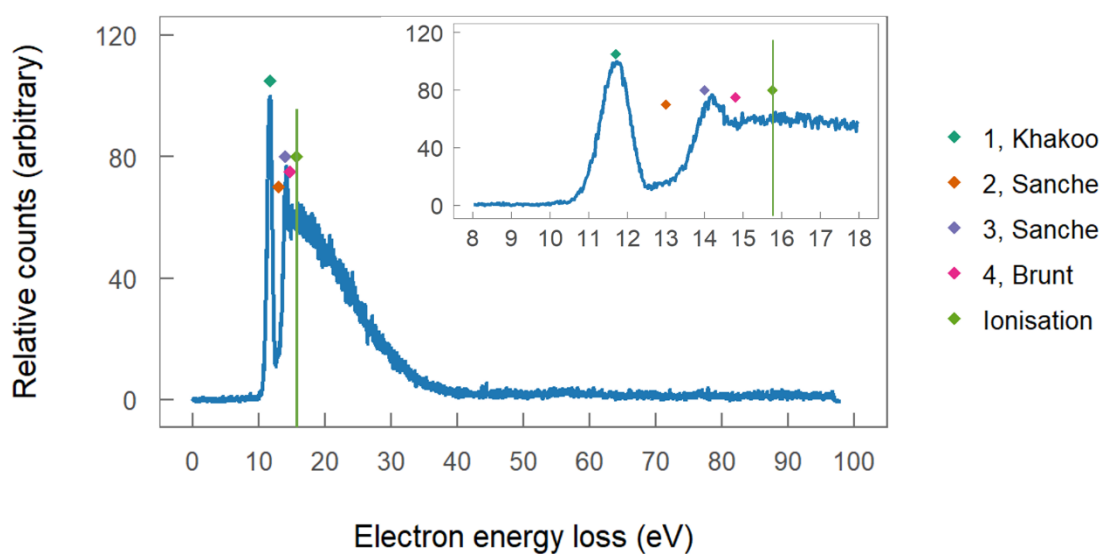
Figure 21 EELS spectra of argon gas at 1 keV electron impact energy. Green line represents the summed ionisation threshold of Argon. Inset shows electronic excitations compared to literature values (scatter points 1-4) investigated further in the text.

Acetylene

Acetylene EELS were measured for electron kinetic energies ranging from 0.5 keV to 2 keV and found to differ little across this energy range. A summed and normalised spectrum is shown for 1 keV electron impact energy in Figure 22.

Assignments of the features of the EELS of acetylene stem from the literature and are as follows. Collin and Delwiche[46] studied the electronic energy levels associated with the

ionisation but also mention an excitation at 5.23 eV, seen as a small peak in this spectrum at 5.4 eV (scatter point 1 in Figure 22). The shoulder at 8.2 eV in this spectra was previously studied by Nostrand *et al.*[47], and identified as an excitation of the carbon triple bond to a Rydberg state (scatter point 2 in Figure 22). Wilkinson[48] recognises a Rydberg excitation in the IR spectra of acetylene at 9.2 eV (scatter point 3 in Figure 22), matching the highest intensity peak at 9.4 eV. Ionisation of acetylene occurs above 11.4 eV[111], and it is clear from the spectra that there are two recognisable resonances above this limit. In accordance with the work of Collin and Delwiche[46] and references therein they are assigned to Rydberg pre-ionised levels, i.e. autoionising decay of a neutral excited state. This is true for both structures, at 13.25 eV and 15 eV respectively (scatter points 4 and 5 in Figure 22), with the presence of a singlet and triplet states of $\sigma_g\pi_u^4\pi_g^*$ or $\sigma_g\pi_u^4\sigma_g^*$ suggested. These two states are assigned to the peaks seen in the spectra that fall at 13.0 and 15.5 eV respectively, still well within the energy resolution of the apparatus. The second ionisation threshold is present at 16.25 eV as the second green line.
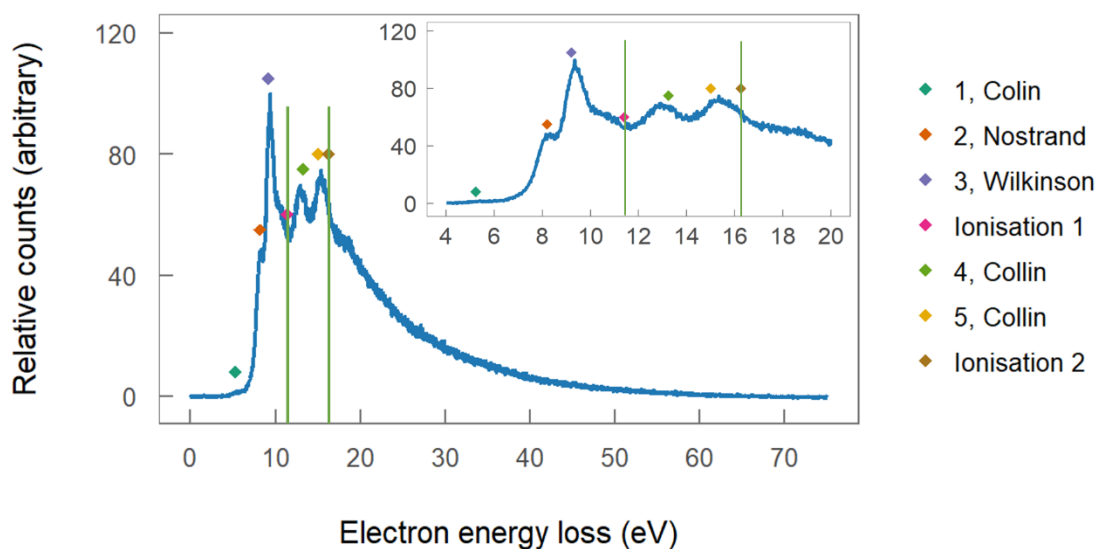
Figure 22 EELS of C$_2$H$_2$, acetylene at 1 keV electron impact energy. Green lines represent first and second ionisation thresholds of acetylene. Inset shows electronic excitations compared to literature values (scatter points 1-5) investigated further in the text.

Furfural

Furfural EELS were measured for energies ranging from 400 eV to 1 keV and found to differ little across this energy range. A summed and normalised spectrum is shown for 1 keV electron impact energy in Figure 23.

The electronic states of furfural have been studied *via* VUV spectroscopy, electron energy loss at high scattering angles, and *ab initio* calculations by Ferreira da Silva *et al.*[120] up to 10.8 eV. Their work has been used to identify and verify the following excitation peaks seen in the furfural EELS. The peak at 5.2 eV is a π to π* transition (scatter point 1 in Figure 23) seen at 5 eV in the literature. 7.895 eV was identified as another π to π* valence transition (scatter point 2 in Figure 23) and corresponds to the shoulder in the EELS at 8.2 eV. Assignment of higher energy electronic excitations is complicated, as da Silva *et al.* recognised at least 4 contributions to the EELS between 7 and 10 eV (scatter point 3 shows upper limit of 10 eV in Figure 23). Aside from the shoulder already identified, the intense peak at 9.6 eV may easily hide lower intensity excitations. As with acetylene autoionising excitations are visible above the ionisation limit of 9.22 eV[111], at 13.3 and 15.6 eV. Unfortunately, no study of pre-ionisation or autoionising states above the first ionisation limit could be found in the literature.
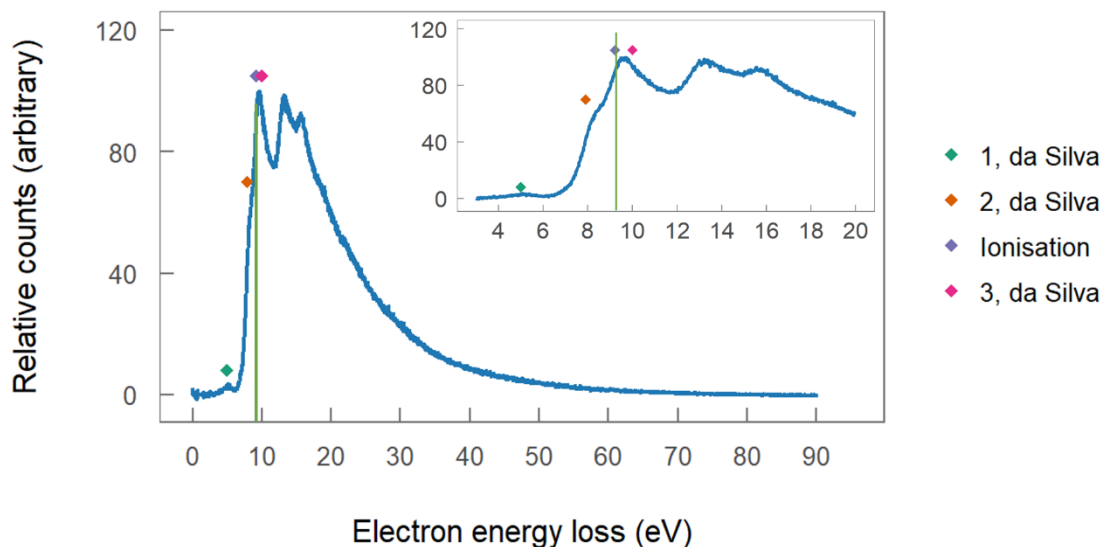
Figure 23 EELS of C$_5$H$_4$O$_2$, furfural at 1 keV electron impact energy. Green line represents the ionisation threshold of furfural. Inset shows electronic excitations compared to literature values (scatter points 1-3) investigated further in the text.

3.1.5 Conclusion

The reconstruction of the transmission beam experiment *via* design and installation of a new scattering chamber, ion optics and electron gun setup was successful in stabilising the instrument. This led to the measurement of electron energy loss spectra for 3 targets: argon, acetylene and furfural, with assignment of excitation structures made where possible. Both acetylene and furfural show evidence of excitations above their ionisation thresholds, indicating autoionising states. These spectra are now a part of the LEPTS database for the modelling of electron and positron scattering. The EELS of furfural is revisited in Chapter 6 regarding the ionisation of the inner shell electrons.

3.2 Anion collision experiment

Radicals are known to cause major damage in cells during ionising radiation, shown most prominently in experiments utilising radical scavengers and investigating cell survival[130]. Collision experiments have difficulty in producing radical beams at low impact energy to provide details on the cross sections and products of interactions between radicals and

molecules of biological importance. To bridge this gap, an experiment at CSIC has been built to provide data on oxygen anion collisions with gas-phase molecules. Preliminary results, an energy resolution study and improvements to beam optics are presented here.

3.2.1 Introduction to discharges and electron transfer

This experiment aims to investigate the transfer of an electron from the anion to the target molecule. The attachment of an electron to a target molecule results in a TNI which can decay *via* either an autodetachment process or the dissociation of the molecule into an anion and one or several neutral fragments, as described in Chapter 2. In the case where the attached electron is not free, but is transferred from a slow moving projectile, the presence of the neutral projectile body post transfer has been shown to have a stabilising effect on the decay[50,131,132]. At higher energies it is known that anionic projectiles are capable of ionising target molecules[51].

The ion source in this experiment is a hollow cathode discharge. Within a discharge electrons are stripped from atoms and molecules and move easily according to the electric and magnetic fields present, whereas ions, being heavier, have lower mobility (for short time frames)[133]. In these systems the electron 'temperature', given by the distribution of velocities, is higher than the ion 'temperature', hence the system in not in equilibrium. Hollow cathode discharges sustain themselves at low voltage, pressure and ion temperature[134]. They are characterised by a significant decrease in voltage after ignition of the discharge. This voltage then follows an oscillatory path, with cycles in the order of $300\mu s$[135].

Within the discharge, anions can be formed by free electron attachment to neutral atoms or molecules. The formation of a thermodynamically stable anion for use in electron transfer experiments depends on the electron affinity of the discharge gas. In general a positive electron affinity for an atom or molecule indicates that a stable anion may be formed[136]. Oxygen is the gas of choice in this case as it easily forms a discharge, is available in high purity and has been well studied[137], as well as being highly important to

radiation chemistry[138]. The electron affinity of O is 1.6 eV and O_2 is 0.45 eV[111], indicating that the atomic anion may be more stable.

O_2 in the ground state has a DEA resonance around 6.7 eV with a maximum cross section near 10^{-18} cm^2 (ref 139). Non-dissociative electron attachment to O_2 proceeds *via* collisions with thermal electrons of energy near 0 eV, followed by deexcitation *via* collisions with a third body[139]. The first singlet state of oxygen has a higher electron attachment cross section than the ground state, and this metastable state is produced in discharges - increasing the likelihood of electron attachment to oxygen using a discharge system[140].

The anion population in the plasma[141] is based on the electron temperature, the electron density, the gas density, the attachment cross sections to the gas molecules, the ion temperature (typically low in hollow cathode plasma), and the populations of excited molecules[142] and singly and doubly ionised O ions. Recombination reactions decrease the quantity of negative ions available[22].

Once formed, oxygen anions can be extracted from a hollow cathode discharge source by electric fields to form a beam suitable for collisions with various gases. As nitromethane collisions with anionic and neutral radicals have been studied in the literature, preliminary collisions experiments on this apparatus were undertaken with nitromethane as the target molecule. This molecule has been introduced in Chapter 1, and a brief review of appropriate literature follows here.

Of note is the study performed with O$^-$ beams impacting nitromethane[51], with an impact energy of 4 keV. This energy is more suitable for atmospheric and astronomical studies, as the charged radicals produced by radiotherapy should have kinetic energies close to 0 eV. Nonetheless, this paper provides a useful benchmark for some collisions, and assists in cation and anion assignment. At 4 keV the anionic collision products detected were the parent anion ($CH_3NO_2^-$), NO_2^- and H$^-$, with the parent clearly dominant. This result shows stabilisation of the parent anion, absent in electron attachment studies[143]. In terms of cations, the group published ionisation data from the anion collisions, indicating major

contributions from 1 m/z, 15 m/z, 30 m/z, 46 m/z and 61 m/z. Different anion projectiles affected the intensity of these fragments.

A pathway for electron transfer is also available from collisions between neutral alkali atoms and molecules, such as the potassium-nitromethane collisions by Atunes *et al.*[50] and potassium-DNA base collisions of Ferreira da Silva *et al.*[132]. Potassium-nitromethane collisions occurred at 30-100 eV collision energy and the anionic products detected were the parent ion ($CH_3NO_2^-$), the singly dehydrogenated ion ($CH_2NO_2^-$), NO_2^-, CNO^-, OH^- and O^-. NO_2^- was the dominant fragment, followed by O^-. The results suggest that the parent anion is formed from an electron attachment to an excited Rydberg state which relaxes to a geometry where autodetachment may be blocked.

The hollow cathode anion source provides a beam of oxygen and molecular oxygen anions for collisions with target molecules, where an electron transfer can occur, resulting in anions and anionic fragments being formed from the target molecule. These product anions can then be detected in a time of flight mass spectrometer. The experiment and preliminary investigations are described in the following sections.

3.3 Experimental set-up
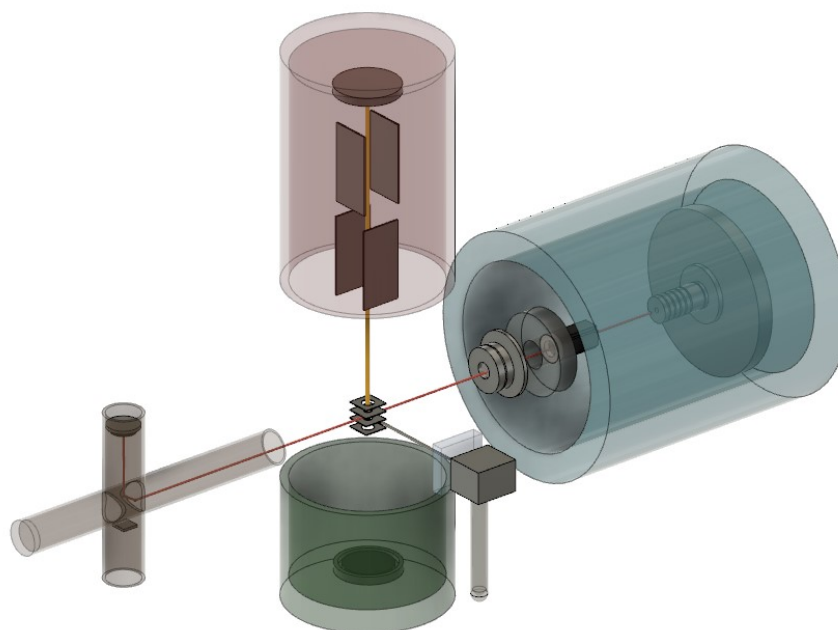
Figure 24 Entire system, with transparent cladding. Blue: ion production, Red: Reaction product time of flight 1, Green: Reaction product time of flight 2, Bronze: Beam analysis time of flight and window

The experimental system itself is shown in Figure 24. Chamber 1 is shown in blue, and is differentially pumped, reaching pressures of 10^{-7} mbar with a running pressure of 10^{-4} mbar during experiments. It houses the hollow cathode apparatus, consisting of a commercial Parker pulse valve (VAC1250) inlet from a gas source leading to the cathode and Einzel lens setup shown in Figure 25 (including dimensions). These pieces have applied voltages from a combination of house-built and Bertran power supply units. As the gas enters *via* supersonic expansion from the valve, open for approximately 200 µs in 500 µs cycles, the increase in pressure within the cathode brings the system into the conditions for discharge. As the pressure inside the cathode reduces with the valve closed, the discharge is no longer sustained. As such, the discharge itself is pulsed by the valve frequency, and anions are formed both during the discharge cycle and in the afterglow where electron attachment has higher probability[140] due to a higher proportion of the

oxygen molecules existing in an excited state[142]. This setup allows for a simple, passive electronic system for the hollow cathode, as shown in the electronic diagram in Figure 26. This diagram exhibits the 'floating voltage difference' method to ensure that the voltage difference between the cathode and anode remains the same (approximately 400 V), while both are able to increase or decrease with respect to ground according to the voltage of the second power supply. This method is used to lower the kinetic energy of the extracted ion beam.
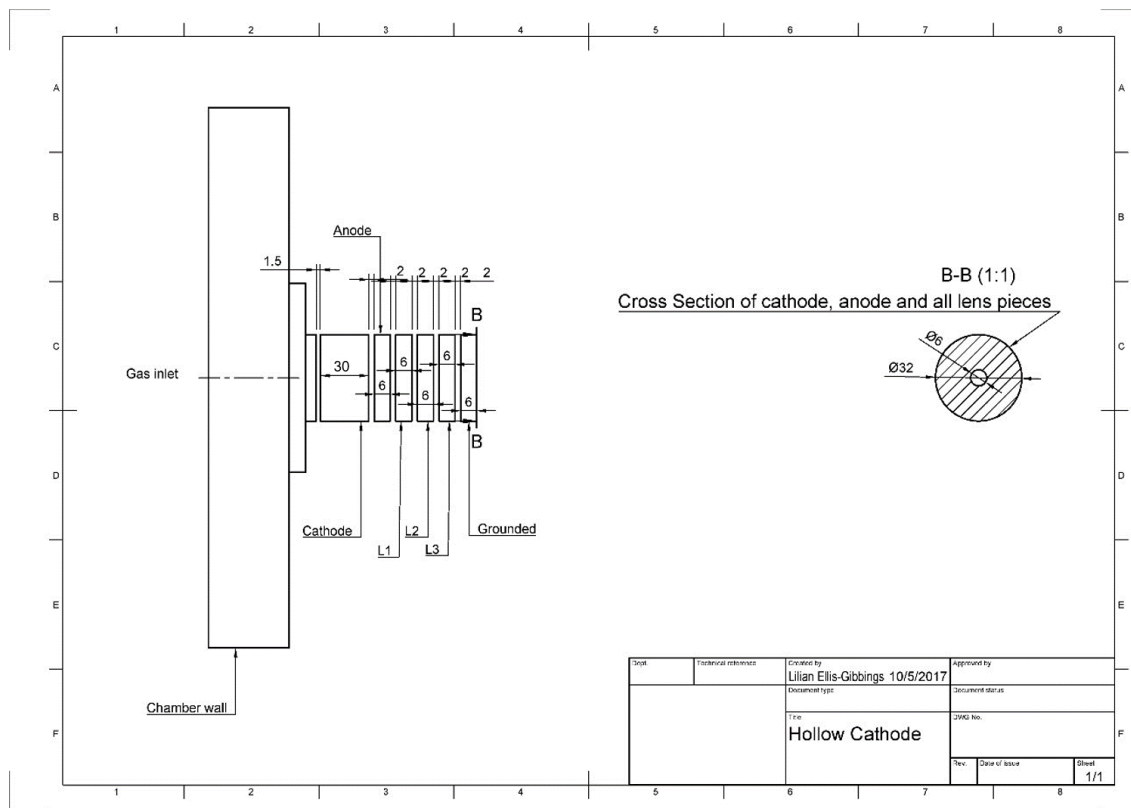
Figure 25 The hollow cathode and lens system
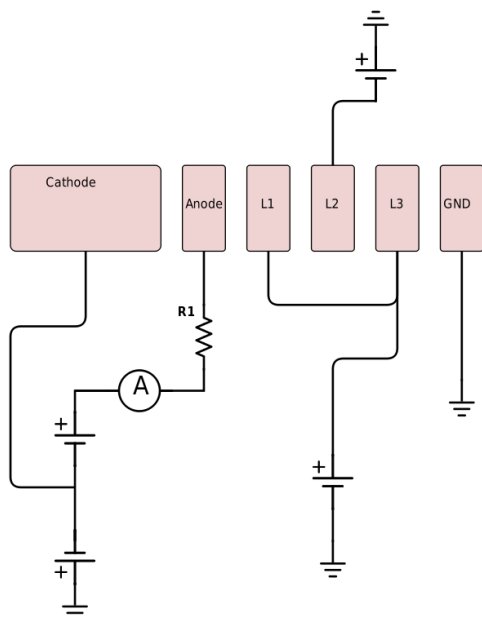
Figure 26 Hollow cathode electronic setup indicating floating voltage used to control the kinetic energy of beam. L1, L2, L3 form an Einzel lens to focus the anion beam.

The anions that are formed during and after the discharge pulse are extracted by the positive voltage of the anode. Extraction is possible from within the hollow cathode and from the region between the anode and the cathode. Accelerated anions pass through the 6 mm wide aperture in the anode and form the anion beam (red line in Figure 24). With this trajectory, the anions then encounter the first Einzel lens (L1, L2 and L3 in Figure 26), which serves to focus the beam and physically block ions with radial velocities. The final electrode in this setup is kept grounded to ensure the kinetic energy of the ions is equal to that of the cathode voltage.

All negatively charged species within the discharge extraction region can be extracted by this setup. To reduce the influence from electrons and extraneous anionic species, a Wein filter is installed before the exit of the source chamber, utilising two neodymium rectangular magnets and two sets of deflection plates. As is well known[144] a Wein filter serves to filter a beam of charged particles by balancing the lateral acceleration of electric

and magnetic fields for a particular mass. It is particularly effective when the aim is to remove an electron component from an ion beam, as is the case here.

Following the Wein filter is an aperture of 4 mm diameter, through which lies the interaction chamber, differentially pumped to below 10^{-7} mbar (central area, no cladding, Figure 24). Here, a second Einzel lens focuses the now collimated beam into the interaction region, a space 10 mm x 10 mm x 10 mm with extraction electrode grids placed above and below for extraction of charged products. The beam crosses with the effusive target gas beam, entered *via* a leak valve represented by the metallic box from lower right in Figure 24. The target can be a gas, liquid or solid, held in a test tube attached to the leak valve. For solid targets, the test tube is placed inside an external home-built oven apparatus for sublimation.

In the interaction region the anion can transfer an electron to the target molecule, forming an anion or inducing dissociation. The charged components are extracted into two time of flight (TOF) tubes, according to their charge. The extraction voltage pulses are synchronised with the gas inlet plus a variable delay, tuned to the collision time (i.e. the appearance of charged species). The anion fragment TOF tube (with red cladding, Figure 24) is 1.12 m long and houses two sets of electric deflectors, while the cation fragment TOF tube (green cladding, Figure 24) is 0.50 m long. Each TOF includes a Microchannel plate detector (MCP) to produce an electron pulse to detect charged particle impact. As with all TOF MS, masses are separated by velocity and charge, allowing mass/charge identification in the time spectrum produced.

The final region of the experiment, the beam analysis region, is depicted with bronze cladding in Figure 24. The incident beam is studied *via* a smaller TOF, with extraction into the TOF region *via* a deflecting plate with an applied voltage of -900 V. This provides information on the composition and intensity of the incident anion beam. A window allows a clear line of sight to the discharge region, facilitating alignment and analysis of the discharge composition by colour and pulse regularity.

3.4 Initial Results

The ion beam resulting from the above setup was collided with a molecular beam of nitromethane as a collaborative experiment between our group in CSIC, Madrid, and the Portuguese group of Professor Paulo Limão-Vieira (Universidade Nova de Lisboa). The results are published in Oller *et al.*[52] with the respective affiliations of the authors, and presented here. Additionally, studies made solely by the author of the energy resolution and beam intensity are also presented.

3.4.1 First fragmentation experiments - Nitromethane

The first results from the experiment as described were on the molecule nitromethane, a test molecule for which the electron transfer fragmentation is well known[50,51]. A common explosive, nitromethane is introduced in Chapter 1.

Oxygen was used as the projectile gas with ion extraction from the plasma at a kinetic energy of 250 eV. The collision product extraction consisted of a pulsed electrostatic field of −600 V, 0-8 μs variable width, 80 ms total cycle and 1500 μs delay from the anionic pulse beam, applied to the extraction grids. Cations resulting from these collisions were not studied. Nitromethane was obtained from Sigma-Aldrich with a stated purity of ≥ 96% and subject to repeated freeze-pump-thaw cycles to eliminate dissolved gases.

The anion beam, as detected in the beam analysis MCP of the system, is shown in a time spectrum in Figure 15. As can be seen, the oxygen pulse is well above background levels and appears at the end of the detected signal, an indication that charged oxygen species are best extracted from the afterglow stage of the plasma.
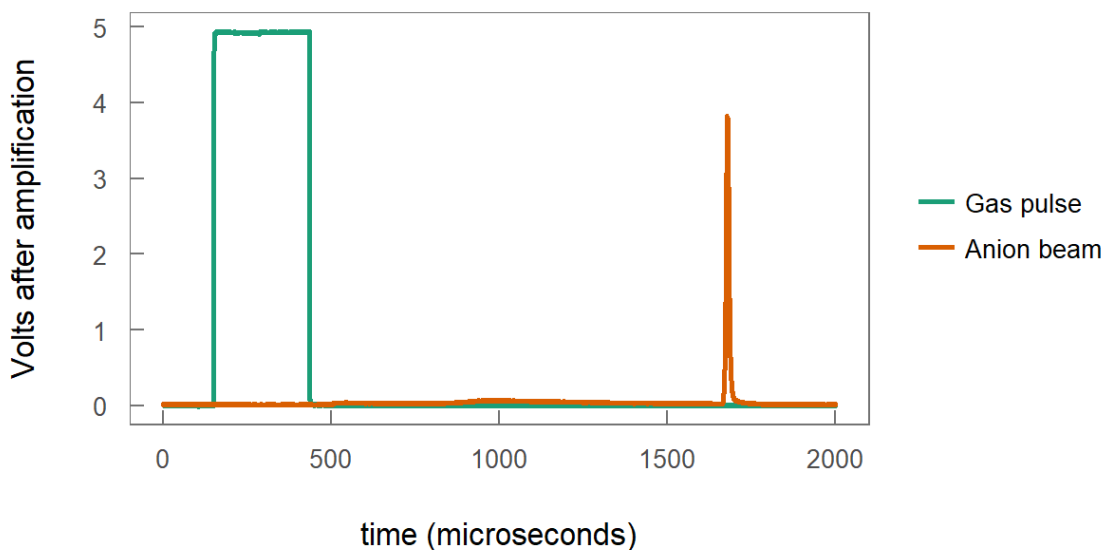
Figure 27 Oxygen beam spectrum overlaid with gas pulse signal detected in final beam analysis MCP.

O^--nitromethane collision product anions were extracted from the collision region into the vertical time of flight tube. Their spectrum is shown in Figure 28, along with the anion beam detected post collision. As can be seen, what appears as a peak in Figure 27 shows pre-peak features when a smaller time scale is used, as in Figure 28.

The anion beam curve shows a dip shortly after the application of the extraction pulse, attributed to deflection of the beam by said pulse. The time difference between these phenomena simply arises from the MCP detector for the anion beam being located approximately 0.4 m from the collision region. The anions that are deflected from their path have 250 eV kinetic energy, and as such this deflection is not sufficient to allow them to reach the TOF detector for the fragment ions. Time of flight analysis has made possible assigning the spectral peaks of the TOF MS signal to fragment anion masses, and these are indicated in Figure 28. In brief, the anion fragments detected include the parent anion, $CH_3NO_2^-$, and the fragment anions CNO^-, NO^-, O^- and H^-. The presence of the parent anion may indicate either a 3-body interaction responsible for stabilisation or radiative decay of the TNI to a stable anion, made possible due to the positive electron affinity of nitromethane[136].
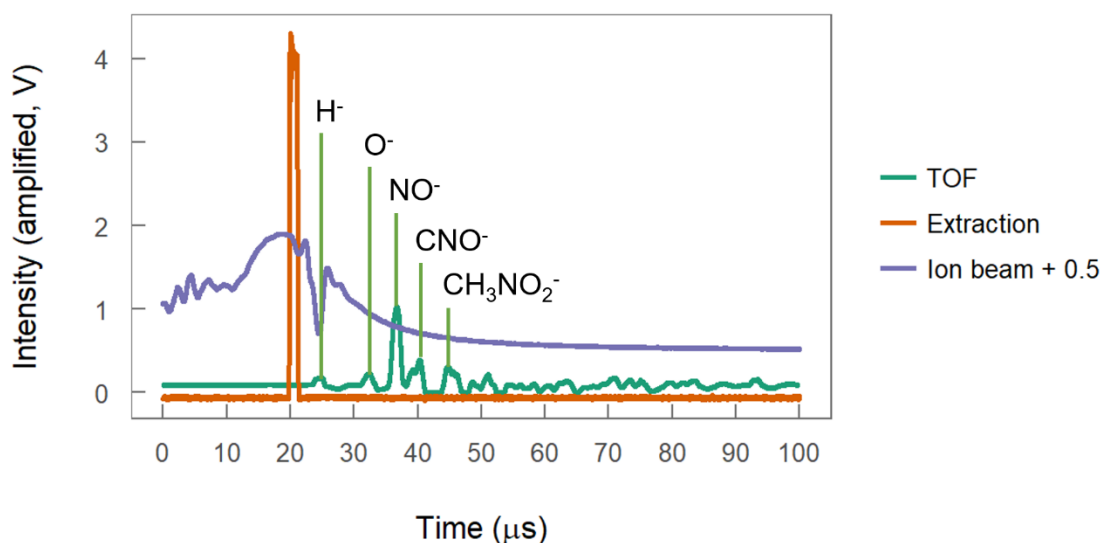
Figure 28 Product anion mass spectra from O⁻ anion collisions with nitromethane, overlaid with the extraction pulse and O- ion beam (+ 0.5 V for visual clarity).

The electron attachment interaction DEA (see Chapter 2 for description of DEA), has been studied previously for nitromethane by Alizadeh *et al.*[143]. The group detected many anions from fragmentation, the strongest signals coming from NO_2^-, O^-, OH^-, CN^- and CNO^-. Of these, CNO^- and O^- are seen in O^--nitromethane collisions. In weaker signals, the authors also reported H^-, but the parent anion and NO^- were not detected. The DEA experiments were carried out in the 0-16 eV electron impact energy range.

In a recent study[51] of closer significance, nitromethane fragments have been detected following collisions with O^- at 4 keV. Both cations and anions were detected, but of the anions $CH_3NO_2^-$, $CH_2NO_2^-$, NO_2^-, CH_3NO^-, O^- and H^- reported, only H^-, O^- and the parent ion $CH_3NO_2^-$ match those detected here. The detection of cations infers that this higher energy collision does not proceed solely by electron transfer.

This result can also be compared with recent electron transfer experiments involving neutral potassium beams at 30, 70 and 100 eV collision energy[50]. All the anions detected in the experiment presented here were seen in potassium electron transfer experiments. There the parent anion was detected *via* the attachment of a Rydberg electron. CNO^- was weakly detected, along with NO^- and H^-, while O^- showed a stronger signal than the parent

anion. NO_2^- was the dominant fragment in potassium-nitromethane collisions and this was not detected here, along with several lower intensity anions ($CH_2NO_2^-$, CN^-, OH^-) that also appeared in the DEA study mentioned previously[143]. Their absence may be due to the difference in impact energy, as neither CN^- nor OH^- were seen in the 4 keV O^--nitromethane study nor in this 250 eV O^--nitromethane study. The potassium beam collisions most closely represent the O^--nitromethane results here and as such electron transfer can be considered a likely source of the ions detected.

3.4.2 Energy resolution

The energy resolution of the O^- beam is of paramount importance in understanding the collision dynamics and in comparing results across different apparatus and theory. This project attempted to profile the kinetic energy distribution of the anion beam using both experiment and simulation.

Additional to the experimental studies, simulation of the ion paths in the system can assist in understanding the energy resolution of the experiment. The ion flying charged particle trajectory simulation program SimIon[145] can analyse the kinetic energy and location of all simulated particles when they 'splat' – that is, when they collide with one of the pieces (instances) built into the system. Instances can be electrostatic or magnetic, and grounded pieces are implemented as electrostatic with applied voltage of 0 V. The electric and magnetic fields are determined by 'refining' the array of user input instances by solving the Laplace Equation (or Poisson Equation for dielectrics). Particle trajectories are then solved using the Lorentz Force of the refined array of instances and user-set initial conditions. Data including ion trajectories and splat details can be exported. As space charge is not easily simulated within SimIon, the distributors recommend caution when interpreting results.

A grid was installed in the (non-simulated) central electrode of the second Einzel lens in order to retard the ion beam. A negative voltage was applied by a Bertran power supply with capacity up to 2 kV. The intensity of the beam detected at the beam MCP, or on a Faraday cup placed after the Einzel lens, should be reduced when the retarding voltage is

equal to the kinetic energy of the ions in the beam. Once the voltage applied surpasses the kinetic energy of all ions, the signal is reduced to background levels. In this way, a study of intensity (total counts for peak minus background) vs retarding voltage for the pure oxygen beam, with no target gas present, gives the energy spread of the ion beam, as in the example in Figure 29. A retarding voltage equal to the applied kinetic energy + 10 V was consistently able to completely stop the beam current.
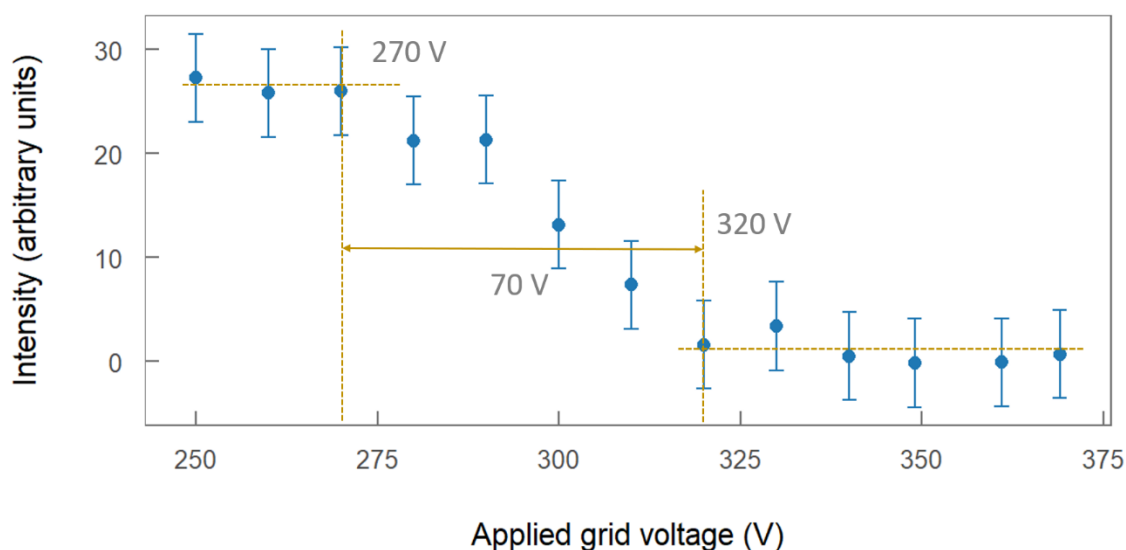
Figure 29 Example of method to determine energy spread of ion beam by the beam intensity decay profile. Accelerating kinetic energy = 340 eV

The energy spread of the O⁻ beam was found from 14 experiments, both using the Faraday cup and MCP to be between 50 and 160 eV with a mean of 105 eV and a standard deviation of 37.9 eV. These values indicate the range of the retarding voltage needed to merely begin to reduce the beam intensity to that needed to cut it to background levels. Between those measurements using the Faraday cup and MCP, the Faraday cup had a slightly lower mean (99.4 vs 107.2 eV), however that was countered by a larger standard deviation (40.6 vs 35.9 eV). These values are quite clearly within range of each other, and as such the combined result of 105 ± 55 eV is adequate.

While the decay profile of the peak area gives vital information on the energy spread, it does not portray the energy populations within the beam. The retarding grid acts as a

high-pass filter. The peak area indicates the total number of counts detected by the MCP in each measurement for each filtering energy. As such, to convert to a kinetic energy distribution each energy bin of width 10 eV is separated by subtracting the total counts of the next highest filter voltage measurement. The experiment seen in Figure 29 is assessed in this way for the retarding voltage range 250 – 340 V, i.e., the decay profile itself. This is compared to a decay profile simulated using SimIon[145] in Figure 30, where the 0 eV energy represents those anions having kinetic energy equal to the extraction energy. The negative values are attributed to the standard error in the intensity measurements of the anion beam.

To investigate the kinetic energy spread of the oxygen anions using SimIon, the hollow cathode and lenses were digitally built and a blocking instance installed 60 mm in the forward direction to collect extracted ions. Ions were chosen to be O⁻ by mass and charge, and were populated into the hollow cathode in a Gaussian 3D distribution with no initial velocity. Ions were flown individually, with up to 1000 ions in each 'Fly', excluding space charge. The electrostatic instances of the array were all grounded except for the hollow cathode itself, which was set to a cathode-anode difference of -400 V, this being a common voltage difference at which the plasma would ignite. Initial conditions were explored, from extraction energies 300 – 400 eV, to the initial population of ions including distribution, location, and small initial velocities. The kinetic energy distribution was not greatly affected by these changes.

Each SimIon simulation indicated that of the ions that were extracted from the electrode (15-25% of the total ions simulated, subject to the initial conditions), the majority had the kinetic energy expected – that of the hollow cathode voltage (SIMION, Figure 30). Trailing ions with lower energies were seen down to 200 eV lower than the applied extraction energy in an exponential decay.
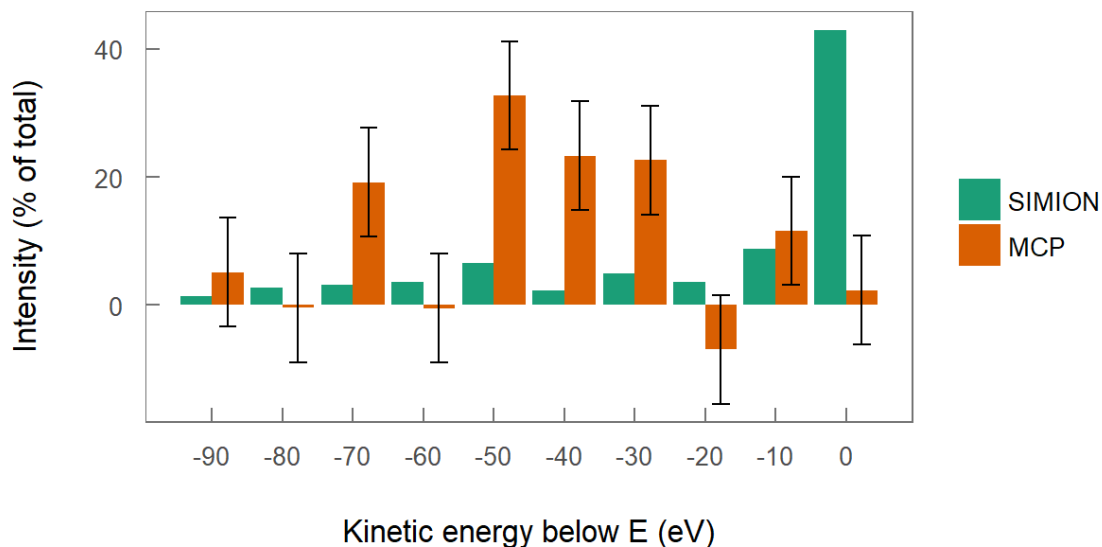
Figure 30 Anion energy population distribution of oxygen anion beam. 10 eV bin width from the applied extraction energy E down to E - 100 eV. MCP experiment had extraction energy of 360 eV, SIMION simulation of 400 eV. Error estimated from experimental range of beam intensity at steady conditions.

The experimentally detected energy distribution of the anion beam is centred at a lower energy than both that of the simulated distribution (Figure 30) and the expected kinetic energy (equal to extraction energy). An explanation for the broad energy spread can be found in the method of ion extraction used in this apparatus. As the gas pulse travels along the hollow cathode, the pressure inside the cathode reaches the point where the plasma can ignite. This plasma continues to glow until the pressure inside the hollow cathode decreases, as the gas pulse spreads through the system. During this time extraction of charged particles is occurring. Once the plasma is extinguished and afterglow processes complete, further production of O^- or O_2^- ceases, and the remaining extractable anions form the end of the detected pulse. This time frame, from the ignition of the plasma, as the gas pulse travels through the system, to the extinguishing of the plasma, accounts for the long duration of detected charged species in the beam. Additionally, as the gas pulse moves into the region between the cathode and anode, where the electric field strength varies sharply across several hundred volts, any ionic species created there will have an

extraction kinetic energy determined by the strength of the electric field at the location of their origin. The observation of plasma in this region during the discharge supports this theory.

Additional possibilities exist to account for this difference. These are: space charge effects surrounding the retarding grid aperture deflect higher energy anions; unrealistic initial conditions of the simulation, and effects of the plasma sheath and electric fields within the gas pulse leading to uneven distribution of anions within hollow cathode.

Of these possibilities, the author concludes that the extraction region is primarily located within the gap between the cathode and anode, centred around the region with electric field strength 30 – 50 eV below the applied extraction energy, and that the initial conditions of the simulation were optimistic in the initial distribution of ions. Further work should be undertaken to pursue a simulated outcome that matches the experimental data in future, however time constraints restrict that possibility for this thesis. Of the other possibilities, space charge effects would be stronger on lower energy ions, the initial conditions of the simulation clearly do need adjusting, and the last option is unlikely due to the experimental conditions, more likely to produce a hot electron, cold ion plasma.

3.4.3 Improving overall beam intensity

The program SimIon[145] was utilised to optimise the voltages and placement of Einzel lenses throughout the system to increase total detected flux and confine the beam within the interaction region.

Various configurations were simulated under the same initial conditions to optimise the total number of anion 'splats' in the second chamber or on the detector. The applied kinetic energy to the ions is 300 eV and they were populated into the hollow cathode region as a Gaussian 3D distribution.

First the configuration of the hollow cathode itself was investigated with examples in Figure 31, with the grounding electrode adjacent to the anode (A), placed 40 mm down from the anode (B), and with an Einzel lens placed between the anode and cathode (C).
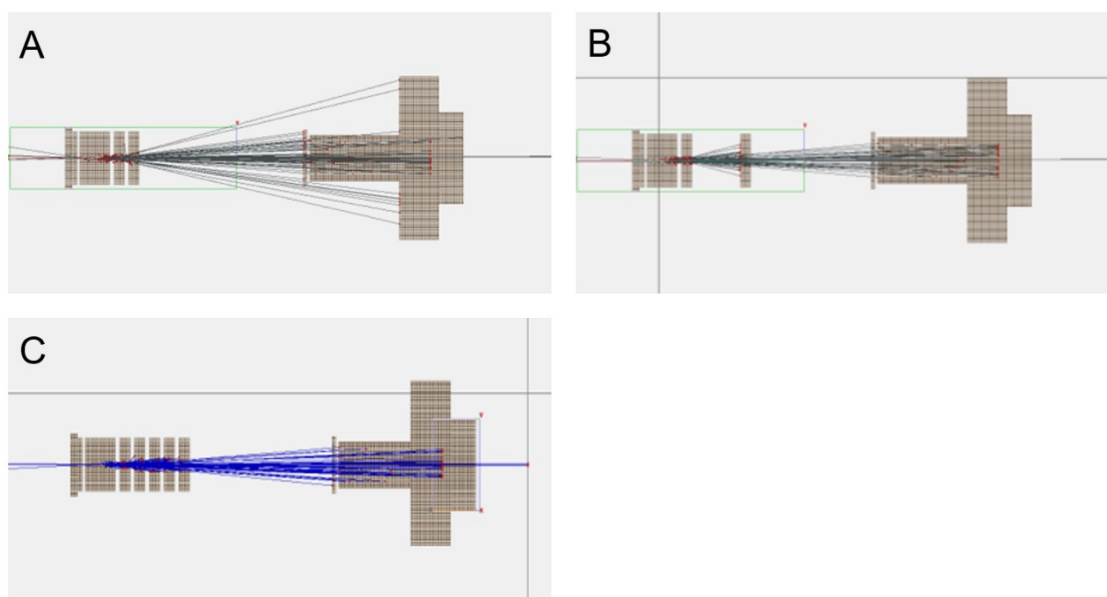
Figure 31 Examples of tested hollow cathode and optics configurations for highest ion throughput, SimIon. A: Grounding electrode adjacent to anode. B: Grounding electrode placed 40 mm down-beam from anode. C: Einzel lens placed between anode and grounding electrode.

In cases A and B, 3 % of anions pass through to the second chamber, despite the visible improvement to beam shape in case B. The addition of the Einzel lens improves the throughput to 5 % with all collimators grounded. This minor improvement likely arises through shielding the beam from the edges of the cathode and anode electric fields. These configurations were tested in the apparatus and C was found to be the most successful.

Optimising the applied voltage to the central electrode of the Einzel lens resulted in a throughput of 17 % at -190 V. Experimentally the optimum value of the Einzel lens voltage tended to be ~ -160 V, and this is expected to be due to the broad energy distribution of the anion beam as shown in the previous section.

When extending the simulation to include the detection of the anion beam *via* deflection (-900 V) into the last MCP, less than 20% of the anions that enter the second chamber (17 % of total produced) are detected by the MCP. When the second Einzel lens is simulated post entry to chamber 2, as in the real experiment, this value can be optimised.

At a voltage to the central electrode of -150 V, 47 % of the anions that pass through to the second chamber were collected by the MCP. This is a total transmission of 8% from the initial number of anions and is shown in Figure 32.
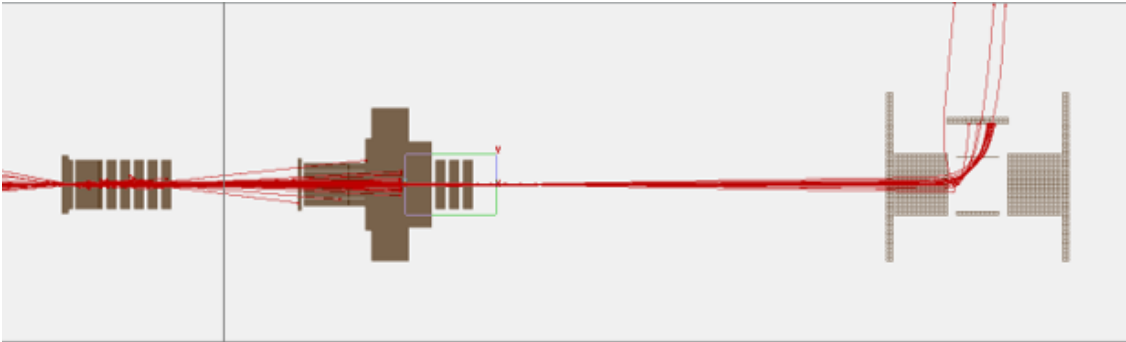
Figure 32 Optimised second Einzel lens at -150 V leads to higher transmission.

Since additional ion beam optics in the second chamber would interfere with the collision region, to increase the overall percentage of detected anions an additional Einzel lens was simulated between the hollow cathode and the deflecting plates, at a distance of 30 mm from the last electrode of the hollow cathode, depicted in Figure 33.
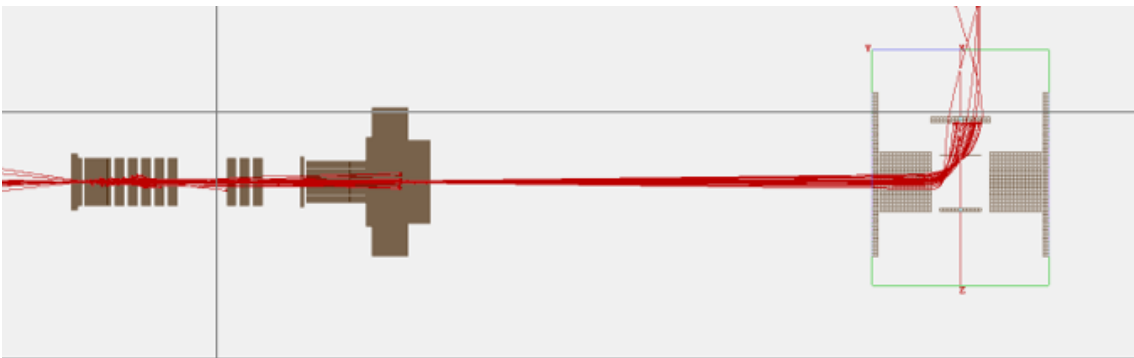
Figure 33 Additional Einzel lens preceding Wein filter increases transmission.

This Einzel lens was optimised at -100 V for the central electrode and allowed transmission to the next chamber of 34 % of initial anions created. Even without the Einzel lens in the second chamber, 73 % of those transmitted anions interacted with the MCP. This gives a total transmission of 25 %, higher than all previous tests. Unfortunately, time did not allow the addition of this newly placed Einzel lens within the

apparatus, however as the voltages optimised by the SimIon simulations were shown to be a good starting point for experimental optimisation, it is expected this Einzel lens would also show success.

Further improvements were sought experimentally throughout the thesis work in several areas, however none proved particularly successful in improving the system. These included attempts to reduce the electrostatic effect of the grounded chamber wall on the electric fields of the cathode and anode by:

- installing ceramic and glass gas transfer tubes to allow the hollow cathode to be placed further from the chamber wall
- placing a second anode electrode between the chamber wall and the cathode
- using an anode 'pin' to initiate the discharge.

Various power supply configurations were sought to enable the apparatus to provide a steady anion beam at low kinetic energies, however at lower than 100 eV the beam is reduced to unworkable intensities. Various configurations for the Wein filter were installed and the appropriate electrostatic deflection values calculated, however due to the large kinetic energy spread of the anions stronger filtering greatly reduced the intensity of the beam. To increase the efficiency of the discharge and thus increase the electron attachment processes, a cathode to the recommendations in 'Plasma Cathode Electron Sources'[146] with a cavity length to cavity diameter ratio of 7 - 10 was built. However, any improvements to anion beam intensity were outweighed by the increased length of the gas pulse required for plasma ignition and therefore decreased time resolution. These changes were largely unsuccessful, and the original configuration was restored. In future further improvements could be sought by altering the plasma source to, for example, a microwave discharge with a standard ion extraction set-up of known behaviour. While these sources only produce low intensities of anions at low energies, installing a field free ion transport tube to allow anions to travel at high kinetic energy until they reach the interaction region, then lowering the kinetic energy *via* a final grounded electrode, would allow for a higher intensity beam.

3.4.4 Conclusion

Preliminary O^--nitromethane collisions in a new experiment showed formation of the anions $CH_3NO_2^-$ (the parent anion), and CNO^-, NO^-, O^- and H^-. These have been compared to similar experiments in the literature and most closely match those of potassium-nitromethane collisions where electron transfer is the dominant fragmentation mechanism. Experimental development was undertaken, focussing on characterisation of the energy spread of the anion beam and methods to attain higher anion signals. The energy spread of the anion beam was found to average 105 eV and peak approximately 40 eV below the applied extraction energy. This is at odds with SimIon simulations indicating a majority of anions at or < 10 eV below the applied extraction energy and a trailing tail of anions with lower energy. Reasons for this discrepancy are discussed in the text. Further SimIon simulations were used to optimise values for Einzel lenses in the system, both those already installed and new configurations that are recommended for testing. In these simulations, the highest number of anions was detected when a new Einzel lens is installed between the hollow cathode arrangement and the Wein filter. Recommendations for future improvements have been made.

3.5 General Conclusion

Experimental design and development form an integral part of physics research, enabling new or improved results for use in models and comparison to theory. In the first case in this chapter the redesign of the scattering chamber and electron optics in an electron transmission beam experiment improved stability and allowed for the apparatus to successfully measure electron energy loss spectra for three targets: argon, acetylene and furfural. These energy loss spectra are used directly in the Monte Carlo particle tracking simulation LEPTS and are not easily obtained from theory, making these experiments immediately useful for the scattering community. The second experiment studied, built to investigate radical-molecule collisions, was validated through O^--nitromethane collisions, the beam energy profiled, and the ion optics optimised. A combination of SimIon simulation and experiment was used to achieve these goals. The electron transfer

occurring during O^- collisions results in anion formation and fragmentation, as was the case here, where the fragmentation profile was most similar to literature studies[50] of neutral potassium-nitromethane collisions. These results are vital to improve our understanding of radiotherapy and plasma applications. Much of the time in scattering physics, experimental work serves as a benchmark for theoretical work, and when experiments can surpass theory to easily provide data, as for electron energy loss spectra, or to provide data that has not been seen before, as with low energy O^--molecule collisions, it is particularly significant.

4 IAM-SCAR+I AND SCATTERING DATABASES

Calculations form a vital part of cross section databases and make possible standard Monte Carlo particle track modelling of collision processes when no experimental data are available in the desired energy range. The Independent Atom Model with Screening Corrected Additivity Rule (IAM-SCAR), developed by Francisco Blanco and Gustavo Garcia in Madrid, has been in use for nearly 2 decades[147–149], and has provided an experimentally verified method to consistently calculate electron and positron collision cross sections (CS) with molecules for incident energies from 30 eV to 10 000 eV[150]. Recent improvements to include scattering interference[44,151] have brought the validity of these calculations to 10 eV impact energy in some cases, allowing accurate and speedy production of data. The speed of the IAM-SCAR+I method is a major advantage over the experimental methods described in previous chapters, and at moderate to high energies, over other calculation methods such as convergent close coupling[98] or R-matrix[99], whilst sacrificing little to accuracy. At lower energies, the described improvements to the IAM-SCAR+I method assist the model in producing cross sections near to experimental values, however they cannot be taken to be reliable.

This method builds on previous work[148,149,152] for both electrons and positrons and has been used successfully in the past for biologically and industrially relevant molecules such as water[8,153], THF[154], assorted macromolecules[155] and many more, in the range of 10 eV to 10 000 eV incident energy. Here the method is described, results are presented for several molecules and a collation of the IAM-SCAR+I results and available experimental or theoretical data are brought together as databases for use in particle tracking models.

4.1 Theory

4.1.1 Independent Atom Model with Screening Corrected Additivity Rule with Interference contributions (IAM-SCAR+I)

The IAM-SCAR+I method, developed by Blanco and García, is a model approach to calculate differential and integral elastic and inelastic scattering cross sections (CS) for electrons and positrons with molecules of known geometry. It has been described in detail in publication[27,44,149,151,156] and a summary is provided here.

4.1.1.1 Base theory

The principle of the IAM-SCAR+I is to consider the electron or positron collision CS, σ, of a molecule as the sum of the screening corrected (reduced) CS of the atomic CSs, according to their respective position in the molecule. Considering the optical potential method, the dispersion function of each atom in the molecule is described by the following local complex potential:

$$V(r) = V_s(r) + V_{ex}(r) + V_{pol}(r) + iV_{abs}(r) \qquad (03)$$

where the real part includes the following three terms: $V_s(r)$ is the static term derived from a Hartree-Fock calculation of the atomic charge distribution by Cowan[157]; $V_{ex}(r)$ is an exchange term which accounts for the indistinguishability of the incident and target electrons, given by the semiclassical energy-dependent formula derived by Riley and Truhlar[158], and $V_{pol}(r)$ is a polarisation potential for the long-range interactions which depend on the target dipole polarisability, in the form given by Zhang *et al.*[159]. Finally,

the absorption potential, $V_{abs}(r)$, accounts for the inelastic scattering events. It is based on the quasifree model by Staszewska[160] but incorporates some improvements to the original formulation, such as the inclusion of screening effects, local velocity corrections and the description of the electron's indistinguishability[147], leading therefore to a model which provides a realistic approximation for electron-atom scattering over a broad energy range.

To build the molecular CS from the sum of the atomic potentials as described above, we use the common expression for multi-center dispersion:

$$F(\theta) = \sum_{i=1}^{N} f_i(\theta) e^{i\mathbf{q} \cdot \mathbf{r}_i} \tag{04}$$

Here, $\boldsymbol{q} = \boldsymbol{K_{out}} - \boldsymbol{K_{in}}$ is the momentum transfer, $\boldsymbol{r_i}$ are the atomic positions and $f_i(\theta)$ are the atomic dispersion functions. Application of the optical theorem[161] results in the "additivity rule" seen below in Equation (05).

$$\sigma_{molecule}^{total} = \frac{4\pi}{k} \text{Im} F(\theta = 0) = \frac{4\pi}{k} \text{Im} f_i(\theta = 0) = \sum_{atoms} \sigma_{atoms}^{total} \tag{05}$$

Here, k = projectile momentum and σ = CS. The differential elastic CS arises from the following, where $q = 2k \sin\frac{\theta}{2}$ and r_{ij} is the distance between the constituent atoms.

$$\frac{d\sigma_{mol}^{el}}{d\Omega} = \sum_{i,j}^{N} f_i(\theta) f_j^* \frac{\sin q r_{ij}}{q r_{ij}} \tag{06}$$

In general solutions to Equation (06) are simplified to Equation (07), in keeping with the additivity rule.

$$\frac{d\sigma_{mol}^{el}}{d\Omega} = \sum_{i=1}^{N} |f_i(\theta)|^2 \tag{07}$$

Which in the original formulation of IAM-SCAR is then integrated to give the integral elastic CS, accounting for all possible orientations of the molecule. This formulation ignores the higher order term of the solution, which represents the scattering of the projectile with more than one atom in the molecule (i and j), is included in Equation (08).

$$\frac{d\sigma_{mol}^{el}}{d\Omega} = \sum_i |f_i(\theta)|^2 + \sum_{i \neq j} f_i(\theta) f_j^*(\theta) \frac{\sin qr_{ij}}{qr_{ij}} \qquad \text{(08)}$$

This higher order term is oscillatory and represents scattering 'interference'. It has been added to the IAM-SCAR method (now IAM-SCAR+I) for the calculation of electron and positron scattering CS since 2015 (Blanco, Ellis-Gibbings and García[44]) and is represented, in addition to Equation (08), by the following alteration of Equation (05). The present author contributed to the 2015 paper were the interference terms were validated using the molecules H_2 and CH_4.

$$\sigma_{mol}^{tot} = \sum_{i=1}^N \sigma_i^{tot} + \sigma^{int} \ . \qquad \text{(09)}$$

Where σ^{int} is the integral of the interference term present in the DCS and provides a higher order approximation of the integral CS.

This interference term has been found to adjust the values of the TCS across the entire energy range[44,151]. It arises from the proper treatment of the DCS according to the multi-center dispersion equations, whereby a non-vanishing interference term also affects the integral CS. This removes the discrepancy in the first-order use of the optical theorem for the integral CS, where the calculated ICS (through additivity rule of existing atomic cross sections) did not match with the integration of the DCS. The interference effect is also subject to the screening correction, described in the following section.

4.1.1.2 Screening correction of the additivity rule

As the energy of the incoming particle decreases, the additivity rule tends to overestimate the molecular CS σ_{mol}. Factor s_i in Equation (10) is a screening correction[156] ($0 \leq s_i \leq$

1), reducing the contribution of each atom to the total molecular CS based on the position of the atom within the molecule and the known total CS of each atom in the molecule.

$$\sigma_{mol}^{tot} = \sum_{i=1}^{N} s_i \sigma_i^{tot} + \sigma^{int}$$

(10)
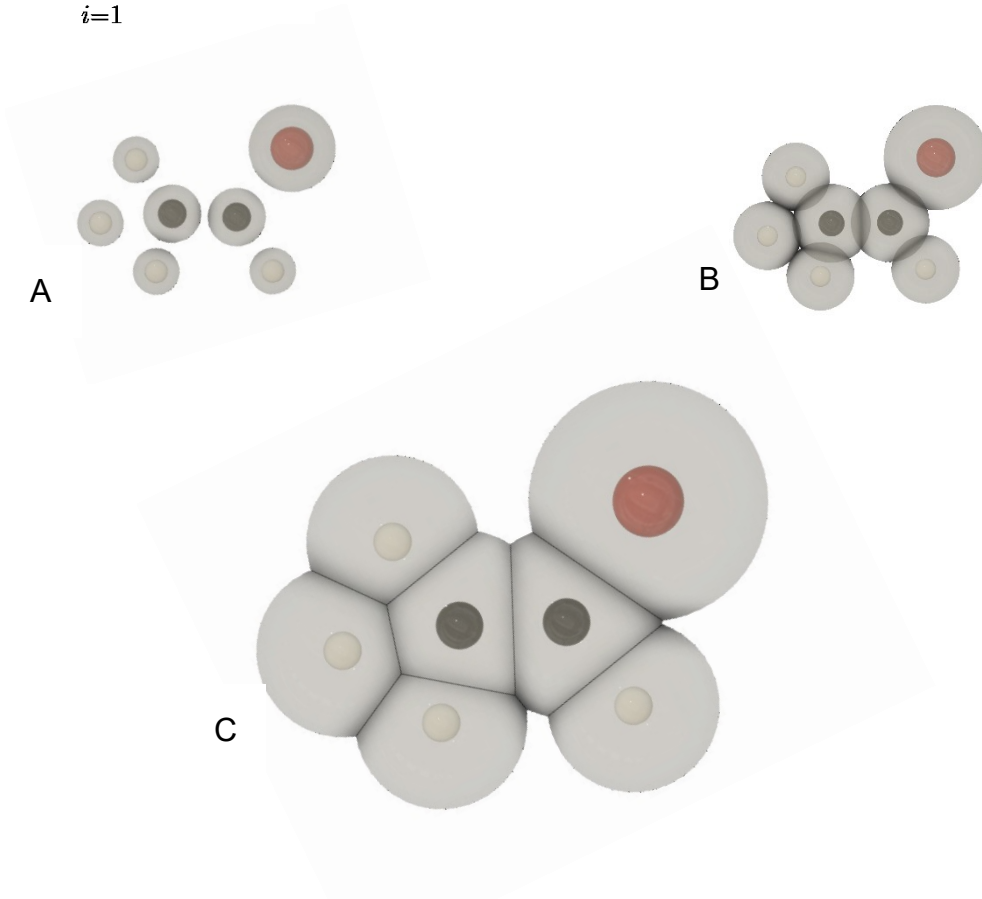
Figure 34 Molecule ethyl aldehyde. Opaque coloured balls: (C₂H₄O). Transparent grey spheres: Geometric representation of atomic CS impact parameter. (A) Representation of additive nature of cross sections at high incident energy, (B) of cross section overlap (i.e. screening) at low incident energy, and (C) of screening corrected cross sections at low incident energy.

This is better described pictorially, as shown for a test molecule in Figure 34. As the projectile energy decreases, the 'impact parameter', a geometrical representation of the CS, increases, leading to overlap as in Figure 34B. The CS is effectively counted twice

where the impact parameters overlap and needs to be removed as in Figure 34C. The screening coefficient removes this excess in a geometrical manner dependent on the CS and the position of the atom within the molecule. For larger molecules, this requires that inner atoms be screened more than outer atoms. The average of the screening over 4π sr accounts for every incident angle in calculating this coefficient.

The screening correction for the elastic scattering is more complicated, due to the screening of the incoming and outgoing wave, and due to the relative probability of redispersion as well as the direct collision. It is described in detail elsewhere[149]. Additionally, implementing the screening into the interference term requires that the DCS calculation include the screening process before integration to the ICS – thus the higher order σ^{int} term from Equation (10) must be formulated as follows[151]:

$$\sigma^{int} = \int \left(\sum_{i \neq j} \nu_{ij} s_i s_j f_i(\theta) f_j^*(\theta) \frac{\sin q r_{ij}}{q r_{ij}} \right) d\Omega \qquad (11)$$

Where $\nu_{ij} = r_{ij}{}^2 / (r_{ij}{}^2 + \rho_{ij}{}^2)$ is a factor to smoothly attenuate the interference terms according to the length parameter $\rho_{ij} = \max\left(\sqrt{\frac{\sigma_i}{\pi}}, \sqrt{\frac{\sigma_j}{\pi}}, \frac{1}{k} \right)$, using the total cross sections and the projectile momentum. s_i and s_j are the screening coefficients for atoms i and j, and all other factors are as above. As the distance between atoms i and j increases, the contribution to the interference decreases.

4.1.1.3 Calculation of inelastic scattering

Inelastic scattering is calculated in the same way, with the imaginary part of the atomic potentials in Equation (03) providing the "absorption" processes. The projectile kinetic energy onset for the inelastic scattering is determined by the atomic lowest optical excitation transition (to include electronic excitation) or the atomic ionisation energy (for solely ionisation). In most cases the onset for electronic excitation is used, and to differentiate between excitation and ionisation cross sections the calculation is performed again using the ionisation limit as the inelastic onset. The electronic excitation cross section component is the difference between these calculations with different onset

energies. This approximation can lead to discrepancies with reality at low energies, as the atomic excitation and ionisation onsets often differ in energy to the corresponding molecular values, and the vibrational and rotational excitation cross sections are excluded.

4.1.1.4 Rotational excitation

The IAM-SCAR+I method does not include any movement of atomic centres, and thus omits vibrational and rotational excitations. As rotational excitation energies are often only a few meV, most spectrometers cannot distinguish elastically scattered electrons from those of the lowest rotational excitations. As such it is important when comparing to experimental values to include the rotational excitations, and this is achieved through a modified First Born Approximation (FBA) method using the Born point dipole model[162]. Here the initial rotational excitation state of the molecular target is determined from the temperature dependent Boltzmann distribution, and collisions alter the rotational quantum number of a molecule by ±1. Initially published by Jain[163], this model uses the dipole moment of the molecule to calculate the free dipole cross sections (integral and differential) for the molecule. To increase the accuracy of the FBA at low energies and wide angles, Jain's method is modified as by Dickinson[164] above a critical angle, again dependent on the dipole moment and incident energy. Both these publications state the FBA method is accurate to incident energies as low as 20 eV.

This calculation is subsequently included with the IAM-SCAR+I cross sections as a separate channel, improving the total cross section results, and allowing for better comparison to those experiments unable to exclude rotational channels from their measurements.

4.1.1.5 Notes on positron calculations

Positron scattering under the IAM-SCAR+I method requires unique atomic potentials, described below, however it functions in much the same way. In this case the exchange potential is excluded, molecular orbital electrons and incident positrons being distinguishable, and the static potential and polarisation change sign to adhere to the

change in charge sign of the projectile. As in Equation (03) the potentials are summed to give the total atomic collision potential (Equation (12)):

$$V(r) = V_s(r) + V_{pol}(r) + iV_{abs}(r) \qquad \textbf{(12)}$$

Which are then used as the atomic potentials to determine $F(\theta)$ *via* the multi-centre dispersion function (Equation (04)), producing the DCS and ICS as for electrons.

$V_s(r)$ is the static potential, describing the interaction between the positron and the atomic charge density, and is repulsive. This is formulated on a derivation of the Hartree-Fock atomic wavefunctions analogously to the work of Reid and Wadehra[165]. $V_{pol}(r)$ is the polarisation potential, the sum of a dipole and quadrupole potential, calculated with the polarised-orbital method by determining the first-order corrections to the atomic orbitals due to a fixed charge field[166]. For small atoms (C, N, O) the dipole and quadrupole polarised orbital potentials of Ne (accurate against measurement[167]), are scaled so that they fit to calculations. In the example of N and O, results of which are shown in this chapter, the polarised orbital potentials of Ne are scaled to the results for N and O presented in Reinsch and Meyer[168] and Werner and Meyer[169], as described in Chiari *et al.*[170]. All $V_a(r) > 0$ describe the 'absorption' processes, i.e. the inelastic processes of excitation, ionisation and positronium (Ps) formation. A scheme modified from that proposed again by Reid and Wadehra[165] is implemented, assuming the target electrons can be considered as a quasi-free electron cloud with which the incoming particles undergo binary collisions.

Positronium formation, as part of the absorption potential, must be treated carefully. Recent improvements to the treatment of Ps formation are outlined in Blanco *et al.*, 2016[34]. In brief the inelastic threshold energy becomes dependent on the collision energy. It coincides with the well-known Ps formation threshold of $\Delta_p = I - 6.8$ eV, (where I = ionisation threshold) for lower energies, and the lowest optically allowed electronic excitation transition Δ (of the atom) for higher impact energies, where the cross section for positronium formation is negligible in comparison with the excitation and ionisation

cross sections. Equation (13) details the smooth transition in inelastic collision threshold energy from low to high impact energy:

$$\Delta(E) = \Delta - (\Delta - \Delta_p)/[1 + (\frac{E}{3I} - 1)^2] \qquad (13)$$

With this inclusion the IAM-SCAR+I calculations reliably provide DCS and ICS for electron and positron scattering with a relatively simple calculation shown to exhibit high accuracy.

4.2 IAM-SCAR+I results and database collection

Databases of interaction CS are necessary for modelling of particle transport through media, and compilation of the available experimental and theoretical work, supplemented by the IAM-SCAR+I calculations, provides these databases. Here for the molecules N_2, O_2 and furfural the IAM-SCAR+I method has been used to compare and assess the validity of the calculation across various energy ranges and to fill in the (sometimes sizeable) gaps in the literature values. Positron scattering with nitrogen and oxygen molecules is explored with regard to the new interference contribution. An electron scattering database collated from literature for the molecule furfural is presented here with further discussion. The results are presented in graphical format, each with a brief explanation of the method used, discussion and comparison to literature. Each molecule is additionally introduced in Chapter 1 of this thesis. Additional IAM-SCAR+I studies in recent years include those on electron collisions with small water clusters (Verkhovtsev et al.[171]) and positron collisions with pyridine (Stevens et al.[172]), on both of which the author of this thesis is a co-author.

4.2.1 Positron - N_2

As one of the simplest and most abundant molecules in our atmosphere, electron-nitrogen and positron-nitrogen scattering processes have been thoroughly investigated. The addition of the interference terms to the IAM-SCAR+I method is compared to this rich existing data set, and the accuracy in the various energy regimes discussed.

The effect of the interference term on the positron scattering was investigated for the N_2 and O_2 molecules (O_2 shown in following section) for two reasons. First, scattering data on these basic molecules are paramount to the modelling of cosmic ray produced beta emitters in the upper atmosphere, and second, there are available several experimental and theoretical sources for comparison to any new data. Figure 35 details the positron integral scattering cross sections for N_2 calculated using the IAM-SCAR+I method as detailed in the preceding sections. It is clear in the figure that the TCS for energies below 10 eV clearly increases, which is reportedly not the case for electron scattering[173,174], confirmed by the electron scattering TCS shown for comparison. This increase is mainly due to the polarisation term of the elastic scattering. The inelastic processes shown in Figure 35 (ionisation, electronic excitation and positronium formation) are determined from their respective thresholds (see sections 4.1.1 and 4.1.1.5) in the total inelastic cross section calculation. As usual this excludes the vibrational and rotational excitations.

This calculation is compared to the theoretical and experimental work on the TCS of positron scattering with the nitrogen diatomic molecule in Figure 36. One drawback of these comparisons is that the experimental data often falls short of the calculation range, particularly at higher energies where the work by Dutton *et al.*[175] becomes the only remaining experimental comparison. The total cross sections have good agreement at higher impact energies with the available experimental data, and the very low energies (<10 eV) show an overestimation of the elastic scattering component. This low energy region is difficult to model with the approximations made here, however the IAM-SCAR+I method provides the best values in this region when compared to the other calculations based on similar approximations. In the region 10 – 30 eV the IAM-SCAR+I calculation overestimates the total cross section, however the location of the local maximum (the region where inelastic processes dominate) matches the experimental data.
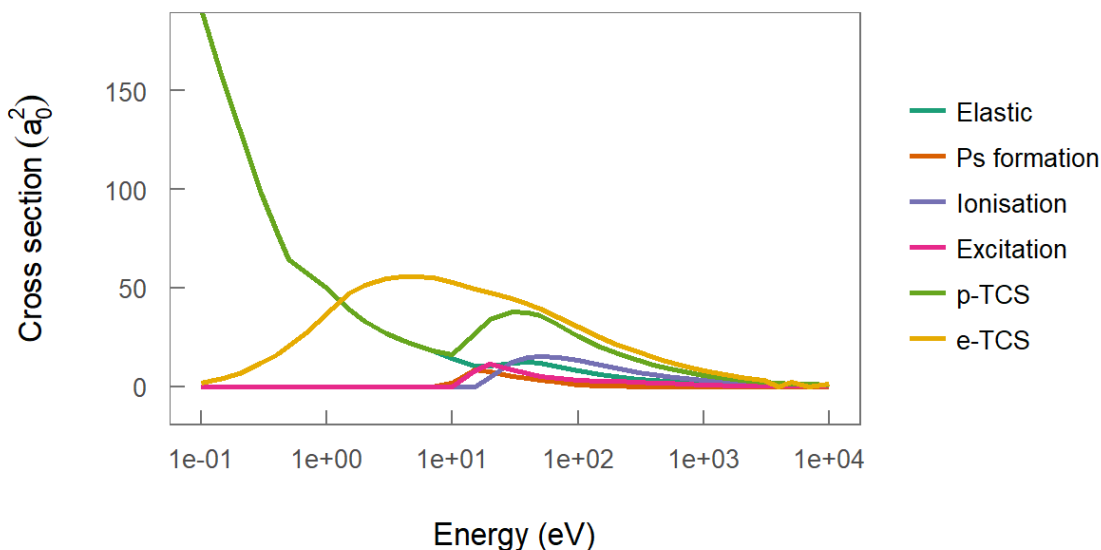
Figure 35 Positron scattering ICS from N_2 for elastic and inelastic processes, with the electron scattering for comparison. Calculated using the IAM-SCAR+I method

At low impact energies (0.1 – 10 eV) the choice of the threshold for Ps formation and electronic excitation is vital to model the point where the dominant scattering process changes from elastic to inelastic, seen as a local minimum. IAM-SCAR+I overestimates the energy of this turning point, placing it around 10 eV. Zecca *et al.*[176] measured this turning point at 6.35 ± 0.1 eV, while Sueoka *et al.*[177] and Hoffman *et al.*[178] did not detect well-defined turning points.. An overestimation of the elastic component at low energies would contribute to this issue, and would indicate the formulation of the IAM-SCAR+I method is still not accurate enough at such as low energies. As seen from Figure 36, the other calculation methods either do not attempt to model this difficult area, or they show greater discrepancies with the available data.

In the mid - low energy region (10 - 100 eV) the IAM-SCAR + I maximum lies 20 - 30% above the closest experimental data (from Dutton *et al.* [175]). Since the uncertainty limits given for the Dutton *et al.* results have a maximum of 9% and the overall uncertainty of the IAM-SCAR+I TCS calculation is 10%, this calculation represents an overestimation of about 6-10 % of the maximum TCS in the range 10 – 100 eV.
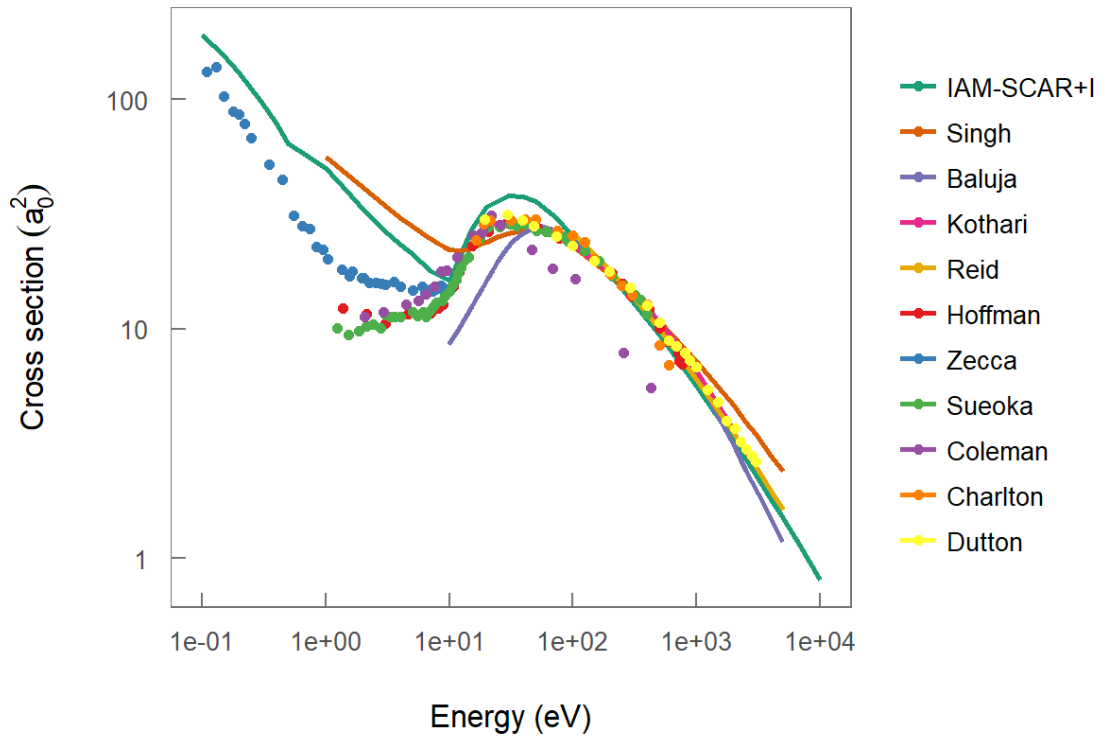
Figure 36 Comparison of the positron TCS for N₂ calculated using the IAM-SCAR+I method to available literature data. Experimental sources denoted by data points, calculated sources by solid lines. References: Singh[179], Baluja[180], Kothari[181], Reid[182], Hoffman[178], Zecca[176], Sueoka[177], Coleman[183], Charlton[184], and Dutton[175].

In the mid to high energy range (100-10 000 eV) Figure 36 shows that the new calculation data shows an excellent fit to the existing experimental and calculation work, save for that of Singh *et al.*[179], which appears to diverge above 300 eV from the dataset. Coincidence with the existing data at these high energies indicates agreement with the First Born approximation, used with accuracy above 10 000 eV, and validates this energy region of the IAM-SCAR+I calculation.
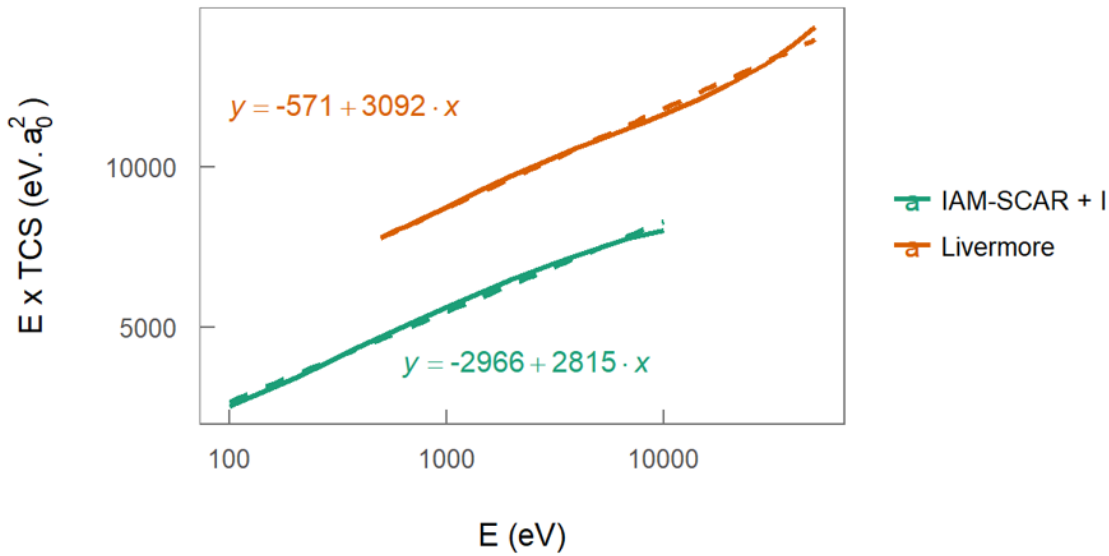
Figure 37 The Fano plot for N$_2$ representing the consistency with the First Born Approximation at high energies, denoted by the matching slopes of the IAM-SCAR+I data and that of the Livermore database[32].

As detailed in a previous paper[170], the positron scattering CS is lower than the electron scattering cross section at energies up to 10 keV due to the repulsive polarisation term in the scattering potentials of the optical potential method. As such a comparison to electron scattering for these energies is no longer quantitatively viable, however the slope of the two curves can be compared to check the consistency with the Born Approximation. Validity to the Born approximation (at higher energies) requires the plot of E × TCS vs log E to be linear[185]. This is a feature of the Born approximation formalism of the total cross section, where the slope tends towards the oscillator strength when plotted under the correct units[185]. As seen in Figure 37, the IAM-SCAR+I method is linear and has a slope similar to the electron TCS from the Lawrence Livermore database[32]. The positron calculations for nitrogen fulfil this requirement, having a difference in slope of < 5 % to the Livermore data.

This analysis affirms the validity for the new IAM-SCAR+I method for positron scattering in both low and high energy ranges. It is of particular use at low energy ranges where accurate calculations are time consuming and a simpler model is required, able to

provide values when absolute accuracy at low energy is of less importance. The model functions excellently at higher energies, though it does overestimate the inelastic peak in the 10 – 100 eV energy range.

4.2.2 Positron - O_2

The total cross sections for O_2 follow much the same analysis as those for N_2, with good agreement at higher energies followed by an overestimation of the ICS around 20 eV and below 10 eV. Figure 38 shows the IAM-SCAR+I calculations for positron scattering from O_2, calculated as for N_2, where the dipole and quadrupole polarized orbital potentials of Ne (accurate against measurement[167]), are scaled so that they fit to the calculations of O presented in Werner and Meyer[169] as described in Chiari *et al.*[170].
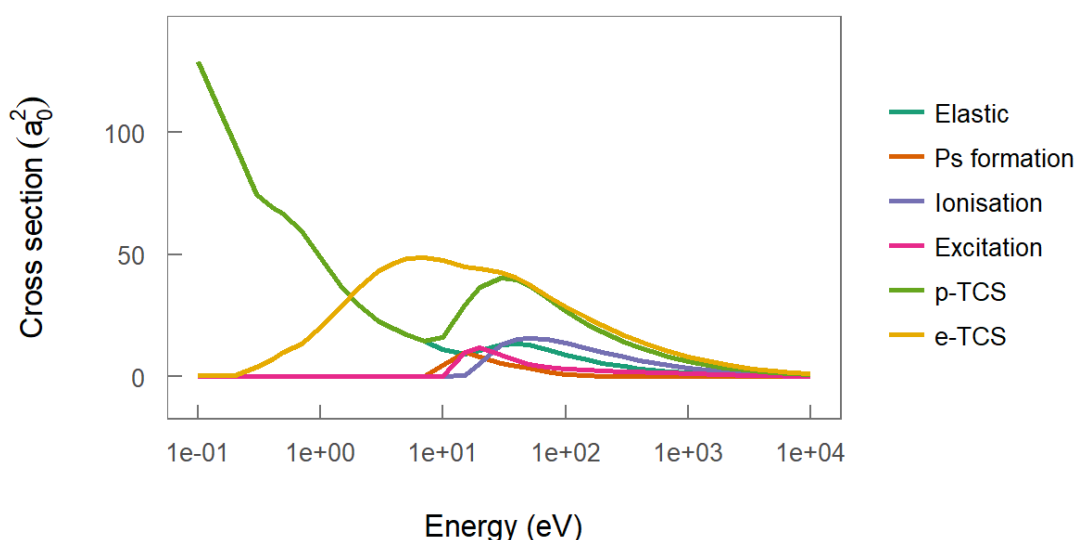

Figure 38 Positron scattering ICS from O_2 for elastic and inelastic processes, with the electron scattering for comparison. Calculated using the IAM-SCAR+I method

Figure 39 shows that again, theoretical and experimenttal work on the TCS of positron scattering with the oxygen diatomic molecule is available in abundance. Here there are only two sources for low energy experimental data, Chiari *et al.*[170] and Dababneh *et al.*[186], and their work is divergent. The highest energies again are only compared to calculations, as the experimental data does not cover this region.

The very low energies (<10 eV) exhibit the dominance of the elastic scattering to too high an energy to correctly model the experiments performed in this region. With the IAM-SCAR+I for O_2 the turning point is 7 eV compared to 3.0 ± 0.05 eV measured by Chiari et al.[170], where the work by Dababneh et at.[186] does not show any turning point at all.
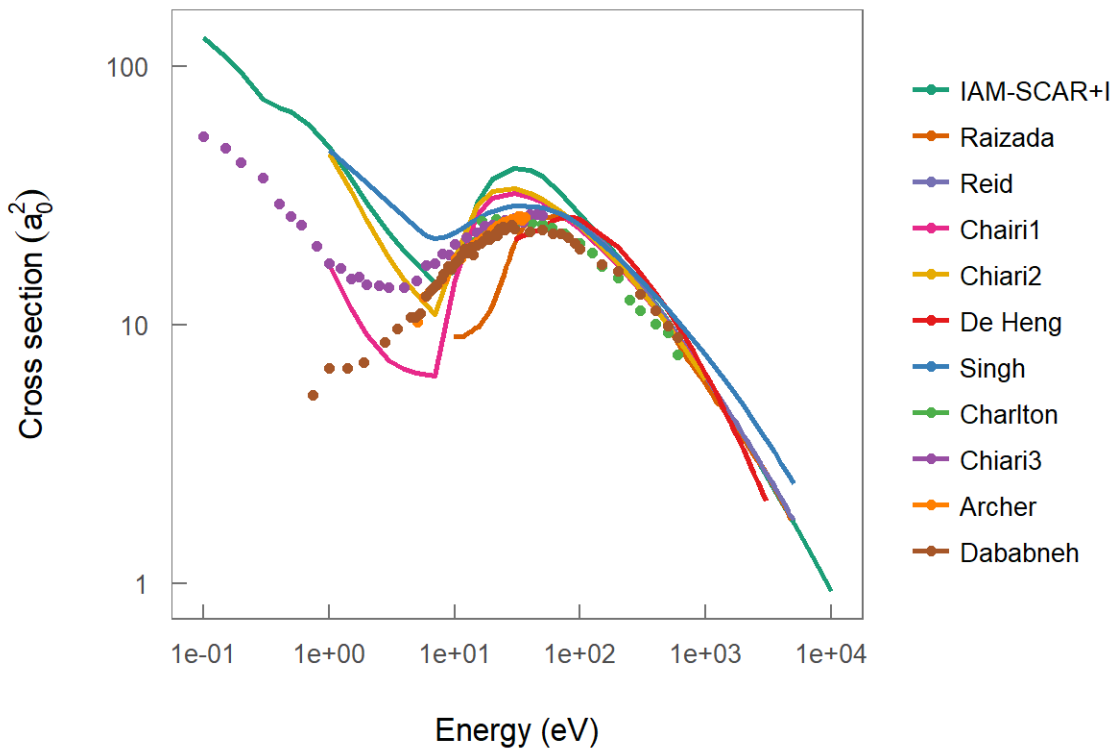
Figure 39 Comparison of the positron total cross section calculated using the IAM-SCAR+I method to available literature data for O_2. Experimental sources denoted by data points, calculated sources by solid lines. References: Raizada[187], Reid[182], Chiari[170] (Chiari1: IAM-SCAR + dipole, Chiari2: IAM-SCAR + dipole + quadrupole, Chiari3: Experimental work), De-Heng[188], Singh[179], Charlton[184], Archer[189], and Dababneh[186].

In the mid energy region (10 - 100 eV) the IAM-SCAR + I method again lies above all experimental data (Figure 39) while still providing the correct peak location. The discrepancy from the experimental data at the maximum for O_2 is 46%, and this is to the Chiari experiments[170] at 50 eV, where their experimental uncertainty was in the 5-13%

range. The experimental papers discuss the angular discrimination and its pertinent effect of lowering the TCS due to increased acceptance of elastically scattered positrons, and this can in some way reduce the observed discrepancy, however it seems that the atomic optical potentials and subsequent treatments used again consistently overestimate the TCS in this range. When comparing to the nearest calculation, the IAM-SCAR including dipole and quadrupole effects is 17% lower than the new calculation.

In comparing the original positron-O_2 CS calculated using the simpler IAM-SCAR method[170], with the new method including the interference effects (IAM-SCAR+I) and the quadrupole term of the polarisation potential, there are both improvements and setbacks. The first obvious improvement is when compared to the dipole only IAM-SCAR calculation, shown in figure as the long dashed purple line. This calculation clearly underestimated the CS below 10 eV, passing well below the experimental values. The dipole + quadrupole calculation shown as the short dashed purple line, while still underestimating the cross section at 10 eV, fared better, however the solid black line of the new IAM-SCAR+I method at this turning point is consistent with the experimental work and thus shows the most accurate representation. Neither the original IAM-SCAR nor the new IAM-SCAR+I method seem more accurate than the other below the turning point. At the peak of the inelastic CS, shown around 30 eV, all three versions of the IAM-SCAR method overestimate the experimental and calculated data provided in the literature, especially the new IAM-SCAR+I method. Note that the main effect of the interference terms is to incrementally increase the elastic DCS for the smaller angles and these angles are missing in the experimental conditions of Chiari[29]. For energies above this maximum the old and new methods eventually converge and follow the literature data.

Figure 40 again is an indication of the consistency of the IAM-SCAR+I method with the higher energy first born approximations currently accepted as standard. Here the important point is that the slope of the accepted Livermore data and the slope of the higher energy region of the IAM-SCAR+I calculation are consistent. Oxygen fares better than Nitrogen (Figure 37), with a slope less than 1% different to the Livermore data. The IAM-

SCAR dipole and dipole+quadrupole calculations are included as they clearly show the region where the interference contributions diverge from the original formulation of the calculation.
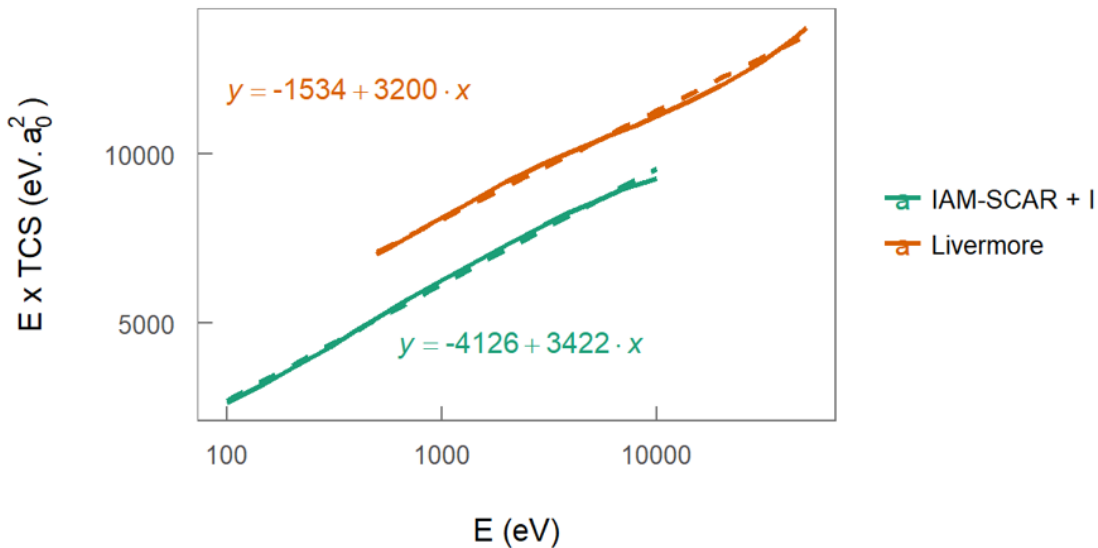
Figure 40 The Fano plot for O_2 representing the adherence to the first born approximation at high energies, denoted by the matching slopes of the IAM-SCAR+I data, IAM-SCAR data[170] and that of the Livermore database[32].

These results for the IAM-SCAR+I calculation of positron scattering with diatomic oxygen show, as with nitrogen, that this method is accurate against literature data for high energies, provides a good simple comparison for low energies, and overestimates the region where the inelastic component is dominant. For oxygen this overestimation is greater, as is the fit to higher impact energy data, where the difference in slope between the database results for electron-O_2 scattering and the IAM-SCAR+I positron results is < 7 %, shown by the Fano plot in Figure 40. As the effect of the new interference term increases the ICS in the mid-energy region, further theoretical and experimental work is suggested to clarify the discrepancies in this region. This work must be consistent with the model as it stands and continue as an "ab initio" method, save for the atomic potentials and geometries.

As to whether the new IAM-SCAR+I method provides better positron scattering CS across all energy ranges, at the low impact energy and high impact energy regions (0.1 – 10 eV and > 100 eV respectively) the new method provides higher accuracy and greater agreement with existing experimental data. Unfortunately for the region where inelastic scattering dominates, from 10 eV to 100 eV, the new method overestimates the experimental data and requires adjustment. It should be noted that this issue was not strongly relevant for electron scattering using the new methodology[44].

4.2.3 Electron - Furfural

The furfural molecule ($C_5H_4O_2$) is a useful precursor to biofuels as well as an important agricultural molecule in its own right[85], as noted in more detail in Chapter 1. As a biofuel precursor it may be subject to plasma treatment, exposing furfural to a multitude of low energy electrons. Modelling this process requires a database of electron scattering cross sections.

All known literature on electron-furfural scattering processes was collated. When building a collisions database various CS are required, this includes integral and differential elastic CS, as well as integral and differential CS for each inelastic process (rotational, vibrational, and electronic excitation, electron attachment and ionisation). D. Jones[62,79,85] and R. da Costa[15] provided published experimental and theoretical data directly, all other data was obtained from literature as published.

The IAM-SCAR+I calculation of the integral and differential cross sections were published in Traore *et al.*[82] in which this author is a co-author, and additionally in Jones *et al.*[79] for comparison to experimental and computational results. The IAM-SCAR without interference corrections were previously published in Ferriera da Silva *et al.*[120] and are shown for comparison. These publications indicate the experimental TCS show good general agreement with the IAM-SCAR+I data across the entire energy range.

The IAM-SCAR + I approximation is used where the experimental or calculated data is not available. When discrepancies arise between various sources of CS, either the data from the more reliable method, or in the case that they are considered equal, the statistical

average with increased error encompassing both original data sets, is used. An example of this process is shown for the integral elastic cross section (IECS) in Figure 41, where the Schwinger multichannel method with psuedopotentials (SMCPP), with the inclusion of either 6 or 63 open electronic states and with or without Born closure scheme[15], are compared with results from the IAM-SCAR+I approximation. The calculation with 63 open states + Born closure is understood to be the most accurate of the three at these energies, and it matches sufficiently well with the IAM-SCAR+I result, including the increase in IECS approaching 0 eV. The uncertainty of the IAM-SCAR+I data is adjusted to include the data points from the 63 Ch Born Closure data, to account for the minor differences. This validates our use of the IAM-SCAR+I for the IECS in this energy range, where it is most likely to show problematic behaviour. As the range of IECS calculations is limited to 5-50 eV and no other data are available, the IAM-SCAR+I method is used as calculated for the rest of the IECS energies investigated.

As the IAM-SCAR+I method is used for the IECS as calculated, the elastic DCS are able to be used as calculated as well. This, and the rotational DCS, are available in tabulated form in Appendices 1 and 2. If the IECS differed from the IAM-SCAR+I calculation, the DCS would need to be adjusted accordingly for consistency. This would be a simple, equal adjustment for the DCS value at each angle, without weighting, as the shape of the DCS calculated using IAM-SCAR+I has been previously validated[63] and any adjustment to the DCS shape would be based on speculation.

The process for the remaining presented cross sections is much the same, where calculations and experimental values were compared to determine the best cross sections for the entire energy range. The integral inelastic cross sections (IICS) are made up of the sum of the extrapolated experimental and calculated inelastic values (not including rotation), and it relies heavily on the IAM-SCAR+I values at higher energies. The total cross sections are the sum of all channels, using the IAM-SCAR+I method as an upper bound.
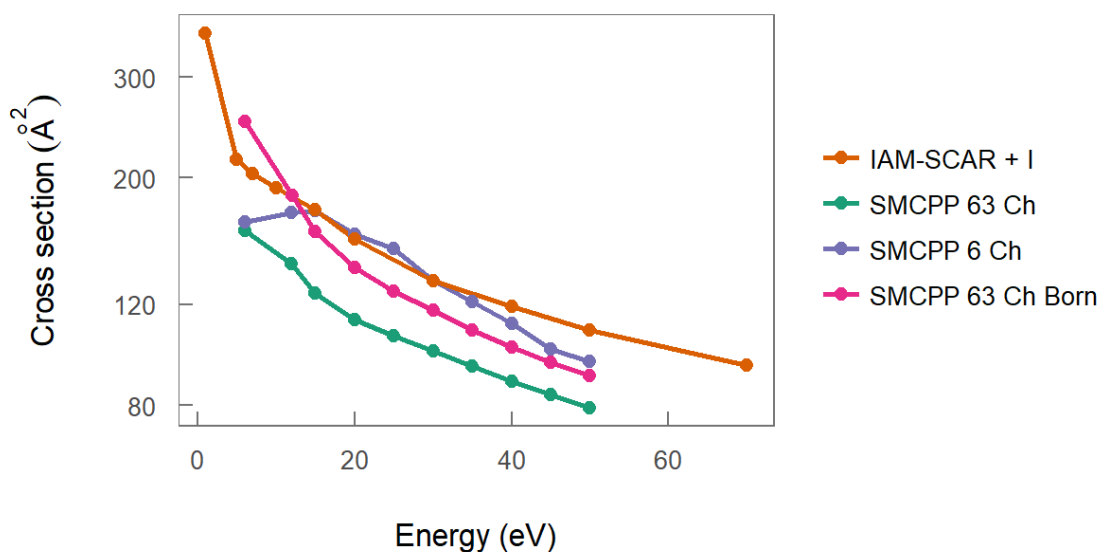
Figure 41 Showing the comparison method used to verify data for the furfural scattering database, comparing various Schwinger multichannel calculations[15] with the IAM-SCAR+I method[82]

The vibrational excitation CS are extrapolated from the experimental work of Jones *et al.*[62] for energies 20, 30 and 40 eV. The lower energy extrapolation uses the shape of the furan vibrational cross section rise from zero to its zenith[190] up to 20 eV. This will introduce a smaller CS than expected due to ignoring the maximum, which should appear between 5 and 15 eV, but without data to support the energy or area of the maximum it is not prudent to speculate. For energies above the experimental region, a simple log-log falloff provides a vibrational CS of the common shape.

Ionisation CS (ionisation limit 9.22 eV[191]) were available from two calculation methods, the Born encounter Bethe model (BEB) used up to 1000 eV[79] and the calculation from the IAM-SCAR+I inelastic CS (see Section 4.1.1.3 of this chapter for details) for above this limit.

Electronic excitation CS were determined *via* a careful fitting procedure using the experimental values of Jones *et al.*[79], the inelastic ICS determined by IAM-SCAR+I, the ionisation and the vibrational excitation CS (described in the preceding paragraphs).

Rotational excitation cross sections were calculated as described above in Section 4.1.1.4.

There have been no measurements for electron attachment CS for furfural and the DEA section in Chapter 2 of this thesis focused on the fragmentation products and resonance locations, and as such DEA CSs have been omitted. The DEA cross section is assumed to be relatively high as strong fragmentation was seen in the spectra in Chapter 2 of this thesis and would contribute most to the inelastic cross section around 8 eV impact energy where the resonances are clustered. No approximations for this behaviour have been included here.

Figure 42 presents the recommended integral and total cross sections of electron scattering with furfural, followed by the tabulated values in Table 13.

This data constitutes a full scattering cross section set for the molecule furfural and has been used in the LEPTS program for modelling electron transport through furfural (See Chapter 6).
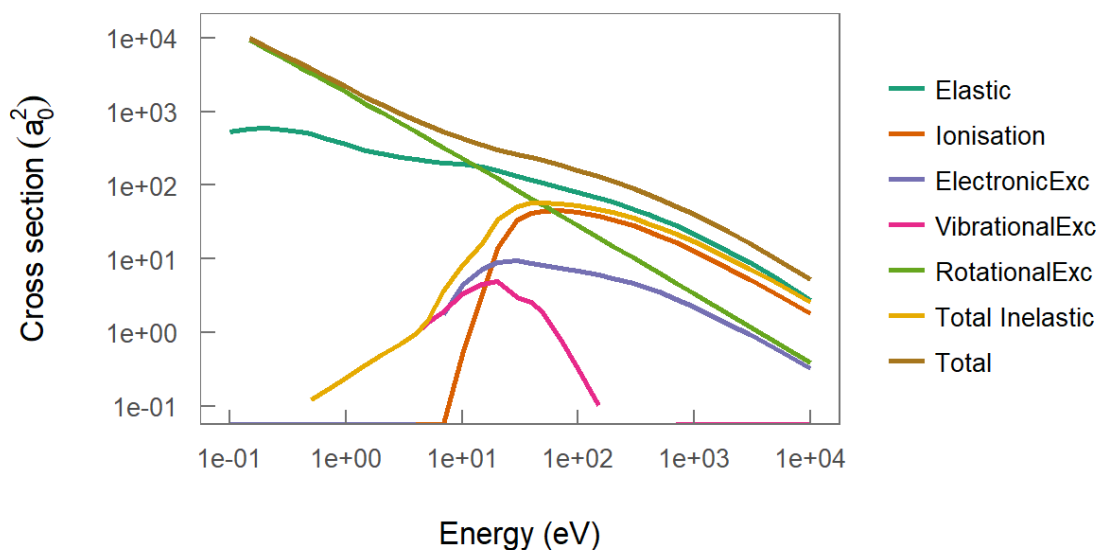
Figure 42 Best integral electron collision cross sections for scattering from furfural in bohr radii squared (a_0^2), see text for details

Table 13 Recommended integral scattering cross sections for electron impact on the furfural molecule in atomic units (a_0^2). Sources are described in text.

E (eV)	Elastic	Ionisation	Electronic excitation	Vibrational excitation	Rotational excitation	Total inelastic	Grand total
0.10	538	0.00	0.00	0	13000	0	13538
0.15	580	0.00	0.00	0.036	9300	0.036	9880.03
0.20	595	0.00	0.00	0.048	7300	0.048	7895.04
0.30	558	0.00	0.00	0.073	5160	0.073	5718.07
0.40	538	0.00	0.00	0.097	4030	0.097	4568.0
0.50	501	0.00	0.00	0.121	3320	0.121	3821.1
0.70	425	0.00	0.00	0.17	2480	0.17	2905.1

1.00	358	0.00	0.00	0.243	1820	0.243	2178.2
1.50	297	0.00	0.00	0.365	1270	0.365	1567.3
2	266	0.00	0.00	0.486	984	0.486	1250.4
3	238	0.00	0.00	0.708	686	0.708	924.70
4	224	0.00	0.00	0.973	531	0.973	755.97
5	215	0.00	0.066	1.338	434	1.404	650.40
7	203	0.00	1.77	1.902	321	3.672	527.67
10	192	0.5	4.395	3.318	232	8.213	432.21
15	176	3.22	7.305	4.518	161	16.318	352.04
20	156	13.8	8.82	4.867	124	34.167	307.48
30	132	34	9.463	2.953	85.6	51.653	264.01
40	119	41.7	8.677	2.585	65.8	57.085	237.76
50	108	44.3	8.28	1.861	53.6	58.061	216.04
70	93.9	45.1	7.55	0.823	39.4	56.723	186.77
100	81	43	6.85	0.323	28.3	53.123	159.47
150	67.5	38.1	6.05	0.102	19.5	47.202	131.25
200	58.7	34	5.45	0.042	14.9	42.442	113.09
300	47.4	28	4.7	0.011	10.3	35.411	90.411
400	40.1	23.7	4	0.004	7.85	30.404	75.654
500	35	20.7	3.6	0.001	6.38	26.901	65.681
700	28	16.5	2.8	0.00	4.66	21.8	51.96
1000	21.7	12.7	2.2	0.00	3.34	17.1	39.94

2000	12.5	7.34	1.25	0.00	1.75	10.1	22.84
3000	8.83	5.19	0.934	0.00	1.2	7.3	16.154
5000	5.52	3.33	0.599	0.00	0.74	4.75	10.189
10000	2.75	1.78	0.32	0.00	0.385	2.58	5.235

4.3 Conclusions

When experimental data is not readily available and theoretical models can provide scattering cross sections quickly and with high accuracy, they should be utilised to their full capacity. Improvements to theoretical models are best checked by comparison to well studied molecules. To this end, new N_2 and updated O_2 positron scattering integral cross section data calculated using the recently improved IAM-SCAR+I method for positron impact energies of 0.1 – 10 000 eV were presented in Sections 4.2.1 and 4.2.2. These results compare well to the breadth of experimental and calculated results available in the literature. Modifications to the calculation method have improved the behaviour near the positronium formation threshold and above 100 eV, though there are still improvements to be made in the 10-100 eV region where the inelastic processes dominate.

Particle tracking models require scattering data over broad ranges of impact kinetic energy, and unfortunately many experimental and theoretical studies can not cover this entire range. To produce complete scattering databases the existing results must be compared, combined and complemented. A scattering database for electron-furfural collisions was developed from a combination of experimental extrapolations and calculated sources, making use of the IAM-SCAR+I calculations where no other data was available. This database was subsequently used in the LEPTS particle tracking program for studying this biofuel precursor (see Chapter 6).

5 ELECTRON STIMULATED DESORPTION

As noted throughout this thesis, radiobiological damage rests on the fragmentation of key molecular species within cells. Condensed phase studies are of particular importance in providing biological context to gas phase results, where differences in transport, angular distribution and fragmentation effects of scattering particles can affect outcomes[192]. Plasma treatments for biofuel[13] and biodiesel[16] are also incident on condensed phase matter, and the low energy processes excited in those treatments should be explored in condensed phase as well as gas phase. This chapter explores the condensed phase effects on low energy electron impact to diazenes, by electron stimulated desorption.

Low energy electron (LEE) interactions and the formation of transient negative ions (TNIs) play a dominant role in radiation-induced dissociation of condensed-phase biomolecules (e.g. in radiotherapy[109]). Here a brief introduction to relevant literature, experimental data, analysis and discussion are presented on the LEE-induced dissociation and desorption of the DNA/RNA-base analogue pyrimidine and radiosensitising agent analogue pyridazine. Vapours of each molecule were condensed on either a Pt or Ar substrate to form a multilayer film or a submonolayer molecular target, respectively.

These were irradiated with electrons of 0-80 eV energy and the desorbing anionic and cationic fragments analysed *via* time of flight mass spectrometry. Anions are formed by dissociative electron attachment (DEA, see Chapter 2) in resonant processes. The anion signal also comprises dipolar dissociation (DD), investigated in both anionic and cationic yield functions. DD is when above a certain energy threshold ($\sim$14-16 eV) relaxation of an electronically excited state of a molecule results in fragmentation, yielding an anion and a cation. Cations are also formed by direct ionisation (DI) above the ionisation threshold. From analysis of anion and cation yields, fragmentation pathways are suggested. Experiments with mixed layers of water and pyrimidine were undertaken to make a more realistic case for in situ fragmentation, however the results were inconclusive due to excessive surface charging and they are not presented here. This work has been published in L. Ellis-Gibbings *et al.*[193].

5.1 Introduction

Pyrimidine and pyridazine are introduced in Chapter 1 and the reader is referred there for more detail. In brief, pyrimidine is an analogue of the DNA and RNA bases[40] cytosine, thymine and uracil and pyridazine a structural part of several clinical radiosensitizers[68]. Below, the available results from appropriate experiments and calculations on these molecules, whose structures appear in Figure 43, are summarised.
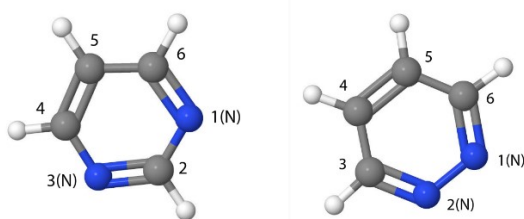
**Figure 43 Molecular structure of pyrimidine (left) and pyridazine (right). Carbon: grey, Nitrogen: blue, Hydrogen: white.**

An important study by Neustetter *et al.*[194] presented results for electron attachment to pyrimidine molecules and clusters in the gas phase. These authors observed two resonances, at 5.5 and 9 eV, where the fragments CN^-, $C_3H_2N^-$ (or $C_2N_2^-$), and (pyr-H)$^-$

were seen. Recent unpublished gas-phase DEA data from T Gilmore and T Field[195] are consistent with the Neustetter publication, observing CN^- and $C_3H_2N^-$, with a weak signal of H^- at 5.3 and 8.8 eV. Gilmore and Field noted that their experiment is not sensitive to H^-. Low-lying π^* TNI resonances at 0.39 ($^2A_2$), 0.82 ($^2B_1$), and 4.26 ($^2B_1$) eV, reported in experimental[65] and theoretical studies[66], were not found to contribute to DEA yields in the gas phase. In pyridazine, Gilmore and Field[195] found two broad resonances at energies of 5.1 – 6 eV and 8.2 eV for the same fragment masses as pyrimidine and again, no evidence of fragmentation *via* lower energy shape resonances. Neustetter *et al.*[194] also reported the stabilisation of excess electronic charge on pyrimidine clusters, both near 0 eV and at the approximate energies of the resonances associated with DEA to the monomer leading to singly negatively charged cluster detection. Moreover, the production of metastable prymidine⁻ ions was also observed at these energies for clusters of n > 4. Careful inspection of the data of Neustetter *et al.*[194] suggests the possibility of an additional stabilisation mechanism at energies near 11 eV. The production of anionic clusters containing molecular fragment of pyrimidine was not observed.

Condensed-phase investigations of the diazines include a study in 2005[101] that considered the vibrational and electronic excitation electron impact cross sections of cold condensed pyrimidine at impact energies between 2 and 12 eV. They reported a series of vibrational excitations below 1 eV, a comparison of the vibrational levels seen in optical spectroscopy to those seen *via* electron energy loss, alongside electronic excitation spectra coupled with state assignment and further comparison to literature. The most intense electronic excitation was that at 7.6 eV of both the $^1B_2$ and $^1A_1$ valence states. Further condensed studies include a report of the cationic fragmentation and desorption of pyrimidine with electron energies above 2 keV[196] with a rich spectra of similar fragments to those seen in photoionisation studies, albeit with differing relative signal intensities favouring desorption of the lower mass cations.

The pyrimidine ring structure, seen in the DNA bases thymine and cytosine, suggests that electron stimulated desorption (ESD) experimental results for diazine molecules might be usefully compared to studies on DNA and DNA bases. Condensed phase adenine,

thymine, guanine and cytosine have been studied from 5-40 eV[197] and from 0-38 eV[198] impact energies by ESD. Notably, an H⁻ ESD DEA resonance was found at 8.6 eV for condensed thymine and uracil on a room temperature substrate. The detected desorbed fragment ions were H⁻, O⁻, OH⁻, CN⁻, OCN⁻ and CH_2^-.

Here pyrimidine and pyridazine were investigated by ESD to determine their fragmentation desorption resonances and products, and how these differ to the gas phase case.

5.2 Electron Stimulated Desorption

ESD measurements record the yields of charged desorbed fragment species from thin, molecular solid films under electron bombardment, as functions of electron impact energy and current. A review of this technique is found in Bass and Sanche, 2003[199]. An ESD ion signal measured as a function of electron impact energy is termed a "yield function" and provides qualitative information on electron-induced dissociation processes occurring in condensed molecular targets. In both gas and condensed phases, two processes contribute to anion production, specifically DEA and DD. DEA involves the resonant capture of an incoming electron to form a TNI, followed by dissociation into an anion and one or more neutral species. DEA and the types of TNI are described in more detail in Chapter 2. The resonance parameters of TNIs are usually modified in the condensed phase[200,201], such that ESD yield functions may differ somewhat from gas-phase anion measurements. An anion ESD signal produced by a DEA resonance appears as a Gaussian shaped peak at a characteristic electron impact energy (usually below 15 eV) in the yield function of a particular mass/charge ratio. Alternatively, DD usually results from a direct electronic excitation of a dissociative state of the target molecule, leading to fragmentation into an anion and cation and occuring at incident energies above that of ionisation[202]. The contributions of DD in anion ESD yield functions are typically observed at energies above ~10 eV and are characterised by a monotonic increase with incident electron energy[203]. Cations can otherwise be produced by dissociative ionisation

(DI)[204], where the ionised molecule dissociates into a cation and one or more corresponding neutral species.

5.3 Experimental Details

Measurements were performed at the University of Sherbrooke under the supervision of Professor León Sanche, Dr. Andrew Bass and Dr. Pierre Cloutier: specific details of the ESD technique are given in other publications[199,205,206]. Essentially, the ESD apparatus is composed of a cooled surface and an electron gun coupled to a reflectron time of flight mass spectrometer (TOF MS). Both are housed in an ultra-high vacuum (UHV) system. The interaction region is shown in Figure 44. The condensed molecular films are deposited onto either a Pt ribbon surface, or a layer of Argon already condensed on the Pt ribbon. The surface can be cooled by a helium cryostat to 18 K and cleaned by resistive heating. Pyridazine (98% purity) and pyrimidine (>98% purity) were purchased from Sigma-Aldrich. For each chemical, exposure to air is minimised and purification is performed *via* multiple freeze pump thaw cycles. The argon gas has a stated purity of 99.9995%. Sample vapor is admitted into UHV, *via* a sample inlet leak valve, in proximity to the Pt surface. The quantity is controlled *via* the change in pressure in the gas manifold holding line, as described by Sanche[207]. Film thicknesses are known within an accuracy of about ±30%[208]. A Kimball Physics ELG-2 electron gun provides incident electrons with energies in the range 0-80 eV and approximate energy resolution of 0.5 eV, in ~800 ns pulses. The electron beam is incident on a ~3 mm^2 area on the sample, as measured with a phosphor screen. The electron transmission spectra of clean Pt and of pyrimidine, pyridazine, argon, or combinations thereof, are used to check the quality of the Pt surface and film. The time-averaged incident current is the same for all experiments with the same molecule, but reduced from 4 to 2 nA when working with pyridazine to diminish charging as pyridazine showed problematic charging rates. To collect charged fragments, a large (~2 kV) voltage (positive or negative as appropriate) is applied to the Pt substrate shortly (10 ns) after each electron pulse to propel charged fragments into the reflectron mass spectrometer inlet and determine their mass/charge ratio. At each electron

energy, several tens of thousands of pulse cycles are recorded to generate a characteristic mass spectrum. Afterwards, the energy is increased by the nominated energy step. Yield functions are obtained by integrating the signal under each peak in each mass spectrum, at each energy. Anions and cations are investigated in separate experiments. Between each experiment, sample films are removed from the Pt by resistive heating and a fresh film deposited.
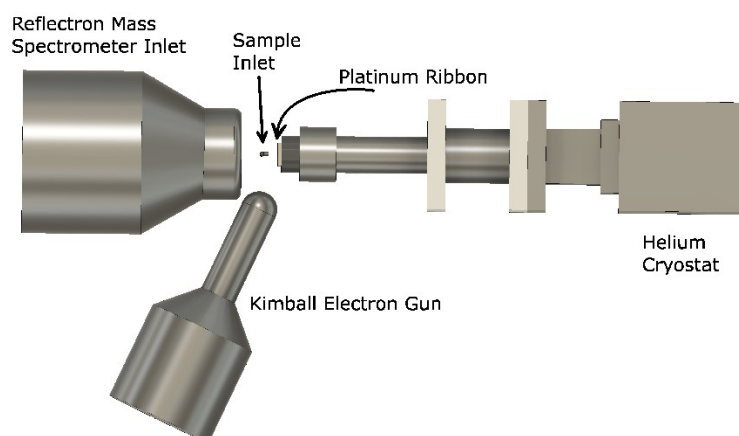
Figure 44 Interaction region of the described ESD experiment

In order to ensure the best conditions for each individual molecule, assessments were undertaken to optimise thickness, layering with the buffer Ar, incident electron current and temperature. As an example of this, the figure below (Figure 45) shows the effects on the detected anion species with increasing pyrimidine coverage condensed on Ar. As can be seen, the highest intensity is seen for H^- and CN^- with deposition of 30 % of a monolayer, and above this density intensity decreases with increasing coverage. This can be attributed to surface charging. Conversely, C^- shows minimal increases with increasing coverage, indicating possible reactive scattering. As such the coverage level of 30 % of a monolayer was used throughout the pyrimidine measurements.

In the case of pyridazine, 30 % proved again an appropriate coverage, however investigations of the electron current (flux to the surface as measured by transmission) showed shifts of resonant desorptions to higher energy with higher electron current, a

clear and common indication of elevated surface charging. As such the incident electron current of 2 nA was utilised for pyridazine, whereas 4 nA was optimal for pyrimidine. At low incident electron energies, below the threshold for ionisation, film charging indicates the accumulation of negative charge in the film, *via* electron stabilisation on a single molecule or groups of molecules, or by DEA. These processes can lead to the formation of anionic fragments that do not desorb[199]. Surface charging is dependent on cross sections for stable electron attachment, inter-molecular stabilisation and DEA, as well on the desorption probabilities of the various fragment anions produced. It is thus not possible to attribute the observation of both enhanced charging and low ESD signals in pyridazine to a single cause such as low desorption probabilities for fragment ions.
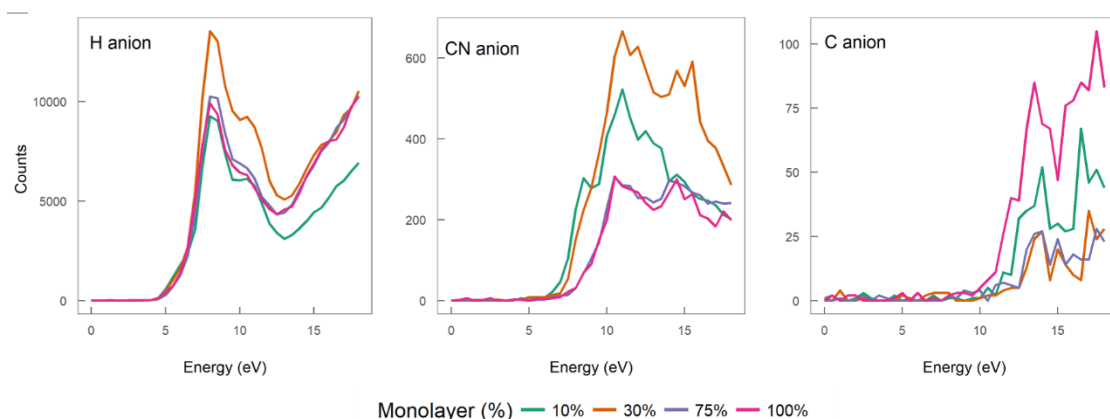
Figure 45 ESD efficiency studies for layer coverage of pyrimidine molecules condensed onto a standard 3 monolayers of condensed Ar

To justify the purity and validity of each individual experiment, the low energy electron transmission spectra were recorded and verified for each cleaning and layer addition, to identify contaminated surfaces and incomplete layer adsorption. As can be seen in Figure 46 the line shape changes according to the surface layer composition – this can be used as an identifier, both in intensity of current transferred and location of maxima and minima. While the structures seen can be deconvoluted to provide some information on electron resonances at low energies, this was not undertaken here in part due to the low resolution (0.5 eV) of the electron gun.

Lilian K. Ellis-Gibbings - June 2018
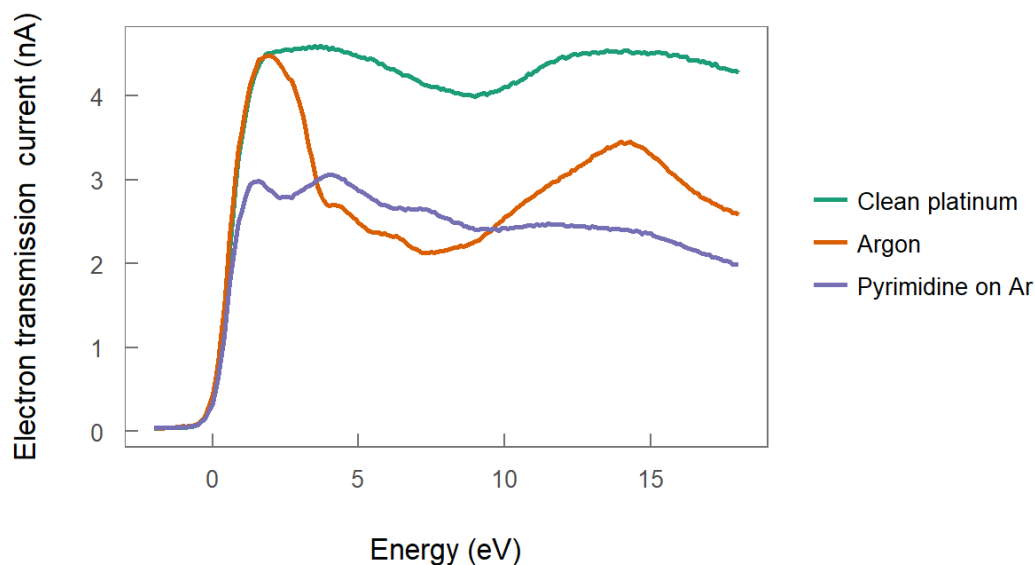
Figure 46 Transmission spectra of electrons vary depending on the surface composition, verifying the cleanliness of the platinum ribbon and the purity and thickness of each additional layer in the experiment

5.4 Results

5.4.1 Anion desorption

The results of anion ESD experiments for different conditions of solid films, followed by a comparison to appropriate literature, are presented here.

Yield functions obtained during electron impact on 5 ML thick films of pyrimidine and 3 ML thick films of pyridazine directly adsorbed on a cooled Pt surface are shown in Figure 47. The three strongest desorption yields from pyrimidine are H^-, CN^- and C_2H^- while only rather weak signals of H^- and CN^- could be obtained from pyridazine. Both samples were deposited on surfaces cooled to between 40 and 95 K, below the desorption temperature of either molecule.
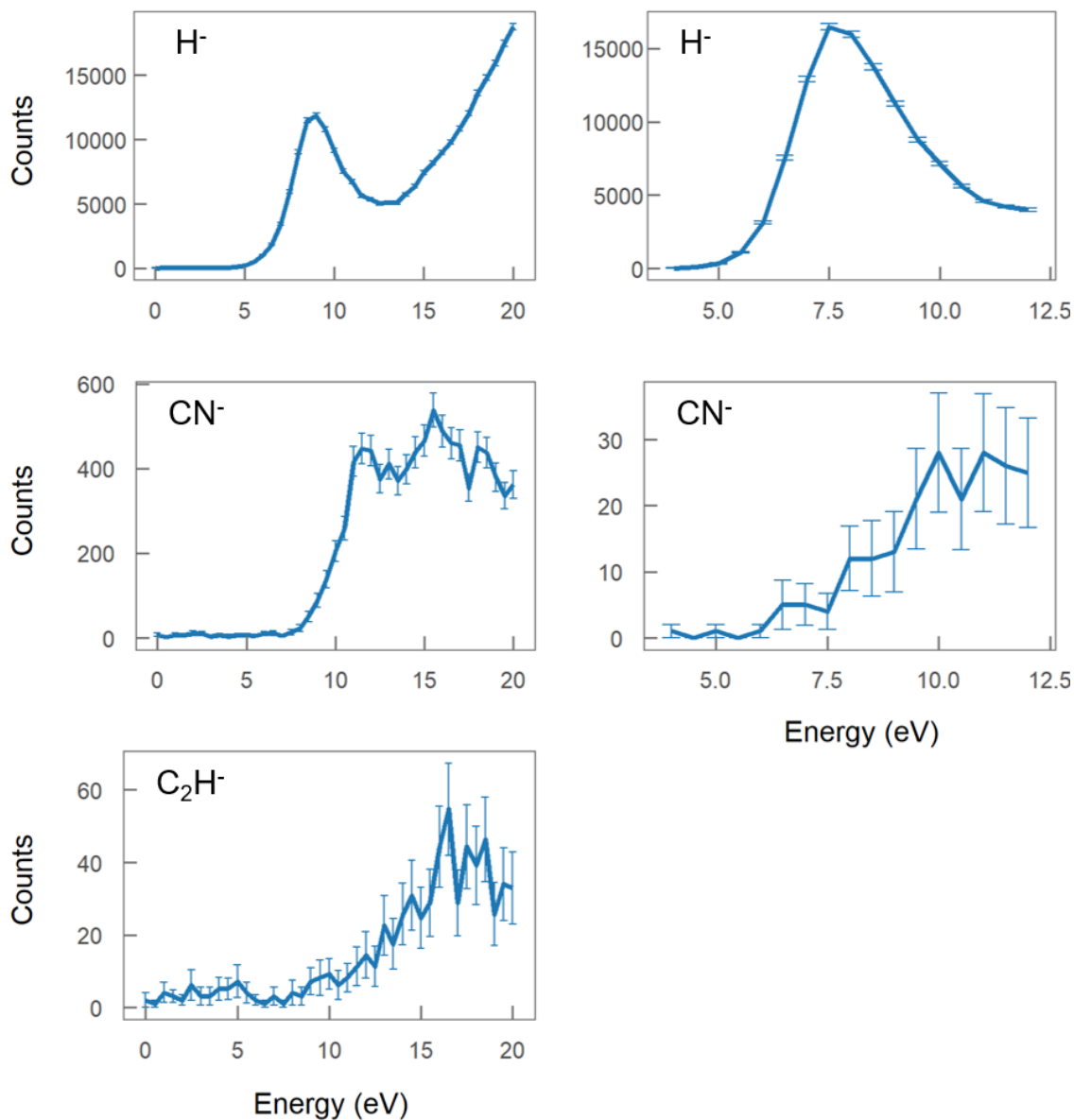
Figure 47 Anion yield functions obtained from: (left column) 5 ML of Pyrimidine on a Pt substrate bombarded with an incident current of 4 nA, 0.5 eV energy steps and 100 000 pulse cycles per energy; (right column) from 2-3 ML of Pyridazine on Pt substrate with an incident current of 2 nA, 0.5 eV energy steps and 50 000 pulse cycles per point. No other fragments were clearly observed. Data represent the sum of 3 yield functions obtained from separate films

Figure 48 shows anion yield functions obtained from sub-monolayer quantities of pyrimidine and pyridazine deposited onto 3 monolayers (ML) of Ar. It is clear when comparing the anion yield functions for the two conditions studied, (*viz*. sub-ML quantities on Ar and multilayer molecular solids) that resonance structures are more apparent when the molecule is deposited on Ar and that the ESD yield per deposited molecule is considerably higher.

Structures associated with TNI and well resolved in the yield functions of Figure 48 are narrower and higher intensity than in Figure 47 for desorption from multilayer films of either molecule. This is particularly evident for the case of the CN$^-$ desorption from pyrimidine. This tendency can be due to the directly deposited films being thicker and thus more prone to electron energy loss events occurring prior to attachment and also to post-dissociation collisions of fragment ions with other molecules, that effectively broaden the resonance features and reduce the yield of desorbing anions per molecule[209]. It is also possible that, in a way similar to that reported by Neustetter *et al.*[194], TNI that lead to molecular dissociation *via* DEA in isolated molecules are stabilized *via* interactions with neighbors in thick films, and therefore a reduction in the DEA leading to ESD.

Within experimental uncertainty, resonances in the multilayer films appear at the same energies as in the Ar-layer spectra. Pyrimidine and pyridazine differ in the energies of their resonances as is expected of molecules with differing structure and symmetry.
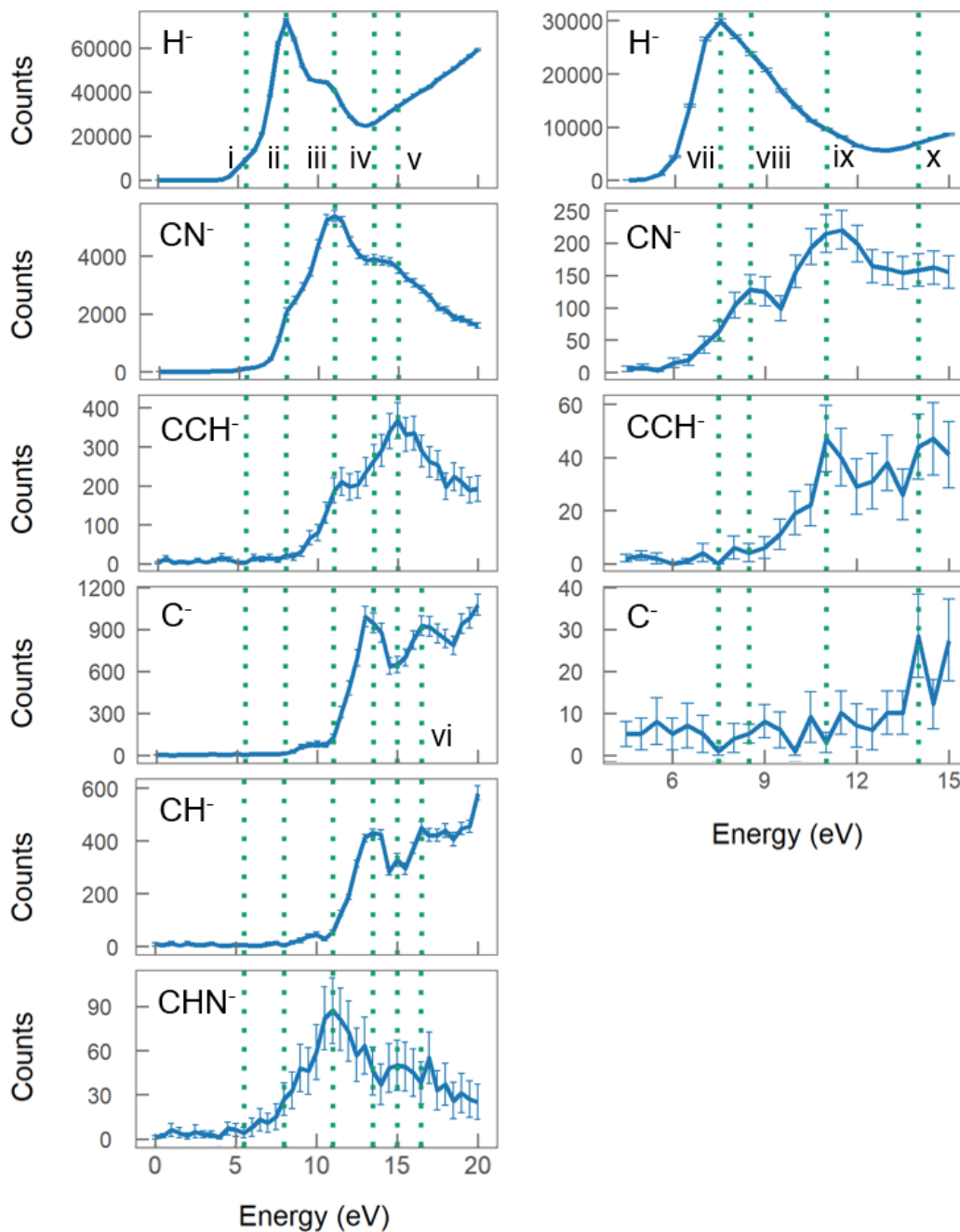
Figure 48 ESD anion yield functions: 30% of a ML on 3ML of Ar. Pyrimidine (left): 6 summed yields, obtained on separate films, electron current of 4 nA, 0.5 eV energy step, 100 000 pulse cycles per energy. Pyridazine (right): 4 summed yields, 2 nA electron current, 0.5 eV energy step, and 50 000 pulse cycles per energy. Dashed lines indicate resonances. Yield functions are not to be compared quantitatively.

Electron impact experiments on multilayer films of large organic molecules can experience severe film charging, which is reduced when sub-monolayer quantities are instead deposited on a thin rare gas solid (RGS) buffer layer[210]. Moreover by separating the molecule from the metal, the RGS film reduces charge induced polarisation[199]. Sub-monolayer quantities also reduce molecule-molecule and fragment-molecule interactions on the surface, so that the main difference between gas and solid film data arise principally from changes in TNI energy and electron-molecule potential and a lesser extent multiple scattering of electrons[201]. Coupling of certain molecular TNI states to electron-exciton complex states of RGS has been reported[211], but is not expected to be observable here due to the comparatively low energy resolution of the incident electron beam. As can be seen in Chapter 3 of this thesis, the electron energy loss spectra does not show strong electronic excitation occurring for impact energies below 10.5 eV, so large energy losses by electrons inelastically scattering in Ar are not expected. Both pyrimidine and pyridazine share H^- as the most intense desorption yield, most probably due to its low mass favouring a retention of a large fraction of available kinetic energy during dissociation. CN^-, C^- and C_2H^- also desorb from both molecules, with less intensity, while CHN^- and CH^- are detected exclusively from pyrimidine (Figure 48). The 26 m/z peak was assigned as CN^- and not $C_2H_2^-$ from the time of flight calibration with known fragments. The presence of all fragments other than H^-, indicates the complete disruption of the molecular ring. It is possible, though not probable, that metastable charged species, with lifetimes longer than the mass spectrometer flight-time, may contribute to the observed signals - giving rise to the addition of an unstabilised fragment to the yield functions.

The dashed lines in Figure 48 provide a visual guide for competing resonances. In brief, it is clear that resonances in the pyrimidine desorption yields occur at i), 5.5 eV (weak shoulder feature determined *via* log plot analysis), ii) 8 eV, iii) 11 eV, iv) 13.5 eV, v) 15 eV and vi) 16.5 eV, with iii and iv being observed in at least three different anion yield functions. The anions H^-, C^- and CH^-, appear to increase monotonically after 13 eV (H^-) and 18 eV (C^-, CH^-) indicating DD. Desorption signals from pyridazine are weaker except

for H⁻, and less diverse. Resonances for pyridazine are seen in yield functions at vii) 7.5 eV, viii) 8.5 eV, ix) 11 eV and x) 14 eV. Only resonances vii and viii appear strongly in more than one yield function. The signature of DD is apparent in H⁻ after 13 eV.

A comparison of the energies of resonances identified in the ESD yield functions of Figure 48 to those of TNIs and DEA reported in the literature is given in Table 14 and Table 15, along with possible state assignments. Error on the resonance energy in these tables is a combination of the electron gun resolution, the peak visibility and the apparent location of the peak maximum across multiple spectra.

It is clear from these tables that the condensed phase ESD yields are not necessarily associated with calculated and experimentally determined TNI resonances in the gas phase. Experimental gas-phase DEA results exhibit similar resonance energies, but the anions detected differ to the condensed phase results. It is expected that gas and condensed phase DEA resonances do not match exactly, since the image-charge induced polarisation at the Pt surface and in the film can lower[199,201,212,213] the energy of a resonance, as well as increase the kinetic energy required for an anion to desorb in vacuum. It is also possible that those resonant structures that appear at similar electron impact energy in both gas and condensed phase correspond to different resonances. However, the differences in resonance energy, fragmentation pathways, and relative intensity observed between the gas- and condensed-phase data often result from changes induced by condensation: addition of the charge-induced polarisation potential mentioned above, relaxation of selection rules adjusting the availability of TNI states[214], modification in resonance lifetime[215,216], number of decay channels and fragmentation channels[217,218], to all of which must be added the possibility of reactive scattering of the fragment with the neutral molecules in the film[199,219].

Table 14 A comparison of ESD resonance energies seen in condensed Pyrimidine to DEA experiments and calculations from the gas and condensed phase found in the literature.

exp a: Neustetter *el al.*, gas phase DEA mass spectra[194]
exp b: Field and Gilmore, gas phase DEA mass spectra[195]
 exp c: Nenner and Schulz, gas phase TNI [65]
exp d: Levesque *et al.*, electron excitation of condensed pyrimidine[101]
exp e: Innes *et al.*, VUV spectra[220]
calc f: Mašín and Gorfinkiel, CC and R-Matrix resonance calculations (note that Feshbach energies may be overestimated)[66]

Energy (eV)	This work: Anion ESD (± error eV)	Anion DEA (ref)	TNIs (ref)	Symmetry suggested
-0.25	-		shape 1 (exp c)	$^2A_2$
0.77	-		shape 2 (exp c)	$^2B_1$
4.24	-		shape 3 (exp c)	$^2B_1$
4.78	-		mixed core excited shape (exp d, e)	B_1
5.3	-	CN^-, $C_3H_2N^-$ (b)	(exp b)	
5.5	H^- (± 0.5)	CN^-, $C_3H_2N^-$ or $C_2N_2^-$, $C_4H_3N_2^-$ (a)	core excited resonance (exp a)	
7.6	-		(exp d)	$^1B_2$ $^1A_1$
7.25	-		(exp e)	
8	H^- (±0.25), CN^- (±0.5)			
8.336	-		feshbach 1 (calc f)	$^2A_1$
8.47	-		core excited shape (calc f)	B_1
8.8	-	CN^-, $C_3H_2N^-$(b)	(exp b)	
9	-	CN^-, $C_3H_2N^-$ or $C_2N_2^-$, $C_4H_3N_2^-$ (a)	(exp a)	

10.182	-		feshbach 2 (calc f)	$^2B_2$
11	H⁻ (±0.5), CN⁻ (±1), CHN⁻ (±0.5)			
11.5	CCH⁻ (±1)			
13.5	C⁻ (±0.5), CH⁻ (±1)			

The closest comparative resonances between condensed and gas phase studies are the yields of H⁻ at 5.5 eV and 8 eV (i, weak and ii, strong) and CN⁻ at 8.0 eV from ESD of pyrimidine on Ar (Figure 48). These are close in energy to the DEA resonances that produce CN⁻ in the gas phase at 5.3 eV and 8.8 eV from the work of Field and Gilmore[195] and 5.5 and 9 eV from the work of Neustetter *et al.*[194] respectively, though in both gas phase studies the lower energy resonance is dominant. The gas phase experiments were not sensitive to H⁻ and showed only weak signals with the reduction of magnetic fields, however the lack of CN⁻ at 5.5 eV in the condensed phase data deserves scrutiny. This could be related to a reduction in the cross section for the DEA production of CN⁻ through some interaction with the condensed environment[199,201], including *via* the stabilisation of the TNI against fragmentation, as observed by Neustetter *et al.*[194] in cluster experiments*,* although this would imply clustering at sub-monolayer coverage. Alternatively it is possible that dissociation into CN⁻ and neutral fragment(s), along the potential energy surface of the TNI, does not impart sufficient kinetic energy to the ions to overcome the polarisation potential induced by the image charge (0.5 - 1 eV)[221].

In pyridazine[195], an 8.5 eV CN⁻ ESD resonance seen in condensed phase (Figure 48 vii) matches well to the CN⁻ peak at 8.2 eV seen in gas phase. A broader gas phase CN⁻ double peak structure at 5.1 - 6.0 eV is not seen in condensed phase.

Table 15 A comparison of ESD resonance energies seen in condensed Pyridazine to DEA experiments and calculations from the gas phase found in the literature.
exp b: Field and Gilmore, gas phase DEA mass spectra[195]
exp c: Nenner and Schulz, gas phase TNI[65]
calc f: Mašín and Gorfinkiel, CC and R-Matrix resonance calculations (note that Feshbach energies may be overestimated)[66]

Energy (eV)	**This work: Anion ESD (± error eV)**	**Anion DEA (exp b)**	**TNIs (ref)**	**Symmetry suggested**
-0.317	-		shape 1 (c)	$^2A_2$
0.73	-		shape 2 (c)	$^2B_1$
4.05	-		shape 3 (c)	$^2A_2$
5.1-6	-	CN^-, $C_3H_2N^-$ (b)	(b)	
7.275	-		feshbach 1 (f)	$^2A_1$
7.5	H^- (±0.5)			
7.934	-		feshbach 2 (f)	$^2B_2$
8.27	-	CN^- (b)	(b)	
8.34	-		Core excited shape (f)	A_2
8.5	CN^- (±0.5)			
8.893	-		feshbach 3 (f)	$^2B_2$
9.868	-		feshbach 4 (f)	$^2B_2$
10.266	-		feshbach 5 (f)	$^2A_1$
11	CCH^- (±1), CN^- (±1)			

The higher mass fragment $C_3H_2N^-$ appearing in the gas phase at 5.5 and 5.0 eV for pyrimidine and pyridazine, respectively, is not detected in ESD for either molecule. As

with CN^- at 5 eV, the kinetic energy imparted to these fragments *via* the lower energy DEA process may not be enough for desorption and detection.

Four fragment species from pyrimidine and two from pyridazine, absent in the gas phase study of Field and Gilmore[195], appear in ESD yields. The anion fragments C^-, CH^-, CCH^- and CHN^- of pyrimidine arise from DEA at electron impact energies above 8 eV in Figure 48. The yields of both CHN^- and CCH^- share a resonance with CN^- and H^-, at 11 eV (iii) with further resonances at 13.5 eV (iv: C^-, CH^-) and 15 eV (v: CCH^-, CN^-). Peaks seen at the same resonance energy may indicate processes such as $CHN^{*-} \rightarrow CN^- + H$ and $CH^{*-} \rightarrow C^- + H$, where the parent fragments are produced in a dissociative excited state. While no TNIs have been reported at these energies previously, it is possible that the 11 eV resonance is related to the weak structure discernable at the same energy in cluster phase measurements of Neustetter *et al.*[194]. A small chance remains that peak iii at 11 eV could be the result of coupling between an electron-exciton complex in the Ar substrate (at 11.6 eV)[211,222] and the dissociative TNI of the target molecule. Normally the limited incident electron energy resolution used would preclude observation of such effects, but this possibility is consistent with the absence of the feature in Figure 47 for pyrimidine condensed directly on Pt. The two anionic fragments of pyridazine appearing only in condensed phase are CCH^-, with a yield function exhibiting a resonance at 11 eV, and C^-, exhibiting only a DD behaviour. All resonances in anion yield functions appearing above the energy of the DD threshold around 13 eV can arise from DEA or resonant decay into an electronically excited state dissociating into an ion pair[223]. Below this threshold, only DEA can produce anion fragments. That the yield of C^- from pyrimidine on Ar increases up to coverages of 1 ML, suggests that it may in fact be the product of reactive scattering by another anion rather than the direct result of DEA to the molecule. This has been reported previously with oxygen/hydrocarbon mixed films[224].

The dominant peak at 8 eV (Figure 48 ii) in the pyrimidine spectra can be compared to a resonance detected in EELS (see Chapter 3 for a description of EELS) for vibrational and electronic excitation of condensed pyrimidine in 2005[101], and assigned to both the $^1B_2$ and $^1A_1$ valence states. Additionally a 4^1A_1 excited state with high cross section has been

suggested theoretically at 7.6 eV[66] in the gas phase. This excited state may be the parent for a core excited resonance decaying into dissociation and producing the ESD peak ii in Figure 48. Since both CN^{-} and H[-] show this resonance, this implies either two competing resonant DEA processes at similar energy, or a single TNI resonance with multiple decay pathways.

Mašín and Gorfinkiel[66] calculated resonances of pyrimidine and pyridazine using the R-Matrix method[99] in 2012. The value of 5.5 eV for DEA to pyrimidine in gas (dominant peak[194,195]) and condensed phase (Figure 48 i) is in contrast to these values, as shown in Table 14, where the closest resonance, consisting of a mixed core excited shape resonance with B_1 symmetry, was calculated to be 4.78 eV. The same paper reported resonances for pyridazine[60], of the core excited shape type, at 8.34 eV with A_2 symmetry and a Feshbach resonance at 8.893 eV with $^2B_2$ symmetry that in Table 15 match both the gas and condensed phase CN^{-} 8.5 eV peak (vii). For the primary H[-] peak in pyridazine at 7.5 eV (vii), the calculated Feshbach resonance[66] at 7.934 eV is the most plausible assignment. Lower energy ESD, expected from DEA seen in calculations and experiments indicating shape resonances at -0.25, and 0.77 eV[60,65] for pyrimidine and -0.317, 0.73 and 4.05 eV for pyridazine are not present in the yields in Figure 48 or below 5 eV in the gas phase[194,195]. There are a number of resonances reported in Mašín and Gorfinkiel[66] for the molecules in excited states. In this study, such resonances do not contribute to the ESD signal, since the molecules are held at cryogenic temperature and hence exist in the ground electronic and vibrational state.

A comparison to DNA bases is relevant in the present context. F. Da Silva *et al.*[132] reported a gas phase investigation into the fragmentation of thymine and uracil, where the appearance of the fragment NCO[-] at 4 eV was shown to originate from a slow (metastable intermediary product detected between 1 - 31.6 μs), complex unimolecular ring opening process. As the detection of CN^{-} in this setup is limited by the delay between the start of the 800 ns electron pulse and the start of the 'push' pulse into the TOF (10 ns after electron pulse), this is also the limit for any long dissociation process and as such we would not expect to see fragmentation processes with time scales larger than 1 μs. They also defined

several fast reaction pathways to produce the NCO⁻ ion, and found resonances at 2.3, 4.4, 6.1, 6.8, 8.1 and 9.7 eV. It is possible that at least the 8.1 and 9.7 eV resonances seen in thymine and uracil could be attributed to the same processes as those seen in the spectra in Figure 48. The H⁻ loss of thymine and uracil was shown to be site selective[225], and there are similarities between the present spectra for H⁻ and the spectra of uracil or thymine with methylated N. Another study on site specificity[204] found that the H⁻ loss in thymine is from N1 (Figure 43) at 5.5 eV, N3 at 6.8 eV, C6 at 8.5 eV (ii peak), and C5 at 10 eV (iii peak). This similarity indicates that the two main H⁻ desorption peaks are from C5 and C6. S. Denifl *et al.*[226] also report gas phase studies of DEA to pyrimidine DNA bases, this time with cytosine and thymine[226]. They observed CN⁻ fragmentation resonances in cytosine at 1.86, 6.77 and 9.61 eV and in thymine at 6.94 and 8.41 eV. The highest resonance they reported could correspond to a similar fragmentation pathway for condensed pyrimidine at 8 eV. H⁻ was not reported from either of these studies on DNA bases and would be an excellent test of the clear similarities between the gas and condensed phase data.

5.4.2 Cation desorption

Cation ESD mass spectra from 35 eV electron impact on sub-monolayer quantities of pyrimidine or pyridazine deposited on Ar are shown in Figure 49, together with the NIST-reference electron-impact (70eV) mass spectrum for each molecule. The cation onsets from a 12 - 80 eV impact energy study in the ESD yield functions are described in Table 16 and Table 17; compared to NIST data, and in the case of pyrimidine, the data from Linert *et al.*[38]. ESD onsets are determined from the visual onset of the rise in the yield function at the point when the intensity reaches 10 × that of the background. The spectra for pyrimidine and pyridazine differ both from each other, and from the gas-phase results. While in the gas phase, the onsets for ionisation are 9.33 eV and 8.74 eV[111] for pyrimidine and pyridazine respectively, in the condensed phase cation desorption signals are not observed until 5-30 eV above these energies.
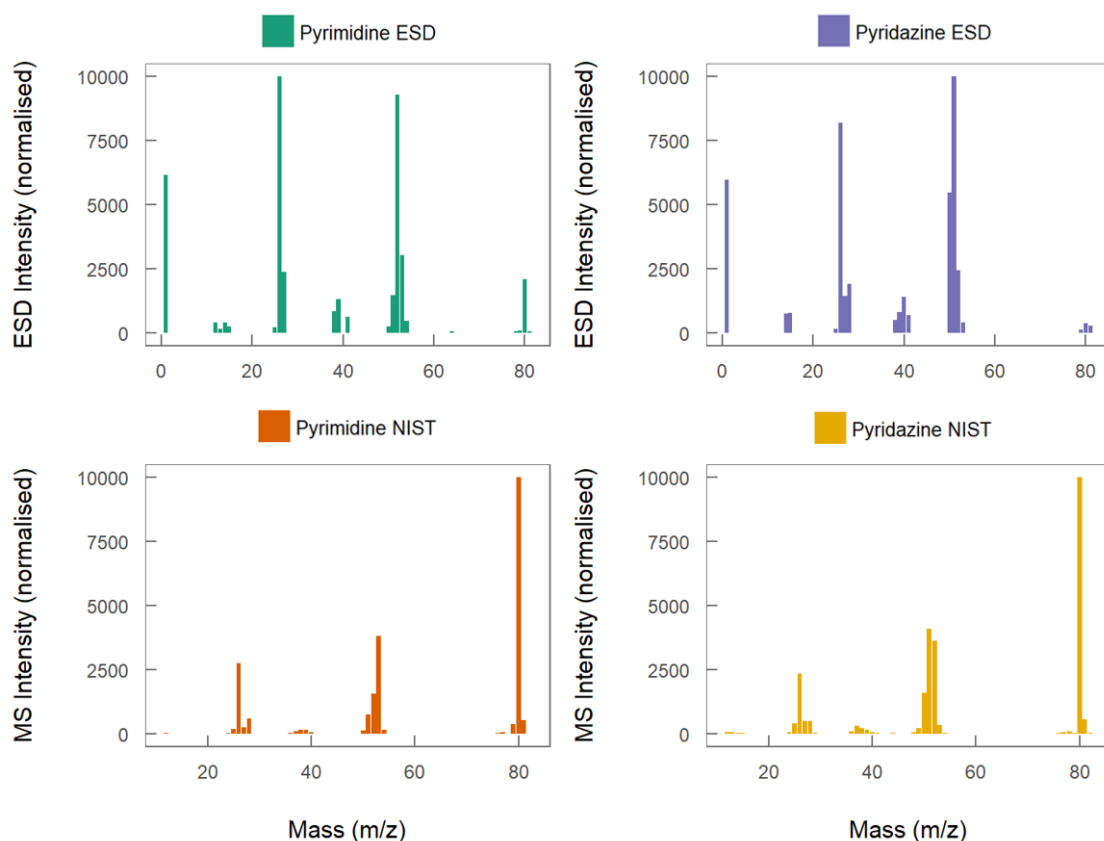
Figure 49 Cation desorption mass spectra compared to gas phase ionisation mass spectra of pyrimidine (left) and pyridazine (right).

In both cases, individual desorption yields increase from their appearance energy up to saturation around 60 eV, as seen for pyridazine in Figure 50. As expected due to their high mass and low momentum transfer in the ionisation process, the ESD yields of the parent ion, at 80 m/z, and of the next largest fragments with 5 ring atoms, are low.

Condensed pyrimidine cation desorption has been studied previously by Ribeiro *et al*.[196] at higher electron energies (approx. 2300 eV). Notably, their results show the most abundant fragment groups are centred around one or two ring atoms, whereas ESD of the one ring atom group is least likely. This result likely derives from a complex dissociation process attributable to multiple ionisation and Coulomb explosion due to the high impact energy. Gas phase pyrimidine fragmentation and cation formation were studied by Linert *et al*.[38] up to 150 eV and their results agree with the ESD fragmentation seen in the lower

energy range, but this agreement falls apart at higher energies. Their most abundant species by far was the parent ion, which is barely seen in the ESD yields. The next most abundant species was the two ring-atom group $C_2H_2^+$ (26 m/z) and the four ring-atom group, $C_3H_3N^+$ (53 m/z), in agreement with the ESD spectra.
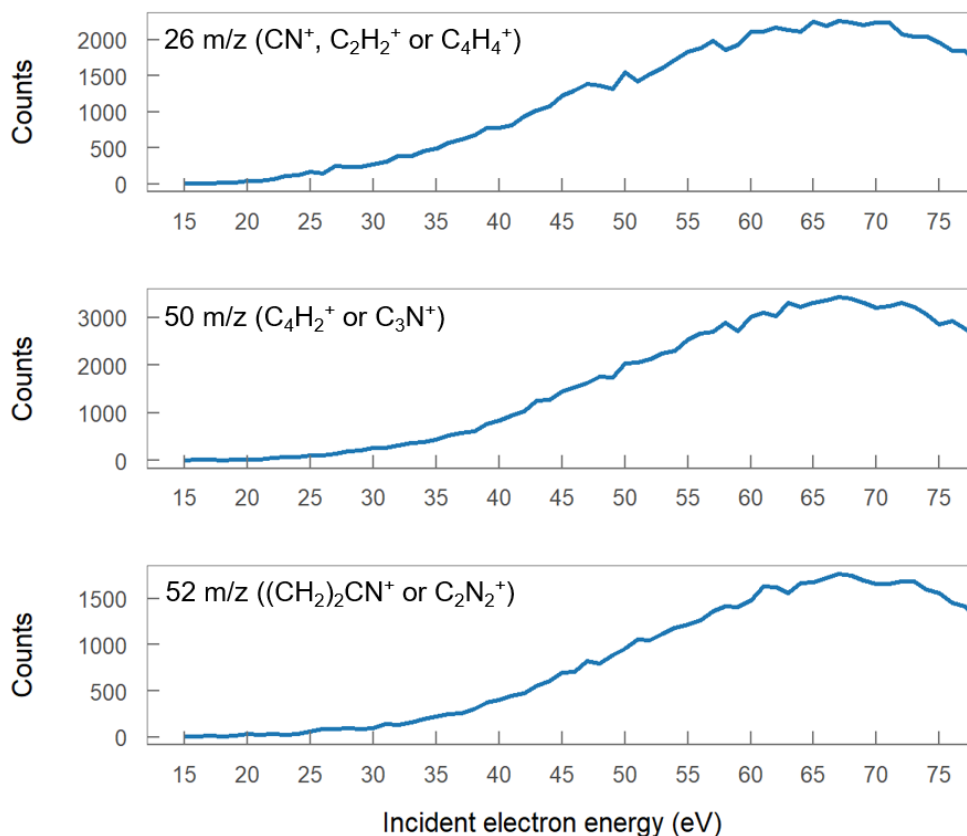
Figure 50 Cation ESD yield functions of submonolayer quantities of Pyridazine

No studies of the ionisation and cation formation of condensed pyridazine were found in the literature and to the author's knowledge presented here are the first such measurements. Pyridazine shows cation desorption yield spectra like those of pyrimidine, albeit with a higher yield for one ring-atom constituents. The ESD yield of the parent ion or (parent ± H)$^+$ ion, is even weaker relative to other fragments for pyridazine than for pyrimidine.

Lilian K. Ellis-Gibbings - June 2018

Cation production from gaseous pyridazine was previously investigated in the range 10-70 eV[74], with a focus on the production of the doubly charged cyclobutadienyl cation ($C_4H_4^{2+}$), which would appear at 26 m/z and constitutes one of the strongest peaks in Table 17, Figure 49 and Figure 50. The appearance energies of cations in condensed phase experiments are higher (Table 16 and Table 17) than seen in gas phase[111], as expected. For pyrimidine the desorption of fragments occurs at an average of 7 eV higher electron impact energy than it does in the gas phase measurements of Linert *et al.*[38]. The most abundant cations, at 25, 26, 52 and 53 m/z, have appearance energies that are closer to those in the gas phase, with a difference of the order of 4 eV. Interestingly the fragments at 12 and 13 m/z (C^+, CH^+), two of the weaker fragments in both gas and condensed phase, are very closely matched in appearance energy with a 2 eV and 4 eV difference respectively. The small difference in appearance energy is likely due to the low mass of the fragments, allowing them to more easily escape the induced surface potential.

Table 16 Onset energies for the appearance of the prominent cation fragments of pyrimidine condensed on argon, bombarded with 12-80 eV electrons. ESD errors calculated individually as the range between visual onset of yield to intensity 10 × background level. Compared to gas phase electron ionisation thresholds from NIST and Linert *et al.*[38]

M/Z	Condensed Phase ESD onset (eV)	Error ± eV	Cation Assignment	NIST gas phase appearance energy (eV)	Gas Phase Appearance Energy [38](eV)
1	13.5	0.75	H^+		
12	23.75	0.625	C^+		21.60
13	25	2.5	CH^+		20.40
14	26	0.5	N^+		
15	27	1	NH^+		

_25_	20	2.5	C_2H^+		16.65
_26_	18.5	0.75	CN^+		14.20
_27_	20.5	1.25	CHN^+		13.40
_38_	27.5	3	C_2N^+		12.60
_39_	21.5	1.75	C_2HN^+		11.00
_41_	22	2	CHN_2^+		
_50_	25.5	3.75	$C_3N^+, C_4H_2^+$		10.25
_51_	20.5	2.25	$C_3HN^+, C_4H_3^+$		11.90
_52_	17.5	1	$C_2N_2^+, C_3H_2N^+, C_4H_4^+$	15.01	13.90
_53_	15.5	2.25	$C_3H_3N^+, C_2HN_2^+$	12.87	11.65
_54_	22	3.25	$C_2H_2N_2^+$		11.85
_64_	26.5	4.25	$C_4H_2N^+, \ C_3N_2^+$		
_78_	25	3.25	$C_4H_2N_2^+$		
_79_	18.5	1.75	$C_4H_3N_2^+$		10.70
_80_	18.5	3	$C_4H_4N_2^+$ (Pyr)	13.01	9.45
_81_	25	1.25	$C_4H_5N_2^+, C^{13}C_3H_4N_2^+$		

Table 17 Onset energies for the appearance of the prominent cation fragments of Pyridazine condensed on Argon bombarded with 12-80 eV electrons. ESD errors calculated individually as the range between visual onset of yield to intensity 10× background level. Compared to gas phase electron ionisation thresholds from NIST

M/Z	Condensed Phase ESD onset (eV)	Error ± eV	Cation Assignment	NIST Gas Phase Appearance Energy (eV)
1	15	1.5	H^+	
14	25.5	2.75	N^+	
15	21	4.75	NH^+	
25	28	5.5	CCH^+	
26	19.5	2	CN^+	
27	24	4.25	CHN^+	
28	20	3.25	CNH_2^+, N_2^+	14.94, 15.79
38	25	4.5	C_2N^+	
39	20	3.5	C_2HN^+	
40	20	1.5	N_2C^+, Ar^+	
41	20	6.5	CHN_2^+	
50	20	3.25	$C_3N^+, C_4H_2^+$	13.67
51	19	2.5	$C_3HN^+, C_4H_3^+$	13.84
52	21	3.25	$C_2N_2^+, C_3H_2N^+, C_4H_4^+$	11.64
53	27	8.5	$C_3H_3N^+, C_2HN_2^+$	
79	37	10	$C_4H_3N_2^+$	
80	34	3.5	$C_4H_4N_2^+$ (Pyrd)	
81	31.5	3.75	$C_4H_5N_2^+, C^{13}C_3H_4N_2^+$	

5.4.3 Dipolar dissociation

An ion pair (anion and cation) is produced simultaneously in the DD process, which begins above the ionisation energy and can be seen in the Figure 48 anion yields between 13 and 20 eV. In this region, it may be possible to correlate the appearance of the DD-linked monotonic increases in anion fragmentation with the appearance energies of the cation ESD fragments.

Signals with the characteristic DD monotonic increase are seen for H^-, C^- and CH^- in pyrimidine (See Figure 51B and Figure 52B). It might be reasonable to see positively charged counterions resulting from the DD process desorbing at similar energies. DD clearly contributes to the ESD yield of H^- at energies above 13 eV, although the threshold for this process could in fact be lower and effectively hidden by the DEA component. No complementary $C_4H_3N_2^+$ cation appears at such low energies almost certainly because there would be insufficient kinetic energy to desorb such a massive fragment. For C^- and CH^-, Figure 51B indicates the DD onset is below 18.5 eV, and Figure 52A shows the cations that exhibit desorption onsets at this energy. In the case that these anions and cations are from the same DD process, there must be neutral fragments present to complete the molecule. An example of the dissociation processes resulting in the CH^- anion DD could be:

Cation M/Z of 26: $C_4H_4N_2 + e^- \rightarrow CH^- + (C_2H_2 \text{ or } CN)^+ + (CHN_2 \text{ or } C_2H_3N)^\cdot + e^-$

Cation M/Z of 52: $C_4H_4N_2 + e^- \rightarrow CH^- + (C_3H_2N \text{ or } C_2N_2)^+ + (NH \text{ or } CH_3)^\cdot + e^-$

Cation M/Z of 53: $C_4H_4N_2 + e^- \rightarrow CH^- + (C_3H_3N \text{ or } C_2HN_2)^+ + (N \text{ or } CH_2)^\cdot + e^-$
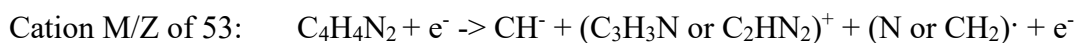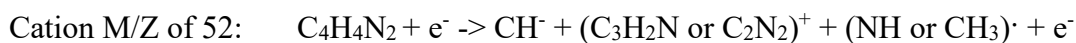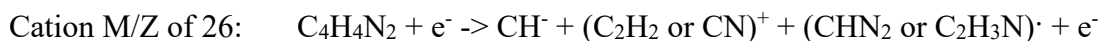
For the anion C^-, similar pathways apply, with an H shifted from the anion to the cation or neutral fragment. Since the ideal case of DD involves only one cation and one anion, it is possible that the cations listed above in fact arise from ID, rather than DD. In this case the signal for cation DD is suggested to be too weak to identify.
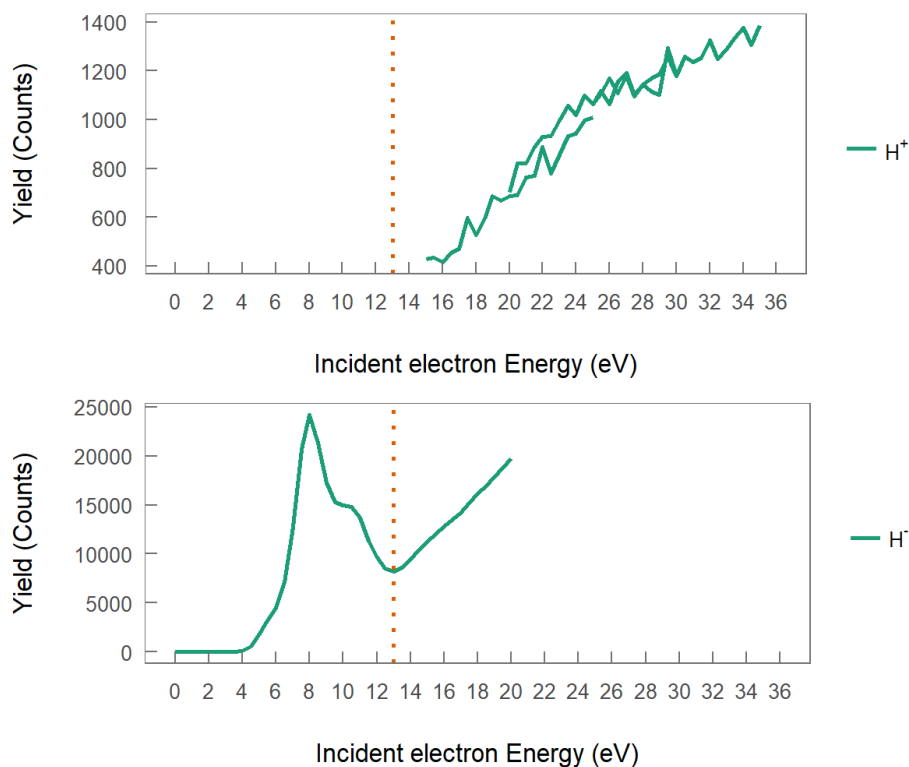
Figure 51 Comparisons of the onset of dipolar desorption for H cations (A) and anions (B) from pyrimidine

DD in pyridazine is apparent in the H$^-$ yield function at 13 ± 0.5 eV, similar to pyrimidine. A hint of DD's monotonic increase is also present in the C$^-$ spectra at 14 eV. Cations in this case do not present themselves until higher energies, with the appearance of the H$^+$ cation at 15 eV, C$_2$H$_2^+$ appearing at 19.5 eV and the C$_3$HN$^+$ (51 m/z) appearing at 19 eV making assignation of the DD pathways in this case mere speculation.

While it is clear from the anion yield functions that DD occurs, identification of suggested fragmentation pathways for both molecules would require yield functions for the corresponding neutral fragments – this is outside of the detection capabilities of the experiment.
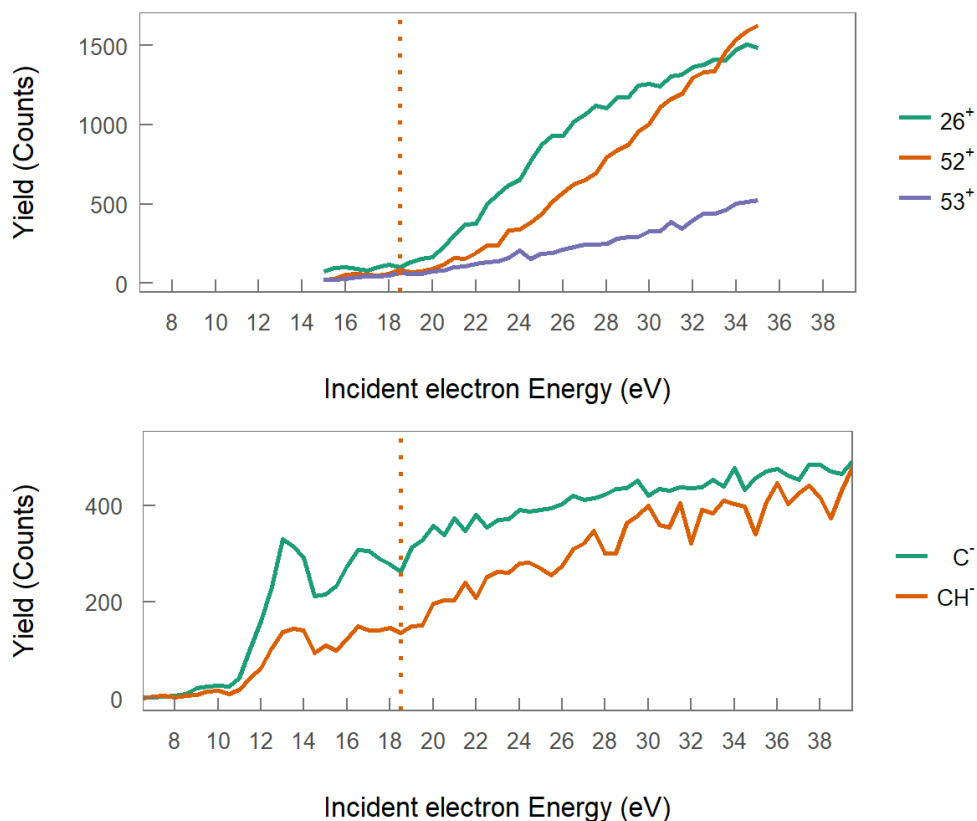
Figure 52 Comparisons of the onset of dipolar desorption for relevant cations (A) and anions (B) from pyrimidine

5.5 Conclusions

Condensed phase processes can differ significantly from gas phase, particularly at low impact energy where resonant processes form dominant inelastic channels. An understanding of the changes occurring between the phases is necessary to appropriately model real situations. To this end, unique ESD measurements of anions and cations from the biologically relevant molecules pyrimidine and pyridazine have been presented for electron impact energies below 80 eV. The two diazines show similar fragmentation products. Pyrimidine however – the fundamental structure for the RNA/DNA bases uracil, thymine and cytosine – is ~ 10x more susceptible to ESD of ring fragmentation products, which in DNA bases is associated with genotoxicity[54]. The reduced fragmentation of pyridazine as a constituent of kinase inhibitors[68,69] indicates that electron

attachment is not the pathway or mechanism of its radiosensitisation effect. While H$^-$ was the most abundant anion desorbed *via* DEA and DD from both molecules, the fragments CN$^-$, C$^-$, and C$_2$H$^-$ desorbed with sufficient intensity to identify the locations of resonances. These were observed at 8, 11, 13 and 15 eV in pyrimidine and 7.5, 8.5 and 11 eV in pyridazine. Comparing to literature, the previously reported shape resonances at energies below 5 eV were not found in ESD; the DEA fragmentation reported from gas phase differs in a shift of the appearance energies by ≤1 eV for the CN$^-$ fragment (26 mass/charge) in both molecules. All other fragments seen in ESD are not present in the gas phase DEA, while the fragment C$_3$H$_2$N$^-$ is only seen in gas phase[194,195]. Additionally, in the condensed phase, clear resonances at energies above the ionisation limit were seen and attributed to relaxed selection rules that could allow resonant ring-rupture. Such information may prove important for the study of the diazines as proxy for biological or radiosensitising materials.

At electron impact energies where DD is operative, the anion and cation appearance energies were compared to study the fragmentation pathways of these molecules. The analysis of the cations for both DD and DI are reported and the cation ESD onset was 13.5 eV for H$^+$. The mass spectra of cations desorbing from the samples are broadly similar to gas phase mass spectra obtained *via* electron impact, although the parent cation was found unlikely to desorb and several differences regarding appearance energies and relative intensities of fragments were observed, particularly a delay in the detection of like fragments from the condensed sample by an average of 7 eV. The differences seen in this study between gas and condensed phase fragmentation are important when considering the use of gas phase data for modelling of condensed phase systems. The data presented here along with the HREELS data already available[101] can provide a reference for the differences expected between the two phases.

6 APPLICATIONS

Many of the results produced in this thesis are applicable to real world situations, be that radiotherapy or plasma treatment of various media. To demonstrate this applicability, this chapter focuses on the use of some of these results in Low Energy Particle Tracking Simulation (LEPTS). Modelling of charged particle tracks is the culmination of all the previous work shown and is the outcome that can be used to inform clinical practices and to provide detailed data on the total effects of scattering processes in various media. Here, one aspect of the input data to Monte Carlo (MC) modelling, the inner shell process of the electron energy loss spectra (EELS), is investigated in detail for the molecule furfural.

6.1 Simulation

MC particle tracking models use collision cross sections (CS) and electron energy loss spectra (EELS, see Chapter 3) to perform event-by-event modelling of radiation induced phenomena[227]. This type of modelling can produce energy deposition profiles, in terms of depth and amount of energy deposited[33]. MC particle tracking is commonly used in treatment planning software for radiotherapy in clinical settings. However, few models include low energy (< 10 keV) processes[228,229]. LEPTS is exclusively focussed on this low energy range[67]. As plasma treatment results in electron and ion bombardment of a

target, MC modelling at low impact energy may prove useful for this process in the future, as it is already used for collisional processes within plasmas[81]. For this reason the biofuel precursor furfural is the target molecule. Furfural is introduced in detail in Chapter 1.

Appropriate modelling is ensured by using accurate input data and experimental verification of the outputs of the models. Feedback between the input and output data can verify which input data are most influential and require the most care. One such input data, as a part of the EELS, is the inclusion of the inner shell excitation and ionisation of the target molecules. This inner shell component has been excluded in some cases[40] and not others[28,230] from the experimental EELS used in the LEPTS models. It is assumed to influence the energy deposition outcomes[231] due to the high energy transferred. In furfural the ionisation potentials are near 291 eV for the carbon 1s orbital and near 540 eV for the oxygen 1s orbital, as in inner shell studies of furan[232]. As stated in the thesis of M. Fuss[126] regarding measuring the EELS of the inner shell with the original experiment described in Chapter 3: "Unfortunately, due to the much lower interaction probability of electrons with the inner shell, the measured signal there was extremely low and no clear features could be discerned."[126]. This low signal is exacerbated by the fact that the electron optics in the apparatus used by Fuss (and the author, in Chapter 3) are not optimised for electrons with such high energy loss, making collection of those electrons difficult. If the inner shell processes contribute more to the energy loss than accounted for, their exclusion would have the effect of lengthening the simulated particle tracks unrealistically.

For this work the simulations were performed, using data from the author, by an associated group at CIEMAT (Centro de Investigaciones Energéticas, Medioambientales y Tecnológicas, Madrid, Spain) using the particle tracking code LEPTS, and the results were analysed by the author. The Monte Carlo code LEPTS has been described in detail in various publications[67,108,230] and only a brief description follows here. LEPTS is an event-by-event simulation procedure written in C++ that processes electron and positron interactions with a chosen medium for collision energies normally between 1 eV and 10 keV. For higher energy interactions LEPTS is compatible with other Monte Carlo particle tracking codes such as GEANT4[233].

The code is capable of outputting energy deposition, total number of interactions, number of interactions of each type (elastic, ionisation, electronic excitation, vibrational excitation, rotational excitation, dissociative electron attachment, positronium formation etc.), number and energy of secondary particles generated and further tracking of those, all for any region specified by the user. After completion the simulation can produce 3D maps of all collisions, including all collision information (type, energy deposited) in the chosen volume, making it suitable for nanodosimetry studies.

The modelling procedure is as follows: the mean free path of the particle is sampled from the total cross section and a collision occurs. This collision is assigned a type by sampling the partial cross sections and, following the collision, the particle continues in a new trajectory, chosen by sampling the scattering angle and the particle's energy loss from corresponding distribution functions (Differential cross sections and EELS). Energy is deposited into the medium (and lost by the particle) according to the type of interaction and energy loss distribution for that type of interaction. Should an ionisation event take place, a second electron is generated by the program and its energy and direction assigned by conservation of momentum and energy. The particle tracking continues until thermalisation of all particles.

Input from the experimentally determined EELS are important for sampling the energy deposited in each interaction. An explanation of EELS and the apparatus used to measure them is given in Chapter 3 of this thesis. The experimentally determined EELS can be augmented by vibrational excitation EELS provided by higher resolution apparatus, with the intensity adjusted according to the respective cross sections. Vibrational and rotational processes are then each assigned a single energy loss value, being the weighted mean energy of known excitations. In the case of absorption of the electron (as for electron attachment) all remaining energy is deposited in the medium at the collision site. For the remaining inelastic channels the energy loss is sampled from the EELS, taking into account the thresholds for each process. It is in this process that the energy deposition resulting from inner shell ionisation processes may be overlooked if it is not adequately represented by the experimental EELS.

Lilian K. Ellis-Gibbings - June 2018

To investigate the significance of the inner shell electron excitation and ionisation processes on the LEPTS simulations, various EELS were given to the CIEMAT group for the test molecule furfural. Furfural has been introduced previously in this thesis in Chapters 1, 3 and 4 and the experimental EELS is presented in Chapter 3. The EELS was adjusted to contain various intensities of inner shell processes and a basic particle transport simulation run using each spectrum in LEPTS. The results, including differences in electron depth and energy deposition density, are presented here.

## 6.2 Inner shell processes in furfural
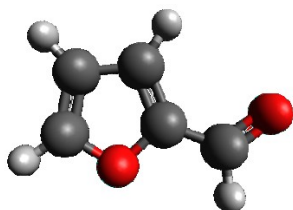
Figure 53 The molecule furfural, a furan aldehyde derivative. Grey: Carbon, Red: Oxygen, White: Hydrogen

Furfural, seen above in Figure 53, has inner shell electrons available from the 2 oxygen and 4 carbon atoms within the molecule. These originate from the 1s orbitals of the respective atoms. To include them in the EELS provided to the LEPTS model, the electron energy loss spectra of the 1s oxygen and carbon orbitals of a similar molecule, furan[232], were adapted for this purpose, each shown in Figure 54. In Duflot *et al.*, the incident electron energy is 2 keV, double that of the 1 keV general spectrum provided in Chapter 3 for furfural. As for the measurement of EELS, where over broad ranges the shape of the spectra do not change, this change in incident energy is not expected to change the shape of the energy loss. The original inner shell spectra only extended to 80 eV past the inner ionisation energy loss, requiring extrapolation for use in the EELS, so the ionisation continuum was extended by use of a log-log curve matched to the existing data as for outer shell ionisations. Small discrepancies in curve smoothness from this extrapolation procedure are not expected to impact this investigation. Excitation and

ionisation were assigned in the literature, however as they do not impact this investigation they are not explored here.
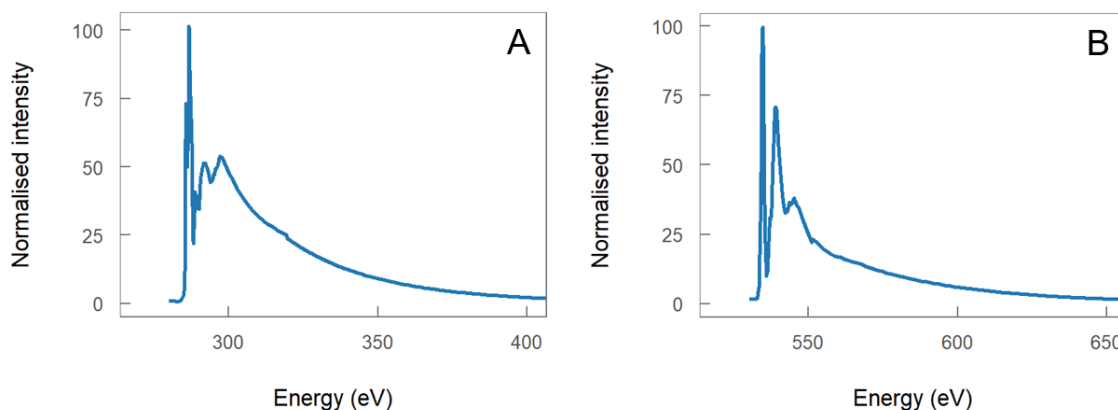
Figure 54 Furan, oxygen (A) and carbon (B) 1s electron energy loss spectra with extrapolation, original spectra in Duflot et al.[232]

To add these inner shell processes to the EELS produced by the electron transmission experiment described in Chapter 3, the intensity of the inner shell processes must be chosen appropriately. In this case the ratio of the oscillator strength of the 8.2 - 9.0 eV electron excitation of furfural[120] (assigned to the strongest electronic excitation in Chapter 3 of this thesis) with the oscillator strength from the O1s excitation[234] from H_2O_2 was used to estimate the appropriate EEL intensity ratio. This ratio was found to be 28.8. As furfural and H_2O_2 both contains 2 oxygen atoms, this ratio was used as is, and the C1s excitation was subsequently derived from the intensity ratio in the O1s to C1s EELS in furan from Duflot et al.[232], adjusting for the different number of carbon atoms present in furfural. This represents an approximate method to determine a realistic intensity for inner shell excitation and ionisation processes in the absence of appropriate experimental data.

To check the validity of this approach, another method for assigning the intensity of inner shell processes was concurrently investigated. The stopping power derived from the EELS as per the process in Oller et al.[235] can be compared to the literature stopping power of similar molecules and the inner shell intensity adjusted to match. Stopping power data is taken from the ESTAR database[236] where the stopping power and range tables for

electrons are available for a limited number of molecules. Of the molecules available in ESTAR, benzene (C_6H_6) was chosen for comparison, being a ring molecule. The relationship between collision stopping power, $\left(\frac{dE}{dx}\right)_{col}$, and the data provided by the EELS is as follows in Equation (14):

$$-\left(\frac{dE}{dx}\right)_{col} = N \sum_n E_n \sigma_n \qquad (\ 14\ )$$

Where N is the molecular density, E_n the energy transferred in the collision, σ_n the integral inelastic cross section of the collision, both summed over n, all accessible states. This is rearranged in Equation (15) to include the density of the target ρ, the "average excitation energy" E_a, Avogadro's number N_a and the molar mass M. For furfural the inelastic cross sections are taken from the scattering database developed in Chapter 4.

$$-\frac{1}{\rho}\left(\frac{dE}{dx}\right)_{col} = \frac{N_a}{M} E_a \sigma_n \qquad (\ 15\ )$$

The average excitation energy E_a can then be extracted from the EELS spectra by a weighted average according to Equation (16), where E is electron energy lost by the incident electron and I is experimentally detected intensity.

$$E_a = \frac{\sum E.I}{\sum I} \qquad (\ 16\ )$$

Using this method, the average excitation energy of the furfural EELS including the inner shell processes, with the intensity given by the ratio of optical oscillator strength, is calculated to be 49.3 eV at 1 keV collision energy. Using the stopping power for benzene from the ESTAR database the furfural average excitation energy should decrease to 41.0 eV by lowering the inner shell intensity. This creates a minor difference in the intensity of the inner shell processes between the two methods, as can be seen in Figure 55. The stopping power method reduces the intensity of the O1s peak by 30% below that of the

optical oscillator method, changing the ratio to the valence excitation band from 3.5 % to 2.5 %.
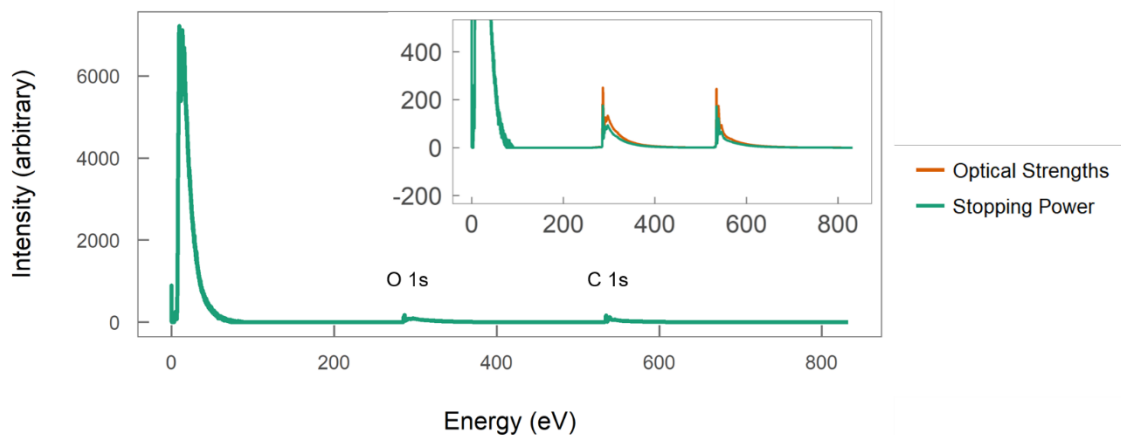
Figure 55 Two methods to set the intensity of inner shell processes for furfural, with close-up inset, details in text.

Both methods used to assign the intensity of the inner shell processes in the EELS can be considered indirect, and so there remains the question of their validity. Importantly, the impact on modelling of variations in the intensity of inner shell processes should be evaluated, to determine how critical these additions are to modelling results.

6.3 Modelling results

The modelling was performed by the CIEMAT group using the LEPTS Monte Carlo code on electron impact to furfural in gas phase. Three simulations were run, using three different EELS provided by the author. One spectrum does not include inner shell processes, one includes them with the intensity set using the oscillator strength method, and the third includes them with the intensity set using the stopping power method (30 % lower). All differential and integral cross sections were taken from the database produced in Chapter 4 of this thesis. The simulation consisted of 100 000 electrons with initial kinetic energy of 10 keV, tracked to thermalisation. In this low energy region individual energy losses become more important in determining the energy deposition and penetration depth of charged particles. The results provided for analysis included the

number of each type of process and the energy deposition at depth intervals of 0.01 μm, as well as additional visualisations of the electron tracks. All electrons were thermalized within 1.8 μm as seen in Figure 56, depositing all of their energy into the medium in a series of elastic and inelastic collisions. Secondary electrons were also tracked to thermalisation as seen by the lower energy collisions occurring as offshoots from the high energy electron traversing from bottom left to upper right in Figure 57.
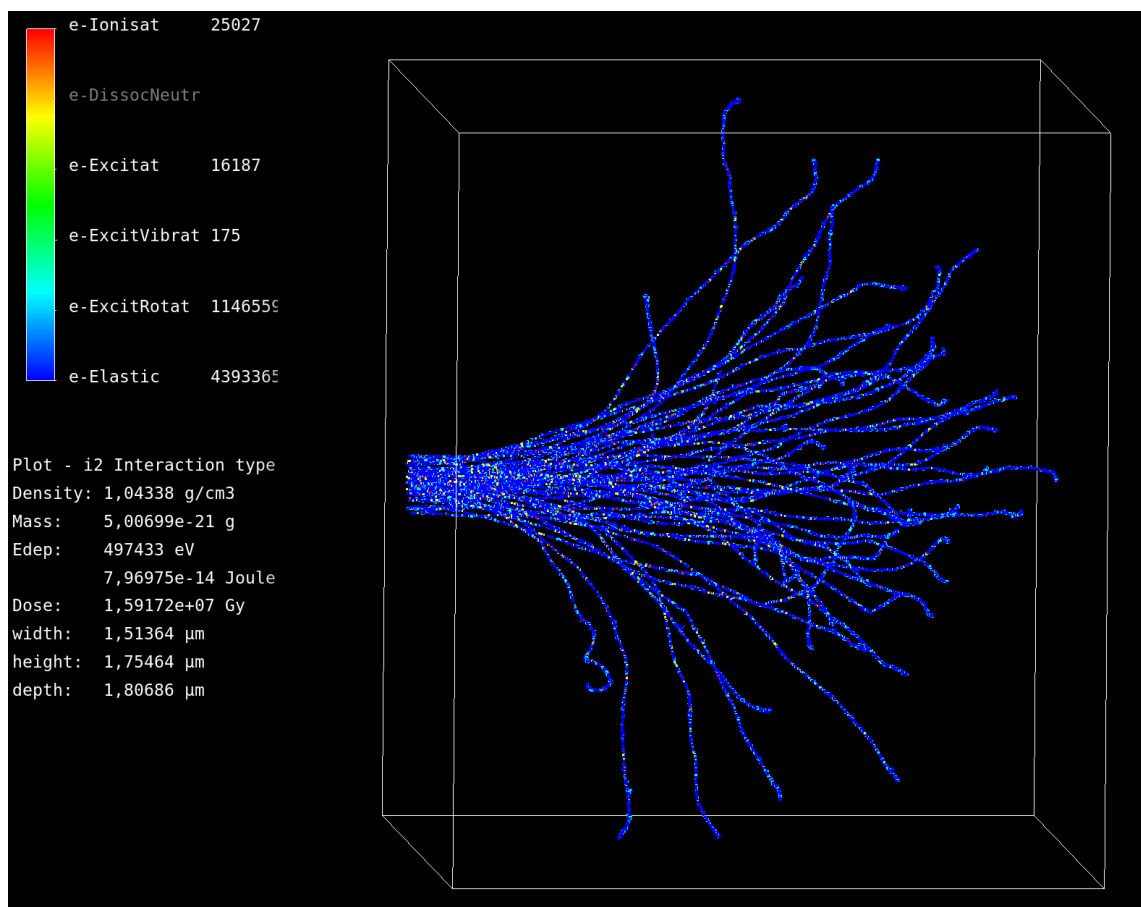

Figure 56 Electron tracks through furfural, LEPTS simulation, provided by CIEMAT group. Dot colour indicates interaction type, showing only 50 electron paths.

The results of interest are those that indicate differences between the three types of EELS. The energy deposition profile can highlight any differences between simulations. This is presented in Figure 58, where differences between the three simulations can be seen.

Including the inner shell processes in the EELS when simulating particle tracks in furfural reduces the scattering depth of electrons, with all electrons thermalised in 1.745 μm for no inner shell considerations, reduced to 1.675 and 1.685 μm for the oscillator strength and stopping power methods respectively. The position of the maximum of the energy deposition is a more important quantity for applications, reaching 83.1 % and 85.1 % of the depth reached when no inner shell processes are considered, for the oscillator strength and stopping power methods respectively. These peak positions are as follows: No inner shell at 1.197 μm, oscillator strength method for intensity of inner shell at 0.995 μm, and stopping power method for the intensity of the inner shell at 1.019 μm. A difference of ~ 0.2 μm may seem minimal, but for activities such as radiotherapy the tolerances for treatment planning are of the order of 1 mm for high energy particles (photons/ions) and low energy secondary electrons deposit their energy outside of this region, not being modelled in common clinical dose planning systems[237].
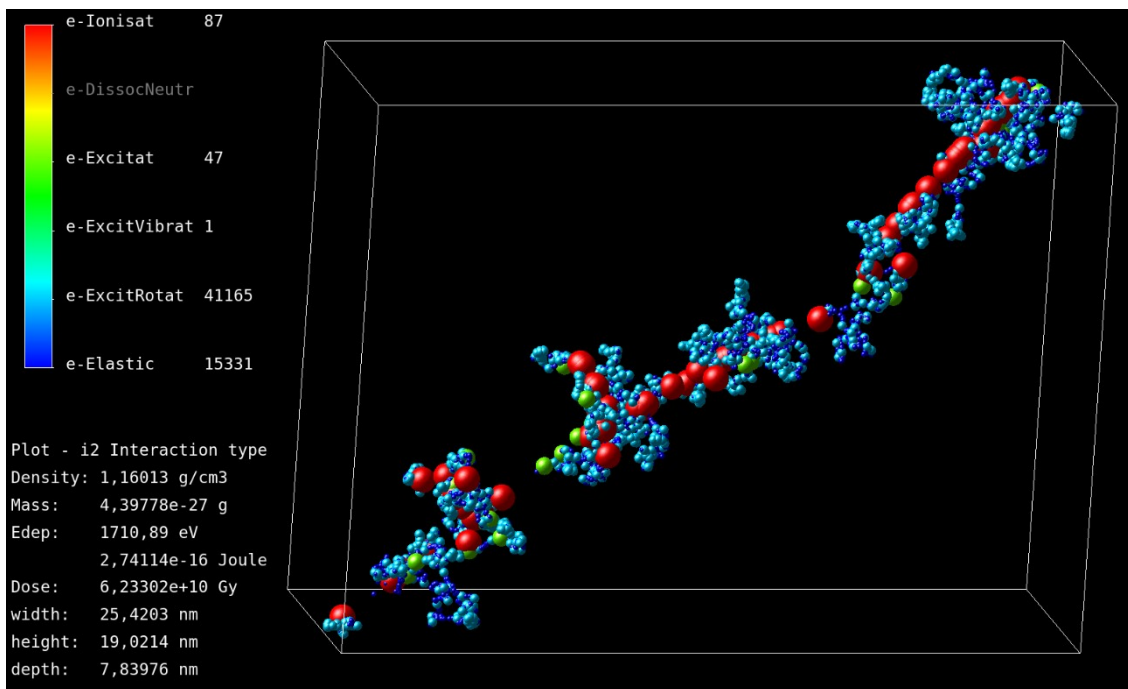

Figure 57 Track of individual electron in furfural, LEPTS simulation, provided by CIEMAT group. Dot colour indicates interaction type.
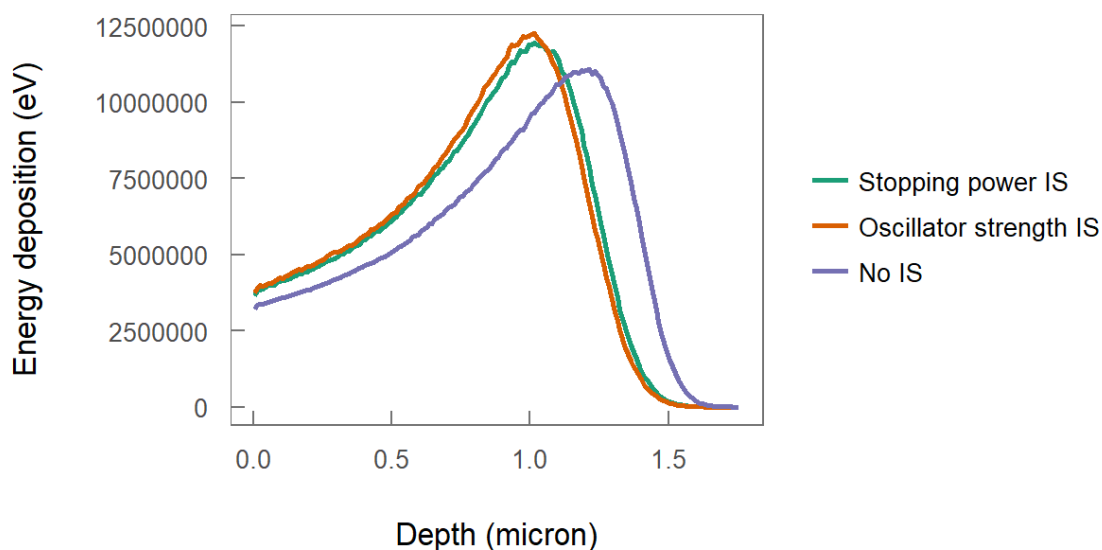
Figure 58 The effect on LEPTS modelling of including the inner shell (IS) processes to the EELS. Energy deposition of 100 000 electrons with initial energy 10 000 eV in furfural. Details in the text.

At this maximum of energy deposition, the types of processes occurring are important for understanding the changes occurring in the medium. As an example of the power of the LEPTS program, Table 18 shows the number of each type of process in the 0.01 μm slice at the maximum of the energy deposition for the EELS produced using the oscillator strength method. Rotational and elastic processes dominate scattering even at the energy deposition peak, with those inelastic processes capable of disrupting the medium combined making up less than 0.3 % of the number of processes occurring. The location of the energy deposition maximum is the same as the location of the maximum number of all processes, as expected.

Table 18 Number of each process at the maximum energy deposition. EELS including inner shell processes with oscillator strength method to define intensity.

Depth (μm)	Ionisation	Excitation	Vibration	Rotation	Elastic	SUM
0.995	604437	381670	3816	2.75E+08	1.05E+08	380719923
% of SUM	0.158	0.100	0.001	72.148	27.591	

The difference between the two methods for implementing inner shell processes are minor when compared to not implementing them at all, and the recommendation is that the method with more robust literature sources be used. This would be the oscillator strength method when appropriate literature values are available for a defined valence and inner shell process for the molecule in question or an appropriately similar molecule, and the stopping power method when data for an appropriately similar molecule exists in the verified databases of the scattering community. Inner shell EELS should be taken from literature from molecules similar to the molecule in question, as the shape of the excitations varies, and sharp peaks can greatly alter the intensity of inner shell processes required to alter the average excitation energy. An appropriately similar molecule would be a compromise between the number and type of atoms in the molecule and the shape, bonding and functional groups of the molecule. Both methods used to assign the intensity of the inner shell processes in the EELS can be considered indirect, however a direct method is possible. The stopping power of furfural at low energies should be confirmed as has been done for water[238] and the average excitation energy compared directly to inform the more accurate method.

6.4 Conclusions

Data provided and collated in this thesis is directly applicable to Monte Carlo modelling of charged particle tracks. The collision scattering database from Chapter 4 for the molecule furfural was provided to the authors of one such code, the LEPTS code for low energy scattering, and successfully implemented for an electron scattering simulation. An analysis of two methods to include inner shell processes in the experimentally determined EELS of Chapter 3 was undertaken, and three separate EELS provided to the LEPTS team for simulating. Analysis of the results they returned indicate that inclusion of the inner shell processes is important for accurate scattering depth and energy deposition profiles, as they reduce the depth of maximum energy deposition by up to 17 %. Two methods were tested for determining an appropriate relative intensity for inner shell processes, by comparing literature oscillator strengths for valence and inner shell excitations or by adjusting the average excitation energy to match the stopping power of the target to a

similar molecule. They were found in this case to be closely matched, altering the relative intensity of inner shell to valence processes from 2.5 to 3.5 %, and not greatly affecting the simulations. Both methods are recommended, and the choice should be determined by the availability of accurate literature values. The use of data provided in this thesis as fuel for modelling scattering processes validates the methods and results herein as both directly useful and informative.

7 CONCLUSIONS

In this thesis collision reactions between charged particles and molecules of biological or biofuel significance have been investigated through a variety of experimental and theoretical means. Focused on low kinetic energy collisions, between 0 and 10 000 eV, studies have been made to provide data for modelling and to understand the fragmentation processes occurring in particle-molecule and ion-molecule collisions.

At low energies, investigations of inelastic collision phenomena are still time-consuming for calculation and rarely provide information on dissociation. Here, experimental work played a key role in adding to scattering databases, validating theory, and providing information on dissociation. Electron collisions below 15 eV with gas phase molecules were investigated experimentally in Chapter 2 with regards to the vibrational differential cross sections and dissociative electron attachment products. These experiments are useful for understanding the effect of near-thermal electrons produced by ionising radiation and plasma treatments, and as such the molecules pyrimidine, a DNA base analogue, furfural, a biofuel precursor, and a series of esters, used as biodiesel, were chosen for their relevance to health and industry applications.

Differential cross sections at 15 eV for the molecule pyrimidine for angles between 20° and 90° showed four distinct vibrational excitation bands and a quasi-isotropic angular distribution. State assignment was made by conferring with the literature, and these cross section values are now part of the pyrimidine scattering database used for the Monte Carlo Low Energy Particle Tracking Simulation (LEPTS).

Dissociative electron attachment resonances were investigated for the biofuel precursor furfural and several biodiesel esters, biofuels being an industry that uses plasma treatments as part of the preparation processes. The esters methyl acetate, methyl propionate, ethyl propionate and butyl propionate were studied to elucidate patterns stemming from the chain length of the alcohol precursor, and in each case many anion species were detected in low intensities. Common resonances appeared near 1.5 eV, 3 eV and 7-10 eV - in particular a resonance at 7.5 eV with a higher energy shoulder peak located ~ 1 eV above this being present in a large number of anion yields for each of the four esters. The ester bond proved particularly susceptible to dissociative electron attachment and may discourage the use of plasma treatments if the plasma electron temperature resides near the resonances specified. The biofuel precursor furfural showed stronger anion yield intensities with two clear resonance energy regions, the first between 4.5 to 5.5 eV and the second 7.5 to 8.9 eV. As furfural can be seen either as a primary or by-product, this fragmentation may be exploitable by industry. The claim that furfural can be used as a deoxyribose analogue at low electron impact energies was investigated and found not to be supported by the dissociative electron attachment results.

Experimental development formed a large part of the work for this thesis, including, in Chapter 3, improvements to an existing apparatus and systematic characterisation of a new experimental apparatus. These apparatuses are an electron transmission experiment for producing electron energy loss spectra and a novel crossed beam experiment intended for low energy electron transfer experiments in anion-molecule collisions, aimed at determining the effect of radicals produced by ionising radiation on the local medium. They produce results that are not calculated, to the author's knowledge, by theory.

Improvements to the stability of the electron transmission experiment, through the installation of a new scattering chamber and ion optics system, enabled production of electron energy loss spectra for the targets argon, acetylene and furfural. Excited states were assigned as per the known literature, with some unassigned autoionising states recognised for furfural. These spectra are used directly as energy transfer distribution input for the Monte Carlo LEPTS code.

The first experiments from the anion-molecule collision experiment were made on the molecule nitromethane. Electron transfer can stabilise the parent anion and open new fragmentation pathways due to the presence of the third body, providing different results to dissociative electron attachment. The detected products of O^--nitromethane collisions included the parent anion $CH_3NO_2^-$ and the fragment anions CNO^-, NO^-, O^- and H^-. These

results are most similar to electron transfer experiments using neutral potassium beams, implicating electron transfer as a dominant mechanism. To further characterise the experiment, analysis of the energy spread of the anion beam, by both experimental and theoretical methods, was undertaken. Using a retarding grid to repel the anions as a high pass filter, results indicated that the energy spread of the anions has a mean of 105 eV with an experimental range of 110 eV. The experiment showed a broad population distribution within the beam, with the kinetic energy mean centred near 50 eV below the applied extraction energy. This large energy spread was agreed to in range by SimIon simulations, but not in the population distribution - the SimIon simulations indicate that the majority of anions have energy within 10 eV of the extraction energy. Reasons for this difference and the broad energy distribution of the anion beam were attributed to the method of anion extraction from the hollow cathode plasma source and optimistic initial ion placement within the SimIon simulation. Improvements to beam intensity were sought by further SimIon simulations, used to optimise Einzel lens placement and voltages. These were validated in the experiment, providing accurate starting points for further optimisation by hand. Improvements are recommended to the experiment including a new source.

Theoretical methods can be of immense value for providing scattering cross sections over broad energy ranges quickly, or in cases where experimental work is unavailable. Below 10 keV, where the Born approximation loses validity, the Independent Atom Model with Screening Corrected Additivity Rule and Interference effects (IAM-SCAR+I) method is able to produce accurate cross sections down to low energies, for both electron and positron scattering. The interference contribution is a new addition to the method, and positron scattering from two well studied molecules, N_2 and O_2, were calculated to validate the new method. When comparing to literature data the calculations show improvement in regions above and below the positronium formation threshold, but overestimate the available data in the maximum of the integral cross section. The computational cost of running the IAM-SCAR+I code is low and the accuracy high, so it is perfect for cases where little to no data is available in the literature and researchers require a dataset for particle tracking models such as LEPTS. As such a database for electron scattering from furfural was selected and collated using experimental and theoretical data from the literature and augmented by the IAM-SCAR+I results where necessary, ready for use in LEPTS along with the electron energy loss spectra produced

experimentally. Both the positron scattering results and furfural database are found in Chapter 4.

Applications for scattering data, including radiotherapy and plasma treatment, require appropriate treatment of condensed phase targets. In many cases this means adjusting gas phase data, such as those described so far in this conclusion, to account for the differences in density, degrees of freedom, and inter-molecular reactions. To understand differences between gas and condensed phase low energy electron scattering, electron stimulated desorption (ESD) experiments were undertaken for the molecules pyrimidine and pyridazine, and presented in Chapter 5. Pyrimidine, being an analogue for the DNA bases thymine, cytosine and uracil, and pyridazine, a common structure found in some radiosensitisers, are both relevant molecules for radiotherapy research. Both molecules produced H^-, CN^-, C^-, C_2H^- in anion desorption below 15 eV. Pyrimidine showed greater resonant fragmentation leading to the detection of the additional anions, CH^- and CHN^-. Detected anions differ between gas dissociative electron attachment and condensed phases ESD, with only the CN^- anion existing in both. Gas phase experiments additionally detect the $C_3H_2N^-$ fragment, not seen in condensed phase. The resonances were also found to differ between gas and condensed phase, with low energy resonances seen in gas phase and not condensed phase, and a shift in appearance energy of the resonances for CN^-. Evidence of dipolar desorption in both anion and cation species was found, however matching pairs could not be identified, indicating only one ionic species of the pairs easily desorbs at the dipolar desorption onset. Cation desorption also differs from the cation profile seen for gas phase electron ionisation. For both condensed molecules, the relative intensities of cations differ to gas phase, and the condensed phase data show delayed onsets for known cation fragments. In both anion and cation electron stimulated desorption, the results indicate that the condensed phase data is not equivalent to gas phase data for diazines, particularly for resonant processes. Care must be taken in using gas phase data for condensed phase particle tracking models below 80 eV impact energies.

A further aspect of particle tracking simulations is that of the accuracy and relevance of the input data, investigated in Chapter 6. The experimentally determined electron energy loss spectra tend to omit inner shell excitation and ionisation processes. To understand their relevance to particle tracking models, simulations were commissioned from the CIEMAT institution to use the scattering database and electron energy loss spectra for the molecule furfural, developed as part of this thesis. Several energy loss spectra were

provided, one missing the inner shell processes and two including them, for separate simulations of 100 000 electrons with 10 000 eV energy each. Of the spectra including inner shell processes, the shape and relative intensity ratios were taken from the O1s and C1s electron energy loss spectra of furan, available in the literature. Two methods were trialled for determining an appropriate intensity ratio of the inner shell peaks to the valence excitations, both reliant on available literature data. For furfural, using literature comparisons of available oscillator strength values for recognisable excitations placed the intensity of the inner shell O1s excitation at 3.5 % of the highest valence excitation. Matching the collisional stopping power of furfural to database values for benzene, by adjusting the inner shell intensity and therefore the average excitation energy, placed the same excitation at 2.5 % of the valence excitation. The simulation showed that while this difference in intensity did not greatly affect the depth of maximum energy deposition, neglecting the inner shell processes entirely was clearly responsible for increasing the maximum energy depth by 20 % above that when including them.

Overall, an analysis of the collision interactions between particles with energy less than 10 keV with molecules of interest to the radiotherapy and energy industries has been undertaken. An exploration of the processes occurring in different collision energy regimes and physical phases, and their dissociation products, has allowed for the production of data directly useful to modelling groups. Experimental and theoretical work produced here have been used in particle tracking models and scattering databases. Exploring the complications arising between gas and condensed phase, and the necessity of highly accurate and finely tuned input to models, is vital for ongoing research in this field. The journey from the experiments and theory of individual collisions, to resonances, to collision products, to condensed phase changes, and finally to application tells a story of a field still in need of new experiments and improvements to models before it can reach a true understanding of the medical and industry realities it seeks to predict.

In future, new and more accurate scattering databases of more complicated and relevant molecules are necessary and the choice of molecule should be made in conjunction with the needs of relevant industries. In the experiments at CSIC, Madrid, several improvements are recommended. New, more stable power supplies for the electron optics of the electron transmission experiment would facilitate a reduction in experimental error and could allow that apparatus to provide total cross sections as well as electron energy loss spectra while electromagnetic shielding could allow a reduction in the electron impact energy. Further development of the anion collision experiment to facilitate a

narrower energy width would enable better comparison to literature. This could be achieved by replacing the ion source with a microwave discharge. More generally, a clear picture and general roadmap for the differences between gas and condensed phase processes, particularly at low collision energies, must be developed to avoid energy deposition and collision product errors. This may take the form of a database of functional chemical groups and generalisations of the gas and condensed phase collision differences, from which modelling adjustments could be estimated. Adaptions to Monte Carlo modelling to ensure that these changes between the gas phase and condensed phase are appropriately modelled could include the restrictions of degrees of freedom and the effect that has on rotational and vibrational excitation, and use of condensed phase data for the resonant processes rather than gas phase data.

7 Conclusiones (Español)

En esta tesis se han investigado las reacciones de colisión entre partículas cargadas y moléculas de importancia biológica o para biocombustible a través de una variedad de métodos experimentales y teóricos. Centrados en las colisiones de baja energía cinética, entre 0 y 10 000 eV, se han realizado estudios para proporcionar datos para la modelización y comprender los procesos de fragmentación que se producen en las colisiones entre partículas y moléculas, y iónicas y moleculas.

A bajas energías, las investigaciones de los fenómenos de colisión inelástica todavía requieren mucho tiempo para el cálculo y rara vez proporcionan información sobre la disociación. En este caso, el trabajo experimental jugó un papel clave en el aporte a las bases de datos de secciones eficaces, validando la teoría y proporcionando información sobre la disociación. Las colisiones de electrones por debajo de 15 eV con moléculas en fase gaseosa fueron investigadas experimentalmente en el Capítulo 2 con respecto a las secciones eficaces diferenciales de vibración y los productos de disociación resonante por captura electrónica. Estos experimentos son útiles para comprender el efecto de los electrones quasi-térmicos producidos por la radiación ionizante y los tratamientos con plasma y, como tales, se eligieron las moléculas pirimidina, un análogo a base de ADN, furfural, un precursor de biocombustibles y una serie de ésteres, utilizados como biodiésel, por su relevancia para la salud y las aplicaciones industriales.

Las secciones eficaces diferenciales a 15 eV de la molécula pirimidina para ángulos entre 20° y 90° mostraron cuatro bandas de excitación vibratoria distintas y una distribución angular casi isotrópica. La asignación de estados se hizo mediante consulta en la literatura, y estos valores de sección eficaz son ahora parte de la base de datos de dispersión de pirimidina utilizada para la simulación de trayectorias de partículas de baja energía mediante Monte Carlo (código LEPTS).

Se investigaron la disociación resonante por captura electrónica para el furfural, precursor del biocombustible, y varios ésteres de biodiésel, siendo los biocombustibles una industria que utiliza tratamientos con plasma como parte de los procesos de preparación. Se estudiaron los ésteres acetato de metilo, propionato de metilo, propionato de etilo y propionato de butilo para dilucidar los parámetros derivados de la longitud de la cadena

del precursor del alcohol, y en cada caso se detectaron muchas especies de aniones en bajas intensidades. Las resonancias comunes aparecieron cerca de 1,5 eV, 3 eV y 7-10 eV - en particular una resonancia a 7,5 eV con un hombro de mayor energía localizado ~ 1 eV por encima de éste, estando presente en un gran número de rendimientos aniónicos para cada uno de los cuatro ésteres. El enlace tipo éster demostró ser particularmente susceptible a la disociación resonante por captura electrónica y puede desalentar el uso de tratamientos de plasma si la temperatura del electrón de plasma reside cerca de las resonancias especificadas. El furfural precursor del biocombustible mostró mayores intensidades de rendimiento aniónico con dos claras regiones energéticas de resonancia, la primera entre 4,5 y 5,5 eV y la segunda entre 7,5 y 8,9 eV. Dado que el furfural puede considerarse un producto primario o un subproducto, esta fragmentación puede ser aprovechada por la industria. Se investigó la hipótesis de que el furfural puede utilizarse como un análogo de la desoxirribosa con energías de bajo impacto electrónico y se constató que los resultados de disociación resonante por captura electrónica no la apoyaban.

El desarrollo experimental representó una gran parte del trabajo de esta tesis, incluyendo, en el Capítulo 3, mejoras a un aparato existente y la caracterización sistemática de un nuevo aparato experimental. Estos aparatos consisten en un experimento de transmisión de electrones para producir espectros de pérdida de energía de electrones y un nuevo experimento de haz cruzado destinado a experimentos de transferencia de electrones de baja energía en colisiones con moléculas aniónicas, con el objetivo de determinar el efecto de los radicales producidos por la radiación ionizante en el medio local. Los experimentos producen resultados que no han sido observados, según el conocimiento del autor, por la teoría.

Las mejoras en la estabilidad del experimento de transmisión de electrones, mediante la instalación de una nueva cámara de dispersión y un sistema óptico de iones, permitieron la obtención de espectros de pérdida de energía de electrones para los blancos argón, acetileno y furfural. Los estados excitados se asignaron de acuerdo con la literatura conocida, y algunos estados autoionizantes no asignados se reconocieron para el furfural. Estos espectros se utilizan directamente como dato de entrada de distribución de transferencia de energía para el código Monte Carlo LEPTS.

Los primeros experimentos de colisión anión-molécula se realizaron para la molécula nitrometano. La transferencia de electrones puede estabilizar el anión padre y abrir nuevas vías de fragmentación debido a la presencia del tercer cuerpo, proporcionando diferentes

resultados a la disociación resonante por captura electrónica. Los productos detectados de las colisiones de O⁻-nitrometano incluyeron el anión padre $CH_3NO_2^-$ y los fragmentos aniónicos CNO^-, NO^-, O^- y H^-. Estos resultados son más similares a los experimentos de transferencia de electrones usando haces neutros de potasio, implicando la transferencia de electrones como un mecanismo dominante. Para caracterizar aún más el experimento, se llevó a cabo un análisis de la dispersión de energía del haz del anión, tanto por métodos experimentales como teóricos. Utilizando una rejilla retardadora para repeler los aniones como filtro de paso alto, los resultados indicaron que la dispersión de energía de los aniones tiene una media de 105 eV con un rango experimental de 110 eV. El experimento mostró una amplia distribución de la población dentro del haz, con la energía cinética media centrada cerca de 50 eV por debajo de la energía de extracción aplicada. Esta gran dispersión en el rango de energía fue confirmada por simulaciones de SimIon. No obstante, este punto no fue confirmado para la distribución de la población - las simulaciones de SimIon indican que la mayoría de los aniones tienen energía dentro de 10 eV de la energía de extracción. Las razones de esta diferencia y la amplia distribución de energía del haz aniónico se atribuyeron al método de extracción aniónica de la fuente de plasma de cátodo hueco y a la optimista colocación inicial de iones dentro de la simulación SimIon. Se buscaron mejoras en la intensidad del haz mediante otras simulaciones SimIon, utilizadas para optimizar la colocación y los voltajes de las lentes Einzel. Estas simulaciones fueron validadas en el experimento, proporcionando puntos de partida precisos para una mayor optimización manualmente. Se recomiendan mejoras al experimento incluyendo una nueva fuente.

Los métodos teóricos pueden ser de gran valor para proporcionar rápidamente secciones eficaces de dispersión en amplios rangos de energía, o en casos donde el trabajo experimental no es posible. Por debajo de 10 keV, donde la primera aproximación de Born pierde validez, el método Independent Atom Model with Screening Corrected Additivity Rule and Interference effects (IAM-SCAR+I) es capaz de producir secciones eficaces precisas hasta bajas energías, tanto para la dispersión de electrones como de positrones. La contribución de interferencia es una nueva adición al método, y se calculó la dispersión de positrones a partir de dos moléculas bien estudiadas, N_2 y O_2, para validar el nuevo método. Cuando se comparan con los datos de la literatura, los cálculos muestran una mejora en las regiones por encima y por debajo del umbral de formación de positronio, pero sobreestiman los datos disponibles en el máximo de la sección eficaz integral. El costo computacional de ejecutar el código IAM-SCAR+I es bajo y la precisión

alta, por lo que es perfecto para casos en los que hay poca o ninguna información disponible en la literatura y los investigadores requieren una base de datos para modelos de seguimiento de partículas como LEPTS. Como tal, se seleccionó y cotejó una base de datos para la dispersión de electrones a partir de furfural utilizando datos experimentales y teóricos de la bibliografía y, cuando fue necesario, se amplió con los resultados de IAM-SCAR+I, listos para su uso en LEPTS junto con los espectros de pérdida de energía de electrones producidos experimentalmente. Tanto los resultados de la dispersión de positrones como la base de datos de furfural se encuentran en el Capítulo 4.

Las aplicaciones de los datos de dispersión, incluyendo la radioterapia y el tratamiento con plasma, requieren una consideración adecuada de los blancos en fase condensada. En muchos casos, esto significa ajustar los datos de fase gaseosa, como los descritos hasta ahora en esta conclusión, para tener en cuenta las diferencias de densidad, grados de libertad y reacciones intermoleculares. Para comprender las diferencias entre la dispersión de electrones de baja energía en fase gaseosa y en fase condensada, se realizaron experimentos de desorción estimulada por electrones (ESD) para las moléculas pirimidina y piridazina, que se presentaron en el Capítulo 5. La pirimidina, que es un análogo de las bases de ADN timina, citosina y uracilo, y la piridazina, una estructura común que se encuentra en algunos radiosensibilizadores, son moléculas relevantes para la investigación en radioterapia. Ambas moléculas produjeron H^-, CN^-, C^-, C_2H^- en desorción aniónica inferior a 15 eV. La pirimidina mostró una mayor fragmentación resonante que condujo a la detección de los aniones adicionales CH^- y CHN^-. Los aniones detectados difieren entre la disociación resonante por captura electrónica del gas y las fases condensadas ESD, existiendo sólo el anión CN en ambos. Los experimentos de fase gaseosa detectan adicionalmente el fragmento $C_3H_2N^-$, no visto en fase condensada. También se encontró que las resonancias difieren entre la fase gaseosa y la fase condensada, con resonancias de baja energía observadas en la fase gaseosa y no en la fase condensada, y un cambio en la energía de aparición de las resonancias para CN^-. Se encontraron pruebas de desorción dipolar tanto en especies de aniones como de cationes; sin embargo, no se pudieron identificar parejas coincidentes, lo que indica que sólo una especie iónica de los pares se desorbe fácilmente al inicio de la desorción dipolar. La desorción catiónica también difiere del perfil catiónico que se observa en la ionización de electrones en fase gaseosa. Para ambas moléculas condensadas, las intensidades relativas de los cationes difieren de las de la fase gaseosa, y los datos de la fase condensada muestran retardo en los fragmentos de cationes conocidos. Tanto en la desorción de

aniones como de cationes estimulada por electrones, los resultados indican que los datos de fase condensada no son equivalentes a los datos de fase gaseosa para las diazinas, particularmente para los procesos resonantes. Se debe tener cuidado al utilizar datos de fase gaseosa para modelos de seguimiento de partículas en fase condensada por debajo de energías de impacto de 80 eV.

Otro aspecto de las simulaciones de seguimiento de partículas es la precisión y relevancia de los datos de entrada, investigados en el Capítulo 6. Los espectros de pérdida de energía de los electrones determinados experimentalmente tienden a omitir los procesos de excitación e ionización de las capas internas. Para entender su relevancia para los modelos de trayectorias de partículas, se comisione simulaciones a la institución del CIEMAT para utilizar la base de datos de dispersión y los espectros de pérdida de energía de electrones para la molécula furfural, desarrollada como parte de esta tesis. Se proporcionaron varios espectros de pérdida de energía, uno de los cuales carecía de los procesos de las capas internas y dos que los incluían, para simulaciones separadas de 100 000 electrones con 10 000 eV de energía cada uno. De los espectros que incluyen procesos de capa interna, la forma y las relaciones de intensidad relativa se tomaron de los espectros de pérdida de energía de los electrones O1s y C1s del furano, disponibles en la literatura. Se probaron dos métodos para determinar una proporción de intensidad apropiada entre los picos de las capas internas y las excitaciones de valencia, ambos basados en datos de la literatura disponible. Para el furfural, usando las comparaciones de la literatura de los valores disponibles de la intensidad del oscilador para excitaciones reconocibles, se colocó la intensidad de la excitación O1s de la capa interna en el 3,5% de la excitación de la valencia más alta. El ajuste del poder de frenado colisional del furfural a los valores de la base de datos del benceno, mediante el ajuste de la intensidad de la capa interna y, por lo tanto, de la energía de excitación media, situó la misma excitación en el 2,5 % de la excitación de valencia. La simulación mostró que aunque esta diferencia de intensidad no afectaba mucho a la profundidad de la máxima deposición de energía, la no consideración de los procesos de las capas internas era claramente responsable de aumentar la profundidad máxima de energía en un 20 % por encima de la profundidad máxima al incluirlos.

En general, se ha realizado un análisis de las interacciones de colisión entre partículas con energía inferior a 10 keV y moléculas de interés para las industrias de la radioterapia y la energía. Una exploración de los procesos que ocurren en diferentes regímenes de energía de colisión y fases físicas, y sus productos de disociación, ha permitido la producción de

datos directamente útiles para grupos de modelización. El trabajo experimental y teórico producido aquí se ha utilizado en modelos de seguimiento de partículas y bases de datos de secciones eficaces. Explorar las complicaciones que surgen entre la fase gaseosa y la fase condensada, y la necesidad de unos datos de entrada altamente precisos y finamente ajustados a los modelos, es vital para la investigación en curso en este campo. El viaje desde los experimentos y la teoría de las colisiones individuales, a las resonancias, a los productos de colisión, a los cambios de fase condensada y, finalmente, a la aplicación, cuenta la historia de un campo que todavía necesita nuevos experimentos y mejoras en los modelos antes de que pueda alcanzar una verdadera comprensión de las realidades médicas e industriales que pretende predecir.

En el futuro, se necesitarán bases de datos de secciones eficaces nuevas y más precisas de moléculas más complicadas y pertinentes, y la elección de la molécula debe hacerse en conjunción con las necesidades de las industrias pertinentes. En los experimentos del CSIC de Madrid se recomiendan varias mejoras. Unas fuentes de potencia nuevas y más estables para la óptica de los electrones del experimento de transmisión de electrones facilitarían una reducción de los errores experimentales y podrían permitir que el aparato proporcionara secciones eficaces totales, así como espectros de pérdida de energía de los electrones, mientras que el blindaje electromagnético podría permitir una reducción de la energía de impacto de los electrones. Un mayor desarrollo del experimento de colisión aniónica para facilitar un espectro de energía más estrecho permitiría una mejor comparación con la literatura. Esto podría lograrse sustituyendo la fuente de iones por una descarga de microondas. En términos más generales, debe desarrollarse una imagen clara y una hoja de ruta general para las diferencias entre los procesos de fase gaseosa y de fase condensada, especialmente con bajas energías de colisión, a fin de evitar el depósito de energía y los errores del producto de colisión. Esto puede adoptar la forma de una base de datos de grupos funcionales químicos y generalizaciones de las diferencias de colisión en fase gaseosa y condensada, a partir de las cuales podrían estimarse los ajustes necesarios en la modelización. Las adaptaciones a la modelización Monte Carlo para garantizar que estas diferencias entre la fase gaseosa y la fase condensada se consideren adecuadamente podrían incluir las restricciones de los grados de libertad y el efecto que tiene sobre la excitación rotacional y vibratoria, y el uso de datos de fase condensada para los procesos resonantes en lugar de datos de fase gaseosa.

8 LIST OF PUBLICATIONS

Here follows the list of publications related to the work obtained during the course of this thesis. They have been mentioned individually or described in detail in the text, as necessary according to their content and inclusion in the thesis work. Chapter 2 contains references [A, C], Chapter 3 contains reference [B], Chapter 4 contains references [D, E, G, H] and Chapter 5 contains reference [F]. Further publications are expected from the work in Chapters 2 and 4. Superscript numbers indicate the citation number in the references and text.

A. M. C. Fuss, L. Ellis-Gibbings, D. B. Jones, M. J. Brunger, F. Blanco, A. Muñoz, P. Limão-Vieira, and G. García, The role of pyrimidine and water as underlying molecular constituents for describing radiation damage in living tissue: A comparative study, J. Appl. Phys. **117**, 214701 (2015). [42]

B. J. C. Oller, L. Ellis-Gibbings, F. Ferreira da Silva, P. Limão-Vieira and G. Garcia, Novel experimental setup for time-of-flight mass spectrometry ion detection in collisions of anionic species with neutral gas-phase molecular targets, Eur. Phys. J. Tech Instrum., **2**, 13 (2015) [52]

C. D. B. Jones, L. Ellis-Gibbings, G. García, K. L. Nixon, M. C. A. Lopes and M. J. Brunger, *Intermediate energy cross sections for electron impact vibrational excitation of pyrimidine*, J. Chem. Phys. **143**, 094304 (2015). [96]

D. F. Blanco, L. Ellis-Gibbings and G. García, *Screening corrections for the interference contributions to the electron and positron scattering cross sections from polyatomic molecules*, Chem. Phys. Lett. **645**, 71 (2016). [239]

E. A.Traore-Dubuis, A. Verkhovtser, L. Ellis-Gibbings, K. Krupa, F. Blanco, D. B. Jones, M. J. Brunger and G. Garcia, *Total cross sections of furfural by electron impact: experiment and theory*, J. Chem. Phys. **147**, 054301 (2017). [82]

F. L. Ellis-Gibbings, A. D. Bass, P. Cloutier, G. Garciaa and L. Sanche, *Electron stimulated desorption from condensed Pyrimidine and Pyridazine*, Phys. Chem. Chem. Phys. **19**, 13038 (2017). [193]

G. A. Verkhovtsev, L. Ellis-Gibbings, F. Blanco, G. García, *Interference effects in electron scattering from small water clusters*, Chem. Phys. Lett. **685**, 504 (2017).[171]

H. D. Stevens, T. J. Babij, J. R. Machacek, S. J. Buckman, M. J. Brunger, R. D. White, G. García, F. Blanco, L. Ellis-Gibbings, J. P. Sullivan, *Positron scattering from pyridine*, J. Chem. Phys, **148,** 144308 (2018). [172]

9 REFERENCES

[1] L. Sanche, Nature **461**, 358 (2009).

[2] B. Boudaïffa, P. Cloutier, D. Hunting, M.A. Huels, and L. Sanche, Science (80-.). **287**, 1658 (2000).

[3] L. Sanche, Chem. Phys. Lett. **474**, 1 (2009).

[4] S.M. Pimblott and J.A. Laverne, Radiat. Phys. Chem. **76**, 1244 (2007).

[5] V. Cobut, Y. Frongillo, J.P. Patau, T. Goulet, M.-J. Fraser, and J.-P. Jay-Gerin, Radiat. Phys. Chem. **51**, 229 (1998).

[6] J.A. LaVerne and S.M. Pimblott, Radiat. Res. **141**, 208 (1995).

[7] I. Baccarelli, F.A. Gianturco, E. Scifoni, A. V. Solov'Yov, and E. Surdutovich, Eur. Phys. J. D **60**, 1 (2010).

[8] A. Muñoz, D. Almeida, F. Ferreira da Silva, P. Limão-Vieira, M.C. Fuss, A.G. Sanz, and G. García, Eur. Phys. J. D **67**, 1 (2013).

[9] D.L. Bailey, D.W. Townsend, P.E. Valk, and M.N. Maisey, editors , *Positron Emission Tomography* (Springer-Verlag, London, 2005).

[10] S.E. Combs, J. Bauer, D. Unholtz, C. Kurz, T. Welzel, D. Habermehl, T. Haberer, J. Debus, and K. Parodi, BMC Cancer **12**, 133 (2012).

[11] R.P. McEachran, J.P. Sullivan, S.J. Buckman, M.J. Brunger, M.C. Fuss, A. Muñoz, F. Blanco, R.D. White, Z.L. Petrović, P. Limão-Vieira, and G. García, J. Phys. B At. Mol. Opt. Phys. **45**, 45207 (2012).

[12] A. Fridman, *Plasma Chemistry* (2008).

[13] M. Mubarak, A. Shaija, and T. V. Suchithra, Algal Res. **7**, 117 (2015).

[14] G. Van Oost, M. Hrabovsky, V. Kopecky, M. Konrad, M. Hlina, and T. Kavka, Vacuum **83**, 209 (2008).

[15] R.F. da Costa, M.T. do N. Varella, M.H.F. Bettega, R.F.C. Neves, M.C.A. Lopes, F. Blanco, G. García, D.B. Jones, M.J. Brunger, and M.A.P. Lima, J. Chem. Phys. **144**, 124310 (2016).

[16] A.L.V. Cubas, M.M. Machado, C.R.S.C. Pinto, E.H.S. Moecke, and A.R.A. Dutra, Waste Manag. **47**, 149 (2016).

[17] Richard E. Smalley, Mater. Matters **30**, 412 (2005).

[18] H. Kobayashi and A. Fukuoka, Green Chem. **15**, 1740 (2013).

[19] A.S. Mamman, J.M. Lee, Y.C. Kim, I.T. Hwang, N.J. Park, Y.K. Hwang, J.S. Chang, and J.S. Hwang, Biofuels, Bioprod. Biorefining **2**, 438 (2008).

[20] J. Knothe, G.; Krahl, J.; Van Gerpen, *The Biodiesel Handbook* (2005).

[21] M.A. Fazal, A.S.M.A. Haseeb, and H.H. Masjuki, Renew. Sustain. Energy Rev. **15**, 1314 (2011).

[22] B. Bederson and H. Walther, *Advances in Atomic, Molecular, and Optical Physics: Fundamentals of Plasma Chemistry* (2000).

[23] J.J.S. Shang, Aerospace **5**, (2018).

[24] A. Muñoz, M.C. Fuss, M.A. Cortés-Giraldo, S. Incerti, V. Ivanchenko, A. Ivanchenko, J.M. Quesada, F. Salvat, C. Champion, and G. García Gómez-Tejedor, in *Radiat. Damage Biomol. Syst.*, edited by G. García Gómez-Tejedor and M.C. Fuss (Springer Netherlands, 2012), pp. 203–225.

[25] M.J. Brunger, S.J. Buckman, and K. Ratnavelu, J. Phys. Chem. Ref. Data **46**, 23102 (2017).

[26] Y. Itikawa and N. Mason, J. Phys. Chem. Ref. Data **34**, 1 (2005).

[27] A.G. Sanz, M.C. Fuss, F. Blanco, Z. Mašín, J.D. Gorfinkiel, F. Carelli, F. Sebastianelli, F. a Gianturco, and G. García, Appl. Radiat. Isot. **83**, 57 (2014).

[28] M.C. Fuss, a. G. Sanz, a. Muñoz, T.P.D. Do, K. Nixon, M.J. Brunger, M.-J. Hubin-Franskin, J.C. Oller, F. Blanco, and G. García, Chem. Phys. Lett. **560**, 22 (2013).

[29] D.C. Cartwright, R.L. Champion, A.A. Christodoulides, L.G. Christophorou, G. Csanak, L.D. Doverskipe, J.B. Hasted, T.D. Mark, D. Mathur, D.L. McCorkle, S.K. Srivastava, S. Trajmar, and E.C. Zipf, *Electron-Molecule Interactions and Their Applications* (Academic Press, 1984).

[30] P. Coleman, *Positron Beams and Their Applications* (WORLD SCIENTIFIC, 2000).

[31] J.P. Marler and C.M. Surko, Phys. Rev. A - At. Mol. Opt. Phys. **72**, 1 (2005).

[32] S.T. Perkins, D.E. Cullen, and S.M. Seltzer, *Tables and Graphs of Electron-Interaction*

Cross Sections from 10 eV to 100 GeV Derived from the LLNL Evaluated Electron Data Library (EEDL), Z = 1--100 (1991).

[33] A.E. Nahum, M.J. Berger, R. Wang, S.M. Seltzer, A.F. Bielajew, D.W.O. Rogers, J. Halbleib, B. Grosswendt, A. Ito, T.M. Jenkins, P. Andreo, R. Mohan, and A. Del Guerra, *Monte Carlo Transport of Electrons and Photons* (1988).

[34] F. Blanco, A.M. Roldán, K. Krupa, R.P. McEachran, R.D. White, S. Marjanović, Z.L. Petrović, M.J. Brunger, J.R. Machacek, S.J. Buckman, J.P. Sullivan, L. Chiari, P. Limão-Vieira, and G. García, J. Phys. B At. Mol. Opt. Phys. **49**, 145001 (2016).

[35] P. Palihawadana, J. Sullivan, M. Brunger, C. Winstead, V. McKoy, G. García, F. Blanco, and S. Buckman, Phys. Rev. A **84**, 62702 (2011).

[36] F. Ferreira da Silva, D. Almeida, G. Martins, A.R. Milosavljevic, B.P. Marinkovic, S. V Hoffmann, N.J. Mason, Y. Nunes, G. García, and P. Limão-Vieira, Phys. Chem. Chem. Phys. **12**, 6717 (2010).

[37] D.B. Jones, S.M. Bellm, P. Limão-Vieira, and M.J. Brunger, Chem. Phys. Lett. **535**, 30 (2012).

[38] I. Linert, M. Dampc, B. Mielewska, and M. Zubek, Eur. Phys. J. D **66**, 20 (2012).

[39] J.D. Builth-Williams, S.M. Bellm, D.B. Jones, H. Chaluvadi, D.H. Madison, C.G. Ning, B. Lohmann, and M.J. Brunger, J. Chem. Phys. **136**, 24304 (2012).

[40] R. Colmenares, A.G. Sanz, M.C. Fuss, F. Blanco, and G. García, Appl. Radiat. Isot. **83**, 91 (2014).

[41] P.Y. Chen and R.A. Holroyd, J Phys Chem **100**, 4491 (1996).

[42] M.C. Fuss, L. Ellis-Gibbings, D.B. Jones, M.J. Brunger, F. Blanco, A. Muñoz, P. Limão-Vieira, and G. García, J. Appl. Phys. **117**, 214701 (2015).

[43] I.A. Mironova, K.L. Aplin, F. Arnold, G.A. Bazilevskaya, R.G. Harrison, A.A. Krivolutsky, K.A. Nicoll, E. V. Rozanov, E. Turunen, and I.G. Usoskin, Space Sci. Rev. **194**, 1 (2015).

[44] F. Blanco and G. García, Chem. Phys. Lett. **635**, 321 (2015).

[45] H. Hattori and K. Mitsuke, J. Electron Spectros. Relat. Phenomena **80**, 1 (1996).

[46] J.E. Collin and J. Delwiche, Can. J. Chem. **45**, 1883 (1967).

[47] E.D. Nostrand and A.B.F. Duncan, J. Am. Chem. Soc. **76**, 3377 (1954).

Lilian K. Ellis-Gibbings - June 2018

[48] P.G. Wilkinson, J. Mol. Spectrosc. **2**, 387 (1958).

[49] J.P. Agrawal, *High Energy Materials : Propellants, Explosives and Pyrotechnics* (Wiley-VCH, 2010).

[50] R. Antunes, D. Almeida, G. Martins, N.J. Mason, G. García, M.J.P. Maneira, Y. Nunes, and P. Limão-Vieira, Phys. Chem. Chem. Phys. **12**, 12513 (2010).

[51] D. Almeida, R. Antunes, G. Martins, G. García, R.W. McCullough, S. Eden, and P. Limão-Vieira, Int. J. Mass Spectrom. **311**, 7 (2012).

[52] J.C. Oller, L. Ellis-Gibbings, F. Ferreira da Silva, P. Limão-Vieira, and G. García, EPJ Tech. Instrum. **2**, 13 (2015).

[53] A. Zecca, L. Chiari, G. García, F. Blanco, E. Trainotti, and M.J. Brunger, J. Phys. B At. Mol. Opt. Phys. **43**, 215204 (2010).

[54] E. Alizadeh, T.M. Orlando, and L. Sanche, Annu. Rev. Phys. Chem. **66**, 379 (2015).

[55] S.K. Sahbani, S. Girouard, P. Cloutier, L. Sanche, and D.J. Hunting, Radiat. Res. **181**, 99 (2014).

[56] S. Kouass Sahbani, P. Cloutier, A.D. Bass, D.J. Hunting, and L. Sanche, J. Phys. Chem. Lett. **6**, 3911 (2015).

[57] M. Maccabee, J.S. Evans, M.P. Glackin, Z. Hatahet, and S.S. Wallace, J. Mol. Biol. **236**, 514 (1994).

[58] S.S. Wallace, Free Radic. Biol. Med. **33**, 1 (2002).

[59] M.C. Fuss, A.G. Sanz, F. Blanco, J.C. Oller, P. Limão-Vieira, M.J. Brunger, and G. García, Phys. Rev. A **88**, 42702 (2013).

[60] Z. Mašín, J.D. Gorfinkiel, D.B. Jones, S.M. Bellm, and M.J. Brunger, J. Chem. Phys. **136**, 144310 (2012).

[61] D.B. Jones, S.M. Bellm, F. Blanco, M. Fuss, G. García, P. Limao-Vieira, and M.J. Brunger, J. Chem. Phys. **137**, 74304 (2012).

[62] D.B. Jones, R.F.C. Neves, M.C.A. Lopes, R.F. da Costa, M.T. do N. Varella, M.H.F. Bettega, M.A.P. Lima, G. García, F. Blanco, and M.J. Brunger, J. Chem. Phys. **143**, 224304 (2015).

[63] J. Maljković, A. Milosavljević, F. Blanco, D. Šević, G. García, and B. Marinković, Phys. Rev. A **79**, 52706 (2009).

[64] J.M. Rice, G.O. Dudek, and M. Barber, J. Am. Chem. Soc. **87**, 4569 (1965).

[65] I. Nenner and G.J. Schulz, J. Chem. Phys. **62**, 1747 (1975).

[66] Z. Mašín and J.D. Gorfinkiel, J. Chem. Phys. **137**, 204312 (2012).

[67] M. Fuss, A.G. Sanz, A. Muñoz, F. Blanco, M. Téllez, C. Huerga, and G. García, in *Biomed. Eng. Trends Electron. Commun. Softw.*, edited by A. Laskovski (2011), pp. 277–294.

[68] K. Kusakabe, N. Ide, Y. Daigo, T. Itoh, T. Yamamoto, H. Hashizume, K. Nozu, H. Yoshida, G. Tadano, S. Tagashira, K. Higashino, Y. Okano, Y. Sato, M. Inoue, M. Iguchi, T. Kanazawa, Y. Ishioka, K. Dohi, Y. Kido, S. Sakamoto, S. Ando, M. Maeda, M. Higaki, Y. Baba, and Y. Nakamura, J. Med. Chem. **58**, 1760 (2015).

[69] W. Kim, H. Youn, T. Kwon, J. Kang, E. Kim, B. Son, H.J. Yang, Y. Jung, and B. Youn, Pharmacol. Res. **70**, 90 (2013).

[70] M.H. Palmer and I.C. Walker, Chem. Phys. **157**, 187 (1991).

[71] D.M.P. Holland, D.A. Shaw, S. Coriani, M. Stener, and P. Decleva, J. Phys. B At. Mol. Opt. Phys. **46**, 175103 (2013).

[72] N. Kishimoto and K. Ohno, J Phys Chem A **104**, 6940 (2000).

[73] D. Mathur and J.B. Hasted, Chem. Phys. **16**, 347 (1976).

[74] M.H. Benn, T.S. Sorensen, and A.M. Hogg, Chem. Commun. **387**, 574 (1967).

[75] H. Ogura, S. Sugimoto, H. Igeta, and T. Tsuchiya, J. Heterocycl. Chem. **8**, 391 (1971).

[76] K. J. Zietsch, *The Chemistry and Technology of Furfural and Its Many By-Products* (Elsevier, 2000).

[77] A.W. Khan, J.-P. Labrie, and J. McKeown, Biotechnol. Bioeng. **28**, 1449 (1986).

[78] J. Amorim, C. Oliveira, J.A. Souza-Corrêa, and M.A. Ridenti, Plasma Process. Polym. **10**, 670 (2013).

[79] D.B. Jones, R.F. da Costa, M.T. do N. Varella, M.H.F. Bettega, M.A.P. Lima, F. Blanco, G. García, and M.J. Brunger, J. Chem. Phys. **144**, 144303 (2016).

[80] L.C. Pitchford, L.L. Alves, K. Bartschat, S.F. Biagi, M.-C. Bordage, I. Bray, C.E. Brion, M.J. Brunger, L. Campbell, A. Chachereau, B. Chaudhury, L.G. Christophorou, E. Carbone, N.A. Dyatko, C.M. Franck, D. V. Fursa, R.K. Gangwar, V. Guerra, P. Haefliger, G.J.M. Hagelaar, A. Hoesl, Y. Itikawa, I. V. Kochetov, R.P. McEachran, W.L.

Morgan, A.P. Napartovich, V. Puech, M. Rabie, L. Sharma, R. Srivastava, A.D. Stauffer, J. Tennyson, J. de Urquijo, J. van Dijk, L.A. Viehland, M.C. Zammit, O. Zatsarinny, and S. Pancheshnyi, Plasma Process. Polym. **14**, 1600098 (2017).

[81] J. Tennyson, S. Rahimi, C. Hill, L. Tse, A. Vibhakar, D. Akello-Egwel, D.B. Brown, A. Dzarasova, J.R. Hamilton, D. Jaksch, S. Mohr, K. Wren-Little, J. Bruckmeier, A. Agarwal, K. Bartschat, A. Bogaerts, J.-P. Booth, M.J. Goeckner, K. Hassouni, Y. Itikawa, B.J. Braams, E. Krishnakumar, A. Laricchiuta, N.J. Mason, S. Pandey, Z.L. Petrovic, Y.-K. Pu, A. Ranjan, S. Rauf, J. Schulze, M.M. Turner, P. Ventzek, J.C. Whitehead, and J.-S. Yoon, Plasma Sources Sci. Technol. **26**, 55014 (2017).

[82] A. Traoré Dubuis, A. Verkhovtsev, L. Ellis-Gibbings, K. Krupa, F. Blanco, D.B. Jones, M.J. Brunger, and G. García, J. Chem. Phys. **147**, 54301 (2017).

[83] D.B. Jones, E. Ali, K.L. Nixon, P. Limão-Vieira, M.-J. Hubin-Franskin, J. Delwiche, C.G. Ning, J. Colgan, A.J. Murray, D.H. Madison, and M.J. Brunger, J. Chem. Phys. **143**, 184310 (2015).

[84] A.R. Smith and G. Meloni, J. Mass Spectrom. **50**, 1206 (2015).

[85] D.B. Jones, R.F.C. Neves, M.C.A. Lopes, R.F. da Costa, M.T. do N Varella, M.H.F. Bettega, M.A.P. Lima, G. García, P. Limão-Vieira, and M.J. Brunger, J. Chem. Phys. **144**, 124309 (2016).

[86] E.F. Aransiola, T. V. Ojumu, O.O. Oyekola, T.F. Madzimbamuto, and D.I.O. Ikhu-Omoregbe, Biomass and Bioenergy **61**, 276 (2014).

[87] N.M. Niza, K.T. Tan, K.T. Lee, and Z. Ahmad, Appl. Energy **101**, 198 (2013).

[88] F. Goembira and S. Saka, Bioresour. Technol. **131**, 47 (2013).

[89] F. Goembira, K. Matsuura, and S. Saka, Fuel **97**, 373 (2012).

[90] B. Bharathiraja, M. Chakravarthy, R.R. Kumar, D. Yuvaraj, J. Jayamuthunagai, R.P. Kumar, and S. Palani, Renew. Sustain. Energy Rev. **38**, 368 (2014).

[91] G.A. Lowe, C.L. Peterson, J.C. Thompson, J.S. Taberski, P.T. Mann, and C.L. Chase, in *ASAE Annu. Int. Meet. Orlando, Florida, USA* (American Society of Agricultural Engineers (ASAE), 1998), p. 27.

[92] N. Schultz-Jensen, A. Thygesen, F. Leipold, S.T. Thomsen, C. Roslander, H. Lilholt, and A.B. Bjerre, Bioresour. Technol. **140**, 36 (2013).

[93] J.M. Simmie, Prog. Energy Combust. Sci. **29**, 599 (2003).

94 A.M. El-Nahas, M. V. Navarro, J.M. Simmie, J.W. Bozzelli, H.J. Curran, S. Dooley, and W. Metcalfe, J. Phys. Chem. A **111**, 3727 (2007).

95 Y. Pariat and M. Allan, Int. J. Mass Spectrom. Ion Process. **103**, 181 (1991).

96 D.B. Jones, L. Ellis-Gibbings, G. García, K.L. Nixon, M.C.A. Lopes, and M.J. Brunger, J. Chem. Phys. **143**, 94304 (2015).

97 S. Kim, P. Thiessen, E. Bolton, J. Chen, G. Fu, A. Gindulyte, L. Han, J. He, S. He, B. Shoemaker, J. Wang, B. Yu, J. Zhang, and S. Bryant, Nucleic Acids Res. **44**, (2016).

98 M.C. Zammit, D. V Fursa, J.S. Savage, and I. Bray, J. Phys. B At. Mol. Opt. Phys. **50**, 123001 (2017).

99 J. Tennyson, Phys. Rep. **491**, 29 (2010).

100 M.J. Brunger and P.J.O. Teubner, Phys. Rev. A **41**, 1413 (1990).

101 P.L. Levesque, M. Michaud, and L. Sanche, J. Chem. Phys. **122**, 94701 (2005).

102 T.P.T. Do, H. V. Duque, M.C.A. Lopes, D.A. Konovalov, R.D. White, M.J. Brunger, and D.B. Jones, J. Chem. Phys. **142**, 124306 (2015).

103 H. V. Duque, T.P.T. Do, M.C.A. Lopes, D.A. Konovalov, R.D. White, M.J. Brunger, and D.B. Jones, J. Chem. Phys. **142**, 124307 (2015).

104 H. V. Duque, L. Chiari, D.B. Jones, P.A. Thorn, Z. Pettifer, G.B. da Silva, P. Limão-Vieira, D. Duflot, M.J. Hubin-Franskin, J. Delwiche, F. Blanco, G. García, M.C.A. Lopes, K. Ratnavelu, R.D. White, and M.J. Brunger, Chem. Phys. Lett. **608**, 161 (2014).

105 R.F.C. Neves, D.B. Jones, M.C. a Lopes, K.L. Nixon, E.M. de Oliveira, R.F. da Costa, M.T. Do N Varella, M.H.F. Bettega, M.A.P. Lima, G.B. da Silva, and M.J. Brunger, J. Chem. Phys. **142**, 194302 (2015).

106 R.F.C. Neves, D.B. Jones, M.C.A. Lopes, F. Blanco, G. García, K. Ratnavelu, and M.J. Brunger, J. Phys. B At. Mol. Opt. Phys. **142**, 194305 (2015).

107 M. Michaud, A. Wen, and L. Sanche, Radiat. Res. **159**, 3 (2003).

108 A.G. Sanz, M.C. Fuss, A. Muñoz, F. Blanco, P. Limão-Vieira, M.J. Brunger, S.J. Buckman, and G. García, Int. J. Radiat. Biol. **88**, 71 (2012).

109 L. Sanche, Eur. Phys. J. D **35**, 367 (2005).

110 M.M. Dawley and S. Ptasińska, Int. J. Mass Spectrom. **365–366**, 143 (2014).

111 NIST, *NIST Webbook* (n.d.).

[112] P. Cicman, G. Senn, G. Denifl, D. Muigg, J.D. Skalny, P. Lukac, A. Stamatovic, and A. Märk, Czechoslov. J. Phys. **48**, 1135 (1998).

[113] D.S. Slaughter, H. Adaniya, T.N. Rescigno, D.J. Haxton, A.E. Orel, C.W. McCurdy, and A. Belkacem, J. Phys. B-Atomic Mol. Opt. Phys. **44**, 20 (2011).

[114] P. Cicman, M. Francis, J.D. Skalný, and T.D. Märk, Int. J. Mass Spectrom. **223**–**224**, 271 (2003).

[115] D.J. Haxton, C.W. McCurdy, and T.N. Rescigno, Phys. Rev. A **75**, 12710 (2007).

[116] M. Ryszka, E. Alizadeh, Z. Li, and S. Ptasińska, J. Chem. Phys. **147**, 94303 (2017).

[117] B.C. Ibănescu, O. May, and M. Allan, Phys. Chem. Chem. Phys. **10**, 1507 (2008).

[118] C. König, J. Kopyra, I. Bald, and E. Illenberger, Phys. Rev. Lett. **97**, 5 (2006).

[119] J.D. Gorfinkiel and S. Ptasinska, J. Phys. B At. Mol. Opt. Phys. **50**, 182001 (2017).

[120] F. Ferreira da Silva, E. Lange, P. Limão-Vieira, N.C. Jones, S. V. Hoffmann, M.-J. Hubin-Franskin, J. Delwiche, M.J. Brunger, R.F.C. Neves, M.C.A. Lopes, E.M. de Oliveira, R.F. da Costa, M.T. do N. Varella, M.H.F. Bettega, F. Blanco, G. García, M.A.P. Lima, and D.B. Jones, J. Chem. Phys. **143**, 144308 (2015).

[121] P. Sulzer, S. Ptasinska, F. Zappa, B. Mielewska, and A.R. Milosavljevic, J. Chem. Phys. **125**, 44304 (2006).

[122] D. Antic, L. Parenteau, M. Lepage, and L. Sanche, J. Phys. Chem. B **103**, 6611 (1999).

[123] M. Allan, J. Phys. Conf. Ser. **388**, 12001 (2012).

[124] C.J. Tung, T.C. Chao, H.W. Hsieh, and W.T. Chan, Nucl. Instruments Methods Phys. Res. B **262**, 231 (2007).

[125] J. Momigny, Nature **199**, 805 (1963).

[126] M.C. Fuss, Electron Interactions with Molecules of Biological Interest, Universidad Autónoma de Madrid, 2013.

[127] M.A. Khakoo, P. Vandeventer, J.G. Childers, I. Kanik, C.J. Fontes, K. Bartschat, V. Zeman, D.H. Madison, S. Saxena, R. Srivastava, and A.D. Stauffer, J. Phys. B At. Mol. Opt. Phys. **37**, 247 (2004).

[128] L. Sanche and G. Schulz, Phys. Rev. A **5**, 1672 (1972).

[129] J.N.H. Brunt, G.C. King, and F.H. Read, J. Phys. B Atom. Molec. Phys. **9**, 2195 (1976).

[130] M. Bolsa Ferruz, V. Ivošev, K. Haume, L. Ellis-Gibbings, A. Traore, V. Thakare, S. Rosa, P. de Vera, V.-L. Tran, A. Mika, D. Boscolo, S. Grellet, A. Verkhovtsev, B.A. Huber, K.T. Butterworth, K.M. Prise, F.J. Currell, N.J. Mason, J. Golding, E. Scifoni, G. García, F. Boschetti, F. Lux, O. Tillement, C. Louis, K. Stokbro, A. V. Solov'yov, and S. Lacombe, in *Nanoscale Insights into Ion-Beam Cancer Ther.* (Springer International Publishing, Cham, 2017), pp. 379–434.

[131] D. Almeida, F. Ferreira da Silva, G. García, and P. Limão-Vieira, Phys. Rev. Lett. **110**, 23201 (2013).

[132] F. Ferreira da Silva, C. Matias, D. Almeida, G. García, O. Ingólfsson, H.D. Flosadóttir, B. Ómarsson, S. Ptasinska, B. Puschnigg, P. Scheier, P. Limão-Vieira, and S. Denifl, J. Am. Soc. Mass Spectrom. **24**, 1787 (2013).

[133] A.M. Howatson, *An Introduction to Gas Discharges* (1976).

[134] R. Mavrodineanu, J. Res. Natl. Bur. Stand. (1934). **89**, 143 (1984).

[135] D. Marić, N. Škoro, G. Malović, Z.L. Petrović, V. Mihailov, and R. Djulgerova, J. Phys. Conf. Ser. **162**, 12007 (2009).

[136] E. Illenberger, in *Gaseous Mol. Ions* (2000).

[137] J. Lee and J.J. Grabowski, Chem. Rev. **92**, 1611 (1992).

[138] I. Abril, R. García-Molina, P. de Vera, I. Kyriakou, and D. Emfietzoglou, *Theory of Heavy Ion Collision Physics in Hadron Therapy* (2013).

[139] Y. Itikawa, A. Ichimura, K. Onda, K. Sakimoto, K. Takayanagi, Y. Hatano, M. Hayashi, H. Nishimura, and S. Tsurubuchi, J. Phys. Chem. Ref. Data **18**, 23 (1989).

[140] T. Jaffke, M. Meinke, R. Hashemi, L.G. Christophorou, and E. Illenberger, Chem. Phys. Lett. **193**, 62 (1992).

[141] B.M. Smirnov, *Theory of Gas Discharge Plasma* (2015).

[142] W. Ding, D.L. McCorkle, and L. a. Pinnaduwage, J. Appl. Phys. **84**, 3051 (1998).

[143] E. Alizadeh, F. Ferreira da Silva, F. Zappa, A. Mauracher, M. Probst, S. Denifl, A. Bacher, T.D. Märk, P. Limão-Vieira, and P. Scheier, Int. J. Mass Spectrom. **271**, 15 (2008).

[144] J.H. Moore, C.C. Davis, M.A. Coplan, and S.C. Greer, *Building Scientific Apparatus* (Cambridge University Press, 2009).

[145] D. Dahl and D. Manura, (2008).

[146] E. Oks, *Plasma Cathode Electron Sources: Physics, Technology, Applications* (2006).

[147] F. Blanco and G. García, Phys. Lett. A **295**, 178 (2002).

[148] F. Blanco and G. García, Phys. Rev. A **67**, 22701 (2003).

[149] F. Blanco and G. García, Phys. Lett. A **330**, 230 (2004).

[150] F. Blanco and G. García, Phys. Lett. A **360**, 707 (2007).

[151] F. Blanco, L. Ellis-Gibbings, and G. García, Chem. Phys. Lett. **645**, 71 (2016).

[152] F. Blanco, J. Rosado, A. Illana, and G. García, Phys. Lett. A **374**, 4420 (2010).

[153] W. Tattersall, L. Chiari, J.R. Machacek, E. Anderson, R.D. White, M.J. Brunger, S.J. Buckman, G. García, F. Blanco, and J.P. Sullivan, J. Chem. Phys. **140**, (2014).

[154] L. Chiari, E. Anderson, W. Tattersall, J.R. Machacek, P. Palihawadana, C. Makochekanwa, J.P. Sullivan, G. García, F. Blanco, R.P. McEachran, M.J. Brunger, and S.J. Buckman, J. Chem. Phys. **138**, 74301 (2013).

[155] F. Blanco and G. García, J. Phys. B At. Mol. Opt. Phys. **42**, 145203 (2009).

[156] F. Blanco and G. García, Phys. Lett. A **317**, 458 (2003).

[157] R.D. Cowan, *The Theory of Atomic Structure and Spectra* (University of California Press, 1981).

[158] M.E. Riley and D.G. Truhlar, J. Chem. Phys. **63**, 2182 (1975).

[159] R. Zhang, A. Faure, and J. Tennyson, Phys. Scr. **80**, 15301 (2009).

[160] G. Staszewska, D.W. Schwenke, D. Thirumalai, and D.G. Truhlar, Phys. Rev. A **28**, 2740 (1983).

[161] N.F. Mott and H.S.W. Massey, *The Theory of Atomic Collisions* (Oxford University Press, 1966).

[162] A.G. Sanz, M.C. Fuss, F. Blanco, F. Sebastianelli, F.A. Gianturco, and G. García, J. Chem. Phys. **137**, 124103 (2012).

[163] A. Jain, J. Phys. B At. Mol. Opt. Phys. **21**, 905 (1988).

[164] A.S. Dickinson, J. Phys. B At. Mol. Phys. **10**, 967 (1977).

[165] D.D. Reid and J.M. Wadehra, J. Phys. B At. Mol. Opt. Phys. **29**, L127 (1996).

[166] R.P. McEachran, A.G. Ryman, A.D. Stauffer, and D.L. Morgan, J. Phys. B At. Mol. Phys. **10**, 663 (1977).

[167] A.C.L. Jones, C. Makochekanwa, P. Caradonna, D.S. Slaughter, J.R. Machacek, R.P. McEachran, J.P. Sullivan, S.J. Buckman, A.D. Stauffer, I. Bray, and D. V. Fursa, Phys. Rev. A **83**, 32701 (2011).

[168] E.-A. Reinsch and W. Meyer, Phys. Rev. A **18**, 1793 (1978).

[169] H.-J. Werner and W. Meyer, Phys. Rev. A **13**, 13 (1976).

[170] L. Chiari, A. Zecca, S. Girardi, E. Trainotti, G. García, F. Blanco, R.P. McEachran, and M.J. Brunger, J. Phys. B At. Mol. Opt. Phys. **45**, 215206 (2012).

[171] A. Verkhovtsev, L. Ellis-Gibbings, F. Blanco, and G. García, Chem. Phys. Lett. **685**, 504 (2017).

[172] D. Stevens, T.J. Babij, J.R. Machacek, S.J. Buckman, M.J. Brunger, R.D. White, G. García, F. Blanco, L. Ellis-Gibbings, and J.P. Sullivan, J. Chem. Phys. **148**, (2018).

[173] W. Sun, M.A. Morrison, W.A. Isaacs, W.K. Trail, D. Alle, R.J. Gulley, M. Brennan, and S.J. Buckman, Phys. Rev. A **52**, 1229 (1995).

[174] Y. Itikawa, J. Phys. Chem. Ref. Data **35**, 31 (2006).

[175] J. Dutton, C.J. Evans, and H.L. Mansour, J. Phys. B At. Mol. Phys. **20**, 2607 (1987).

[176] A. Zecca, L. Chiari, A. Sarkar, and M.J. Brunger, New J. Phys. **13**, 115001 (2011).

[177] O. Sueoka and S. Mori, J. Phys. Soc. Japan **53**, 2491 (1984).

[178] K.R. Hoffman, M.S. Dababneh, Y.F. Hsieh, W.E. Kauppila, V. Pol, J.H. Smart, and T.S. Stein, Phys. Rev. A **25**, 1393 (1982).

[179] S. Singh, S. Dutta, R. Naghma, and B. Antony, J. Phys. Chem. A **120**, 5685 (2016).

[180] K.L. Baluja and A. Jain, Phys. Rev. A **45**, 7838 (1992).

[181] H.N. Kothari and K.N. Joshipura, PRAMANA J. Phys. **76**, 477 (2011).

[182] D.D. Reid and J.M. Wadehra, Chem. Phys. Lett. **311**, 385 (1999).

[183] P.G. Coleman, T.C. Griffith, and G.R. Heyland, Appl. Phys. **4**, 89 (1974).

[184] M. Charlton, T.C. Griffith, G.R. Heyland, and G.L. Wright, J. Phys. B At. Mol. Phys. **16**, 323 (1983).

[185] U. Fano and A.R.P. Rau, in *At. Collisions Spectra* (1986), pp. 51–54.

[186] M.S. Dababneh, Y.-F. Hsieh, W.E. Kauppila, C.K. Kwan, S.J. Smith, T.S. Stein, and M.N. Uddin, Phys. Rev. A **38**, 1207 (1988).

[187] R. Raizada and K.L. Baluja, Phys. Rev. A **55**, 1533 (1997).

[188] S. De-Heng, L. Yu-Fang, S. Jin-Feng, Z. Zun-Lue, and Y. Xiang-Dong, Chinese Phys. **14**, 964 (2005).

[189] J. Archer, S.M. Trilov, and P.G. Coleman, J. Phys. Conf. Ser. **443**, 12001 (2013).

[190] M. Allan, J. Phys. B At. Mol. Opt. Phys. **40**, 3531 (2007).

[191] A.R. Smith and G. Meloni, J. Mass Spectrom. **50**, 1206 (2015).

[192] P. de Vera, R. Garcia-Molina, and I. Abril, in *Nanoscale Insights into Ion-Beam Cancer Ther.* (Springer International Publishing, Cham, 2017), pp. 61–98.

[193] L. Ellis-Gibbings, A.D. Bass, P. Cloutier, G. García, and L. Sanche, Phys. Chem. Chem. Phys. **19**, 13038 (2017).

[194] M. Neustetter, J. Aysina, F.F. Da Silva, and S. Denifl, Angew. Chemie - Int. Ed. **54**, 9124 (2015).

[195] T. Field and T. Gilmore, (2016).

[196] F. de A. Ribeiro, G.C. Almeida, W. Wolff, H.M. Boechat-Roberty, and M.L.M. Rocco, J. Phys. Chem. C **118**, 25978 (2014).

[197] H. Abdoul-Carime, P. Cloutier, and L. Sanche, Radiat. Res. **155**, 625 (2001).

[198] M.-A. Hervé du Penhoat, M.A. Huels, P. Cloutier, J.-P. Jay-Gerin, and L. Sanche, J. Chem. Phys. **114**, 5755 (2001).

[199] A.D. Bass and L. Sanche, Low Temp. Phys. **29**, 202 (2003).

[200] O. Ingólfsson, F. Weik, and E. Illenberger, Int. J. Mass Spectrom. Ion Process. **155**, 1 (1996).

[201] P. Możejko, A.D. Bass, L. Parenteau, and L. Sanche, J. Chem. Phys. **121**, 10181 (2004).

[202] L. Parenteau, J.-P. Jay-Gerin, and L. Sanche, J. Phys. Chem. **98**, 10277 (1994).

[203] C.R. Arumainayagam, H.-L. Lee, R.B. Nelson, D.R. Haines, and R.P. Gunawardane, Surf. Sci. Rep. **65**, 1 (2010).

[204] E. Böhler, J. Warneke, and P. Swiderek, Chem. Soc. Rev. **42**, 9219 (2013).

[205] A.D. Bass, C.R. Arumainayagam, and L. Sanche, Int. J. Mass Spectrom. **277**, 251 (2008).

[206] M.N. Hedhili, P. Cloutier, A.D. Bass, T.E. Madey, and L. Sanche, J. Chem. Phys. **125**, 94704 (2006).

[207] L. Sanche, J. Chem. Phys. **71**, 4860 (1979).

[208] G. Bader, G. Perluzzo, L.G. Caron, and L. Sanche, Phys. Rev. B **26**, 6019 (1982).

[209] M.A. Huels, L. Parenteau, and L. Sanche, J. Chem. Phys. **100**, 3940 (1994).

[210] P. Swiderek, M. Michaud, and L. Sanche, J. Chem. Phys. **103**, 8424 (1995).

[211] P. Rowntree, H. Sambe, L. Parenteau, and L. Sanche, Phys. Rev. B **47**, 4537 (1993).

[212] M. Michaud and L. Sanche, J. Electron Spectros. Relat. Phenomena **51**, 237 (1990).

[213] M.A. Huels, L. Parenteau, M. Michaud, and L. Sanche, Phys. Rev. A **51**, 337 (1995).

[214] R. Azria, L. Parenteau, and L. Sanche, Phys. Rev. Lett. **59**, 638 (1987).

[215] L. Sanche, A.D. Bass, P. Ayotte, and I.I. Fabrikant, Phys. Rev. Lett. **75**, 3568 (1995).

[216] P. Ayotte, J. Gamache, A.D. Bass, I.I. Fabrikant, and L. Sanche, J. Chem. Phys. **106**, 749 (1998).

[217] F. Brüning, P. Tegeder, J. Langer, and E. Illenberger, Int. J. Mass Spectrom. **195**, 507 (2000).

[218] H. Sambe, D.E. Ramaker, M. Deschenes, A.D. Bass, and L. Sanche, Phys. Rev. Lett. **64**, 523 (1990).

[219] L. Sanche and L. Parenteau, J. Chem. Phys. **93**, 7476 (1990).

[220] K.K. Innes, I.G. Ross, and W.R. Moomaw, J. Mol. Spectrosc. **132**, 492 (1988).

[221] H. Sambe, D.E. Ramaker, L. Parenteau, and L. Sanche, Phys. Rev. Lett. **59**, 236 (1987).

[222] M. Michaud, P. Cloutier, and L. Sanche, Phys. Rev. B **48**, 11336 (1993).

[223] D. Antic, L. Parenteau, and L. Sanche, J Phys Chem B **104**, 4711 (2000).

[224] A.D. Bass, L. Parenteau, M.A. Huels, and L. Sanche, J. Chem. Phys. **109**, 8635 (1998).

[225] S. Ptasińska, S. Denifl, V. Grill, T.D. Märk, E. Illenberger, and P. Scheier, Phys. Rev. Lett. **95**, 93201 (2005).

[226] S. Denifl, S. Ptasińska, M. Probst, J. Hrušák, P. Scheier, and T.D. Märk, J. Phys. Chem. A **108**, 6562 (2004).

[227] A. Muñoz, D. Almeida, F. Ferreira da Silva, P. Limão-Vieira, M.C. Fuss, A.G. Sanz, and G. García, Eur. Phys. J. D **67**, 1 (2013).

[228] I. El Naqa, P. Pater, and J. Seuntjens, Phys. Med. Biol. **57**, R75 (2012).

[229] H. Nikjoo, S. Uehara, D. Emfietzoglou, and F.A. Cucinotta, Radiat. Meas. **41**, 1052 (2006).

[230] M.C. Fuss, A. Muñoz, J.C. Oller, F. Blanco, A. Williart, P. Limão-Vieira, M.J.G. Borge, O. Tengblad, C. Huerga, M. Téllez, and G. García, Appl. Radiat. Isot. **69**, 1198 (2011).

[231] P. Limão-Vieira, F. Ferreira da Silva, and G. García Gómez-Tejedor, in *Radiat. Damage Biomol. Syst.*, edited by G. García Gómez-Tejedor and M. Fuss (Springer, 2012), pp. 59–70.

[232] D. Duflot, J.P. Flament, A. Giuliani, J. Heinesch, and M.J. Hubin-Franskin, J. Chem. Phys. **119**, 8946 (2003).

[233] S. Agostinelli, J. Allison, K. Amako, J. Apostolakis, H. Araujo, P. Arce, M. Asai, D. Axen, S. Banerjee, G. Barrand, F. Behner, L. Bellagamba, J. Boudreau, L. Broglia, A. Brunengo, H. Burkhardt, S. Chauvie, J. Chuma, R. Chytracek, G. Cooperman, G. Cosmo, P. Degtyarenko, A. Dell'Acqua, G. Depaola, D. Dietrich, R. Enami, A. Feliciello, C. Ferguson, H. Fesefeldt, G. Folger, F. Foppiano, A. Forti, S. Garelli, S. Giani, R. Giannitrapani, D. Gibin, J.J. Gómez Cadenas, I. González, G. Gracia Abril, G. Greeniaus, W. Greiner, V. Grichine, A. Grossheim, S. Guatelli, P. Gumplinger, R. Hamatsu, K. Hashimoto, H. Hasui, A. Heikkinen, A. Howard, V. Ivanchenko, A. Johnson, F.W. Jones, J. Kallenbach, N. Kanaya, M. Kawabata, Y. Kawabata, M. Kawaguti, S. Kelner, P. Kent, A. Kimura, T. Kodama, R. Kokoulin, M. Kossov, H. Kurashige, E. Lamanna, T. Lampén, V. Lara, V. Lefebure, F. Lei, M. Liendl, W. Lockman, F. Longo, S. Magni, M. Maire, E. Medernach, K. Minamimoto, P. Mora de Freitas, Y. Morita, K. Murakami, M. Nagamatu, R. Nartallo, P. Nieminen, T. Nishimura, K. Ohtsubo, M. Okamura, S. O'Neale, Y. Oohata, K. Paech, J. Perl, A. Pfeiffer, M.G. Pia, F. Ranjard, A. Rybin, S. Sadilov, E. Di Salvo, G. Santin, T. Sasaki, N. Savvas, Y. Sawada, S. Scherer, S. Sei, V. Sirotenko, D. Smith, N. Starkov, H. Stoecker, J. Sulkimo, M. Takahata, S. Tanaka, E. Tcherniaev, E. Safai Tehrani, M. Tropeano, P. Truscott, H. Uno, L. Urban, P. Urban, M. Verderi, A.

Walkden, W. Wander, H. Weber, J.P. Wellisch, T. Wenaus, D.C. Williams, D. Wright, T. Yamada, H. Yoshida, and D. Zschiesche, Nucl. Instruments Methods Phys. Res. Sect. A Accel. Spectrometers, Detect. Assoc. Equip. **506**, 250 (2003).

[234] E. Rühl and A.P.P. Hitchcock, Chem. Phys. **154**, 323 (1991).

[235] J.C. Oller, A. Muñoz, J.M. Pérez, F. Blanco, P. Limão-Vieira, and G. García, Chem. Phys. Lett. **421**, 439 (2006).

[236] NIST, Stopping Power and Ranges for Electrons (n.d.).

[237] L. De Marzi, A. Patriarca, A. Mazal, and J.-L. Habrand, in *Nanoscale Insights into Ion-Beam Cancer Ther.* (Springer International Publishing, Cham, 2017), pp. 467–494.

[238] J.C. Ashley, Radiat. Res. **89**, 25 (1982).

[239] F. Blanco, L. Ellis-Gibbings, and G. García, Chem. Phys. Lett. **645**, (2016).

10 APPENDICES

APPENDIX 1 FURFURAL ELASTIC DIFFERENTIAL CROSS SECTIONS

As noted in Chapter 4, the elastic differential cross sections produced by the IAM-SCAR+I method are tabulated here, for electron scattering from the molecule furfural in the incident kinetic energy range 0.1 - 10 000 eV. All cross section values are in atomic units and collision energy in eV.

Table 19 Elastic differential cross sections of electron-furfural scattering in bohr^2. Energy range 0.1 eV - 7 eV. Angle in degrees.

θ	0.1	0.15	0.2	0.3	0.4	0.5	0.7	1	1.5	2	3	4	5	7
0	38.7	40.8	42.5	39.8	40.8	40.4	37.1	36.9	39.4	43.4	56.2	73.1	91.1	129
1	38.7	40.8	42.5	39.8	40.8	40.4	37.1	37	39.4	43.4	56.1	72.9	90.8	129
2	38.7	40.8	42.5	39.8	40.8	40.4	37.1	37.1	39.5	43.4	55.9	72.5	89.9	126
3	38.7	40.8	42.5	39.8	40.9	40.5	37.2	37.2	39.5	43.4	55.7	71.8	88.5	123
4	38.7	40.8	42.6	39.9	40.9	40.6	37.3	37.3	39.7	43.4	55.4	70.9	86.9	120
5	38.7	40.8	42.6	39.9	41	40.7	37.5	37.6	39.8	43.5	55	70	85.2	116
6	38.8	40.9	42.6	40	41.1	40.8	37.6	37.8	40	43.5	54.7	69	83.5	112
7	38.8	40.9	42.7	40.1	41.2	40.9	37.8	38	40.1	43.5	54.3	68.1	81.8	109
8	38.8	40.9	42.7	40.2	41.4	41.1	38.1	38.3	40.3	43.5	53.9	67.1	80.2	106
9	38.8	41	42.8	40.3	41.5	41.3	38.3	38.6	40.4	43.5	53.5	66.2	78.5	102
10	38.9	41	42.9	40.5	41.7	41.5	38.5	38.8	40.5	43.4	53.1	65.2	76.9	98.8
11	38.9	41.1	43	40.6	41.9	41.7	38.8	39	40.6	43.4	52.7	64.2	75.2	95.4
12	38.9	41.2	43.1	40.8	42.1	41.9	39	39.3	40.7	43.3	52.2	63.2	73.5	92.1
13	39	41.3	43.1	40.9	42.3	42.1	39.2	39.5	40.8	43.2	51.8	62.2	71.8	88.8
14	39	41.3	43.3	41.1	42.5	42.4	39.5	39.7	40.9	43.2	51.3	61.2	70.1	85.5
15	39.1	41.4	43.4	41.3	42.7	42.6	39.7	39.8	40.9	43	50.7	60.1	68.4	82.3
16	39.1	41.5	43.5	41.5	43	42.9	40	40	41	42.9	50.2	59	66.7	79.1
17	39.2	41.6	43.6	41.6	43.2	43.1	40.2	40.2	41	42.8	49.7	58	65	76
18	39.3	41.7	43.7	41.9	43.5	43.4	40.5	40.4	41	42.6	49.1	56.9	63.3	73

19	39.3	41.8	43.8	42.1	43.7	43.6	40.7	40.5	41	42.4	48.6	55.8	61.6	70
20	39.4	41.9	43.9	42.3	44	43.9	40.9	40.7	41	42.2	48	54.7	60	67.2
21	39.5	42	44.1	42.5	44.2	44.1	41.1	40.8	41	42	47.4	53.6	58.3	64.4
22	39.5	42.1	44.2	42.7	44.4	44.4	41.3	40.9	40.9	41.8	46.7	52.4	56.6	61.6
23	39.6	42.2	44.4	42.9	44.7	44.7	41.5	41	40.9	41.6	46.1	51.3	55	59
24	39.7	42.3	44.5	43.1	44.9	44.9	41.7	41.1	40.8	41.4	45.5	50.2	53.4	56.4
25	39.8	42.4	44.6	43.3	45.2	45.1	41.9	41.2	40.7	41.1	44.8	49	51.8	53.9
26	39.8	42.6	44.8	43.6	45.4	45.4	42.1	41.3	40.6	40.8	44.1	47.9	50.2	51.5
27	39.9	42.7	44.9	43.8	45.7	45.6	42.2	41.4	40.5	40.5	43.4	46.8	48.6	49.3
28	40	42.8	45.1	44	45.9	45.8	42.4	41.4	40.4	40.2	42.7	45.6	47.1	47
29	40.1	42.9	45.2	44.2	46.1	46	42.6	41.5	40.2	39.8	42	44.5	45.6	44.9
30	40.2	43	45.4	44.4	46.3	46.2	42.7	41.5	40	39.5	41.2	43.4	44.1	42.9
31	40.2	43.1	45.5	44.6	46.5	46.4	42.8	41.5	39.8	39.1	40.5	42.3	42.6	40.9
32	40.3	43.3	45.7	44.8	46.7	46.5	42.9	41.5	39.7	38.7	39.7	41.1	41.2	39.1
33	40.4	43.4	45.8	45	46.8	46.7	43	41.5	39.4	38.3	39	40	39.8	37.3
34	40.5	43.5	45.9	45.2	47	46.8	43.1	41.4	39.2	37.9	38.2	38.9	38.5	35.7
35	40.6	43.6	46.1	45.4	47.2	46.9	43.2	41.4	39	37.5	37.5	37.8	37.2	34.1
36	40.7	43.8	46.2	45.5	47.3	47.1	43.3	41.3	38.7	37.1	36.7	36.8	35.9	32.5
37	40.8	43.9	46.3	45.7	47.5	47.2	43.3	41.2	38.4	36.6	35.9	35.7	34.6	31.1
38	40.8	44	46.5	45.9	47.6	47.2	43.3	41.1	38.1	36.1	35.2	34.7	33.4	29.8
39	40.9	44.1	46.6	46	47.7	47.3	43.3	41	37.8	35.7	34.4	33.7	32.2	28.5
40	41	44.2	46.7	46.2	47.8	47.4	43.3	40.9	37.5	35.2	33.6	32.7	31.1	27.4
41	41.1	44.3	46.8	46.3	47.9	47.5	43.3	40.8	37.2	34.7	32.8	31.7	30	26.3
42	41.2	44.4	47	46.5	48	47.5	43.3	40.6	36.8	34.2	32.1	30.7	29	25.2
43	41.3	44.6	47.1	46.6	48.1	47.5	43.3	40.4	36.5	33.7	31.3	29.8	28	24.3
44	41.3	44.7	47.2	46.7	48.2	47.5	43.2	40.3	36.1	33.2	30.6	28.9	27	23.4
45	41.4	44.8	47.3	46.8	48.3	47.6	43.2	40.1	35.7	32.6	29.8	28	26.1	22.6
46	41.5	44.9	47.4	46.9	48.3	47.6	43.1	39.9	35.3	32.1	29.1	27.1	25.2	21.8
47	41.6	45	47.5	47	48.4	47.5	43	39.7	34.9	31.6	28.3	26.3	24.3	21.1
48	41.7	45.1	47.6	47.1	48.4	47.5	42.9	39.4	34.5	31	27.6	25.5	23.5	20.4

49	41.7	45.2	47.7	47.2	48.4	47.5	42.8	39.2	34.1	30.5	26.9	24.7	22.8	19.8
50	41.8	45.3	47.8	47.3	48.4	47.5	42.7	38.9	33.7	30	26.2	24	22	19.2
51	41.9	45.4	47.9	47.3	48.4	47.4	42.6	38.7	33.2	29.4	25.5	23.2	21.4	18.7
52	42	45.5	48	47.4	48.4	47.3	42.5	38.4	32.8	28.9	24.9	22.5	20.7	18.2
53	42	45.6	48	47.5	48.4	47.3	42.3	38.1	32.4	28.4	24.2	21.9	20.1	17.8
54	42.1	45.7	48.1	47.5	48.4	47.2	42.2	37.8	31.9	27.8	23.6	21.2	19.5	17.4
55	42.2	45.7	48.2	47.6	48.4	47.1	42.1	37.6	31.5	27.3	23	20.6	19	17
56	42.3	45.8	48.3	47.6	48.4	47	41.9	37.3	31.1	26.8	22.4	20.1	18.5	16.6
57	42.3	45.9	48.3	47.6	48.3	46.9	41.7	37	30.6	26.3	21.8	19.5	18	16.3
58	42.4	46	48.4	47.6	48.3	46.8	41.6	36.6	30.2	25.8	21.3	19	17.5	16
59	42.4	46	48.4	47.6	48.2	46.7	41.4	36.3	29.7	25.3	20.7	18.5	17.1	15.7
60	42.5	46.1	48.5	47.6	48.2	46.6	41.2	36	29.3	24.8	20.2	18	16.7	15.4
61	42.6	46.2	48.5	47.7	48.1	46.5	41	35.7	28.8	24.3	19.7	17.6	16.3	15.1
62	42.6	46.3	48.6	47.6	48	46.3	40.8	35.3	28.4	23.8	19.3	17.1	16	14.9
63	42.7	46.3	48.6	47.6	48	46.2	40.6	35	27.9	23.3	18.8	16.8	15.7	14.6
64	42.7	46.4	48.7	47.6	47.9	46	40.3	34.6	27.5	22.9	18.4	16.4	15.4	14.4
65	42.8	46.4	48.7	47.6	47.8	45.9	40.1	34.3	27.1	22.4	17.9	16	15.1	14.2
66	42.8	46.5	48.7	47.6	47.7	45.7	39.9	34	26.6	22	17.5	15.7	14.8	13.9
67	42.9	46.5	48.7	47.5	47.6	45.5	39.7	33.6	26.2	21.6	17.1	15.4	14.6	13.7
68	42.9	46.6	48.8	47.5	47.5	45.4	39.4	33.3	25.8	21.2	16.8	15.1	14.3	13.5
69	43	46.6	48.8	47.5	47.4	45.2	39.2	32.9	25.4	20.8	16.4	14.8	14.1	13.3
70	43	46.7	48.8	47.4	47.3	45	38.9	32.6	25	20.4	16.1	14.6	13.9	13
71	43.1	46.7	48.8	47.4	47.1	44.8	38.7	32.2	24.6	20	15.8	14.3	13.7	12.8
72	43.1	46.8	48.8	47.3	47	44.6	38.4	31.8	24.2	19.6	15.5	14.1	13.5	12.6
73	43.1	46.8	48.8	47.3	46.9	44.4	38.2	31.5	23.8	19.3	15.2	13.9	13.3	12.4
74	43.2	46.9	48.8	47.2	46.8	44.2	37.9	31.2	23.5	18.9	15	13.7	13.1	12.2
75	43.2	46.9	48.8	47.1	46.6	44	37.6	30.8	23.1	18.6	14.7	13.5	13	11.9
76	43.2	46.9	48.8	47.1	46.5	43.8	37.4	30.5	22.7	18.3	14.5	13.3	12.8	11.7
77	43.3	47	48.8	47	46.3	43.6	37.1	30.1	22.4	18	14.3	13.2	12.6	11.5
78	43.3	47	48.8	46.9	46.2	43.4	36.8	29.8	22.1	17.7	14.1	13	12.5	11.3

79	43.3	47	48.8	46.8	46	43.1	36.6	29.4	21.7	17.4	13.9	12.9	12.3	11.1
80	43.4	47	48.8	46.8	45.9	42.9	36.3	29.1	21.4	17.2	13.8	12.7	12.2	10.8
81	43.4	47.1	48.8	46.7	45.7	42.7	36	28.8	21.1	16.9	13.6	12.6	12	10.6
82	43.4	47.1	48.8	46.6	45.5	42.5	35.7	28.5	20.8	16.7	13.5	12.5	11.9	10.4
83	43.4	47.1	48.7	46.5	45.4	42.2	35.5	28.1	20.5	16.5	13.3	12.4	11.7	10.2
84	43.4	47.1	48.7	46.4	45.2	42	35.2	27.8	20.2	16.3	13.2	12.3	11.6	9.98
85	43.5	47.1	48.7	46.4	45	41.8	34.9	27.5	20	16.1	13.1	12.2	11.4	9.77
86	43.5	47.2	48.7	46.3	44.9	41.6	34.6	27.2	19.7	15.9	13	12.1	11.3	9.57
87	43.5	47.2	48.7	46.2	44.7	41.3	34.4	26.9	19.5	15.7	12.9	12	11.2	9.37
88	43.5	47.2	48.6	46.1	44.5	41.1	34.1	26.6	19.2	15.6	12.8	11.9	11	9.18
89	43.5	47.2	48.6	46	44.3	40.9	33.8	26.4	19	15.4	12.8	11.8	10.9	8.99
90	43.6	47.2	48.6	45.9	44.1	40.6	33.6	26.1	18.8	15.3	12.7	11.7	10.8	8.81
91	43.6	47.2	48.5	45.8	44	40.4	33.3	25.8	18.6	15.2	12.6	11.7	10.7	8.63
92	43.6	47.2	48.5	45.7	43.8	40.2	33	25.5	18.4	15	12.6	11.6	10.5	8.47
93	43.6	47.2	48.5	45.6	43.6	39.9	32.8	25.3	18.2	14.9	12.5	11.5	10.4	8.31
94	43.6	47.2	48.4	45.5	43.4	39.7	32.5	25	18.1	14.8	12.5	11.5	10.3	8.15
95	43.6	47.2	48.4	45.4	43.2	39.5	32.3	24.8	17.9	14.8	12.5	11.4	10.2	8.01
96	43.6	47.2	48.3	45.3	43.1	39.2	32	24.5	17.7	14.7	12.5	11.3	10.1	7.87
97	43.6	47.2	48.3	45.2	42.9	39	31.8	24.3	17.6	14.6	12.4	11.3	9.94	7.75
98	43.6	47.2	48.3	45.1	42.7	38.8	31.6	24.1	17.5	14.6	12.4	11.2	9.84	7.63
99	43.6	47.2	48.2	45	42.5	38.6	31.3	23.9	17.4	14.5	12.4	11.1	9.74	7.52
100	43.6	47.2	48.2	44.8	42.3	38.3	31.1	23.7	17.2	14.5	12.4	11.1	9.64	7.42
101	43.6	47.2	48.2	44.7	42.1	38.1	30.9	23.5	17.1	14.5	12.4	11	9.54	7.32
102	43.6	47.2	48.1	44.6	41.9	37.9	30.6	23.2	17	14.4	12.4	11	9.46	7.24
103	43.6	47.2	48.1	44.5	41.8	37.7	30.4	23.1	16.9	14.4	12.4	10.9	9.37	7.17
104	43.6	47.1	48	44.4	41.6	37.5	30.2	22.9	16.9	14.4	12.4	10.9	9.29	7.1
105	43.6	47.1	48	44.3	41.4	37.2	30	22.7	16.8	14.4	12.4	10.9	9.22	7.04
106	43.6	47.1	47.9	44.2	41.2	37	29.8	22.5	16.7	14.4	12.4	10.8	9.15	7
107	43.6	47.1	47.9	44	41	36.8	29.6	22.4	16.7	14.4	12.5	10.8	9.09	6.96
108	43.6	47.1	47.8	43.9	40.9	36.6	29.4	22.2	16.6	14.5	12.5	10.8	9.03	6.93

109	43.6	47.1	47.8	43.8	40.7	36.4	29.2	22.1	16.6	14.5	12.5	10.7	8.98	6.91
110	43.6	47.1	47.7	43.7	40.5	36.2	29	21.9	16.6	14.5	12.5	10.7	8.94	6.9
111	43.6	47	47.7	43.6	40.4	36	28.8	21.8	16.5	14.5	12.5	10.7	8.9	6.89
112	43.6	47	47.6	43.5	40.2	35.8	28.6	21.7	16.5	14.6	12.6	10.7	8.87	6.89
113	43.6	47	47.6	43.3	40	35.6	28.5	21.5	16.5	14.6	12.6	10.6	8.84	6.9
114	43.6	47	47.5	43.2	39.9	35.4	28.3	21.4	16.5	14.7	12.6	10.6	8.83	6.92
115	43.6	47	47.5	43.1	39.7	35.2	28.1	21.3	16.5	14.7	12.7	10.6	8.81	6.95
116	43.6	46.9	47.4	43	39.5	35	28	21.2	16.5	14.8	12.7	10.6	8.81	6.98
117	43.6	46.9	47.4	42.9	39.4	34.9	27.8	21.1	16.5	14.8	12.7	10.6	8.81	7.02
118	43.6	46.9	47.3	42.8	39.2	34.7	27.7	21	16.5	14.9	12.8	10.6	8.81	7.06
119	43.6	46.9	47.3	42.7	39.1	34.5	27.5	20.9	16.6	15	12.8	10.6	8.82	7.11
120	43.6	46.8	47.2	42.5	38.9	34.3	27.3	20.9	16.6	15	12.8	10.6	8.84	7.17
121	43.6	46.8	47.2	42.4	38.7	34.2	27.2	20.8	16.6	15.1	12.9	10.6	8.86	7.23
122	43.6	46.8	47.1	42.3	38.6	34	27.1	20.7	16.6	15.2	12.9	10.6	8.9	7.3
123	43.6	46.8	47.1	42.2	38.4	33.9	26.9	20.7	16.7	15.2	13	10.7	8.93	7.38
124	43.6	46.7	47	42.1	38.3	33.7	26.8	20.6	16.7	15.3	13	10.7	8.97	7.46
125	43.6	46.7	47	42	38.2	33.6	26.7	20.5	16.8	15.4	13	10.7	9.02	7.54
126	43.6	46.7	47	41.9	38	33.4	26.6	20.5	16.8	15.5	13.1	10.7	9.06	7.63
127	43.6	46.7	46.9	41.8	37.9	33.3	26.4	20.4	16.9	15.5	13.1	10.8	9.12	7.73
128	43.6	46.7	46.9	41.7	37.7	33.1	26.3	20.4	16.9	15.6	13.2	10.8	9.18	7.82
129	43.6	46.7	46.8	41.6	37.6	33	26.2	20.4	17	15.7	13.2	10.9	9.24	7.93
130	43.6	46.6	46.8	41.5	37.5	32.9	26.1	20.3	17	15.8	13.3	10.9	9.31	8.03
131	43.6	46.6	46.7	41.5	37.4	32.7	26	20.3	17.1	15.9	13.3	10.9	9.38	8.15
132	43.6	46.6	46.7	41.4	37.2	32.6	25.9	20.3	17.2	15.9	13.4	11	9.46	8.26
133	43.6	46.6	46.6	41.3	37.1	32.5	25.8	20.3	17.2	16	13.4	11	9.54	8.38
134	43.6	46.5	46.6	41.2	37	32.4	25.7	20.2	17.3	16.1	13.5	11.1	9.62	8.5
135	43.5	46.5	46.5	41.1	36.9	32.3	25.7	20.2	17.4	16.2	13.5	11.1	9.7	8.62
136	43.5	46.5	46.5	41	36.8	32.1	25.6	20.2	17.4	16.3	13.6	11.2	9.79	8.75
137	43.5	46.5	46.4	40.9	36.7	32	25.5	20.2	17.5	16.4	13.6	11.3	9.88	8.87
138	43.5	46.5	46.4	40.9	36.6	31.9	25.4	20.2	17.6	16.4	13.7	11.3	9.98	9

139	43.5	46.5	46.3	40.8	36.5	31.8	25.4	20.2	17.6	16.5	13.7	11.4	10.1	9.14
140	43.5	46.4	46.3	40.7	36.3	31.7	25.3	20.2	17.7	16.6	13.8	11.5	10.2	9.27
141	43.5	46.4	46.3	40.6	36.2	31.6	25.2	20.2	17.8	16.7	13.9	11.5	10.3	9.4
142	43.5	46.4	46.2	40.5	36.2	31.5	25.2	20.2	17.8	16.8	13.9	11.6	10.4	9.54
143	43.5	46.4	46.2	40.5	36.1	31.4	25.1	20.2	17.9	16.8	14	11.7	10.5	9.68
144	43.5	46.4	46.1	40.4	36	31.4	25.1	20.2	18	16.9	14	11.7	10.6	9.81
145	43.5	46.4	46.1	40.3	35.9	31.3	25	20.2	18	17	14.1	11.8	10.7	9.95
146	43.5	46.4	46.1	40.3	35.8	31.2	24.9	20.2	18.1	17.1	14.1	11.9	10.8	10.1
147	43.4	46.3	46	40.2	35.7	31.1	24.9	20.2	18.2	17.1	14.2	11.9	10.9	10.2
148	43.4	46.3	46	40.1	35.7	31	24.9	20.3	18.3	17.2	14.2	12	11	10.4
149	43.4	46.3	46	40.1	35.6	30.9	24.8	20.3	18.3	17.3	14.3	12.1	11.1	10.5
150	43.4	46.3	45.9	40	35.5	30.9	24.8	20.3	18.4	17.3	14.3	12.2	11.2	10.6
151	43.4	46.3	45.9	39.9	35.4	30.8	24.7	20.3	18.5	17.4	14.4	12.2	11.3	10.8
152	43.4	46.3	45.9	39.9	35.4	30.7	24.7	20.3	18.5	17.5	14.4	12.3	11.4	10.9
153	43.4	46.3	45.8	39.8	35.3	30.7	24.7	20.3	18.6	17.5	14.5	12.4	11.5	11
154	43.4	46.3	45.8	39.8	35.2	30.6	24.6	20.4	18.6	17.6	14.5	12.4	11.6	11.2
155	43.4	46.3	45.8	39.7	35.2	30.5	24.6	20.4	18.7	17.7	14.6	12.5	11.6	11.3
156	43.4	46.3	45.7	39.7	35.1	30.5	24.6	20.4	18.8	17.7	14.6	12.6	11.7	11.4
157	43.4	46.3	45.7	39.6	35.1	30.4	24.6	20.4	18.8	17.8	14.7	12.6	11.8	11.5
158	43.4	46.2	45.7	39.6	35	30.4	24.5	20.4	18.9	17.8	14.7	12.7	11.9	11.7
159	43.4	46.2	45.6	39.5	35	30.3	24.5	20.4	18.9	17.9	14.8	12.8	12	11.8
160	43.3	46.2	45.6	39.5	34.9	30.3	24.5	20.5	19	17.9	14.8	12.8	12.1	11.9
161	43.4	46.2	45.6	39.4	34.9	30.3	24.5	20.5	19	18	14.8	12.9	12.2	12
162	43.4	46.2	45.6	39.4	34.8	30.2	24.4	20.5	19.1	18	14.9	12.9	12.2	12.1
163	43.3	46.2	45.5	39.4	34.8	30.2	24.4	20.5	19.1	18.1	14.9	13	12.3	12.2
164	43.3	46.2	45.5	39.3	34.7	30.1	24.4	20.5	19.2	18.1	14.9	13	12.4	12.3
165	43.3	46.2	45.5	39.3	34.7	30.1	24.4	20.5	19.2	18.1	15	13.1	12.4	12.4
166	43.3	46.2	45.5	39.3	34.7	30.1	24.4	20.6	19.2	18.2	15	13.1	12.5	12.5
167	43.3	46.2	45.5	39.2	34.6	30.1	24.4	20.6	19.3	18.2	15	13.2	12.6	12.6
168	43.3	46.2	45.5	39.2	34.6	30	24.3	20.6	19.3	18.2	15.1	13.2	12.6	12.6

169	43.3	46.2	45.4	39.2	34.6	30	24.3	20.6	19.3	18.3	15.1	13.3	12.7	12.7
170	43.3	46.2	45.4	39.2	34.5	30	24.3	20.6	19.4	18.3	15.1	13.3	12.7	12.8
171	43.3	46.2	45.4	39.2	34.5	30	24.3	20.6	19.4	18.3	15.1	13.3	12.7	12.8
172	43.3	46.2	45.4	39.1	34.5	30	24.3	20.6	19.4	18.3	15.2	13.4	12.8	12.9
173	43.3	46.2	45.4	39.1	34.5	30	24.3	20.6	19.4	18.4	15.2	13.4	12.8	12.9
174	43.3	46.2	45.4	39.1	34.5	29.9	24.3	20.6	19.4	18.4	15.2	13.4	12.8	13
175	43.3	46.2	45.4	39.1	34.4	29.9	24.3	20.6	19.5	18.4	15.2	13.4	12.9	13
176	43.3	46.2	45.4	39.1	34.4	29.9	24.3	20.7	19.5	18.4	15.2	13.5	12.9	13
177	43.3	46.2	45.4	39.1	34.4	29.9	24.3	20.7	19.5	18.4	15.2	13.5	12.9	13.1
178	43.3	46.2	45.4	39.1	34.4	29.9	24.3	20.7	19.5	18.4	15.2	13.5	12.9	13.1
179	43.3	46.2	45.4	39.1	34.4	29.9	24.3	20.7	19.5	18.4	15.2	13.5	12.9	13.1
180	43.3	46.2	45.4	39.1	34.4	29.9	24.3	20.7	19.5	18.4	15.2	13.5	12.9	13.1

Table 20 Elastic differential cross sections of electron-furfural scattering in bohr^2. Energy range 10 eV - 500 eV. Angle in degrees.

θ	10	15	20	30	40	50	70	100	150	200	300	400	500
0	189	304	407	551	665	760	912	1080	1270	1420	1640	1780	1910
1	187	300	400	540	648	738	878	1030	1200	1320	1480	1570	1640
2	182	289	383	512	608	686	802	918	1040	1110	1190	1220	1220
3	176	275	362	478	561	627	720	804	879	911	915	880	832
4	168	260	340	443	514	568	639	692	721	716	664	595	526
5	161	246	318	409	467	509	557	582	575	543	461	383	318
6	154	232	297	375	420	451	479	480	446	399	310	242	193
7	148	218	276	341	375	395	405	388	338	287	207	155	122
8	141	204	255	308	331	342	338	309	253	205	140	105	82.9
9	134	190	234	276	290	293	279	243	187	146	98.7	74.4	59.1
10	128	177	214	246	252	249	228	189	139	107	72.7	55.1	43.5
11	122	164	195	217	217	210	185	147	104	80.2	55.5	41.8	33
12	115	152	177	191	186	176	149	114	80.1	62.3	43.4	32.5	26.4

13	109	140	160	167	158	146	119	89.5	63.2	49.8	34.5	26.2	22.2
14	104	129	144	146	134	121	96.2	71.3	51.1	40.5	27.9	22	19.5
15	97.9	118	129	126	113	100	78	57.9	42.2	33.4	23.2	19.2	17.3
16	92.4	108	116	109	95.5	83.1	63.9	47.9	35.3	27.7	19.8	17.1	15.1
17	87.1	99	103	94.2	80.5	69.2	53	40.4	29.9	23.3	17.4	15.2	12.9
18	82.1	90.4	92.1	81.1	68	58	44.7	34.6	25.4	19.9	15.6	13.3	10.7
19	77.3	82.4	81.8	69.8	57.7	49	38.3	29.9	21.7	17.3	14	11.5	8.71
20	72.7	75	72.7	60.2	49.3	41.9	33.2	26	18.8	15.3	12.5	9.67	7.02
21	68.3	68.2	64.5	52.1	42.4	36.3	29.1	22.7	16.4	13.8	11	8	5.68
22	64.2	62	57.3	45.3	36.9	31.8	25.7	19.9	14.5	12.5	9.56	6.57	4.67
23	60.3	56.4	50.9	39.6	32.4	28.2	22.9	17.5	13	11.3	8.16	5.38	3.94
24	56.6	51.3	45.4	34.8	28.7	25.2	20.4	15.5	11.8	10.2	6.89	4.46	3.43
25	53.1	46.7	40.5	30.9	25.8	22.7	18.2	13.8	10.7	9.09	5.76	3.75	3.1
26	49.8	42.6	36.3	27.7	23.3	20.5	16.3	12.3	9.75	8.06	4.82	3.23	2.89
27	46.7	38.9	32.7	25	21.2	18.7	14.6	11.2	8.86	7.08	4.04	2.86	2.75
28	43.9	35.7	29.7	22.7	19.4	17	13.2	10.1	8	6.16	3.42	2.61	2.62
29	41.3	32.8	27	20.9	17.8	15.5	11.9	9.26	7.19	5.32	2.94	2.44	2.47
30	38.8	30.3	24.8	19.3	16.4	14.1	10.8	8.49	6.42	4.58	2.58	2.32	2.26
31	36.5	28.1	22.9	17.9	15.1	12.9	9.82	7.79	5.7	3.92	2.3	2.22	2
32	34.4	26.1	21.3	16.7	13.9	11.8	8.99	7.14	5.03	3.37	2.11	2.12	1.73
33	32.5	24.4	19.9	15.6	12.9	10.8	8.27	6.52	4.42	2.9	1.97	1.98	1.48
34	30.7	22.9	18.7	14.6	11.9	9.88	7.63	5.94	3.87	2.52	1.87	1.81	1.26
35	29.1	21.7	17.7	13.7	11	9.09	7.05	5.4	3.38	2.21	1.8	1.62	1.09
36	27.6	20.6	16.8	12.9	10.2	8.4	6.53	4.89	2.95	1.97	1.73	1.43	0.952
37	26.3	19.6	16	12.1	9.45	7.78	6.05	4.42	2.58	1.78	1.66	1.25	0.845
38	25	18.8	15.3	11.4	8.78	7.24	5.6	3.98	2.27	1.63	1.57	1.09	0.754
39	23.9	18	14.7	10.7	8.18	6.75	5.17	3.58	2.01	1.51	1.47	0.96	0.676
40	22.9	17.4	14.1	10.1	7.64	6.32	4.78	3.22	1.79	1.43	1.35	0.858	0.61
41	22	16.9	13.6	9.49	7.16	5.92	4.4	2.89	1.62	1.37	1.23	0.775	0.56
42	21.2	16.4	13.1	8.95	6.72	5.55	4.05	2.6	1.47	1.32	1.11	0.705	0.528

43	20.5	15.9	12.7	8.45	6.33	5.21	3.72	2.33	1.36	1.28	0.991	0.643	0.513
44	19.8	15.5	12.2	8	5.98	4.9	3.42	2.1	1.27	1.24	0.892	0.588	0.51
45	19.2	15.2	11.8	7.58	5.66	4.6	3.14	1.89	1.2	1.21	0.807	0.541	0.51
46	18.7	14.8	11.4	7.19	5.36	4.32	2.89	1.71	1.15	1.16	0.738	0.504	0.508
47	18.2	14.5	11	6.84	5.1	4.05	2.65	1.55	1.11	1.12	0.681	0.478	0.497
48	17.7	14.2	10.7	6.52	4.84	3.8	2.44	1.42	1.08	1.06	0.633	0.464	0.477
49	17.3	13.9	10.3	6.23	4.6	3.57	2.25	1.3	1.05	1	0.59	0.46	0.449
50	16.9	13.6	9.97	5.97	4.38	3.35	2.07	1.21	1.03	0.939	0.551	0.46	0.419
51	16.6	13.3	9.64	5.72	4.16	3.14	1.91	1.13	1.01	0.875	0.515	0.46	0.389
52	16.3	13	9.33	5.5	3.96	2.95	1.76	1.06	0.982	0.814	0.483	0.457	0.365
53	16	12.7	9.02	5.29	3.77	2.77	1.63	1.01	0.957	0.756	0.455	0.448	0.345
54	15.7	12.4	8.73	5.09	3.58	2.6	1.51	0.972	0.929	0.705	0.433	0.432	0.33
55	15.4	12.1	8.46	4.9	3.41	2.45	1.4	0.939	0.896	0.659	0.418	0.412	0.319
56	15.1	11.8	8.2	4.73	3.24	2.3	1.31	0.913	0.862	0.619	0.409	0.388	0.308
57	14.9	11.6	7.95	4.56	3.09	2.17	1.22	0.894	0.825	0.586	0.406	0.365	0.295
58	14.6	11.3	7.72	4.4	2.94	2.05	1.15	0.877	0.787	0.557	0.406	0.344	0.281
59	14.3	11	7.51	4.25	2.8	1.93	1.09	0.864	0.748	0.532	0.407	0.327	0.265
60	14.1	10.7	7.29	4.1	2.67	1.83	1.03	0.853	0.71	0.51	0.407	0.314	0.249
61	13.8	10.5	7.1	3.96	2.54	1.73	0.985	0.842	0.674	0.489	0.404	0.304	0.232
62	13.5	10.2	6.91	3.82	2.42	1.63	0.946	0.831	0.64	0.469	0.398	0.296	0.218
63	13.3	9.94	6.73	3.68	2.31	1.55	0.914	0.82	0.609	0.45	0.388	0.288	0.205
64	13	9.69	6.56	3.55	2.21	1.47	0.887	0.807	0.581	0.432	0.374	0.28	0.194
65	12.7	9.44	6.4	3.42	2.11	1.39	0.865	0.794	0.557	0.415	0.359	0.27	0.184
66	12.5	9.2	6.25	3.3	2.01	1.33	0.848	0.779	0.536	0.4	0.343	0.259	0.176
67	12.2	8.97	6.1	3.18	1.92	1.26	0.833	0.762	0.518	0.387	0.328	0.246	0.168
68	11.9	8.74	5.95	3.06	1.84	1.21	0.821	0.745	0.502	0.377	0.314	0.233	0.161
69	11.7	8.52	5.81	2.94	1.75	1.15	0.812	0.726	0.488	0.371	0.302	0.22	0.153
70	11.4	8.31	5.66	2.83	1.68	1.11	0.803	0.707	0.475	0.367	0.293	0.208	0.147
71	11.1	8.11	5.53	2.72	1.61	1.06	0.796	0.687	0.464	0.366	0.287	0.198	0.141
72	10.8	7.91	5.39	2.62	1.54	1.02	0.79	0.668	0.453	0.367	0.281	0.19	0.136

73	10.6	7.71	5.25	2.52	1.47	0.99	0.783	0.649	0.443	0.37	0.277	0.182	0.132
74	10.3	7.53	5.11	2.42	1.41	0.96	0.776	0.631	0.433	0.373	0.273	0.176	0.129
75	10.1	7.35	4.97	2.33	1.35	0.933	0.769	0.614	0.423	0.376	0.269	0.17	0.127
76	9.8	7.17	4.83	2.23	1.3	0.91	0.761	0.597	0.414	0.377	0.263	0.165	0.126
77	9.55	7	4.69	2.15	1.25	0.89	0.753	0.582	0.405	0.378	0.256	0.16	0.125
78	9.31	6.83	4.56	2.06	1.2	0.872	0.745	0.569	0.397	0.376	0.249	0.155	0.123
79	9.07	6.66	4.42	1.98	1.16	0.858	0.736	0.557	0.391	0.372	0.241	0.15	0.12
80	8.84	6.5	4.28	1.91	1.12	0.845	0.727	0.547	0.386	0.367	0.232	0.146	0.117
81	8.62	6.34	4.14	1.83	1.09	0.835	0.718	0.538	0.382	0.361	0.224	0.142	0.113
82	8.4	6.18	4.01	1.76	1.05	0.826	0.709	0.53	0.381	0.354	0.216	0.138	0.109
83	8.19	6.03	3.87	1.7	1.02	0.819	0.701	0.524	0.382	0.346	0.209	0.135	0.105
84	8	5.87	3.74	1.64	0.998	0.813	0.693	0.519	0.384	0.338	0.204	0.133	0.102
85	7.81	5.72	3.61	1.58	0.975	0.808	0.686	0.516	0.387	0.332	0.198	0.132	0.0982
86	7.62	5.57	3.49	1.52	0.956	0.805	0.679	0.514	0.392	0.326	0.194	0.131	0.095
87	7.45	5.42	3.37	1.47	0.939	0.803	0.674	0.512	0.397	0.321	0.19	0.13	0.092
88	7.28	5.28	3.25	1.43	0.926	0.802	0.67	0.511	0.403	0.318	0.187	0.13	0.089
89	7.12	5.14	3.14	1.38	0.915	0.802	0.666	0.511	0.409	0.316	0.184	0.129	0.0861
90	6.97	5	3.03	1.35	0.907	0.803	0.664	0.512	0.415	0.315	0.181	0.128	0.0834
91	6.83	4.86	2.93	1.31	0.902	0.805	0.663	0.513	0.421	0.315	0.178	0.126	0.0809
92	6.7	4.73	2.83	1.28	0.9	0.808	0.664	0.514	0.425	0.316	0.176	0.124	0.0786
93	6.57	4.61	2.74	1.25	0.9	0.813	0.665	0.515	0.429	0.317	0.173	0.122	0.0766
94	6.45	4.48	2.66	1.23	0.903	0.819	0.668	0.517	0.432	0.319	0.171	0.12	0.0747
95	6.34	4.37	2.59	1.21	0.909	0.827	0.672	0.519	0.434	0.32	0.168	0.117	0.073
96	6.24	4.25	2.52	1.2	0.917	0.836	0.677	0.521	0.436	0.321	0.166	0.115	0.0715
97	6.14	4.15	2.46	1.19	0.928	0.848	0.684	0.524	0.436	0.322	0.164	0.112	0.0702
98	6.05	4.05	2.41	1.18	0.941	0.861	0.691	0.527	0.436	0.322	0.162	0.11	0.069
99	5.97	3.96	2.37	1.18	0.957	0.876	0.7	0.531	0.436	0.321	0.161	0.108	0.0681
100	5.89	3.88	2.34	1.19	0.976	0.894	0.71	0.535	0.435	0.319	0.16	0.106	0.0674
101	5.82	3.81	2.31	1.19	0.998	0.914	0.721	0.54	0.434	0.317	0.159	0.104	0.0668
102	5.76	3.74	2.29	1.21	1.02	0.936	0.733	0.545	0.434	0.315	0.159	0.102	0.0664

103	5.71	3.69	2.28	1.23	1.05	0.961	0.746	0.552	0.434	0.312	0.16	0.1	0.0659
104	5.66	3.64	2.28	1.25	1.08	0.988	0.761	0.56	0.434	0.309	0.161	0.0983	0.0654
105	5.62	3.61	2.29	1.27	1.11	1.02	0.778	0.568	0.435	0.306	0.162	0.0965	0.0648
106	5.58	3.59	2.3	1.31	1.15	1.05	0.795	0.578	0.436	0.304	0.163	0.0948	0.064
107	5.55	3.58	2.33	1.34	1.19	1.09	0.813	0.59	0.438	0.302	0.164	0.0933	0.0631
108	5.53	3.58	2.36	1.38	1.23	1.12	0.833	0.602	0.441	0.3	0.164	0.0918	0.062
109	5.51	3.59	2.4	1.43	1.28	1.16	0.854	0.616	0.445	0.299	0.165	0.0907	0.0608
110	5.51	3.61	2.44	1.48	1.33	1.2	0.876	0.631	0.449	0.298	0.164	0.0897	0.0595
111	5.5	3.64	2.5	1.54	1.39	1.25	0.899	0.647	0.454	0.297	0.164	0.0889	0.0584
112	5.51	3.69	2.56	1.6	1.44	1.29	0.923	0.665	0.459	0.297	0.163	0.0881	0.0574
113	5.52	3.75	2.63	1.66	1.51	1.34	0.948	0.683	0.465	0.297	0.162	0.0875	0.0566
114	5.55	3.81	2.71	1.73	1.57	1.39	0.974	0.703	0.471	0.298	0.161	0.087	0.056
115	5.57	3.89	2.79	1.81	1.64	1.44	1	0.722	0.477	0.298	0.16	0.0866	0.0557
116	5.61	3.99	2.88	1.89	1.72	1.49	1.03	0.743	0.484	0.299	0.159	0.0863	0.0555
117	5.66	4.09	2.98	1.97	1.79	1.54	1.05	0.764	0.49	0.3	0.158	0.0861	0.0555
118	5.71	4.2	3.09	2.06	1.87	1.6	1.08	0.786	0.496	0.301	0.157	0.0859	0.0555
119	5.77	4.33	3.2	2.15	1.96	1.65	1.11	0.808	0.502	0.302	0.156	0.0857	0.0555
120	5.84	4.46	3.31	2.25	2.05	1.71	1.14	0.83	0.508	0.303	0.155	0.0856	0.0556
121	5.91	4.61	3.44	2.35	2.14	1.76	1.17	0.852	0.513	0.304	0.155	0.0855	0.0554
122	6	4.76	3.57	2.46	2.23	1.82	1.2	0.874	0.518	0.304	0.154	0.0853	0.0552
123	6.09	4.92	3.7	2.57	2.33	1.88	1.23	0.896	0.523	0.305	0.153	0.085	0.0549
124	6.19	5.09	3.84	2.69	2.43	1.94	1.26	0.917	0.527	0.306	0.152	0.0847	0.0544
125	6.3	5.27	3.99	2.81	2.53	1.99	1.29	0.938	0.531	0.306	0.152	0.0844	0.0539
126	6.42	5.46	4.14	2.93	2.63	2.05	1.32	0.959	0.535	0.307	0.151	0.084	0.0532
127	6.54	5.66	4.3	3.06	2.74	2.11	1.35	0.978	0.538	0.307	0.15	0.0836	0.0526
128	6.68	5.86	4.46	3.2	2.84	2.17	1.38	0.998	0.541	0.308	0.149	0.0831	0.052
129	6.82	6.07	4.62	3.33	2.95	2.24	1.41	1.02	0.543	0.308	0.148	0.0826	0.0515
130	6.96	6.29	4.8	3.47	3.06	2.3	1.44	1.03	0.546	0.309	0.147	0.082	0.0509
131	7.12	6.51	4.97	3.62	3.17	2.36	1.47	1.05	0.548	0.31	0.147	0.0815	0.0505
132	7.28	6.74	5.15	3.77	3.28	2.42	1.5	1.07	0.551	0.31	0.146	0.081	0.0502

133	7.44	6.97	5.33	3.92	3.4	2.49	1.53	1.08	0.553	0.311	0.145	0.0804	0.0499
134	7.62	7.2	5.52	4.08	3.51	2.55	1.56	1.1	0.555	0.312	0.145	0.0799	0.0498
135	7.8	7.44	5.71	4.23	3.62	2.61	1.59	1.11	0.558	0.313	0.144	0.0794	0.0495
136	7.98	7.68	5.9	4.39	3.73	2.68	1.62	1.13	0.56	0.314	0.144	0.0789	0.0494
137	8.18	7.93	6.1	4.55	3.84	2.74	1.65	1.14	0.563	0.315	0.144	0.0784	0.0491
138	8.37	8.18	6.29	4.72	3.95	2.81	1.68	1.16	0.565	0.317	0.143	0.0781	0.0489
139	8.57	8.43	6.5	4.88	4.06	2.87	1.71	1.17	0.568	0.318	0.143	0.0778	0.0486
140	8.77	8.68	6.7	5.05	4.17	2.94	1.74	1.18	0.571	0.32	0.143	0.0775	0.0483
141	8.98	8.93	6.9	5.22	4.28	3	1.78	1.19	0.574	0.321	0.142	0.0774	0.0479
142	9.19	9.18	7.1	5.39	4.39	3.07	1.81	1.21	0.577	0.323	0.142	0.0773	0.0475
143	9.41	9.44	7.31	5.57	4.49	3.13	1.84	1.22	0.58	0.325	0.142	0.0774	0.0472
144	9.62	9.69	7.51	5.73	4.6	3.2	1.87	1.23	0.583	0.327	0.142	0.0774	0.0468
145	9.84	9.94	7.71	5.91	4.7	3.26	1.91	1.24	0.586	0.329	0.141	0.0777	0.0465
146	10.1	10.2	7.92	6.08	4.8	3.32	1.94	1.25	0.589	0.331	0.141	0.0778	0.0462
147	10.3	10.4	8.12	6.25	4.9	3.39	1.97	1.26	0.592	0.334	0.141	0.0781	0.046
148	10.5	10.7	8.32	6.42	4.99	3.45	2.01	1.28	0.595	0.336	0.141	0.0784	0.0459
149	10.7	10.9	8.53	6.59	5.09	3.51	2.04	1.29	0.598	0.338	0.14	0.0786	0.0458
150	10.9	11.2	8.73	6.76	5.18	3.57	2.07	1.3	0.601	0.341	0.14	0.0789	0.0458
151	11.1	11.4	8.92	6.92	5.27	3.63	2.11	1.31	0.604	0.343	0.14	0.079	0.0458
152	11.4	11.6	9.11	7.08	5.36	3.69	2.14	1.32	0.607	0.345	0.141	0.0791	0.0459
153	11.6	11.9	9.31	7.24	5.45	3.75	2.17	1.33	0.61	0.348	0.141	0.0791	0.046
154	11.8	12.1	9.49	7.4	5.53	3.81	2.21	1.34	0.612	0.35	0.141	0.079	0.0461
155	12	12.3	9.68	7.55	5.62	3.87	2.24	1.35	0.616	0.352	0.141	0.0789	0.0461
156	12.2	12.5	9.86	7.7	5.69	3.92	2.27	1.36	0.618	0.354	0.141	0.0787	0.0461
157	12.4	12.7	10	7.85	5.77	3.97	2.3	1.37	0.621	0.356	0.142	0.0785	0.0461
158	12.6	12.9	10.2	8	5.84	4.02	2.33	1.38	0.624	0.358	0.142	0.0782	0.046
159	12.8	13.1	10.4	8.13	5.92	4.07	2.36	1.39	0.627	0.359	0.142	0.078	0.046
160	12.9	13.3	10.5	8.26	5.98	4.12	2.39	1.4	0.63	0.361	0.142	0.0778	0.0459
161	13.1	13.5	10.7	8.39	6.05	4.17	2.41	1.41	0.632	0.362	0.143	0.0778	0.046
162	13.3	13.7	10.8	8.52	6.11	4.21	2.44	1.41	0.635	0.363	0.143	0.0776	0.046

163	13.4	13.9	11	8.63	6.17	4.25	2.46	1.42	0.637	0.364	0.143	0.0777	0.0461
164	13.6	14	11.1	8.75	6.23	4.3	2.49	1.43	0.639	0.365	0.143	0.0777	0.0462
165	13.7	14.2	11.2	8.86	6.28	4.33	2.51	1.44	0.642	0.366	0.143	0.0777	0.0463
166	13.9	14.3	11.4	8.96	6.33	4.37	2.53	1.44	0.644	0.367	0.143	0.0779	0.0465
167	14	14.4	11.5	9.05	6.37	4.4	2.55	1.45	0.645	0.367	0.143	0.0779	0.0467
168	14.1	14.6	11.6	9.14	6.42	4.43	2.57	1.46	0.647	0.368	0.143	0.078	0.0469
169	14.3	14.7	11.7	9.22	6.46	4.46	2.59	1.46	0.648	0.369	0.143	0.0779	0.047
170	14.4	14.8	11.8	9.3	6.49	4.49	2.61	1.47	0.65	0.37	0.143	0.0779	0.0472
171	14.5	14.9	11.9	9.37	6.52	4.51	2.62	1.47	0.651	0.371	0.143	0.0777	0.0472
172	14.5	15	11.9	9.43	6.56	4.53	2.64	1.48	0.652	0.372	0.144	0.0775	0.0472
173	14.6	15.1	12	9.48	6.58	4.55	2.65	1.48	0.653	0.372	0.144	0.0772	0.047
174	14.7	15.1	12.1	9.53	6.6	4.57	2.66	1.49	0.653	0.373	0.144	0.0769	0.0468
175	14.7	15.2	12.1	9.57	6.63	4.58	2.67	1.49	0.654	0.374	0.145	0.0766	0.0467
176	14.8	15.2	12.2	9.61	6.64	4.59	2.68	1.49	0.654	0.374	0.145	0.0762	0.0464
177	14.8	15.3	12.2	9.63	6.65	4.6	2.68	1.49	0.655	0.375	0.145	0.076	0.0463
178	14.8	15.3	12.2	9.65	6.67	4.61	2.69	1.5	0.655	0.375	0.146	0.0757	0.046
179	14.9	15.3	12.2	9.66	6.66	4.61	2.69	1.5	0.655	0.375	0.146	0.0756	0.046
180	14.9	15.3	12.2	9.67	6.66	4.61	2.69	1.49	0.655	0.376	0.146	0.0754	0.0457

Table 21 Elastic differential cross sections of electron-furfural scattering in bohr^2. Energy range 700 eV - 10 000 eV. Angle in degrees.

θ	700	1000	3000	5000	10000
0	2060	2210	2490	2540	2560
1	1710	1750	1500	1210	735
2	1180	1070	513	279	107
3	723	574	168	82.9	35.4
4	409	286	70.5	36.8	22
5	227	150	37.1	26.4	10.6
6	133	87.8	27.7	16.9	8.59

7	84.7	55.5	21	9.93	6.14
8	57.4	37.6	13.9	7.77	2.88
9	40.5	28.5	9.2	7.25	1.52
10	30.4	23.9	7.2	5.17	1.34
11	24.8	20.6	6.71	2.95	1.02
12	21.5	17.1	6.03	1.81	0.727
13	18.8	13.4	4.37	1.26	0.561
14	16	10.1	2.81	1.18	0.401
15	13.2	7.72	1.9	1.05	0.298
16	10.5	6.11	1.34	0.799	0.272
17	8.2	5.14	1.08	0.651	0.227
18	6.47	4.62	1.04	0.542	0.171
19	5.25	4.37	0.984	0.43	0.131
20	4.44	4.13	0.821	0.344	0.117
21	3.94	3.71	0.668	0.275	0.0961
22	3.65	3.1	0.576	0.247	0.0804
23	3.47	2.46	0.502	0.235	0.0692
24	3.28	1.92	0.423	0.203	0.0555
25	3	1.53	0.351	0.167	0.0438
26	2.62	1.25	0.298	0.135	0.0415
27	2.19	1.03	0.251	0.111	0.035
28	1.8	0.87	0.223	0.101	0.0285
29	1.48	0.763	0.215	0.0924	0.0248
30	1.24	0.715	0.203	0.078	0.0212
31	1.05	0.706	0.179	0.0674	0.0182
32	0.909	0.7	0.154	0.0624	0.016
33	0.789	0.673	0.131	0.0537	0.0145
34	0.696	0.62	0.11	0.0451	0.0119
35	0.635	0.554	0.0955	0.0376	0.0104
36	0.606	0.494	0.0873	0.0332	0.00951

37	0.599	0.449	0.0822	0.032	0.0084
38	0.598	0.417	0.0753	0.0291	0.00743
39	0.589	0.391	0.0656	0.025	0.00657
40	0.564	0.364	0.0573	0.0216	0.00585
41	0.525	0.334	0.0533	0.0192	0.0052
42	0.48	0.302	0.0492	0.0172	0.00477
43	0.439	0.273	0.0434	0.0153	0.00436
44	0.405	0.248	0.038	0.0138	0.00394
45	0.38	0.227	0.0335	0.0124	0.00349
46	0.361	0.208	0.0294	0.0117	0.00317
47	0.344	0.191	0.0271	0.0109	0.00299
48	0.326	0.175	0.0262	0.00956	0.00267
49	0.304	0.162	0.0248	0.00838	0.00252
50	0.281	0.155	0.0224	0.00755	0.0023
51	0.258	0.15	0.0198	0.00704	0.00214
52	0.238	0.147	0.0178	0.00668	0.00192
53	0.22	0.142	0.0161	0.00623	0.00181
54	0.206	0.134	0.015	0.00572	0.00171
55	0.193	0.125	0.0139	0.00531	0.00156
56	0.181	0.116	0.0128	0.00491	0.00148
57	0.169	0.107	0.012	0.00445	0.00139
58	0.158	0.099	0.0111	0.0041	0.0013
59	0.149	0.0913	0.0102	0.00385	0.00117
60	0.142	0.0837	0.00958	0.00364	0.00113
61	0.137	0.0773	0.00923	0.00347	0.00107
62	0.134	0.0719	0.00871	0.00333	0.00101
63	0.132	0.0676	0.00798	0.00315	0.000961
64	0.129	0.0641	0.00732	0.00292	0.000895
65	0.125	0.0613	0.0068	0.00268	0.000847
66	0.12	0.0591	0.00643	0.00252	0.000787

67	0.113	0.0569	0.00609	0.0024	0.000766
68	0.107	0.0547	0.00585	0.00232	0.00073
69	0.101	0.0518	0.00561	0.00224	0.000705
70	0.0958	0.0487	0.00534	0.00211	0.000655
71	0.0905	0.0454	0.00504	0.002	0.000615
72	0.0853	0.0427	0.00478	0.00193	0.000594
73	0.0804	0.0408	0.00461	0.00185	0.000572
74	0.0759	0.0395	0.00444	0.00176	0.000552
75	0.072	0.0386	0.00425	0.00168	0.000521
76	0.0686	0.0374	0.004	0.00159	0.0005
77	0.0659	0.036	0.00378	0.00152	0.000474
78	0.0634	0.0342	0.0036	0.00146	0.000457
79	0.0613	0.0324	0.00346	0.00142	0.00044
80	0.0596	0.0308	0.00333	0.00138	0.000425
81	0.0582	0.0293	0.00322	0.00133	0.000412
82	0.057	0.0281	0.00316	0.00127	0.000384
83	0.0557	0.0267	0.0031	0.00124	0.000373
84	0.0544	0.0255	0.00304	0.00121	0.000359
85	0.0526	0.0244	0.00294	0.00115	0.000356
86	0.0507	0.0235	0.00283	0.0011	0.000336
87	0.0486	0.0229	0.00268	0.00105	0.000319
88	0.0466	0.0226	0.00256	0.00101	0.00031
89	0.0448	0.0224	0.00246	0.000989	0.000303
90	0.0435	0.0221	0.00239	0.00098	0.000297
91	0.0425	0.0217	0.00234	5000	0.00098
92	0.0419	0.0211	0.00229	2540	0.000966
93	0.0415	0.0205	0.00226	1210	0.000929
94	0.041	0.0198	0.00221	279	0.000891
95	0.0404	0.0191	0.00214	82.9	0.000853
96	0.0396	0.0185	0.00206	36.8	0.00083

97	0.0387	0.018	0.00201	26.4	0.000812
98	0.0376	0.0176	0.00198	16.9	0.000795
99	0.0365	0.0171	0.00195	9.93	0.000776
100	0.0356	0.0168	0.00192	7.77	0.000752
101	0.0346	0.0163	0.00187	7.25	0.000729
102	0.0339	0.016	0.00183	5.17	0.000701
103	0.033	0.0157	0.00177	2.95	0.000684
104	0.0323	0.0154	0.00172	1.81	0.00067
105	0.0315	0.0151	0.00166	1.26	0.000663
106	0.0308	0.0148	0.0016	1.18	0.000654
107	0.0301	0.0146	0.00158	1.05	0.00064
108	0.0295	0.0143	0.00155	0.799	0.000621
109	0.0291	0.0142	0.00155	0.651	0.000596
110	0.0288	0.014	0.00152	0.542	0.000581
111	0.0287	0.0139	0.00152	0.43	0.000564
112	0.0286	0.0137	0.00149	0.344	0.000557
113	0.0286	0.0135	0.00146	0.275	0.000549
114	0.0286	0.0133	0.00143	0.247	0.000545
115	0.0285	0.0131	0.00138	0.235	0.000534
116	0.0284	0.0129	0.00135	0.203	0.000516
117	0.0282	0.0127	0.00133	0.167	0.000502
118	0.0279	0.0126	0.00132	0.135	0.000488
119	0.0275	0.0125	0.0013	0.111	0.000487
120	0.0272	0.0125	0.00129	0.101	0.00048
121	0.0268	0.0124	0.00127	0.0924	0.000477
122	0.0265	0.0124	0.00124	0.078	0.000466
123	0.0262	0.0124	0.00122	0.0674	0.000456
124	0.0259	0.0124	0.00119	0.0624	0.000445
125	0.0257	0.0123	0.00117	0.0537	0.000434
126	0.0254	0.0122	0.00115	0.0451	0.000429

127	0.0252	0.012	0.00114	0.0376	0.000421
128	0.025	0.0118	0.00112	0.0332	0.00042
129	0.0248	0.0116	0.00111	0.032	0.00041
130	0.0245	0.0114	0.0011	0.0291	0.000404
131	0.0243	0.0112	0.00109	0.025	0.000394
132	0.0241	0.011	0.00108	0.0216	0.000388
133	0.0238	0.0109	0.00106	0.0192	0.000386
134	0.0237	0.0108	0.00106	0.0172	0.000384
135	0.0235	0.0107	0.00104	0.0153	0.000385
136	0.0234	0.0106	0.00104	0.0138	0.000377
137	0.0233	0.0106	0.00103	0.0124	0.000372
138	0.0232	0.0106	0.00102	0.0117	0.00036
139	0.0232	0.0105	0.001	0.0109	0.000354
140	0.0232	0.0105	0.000985	0.00956	0.000348
141	0.0231	0.0104	0.000972	0.00838	0.000347
142	0.023	0.0103	0.000952	0.00755	0.000348
143	0.023	0.0103	0.00095	0.00704	0.000344
144	0.0228	0.0102	0.000934	0.00668	0.000344
145	0.0227	0.0102	0.00094	0.00623	0.000334
146	0.0226	0.0101	0.000929	0.00572	0.000332
147	0.0224	0.0101	0.000928	0.00531	0.000325
148	0.0223	0.0101	0.000918	0.00491	0.000325
149	0.0222	0.0101	0.000905	0.00445	0.000324
150	0.0222	0.0101	0.000898	0.0041	0.000323
151	0.0221	0.0101	0.000879	0.00385	0.000321
152	0.0222	0.0101	0.00088	0.00364	0.000312
153	0.0221	0.0101	0.000866	0.00347	0.000308
154	0.0222	0.0101	0.000873	0.00333	0.000299
155	0.0222	0.0101	0.000866	0.00315	0.000301
156	0.0222	0.01	0.000867	0.00292	0.000301

157	0.0222	0.01	0.000863	0.00268	0.000305
158	0.0221	0.00995	0.000851	0.00252	0.000306
159	0.0221	0.00995	0.000849	0.0024	0.000302
160	0.022	0.00991	0.000831	0.00232	0.000299
161	0.0219	0.00995	0.000838	0.00224	0.00029
162	0.0218	0.00992	0.000826	0.00211	0.000293
163	0.0217	0.00998	0.000836	0.002	0.00029
164	0.0217	0.00997	0.000831	0.00193	0.000297
165	0.0217	0.00998	0.000834	0.00185	0.000296
166	0.0217	0.00997	0.000832	0.00176	0.000295
167	0.0217	0.00991	0.000817	0.00168	0.000291
168	0.0218	0.00989	0.000819	0.00159	0.000282
169	0.0219	0.00978	0.000797	0.00152	0.000283
170	0.0219	0.00977	0.000808	0.00146	0.000278
171	0.0219	0.00967	0.000794	0.00142	0.000288
172	0.0219	0.00968	0.000811	0.00138	0.000287
173	0.0218	0.00965	0.000811	0.00133	0.000293
174	0.0217	0.00968	0.000815	0.00127	0.000286
175	0.0215	0.00975	0.000822	0.00124	0.000277
176	0.0213	0.00977	0.000798	0.00121	0.000274
177	0.0212	0.00992	0.000809	0.00115	0.000267
178	0.021	0.00988	0.000765	0.0011	0.000283
179	0.0211	0.0101	0.000797	0.00105	0.000282
180	0.0207	0.00982	0.000716	0.00101	0.000311

APPENDIX 2 FURFURAL ROTATIONAL EXCITATION DIFFERENTIAL CROSS SECTIONS

As noted in Chapter 4, the rotational differential cross sections produced by the Born first dipole model method are tabulated here, for electron scattering from the molecule furfural in the incident kinetic energy range 0.1 - 10 000 eV. All cross section values are in atomic units and collision energy in eV.

Table 22 Rotational differential cross sections of electron-furfural scattering in bohr^2. Energy range 0.1 eV - 2 eV. Angle in degrees.

θ	0.1	0.15	0.2	0.3	0.4	0.5	0.7	1	1.5	2
0	14200000	2E+07	3E+07	4E+07	6E+07	7E+07	1E+08	1E+08	2E+08	3E+08
1	1070000	744000	566000	382000	287000	230000	165000	115000	77000	57800
2	283000	191000	144000	96100	72100	57700	41300	28900	19300	14400
3	127000	85300	64100	42800	32100	25700	18300	12800	8560	6420
4	71900	48100	36100	24100	18100	14400	10300	7230	4820	3610
5	46100	30800	23100	15400	11600	9250	6610	4630	3080	2310
6	32100	21400	16100	10700	8030	6430	4590	3210	2140	1610
7	23600	15700	11800	7870	5900	4720	3370	2360	1570	1180
8	18100	12100	9040	6030	4520	3620	2580	1810	1210	904
9	14300	9530	7150	4760	3570	2860	2040	1430	953	715
10	11600	7720	5790	3860	2900	2320	1660	1160	772	579
11	9570	6380	4790	3190	2390	1920	1370	958	639	479
12	8050	5370	4030	2680	2010	1610	1150	805	537	403
13	6860	4580	3430	2290	1720	1370	981	687	458	343
14	5920	3950	2960	1980	1480	1190	846	593	395	296
15	5160	3440	2580	1720	1290	1030	738	517	344	258
16	4540	3030	2270	1510	1140	909	649	454	303	227
17	4030	2690	2010	1340	1010	806	575	403	269	201
18	3600	2400	1800	1200	899	719	514	360	240	180

19	3230	2150	1620	1080	808	646	462	323	215	162
20	2920	1950	1460	973	730	584	417	292	195	146
21	2650	1770	1320	883	662	530	379	265	177	132
22	2420	1610	1210	806	604	483	345	242	161	121
23	2210	1480	1110	738	554	443	316	221	148	111
24	2040	1360	1020	679	509	407	291	204	136	102
25	1830	1220	918	612	459	367	262	184	122	91.8
26	1630	1090	817	545	409	327	234	163	109	81.7
27	1460	975	731	488	366	293	209	146	97.5	73.1
28	1310	876	657	438	329	263	188	131	87.6	65.7
29	1190	790	593	395	296	237	169	119	79	59.3
30	1070	715	537	358	268	215	153	107	71.5	53.7
31	975	650	487	325	244	195	139	97.5	65	48.7
32	888	592	444	296	222	178	127	88.9	59.2	44.4
33	812	541	406	271	203	162	116	81.2	54.1	40.6
34	744	496	372	248	186	149	106	74.5	49.6	37.2
35	684	456	342	228	171	137	97.8	68.4	45.6	34.2
36	631	420	315	210	158	126	90.1	63.1	42	31.5
37	582	388	291	194	146	116	83.2	58.2	38.8	29.1
38	539	359	270	180	135	108	77	53.9	35.9	27
39	500	333	250	167	125	100	71.5	50	33.4	25
40	465	310	233	155	116	93	66.4	46.5	31	23.3
41	433	289	217	144	108	86.6	61.9	43.3	28.9	21.7
42	404	270	202	135	101	80.9	57.8	40.4	27	20.2
43	378	252	189	126	94.5	75.6	54	37.8	25.2	18.9
44	354	236	177	118	88.5	70.8	50.6	35.4	23.6	17.7
45	332	221	166	111	83	66.4	47.4	33.2	22.1	16.6
46	312	208	156	104	78	62.4	44.6	31.2	20.8	15.6
47	293	196	147	97.8	73.4	58.7	41.9	29.3	19.6	14.7
48	277	184	138	92.2	69.1	55.3	39.5	27.7	18.4	13.8

49	261	174	130	87	65.2	52.2	37.3	26.1	17.4	13
50	247	164	123	82.2	61.6	49.3	35.2	24.7	16.4	12.3
51	233	155	117	77.7	58.3	46.6	33.3	23.3	15.5	11.7
52	221	147	110	73.6	55.2	44.2	31.6	22.1	14.7	11
53	209	140	105	69.8	52.4	41.9	29.9	20.9	14	10.5
54	199	133	99.4	66.3	49.7	39.8	28.4	19.9	13.3	9.94
55	189	126	94.5	63	47.2	37.8	27	18.9	12.6	9.45
56	180	120	89.9	59.9	45	36	25.7	18	12	8.99
57	171	114	85.6	57.1	42.8	34.3	24.5	17.1	11.4	8.56
58	163	109	81.6	54.4	40.8	32.7	23.3	16.3	10.9	8.16
59	156	104	77.9	51.9	39	31.2	22.3	15.6	10.4	7.79
60	149	99.2	74.4	49.6	37.2	29.8	21.3	14.9	9.92	7.44
61	142	94.9	71.2	47.4	35.6	28.5	20.3	14.2	9.49	7.12
62	136	90.8	68.1	45.4	34	27.2	19.5	13.6	9.08	6.81
63	130	87	65.2	43.5	32.6	26.1	18.6	13	8.7	6.52
64	125	83.4	62.5	41.7	31.3	25	17.9	12.5	8.34	6.25
65	120	80	60	40	30	24	17.1	12	8	6
66	115	76.8	57.6	38.4	28.8	23	16.5	11.5	7.68	5.76
67	111	73.8	55.3	36.9	27.7	22.1	15.8	11.1	7.38	5.53
68	106	70.9	53.2	35.5	26.6	21.3	15.2	10.6	7.09	5.32
69	102	68.3	51.2	34.1	25.6	20.5	14.6	10.2	6.83	5.12
70	98.6	65.7	49.3	32.9	24.7	19.7	14.1	9.86	6.57	4.93
71	95	63.3	47.5	31.7	23.8	19	13.6	9.5	6.33	4.75
72	91.6	61.1	45.8	30.5	22.9	18.3	13.1	9.16	6.11	4.58
73	88.4	58.9	44.2	29.5	22.1	17.7	12.6	8.84	5.89	4.42
74	85.4	56.9	42.7	28.5	21.3	17.1	12.2	8.54	5.69	4.27
75	82.5	55	41.2	27.5	20.6	16.5	11.8	8.25	5.5	4.12
76	79.7	53.2	39.9	26.6	19.9	15.9	11.4	7.97	5.32	3.99
77	77.1	51.4	38.6	25.7	19.3	15.4	11	7.71	5.14	3.86
78	74.7	49.8	37.3	24.9	18.7	14.9	10.7	7.47	4.98	3.73

79	72.3	48.2	36.2	24.1	18.1	14.5	10.3	7.23	4.82	3.62
80	70.1	46.7	35	23.4	17.5	14	10	7.01	4.67	3.5
81	67.9	45.3	34	22.6	17	13.6	9.7	6.79	4.53	3.4
82	65.9	43.9	32.9	22	16.5	13.2	9.41	6.59	4.39	3.29
83	64	42.6	32	21.3	16	12.8	9.14	6.4	4.26	3.2
84	62.1	41.4	31.1	20.7	15.5	12.4	8.87	6.21	4.14	3.11
85	60.3	40.2	30.2	20.1	15.1	12.1	8.62	6.03	4.02	3.02
86	58.7	39.1	29.3	19.6	14.7	11.7	8.38	5.87	3.91	2.93
87	57	38	28.5	19	14.3	11.4	8.15	5.7	3.8	2.85
88	55.5	37	27.8	18.5	13.9	11.1	7.93	5.55	3.7	2.78
89	54	36	27	18	13.5	10.8	7.72	5.4	3.6	2.7
90	52.6	35.1	26.3	17.5	13.2	10.5	7.52	5.26	3.51	2.63
91	51.3	34.2	25.6	17.1	12.8	10.3	7.33	5.13	3.42	2.56
92	50	33.3	25	16.7	12.5	10	7.14	5	3.33	2.5
93	48.8	32.5	24.4	16.3	12.2	9.75	6.96	4.88	3.25	2.44
94	47.6	31.7	23.8	15.9	11.9	9.51	6.8	4.76	3.17	2.38
95	46.4	31	23.2	15.5	11.6	9.29	6.63	4.64	3.1	2.32
96	45.3	30.2	22.7	15.1	11.3	9.07	6.48	4.53	3.02	2.27
97	44.3	29.5	22.1	14.8	11.1	8.86	6.33	4.43	2.95	2.21
98	43.3	28.9	21.6	14.4	10.8	8.66	6.18	4.33	2.89	2.16
99	42.3	28.2	21.2	14.1	10.6	8.46	6.05	4.23	2.82	2.12
100	41.4	27.6	20.7	13.8	10.3	8.28	5.91	4.14	2.76	2.07
101	40.5	27	20.3	13.5	10.1	8.1	5.79	4.05	2.7	2.03
102	39.6	26.4	19.8	13.2	9.91	7.93	5.66	3.96	2.64	1.98
103	38.8	25.9	19.4	12.9	9.7	7.76	5.55	3.88	2.59	1.94
104	38	25.4	19	12.7	9.51	7.61	5.43	3.8	2.54	1.9
105	37.3	24.8	18.6	12.4	9.32	7.45	5.32	3.73	2.48	1.86
106	36.5	24.4	18.3	12.2	9.13	7.31	5.22	3.65	2.44	1.83
107	35.8	23.9	17.9	11.9	8.96	7.16	5.12	3.58	2.39	1.79
108	35.1	23.4	17.6	11.7	8.79	7.03	5.02	3.51	2.34	1.76

109	34.5	23	17.2	11.5	8.62	6.9	4.93	3.45	2.3	1.72
110	33.9	22.6	16.9	11.3	8.46	6.77	4.84	3.39	2.26	1.69
111	33.2	22.2	16.6	11.1	8.31	6.65	4.75	3.32	2.22	1.66
112	32.7	21.8	16.3	10.9	8.16	6.53	4.67	3.27	2.18	1.63
113	32.1	21.4	16	10.7	8.02	6.42	4.58	3.21	2.14	1.6
114	31.5	21	15.8	10.5	7.89	6.31	4.51	3.15	2.1	1.58
115	31	20.7	15.5	10.3	7.75	6.2	4.43	3.1	2.07	1.55
116	30.5	20.3	15.3	10.2	7.63	6.1	4.36	3.05	2.03	1.53
117	30	20	15	10	7.5	6	4.29	3	2	1.5
118	29.5	19.7	14.8	9.85	7.39	5.91	4.22	2.95	1.97	1.48
119	29.1	19.4	14.5	9.7	7.27	5.82	4.16	2.91	1.94	1.45
120	28.6	19.1	14.3	9.55	7.16	5.73	4.09	2.86	1.91	1.43
121	28.2	18.8	14.1	9.41	7.06	5.64	4.03	2.82	1.88	1.41
122	27.8	18.5	13.9	9.27	6.95	5.56	3.97	2.78	1.85	1.39
123	27.4	18.3	13.7	9.14	6.85	5.48	3.92	2.74	1.83	1.37
124	27	18	13.5	9.01	6.76	5.41	3.86	2.7	1.8	1.35
125	26.7	17.8	13.3	8.89	6.67	5.33	3.81	2.67	1.78	1.33
126	26.3	17.5	13.2	8.77	6.58	5.26	3.76	2.63	1.75	1.32
127	26	17.3	13	8.65	6.49	5.19	3.71	2.6	1.73	1.3
128	25.6	17.1	12.8	8.54	6.41	5.13	3.66	2.56	1.71	1.28
129	25.3	16.9	12.7	8.44	6.33	5.06	3.62	2.53	1.69	1.27
130	25	16.7	12.5	8.33	6.25	5	3.57	2.5	1.67	1.25
131	24.7	16.5	12.3	8.23	6.17	4.94	3.53	2.47	1.65	1.23
132	24.4	16.3	12.2	8.14	6.1	4.88	3.49	2.44	1.63	1.22
133	24.1	16.1	12.1	8.04	6.03	4.83	3.45	2.41	1.61	1.21
134	23.9	15.9	11.9	7.95	5.96	4.77	3.41	2.39	1.59	1.19
135	23.6	15.7	11.8	7.87	5.9	4.72	3.37	2.36	1.57	1.18
136	23.3	15.6	11.7	7.78	5.84	4.67	3.33	2.33	1.56	1.17
137	23.1	15.4	11.6	7.7	5.78	4.62	3.3	2.31	1.54	1.16
138	22.9	15.2	11.4	7.62	5.72	4.57	3.27	2.29	1.52	1.14

139	22.6	15.1	11.3	7.55	5.66	4.53	3.23	2.26	1.51	1.13
140	22.4	14.9	11.2	7.47	5.61	4.48	3.2	2.24	1.49	1.12
141	22.2	14.8	11.1	7.4	5.55	4.44	3.17	2.22	1.48	1.11
142	22	14.7	11	7.34	5.5	4.4	3.14	2.2	1.47	1.1
143	21.8	14.5	10.9	7.27	5.45	4.36	3.12	2.18	1.45	1.09
144	21.6	14.4	10.8	7.21	5.41	4.33	3.09	2.16	1.44	1.08
145	21.4	14.3	10.7	7.15	5.36	4.29	3.06	2.14	1.43	1.07
146	21.3	14.2	10.6	7.09	5.32	4.26	3.04	2.13	1.42	1.06
147	21.1	14.1	10.6	7.04	5.28	4.22	3.02	2.11	1.41	1.06
148	20.9	14	10.5	6.98	5.24	4.19	2.99	2.09	1.4	1.05
149	20.8	13.9	10.4	6.93	5.2	4.16	2.97	2.08	1.39	1.04
150	20.6	13.8	10.3	6.88	5.16	4.13	2.95	2.06	1.38	1.03
151	20.5	13.7	10.3	6.83	5.13	4.1	2.93	2.05	1.37	1.03
152	20.4	13.6	10.2	6.79	5.09	4.07	2.91	2.04	1.36	1.02
153	20.2	13.5	10.1	6.75	5.06	4.05	2.89	2.02	1.35	1.01
154	20.1	13.4	10.1	6.7	5.03	4.02	2.87	2.01	1.34	1.01
155	20	13.3	10	6.67	5	4	2.86	2	1.33	1
156	19.9	13.3	9.94	6.63	4.97	3.98	2.84	1.99	1.33	0.994
157	19.8	13.2	9.89	6.59	4.94	3.95	2.82	1.98	1.32	0.989
158	19.7	13.1	9.84	6.56	4.92	3.93	2.81	1.97	1.31	0.984
159	19.6	13	9.79	6.52	4.89	3.91	2.8	1.96	1.3	0.979
160	19.5	13	9.74	6.49	4.87	3.9	2.78	1.95	1.3	0.974
161	19.4	12.9	9.7	6.46	4.85	3.88	2.77	1.94	1.29	0.97
162	19.3	12.9	9.66	6.44	4.83	3.86	2.76	1.93	1.29	0.966
163	19.2	12.8	9.62	6.41	4.81	3.85	2.75	1.92	1.28	0.962
164	19.2	12.8	9.58	6.39	4.79	3.83	2.74	1.92	1.28	0.958
165	19.1	12.7	9.55	6.36	4.77	3.82	2.73	1.91	1.27	0.955
166	19	12.7	9.51	6.34	4.76	3.81	2.72	1.9	1.27	0.951
167	19	12.6	9.49	6.32	4.74	3.79	2.71	1.9	1.26	0.949
168	18.9	12.6	9.46	6.31	4.73	3.78	2.7	1.89	1.26	0.946

169	18.9	12.6	9.43	6.29	4.72	3.77	2.7	1.89	1.26	0.943
170	18.8	12.5	9.41	6.27	4.71	3.76	2.69	1.88	1.25	0.941
171	18.8	12.5	9.39	6.26	4.7	3.76	2.68	1.88	1.25	0.939
172	18.7	12.5	9.37	6.25	4.69	3.75	2.68	1.87	1.25	0.937
173	18.7	12.5	9.36	6.24	4.68	3.74	2.67	1.87	1.25	0.936
174	18.7	12.5	9.34	6.23	4.67	3.74	2.67	1.87	1.25	0.934
175	18.7	12.4	9.33	6.22	4.67	3.73	2.67	1.87	1.24	0.933
176	18.6	12.4	9.32	6.21	4.66	3.73	2.66	1.86	1.24	0.932
177	18.6	12.4	9.31	6.21	4.66	3.73	2.66	1.86	1.24	0.931
178	18.6	12.4	9.31	6.21	4.65	3.72	2.66	1.86	1.24	0.931
179	18.6	12.4	9.3	6.2	4.65	3.72	2.66	1.86	1.24	0.93
180	18.6	12.4	9.3	6.2	4.65	3.72	2.66	1.86	1.24	0.93

Table 23 Rotational differential cross sections of electron-furfural scattering in bohr^2. Energy range 3 eV - 50 eV. Angle in degrees.

θ	3	4	5	7	10	15	20	30	40	50
0	4E+08	6E+08	7E+08	1E+09	1E+09	2E+09	2.8E+09	4.3E+09	5.7E+09	7.1E+09
1	38500	28900	23100	16500	11600	7700	5780	3850	2890	2310
2	9630	7220	5780	4130	2890	1930	1440	963	722	578
3	4280	3210	2570	1830	1280	856	642	428	321	257
4	2410	1810	1450	1030	723	482	361	241	181	145
5	1540	1160	925	661	463	308	231	154	116	92.5
6	1070	803	643	459	321	214	161	107	80.3	64.3
7	787	590	472	337	236	157	118	78.7	59	47.2
8	603	452	362	258	181	121	90.4	60.3	45.2	36.2
9	477	357	286	204	143	95.3	71.5	47.7	35.7	28.6
10	386	290	232	166	116	77.2	57.9	38.6	29	23.2
11	319	239	192	137	95.8	63.9	47.9	31.9	23.9	19.2
12	268	201	161	115	80.5	53.7	40.3	26.8	20.1	16.1

13	229	172	137	98.1	68.7	45.8	34.3	22.9	17.2	13.7
14	198	148	119	84.6	59.3	39.5	29.6	19.8	14.8	11.9
15	172	129	103	73.8	51.7	34.4	25.8	17.2	12.9	10.3
16	151	114	90.9	64.9	45.4	30.3	22.7	15.1	11.4	9.09
17	134	101	80.6	57.5	40.3	26.9	20.1	13.4	10.1	8.06
18	120	89.9	71.9	51.4	36	24	18	12	8.99	7.19
19	108	80.8	64.6	46.2	32.3	21.5	16.2	10.8	8.08	6.46
20	97.3	73	58.4	41.7	29.2	19.5	14.6	9.73	7.3	5.84
21	88.3	66.2	53	37.9	26.5	17.7	13.2	8.83	6.62	5.3
22	80.6	60.4	48.3	34.5	24.2	16.1	12.1	8.06	6.04	4.83
23	73.8	55.4	44.3	31.6	22.1	14.8	11.1	7.38	5.54	4.43
24	67.9	50.9	40.7	29.1	20.4	13.6	10.2	6.79	5.09	4.07
25	61.2	45.9	36.7	26.2	18.4	12.2	9.18	6.12	4.59	3.67
26	54.5	40.9	32.7	23.4	16.3	10.9	8.17	5.45	4.09	3.27
27	48.8	36.6	29.3	20.9	14.6	9.75	7.31	4.88	3.66	2.93
28	43.8	32.9	26.3	18.8	13.1	8.76	6.57	4.38	3.29	2.63
29	39.5	29.6	23.7	16.9	11.9	7.9	5.93	3.95	2.96	2.37
30	35.8	26.8	21.5	15.3	10.7	7.15	5.37	3.58	2.68	2.15
31	32.5	24.4	19.5	13.9	9.75	6.5	4.87	3.25	2.44	1.95
32	29.6	22.2	17.8	12.7	8.89	5.92	4.44	2.96	2.22	1.78
33	27.1	20.3	16.2	11.6	8.12	5.41	4.06	2.71	2.03	1.62
34	24.8	18.6	14.9	10.6	7.45	4.96	3.72	2.48	1.86	1.49
35	22.8	17.1	13.7	9.78	6.84	4.56	3.42	2.28	1.71	1.37
36	21	15.8	12.6	9.01	6.31	4.2	3.15	2.1	1.58	1.26
37	19.4	14.6	11.6	8.32	5.82	3.88	2.91	1.94	1.46	1.16
38	18	13.5	10.8	7.7	5.39	3.59	2.7	1.8	1.35	1.08
39	16.7	12.5	10	7.15	5	3.34	2.5	1.67	1.25	1
40	15.5	11.6	9.3	6.64	4.65	3.1	2.33	1.55	1.16	0.93
41	14.4	10.8	8.66	6.19	4.33	2.89	2.17	1.44	1.08	0.866
42	13.5	10.1	8.09	5.78	4.04	2.7	2.02	1.35	1.01	0.809

43	12.6	9.45	7.56	5.4	3.78	2.52	1.89	1.26	0.945	0.756
44	11.8	8.85	7.08	5.06	3.54	2.36	1.77	1.18	0.885	0.708
45	11.1	8.3	6.64	4.74	3.32	2.21	1.66	1.11	0.83	0.664
46	10.4	7.8	6.24	4.46	3.12	2.08	1.56	1.04	0.78	0.624
47	9.78	7.34	5.87	4.19	2.93	1.96	1.47	0.978	0.734	0.587
48	9.22	6.91	5.53	3.95	2.77	1.84	1.38	0.922	0.691	0.553
49	8.7	6.52	5.22	3.73	2.61	1.74	1.3	0.87	0.652	0.522
50	8.22	6.16	4.93	3.52	2.47	1.64	1.23	0.822	0.616	0.493
51	7.77	5.83	4.66	3.33	2.33	1.55	1.17	0.777	0.583	0.466
52	7.36	5.52	4.42	3.16	2.21	1.47	1.1	0.736	0.552	0.442
53	6.98	5.24	4.19	2.99	2.09	1.4	1.05	0.698	0.524	0.419
54	6.63	4.97	3.98	2.84	1.99	1.33	0.994	0.663	0.497	0.398
55	6.3	4.72	3.78	2.7	1.89	1.26	0.945	0.63	0.472	0.378
56	5.99	4.5	3.6	2.57	1.8	1.2	0.899	0.599	0.45	0.36
57	5.71	4.28	3.43	2.45	1.71	1.14	0.856	0.571	0.428	0.343
58	5.44	4.08	3.27	2.33	1.63	1.09	0.816	0.544	0.408	0.327
59	5.19	3.9	3.12	2.23	1.56	1.04	0.779	0.519	0.39	0.312
60	4.96	3.72	2.98	2.13	1.49	0.992	0.744	0.496	0.372	0.298
61	4.74	3.56	2.85	2.03	1.42	0.949	0.712	0.474	0.356	0.285
62	4.54	3.4	2.72	1.95	1.36	0.908	0.681	0.454	0.34	0.272
63	4.35	3.26	2.61	1.86	1.3	0.87	0.652	0.435	0.326	0.261
64	4.17	3.13	2.5	1.79	1.25	0.834	0.625	0.417	0.313	0.25
65	4	3	2.4	1.71	1.2	0.8	0.6	0.4	0.3	0.24
66	3.84	2.88	2.3	1.65	1.15	0.768	0.576	0.384	0.288	0.23
67	3.69	2.77	2.21	1.58	1.11	0.738	0.553	0.369	0.277	0.221
68	3.55	2.66	2.13	1.52	1.06	0.709	0.532	0.355	0.266	0.213
69	3.41	2.56	2.05	1.46	1.02	0.683	0.512	0.341	0.256	0.205
70	3.29	2.47	1.97	1.41	0.986	0.657	0.493	0.329	0.247	0.197
71	3.17	2.38	1.9	1.36	0.95	0.633	0.475	0.317	0.238	0.19
72	3.05	2.29	1.83	1.31	0.916	0.611	0.458	0.305	0.229	0.183

73	2.95	2.21	1.77	1.26	0.884	0.589	0.442	0.295	0.221	0.177
74	2.85	2.13	1.71	1.22	0.854	0.569	0.427	0.285	0.213	0.171
75	2.75	2.06	1.65	1.18	0.825	0.55	0.412	0.275	0.206	0.165
76	2.66	1.99	1.59	1.14	0.797	0.532	0.399	0.266	0.199	0.159
77	2.57	1.93	1.54	1.1	0.771	0.514	0.386	0.257	0.193	0.154
78	2.49	1.87	1.49	1.07	0.747	0.498	0.373	0.249	0.187	0.149
79	2.41	1.81	1.45	1.03	0.723	0.482	0.362	0.241	0.181	0.145
80	2.34	1.75	1.4	1	0.701	0.467	0.35	0.234	0.175	0.14
81	2.26	1.7	1.36	0.97	0.679	0.453	0.34	0.226	0.17	0.136
82	2.2	1.65	1.32	0.941	0.659	0.439	0.329	0.22	0.165	0.132
83	2.13	1.6	1.28	0.914	0.64	0.426	0.32	0.213	0.16	0.128
84	2.07	1.55	1.24	0.887	0.621	0.414	0.311	0.207	0.155	0.124
85	2.01	1.51	1.21	0.862	0.603	0.402	0.302	0.201	0.151	0.121
86	1.96	1.47	1.17	0.838	0.587	0.391	0.293	0.196	0.147	0.117
87	1.9	1.43	1.14	0.815	0.57	0.38	0.285	0.19	0.143	0.114
88	1.85	1.39	1.11	0.793	0.555	0.37	0.278	0.185	0.139	0.111
89	1.8	1.35	1.08	0.772	0.54	0.36	0.27	0.18	0.135	0.108
90	1.75	1.32	1.05	0.752	0.526	0.351	0.263	0.175	0.132	0.105
91	1.71	1.28	1.03	0.733	0.513	0.342	0.256	0.171	0.128	0.103
92	1.67	1.25	1	0.714	0.5	0.333	0.25	0.167	0.125	0.1
93	1.63	1.22	0.975	0.696	0.488	0.325	0.244	0.163	0.122	0.0975
94	1.59	1.19	0.951	0.68	0.476	0.317	0.238	0.159	0.119	0.0951
95	1.55	1.16	0.929	0.663	0.464	0.31	0.232	0.155	0.116	0.0929
96	1.51	1.13	0.907	0.648	0.453	0.302	0.227	0.151	0.113	0.0907
97	1.48	1.11	0.886	0.633	0.443	0.295	0.221	0.148	0.111	0.0886
98	1.44	1.08	0.866	0.618	0.433	0.289	0.216	0.144	0.108	0.0866
99	1.41	1.06	0.846	0.605	0.423	0.282	0.212	0.141	0.106	0.0846
100	1.38	1.03	0.828	0.591	0.414	0.276	0.207	0.138	0.103	0.0828
101	1.35	1.01	0.81	0.579	0.405	0.27	0.203	0.135	0.101	0.081
102	1.32	0.991	0.793	0.566	0.396	0.264	0.198	0.132	0.0991	0.0793

103	1.29	0.97	0.776	0.555	0.388	0.259	0.194	0.129	0.097	0.0776
104	1.27	0.951	0.761	0.543	0.38	0.254	0.19	0.127	0.0951	0.0761
105	1.24	0.932	0.745	0.532	0.373	0.248	0.186	0.124	0.0932	0.0745
106	1.22	0.913	0.731	0.522	0.365	0.244	0.183	0.122	0.0913	0.0731
107	1.19	0.896	0.716	0.512	0.358	0.239	0.179	0.119	0.0896	0.0716
108	1.17	0.879	0.703	0.502	0.351	0.234	0.176	0.117	0.0879	0.0703
109	1.15	0.862	0.69	0.493	0.345	0.23	0.172	0.115	0.0862	0.069
110	1.13	0.846	0.677	0.484	0.339	0.226	0.169	0.113	0.0846	0.0677
111	1.11	0.831	0.665	0.475	0.332	0.222	0.166	0.111	0.0831	0.0665
112	1.09	0.816	0.653	0.467	0.327	0.218	0.163	0.109	0.0816	0.0653
113	1.07	0.802	0.642	0.458	0.321	0.214	0.16	0.107	0.0802	0.0642
114	1.05	0.789	0.631	0.451	0.315	0.21	0.158	0.105	0.0789	0.0631
115	1.03	0.775	0.62	0.443	0.31	0.207	0.155	0.103	0.0775	0.062
116	1.02	0.763	0.61	0.436	0.305	0.203	0.153	0.102	0.0763	0.061
117	1	0.75	0.6	0.429	0.3	0.2	0.15	0.1	0.075	0.06
118	0.985	0.739	0.591	0.422	0.295	0.197	0.148	0.0985	0.0739	0.0591
119	0.97	0.727	0.582	0.416	0.291	0.194	0.145	0.097	0.0727	0.0582
120	0.955	0.716	0.573	0.409	0.286	0.191	0.143	0.0955	0.0716	0.0573
121	0.941	0.706	0.564	0.403	0.282	0.188	0.141	0.0941	0.0706	0.0564
122	0.927	0.695	0.556	0.397	0.278	0.185	0.139	0.0927	0.0695	0.0556
123	0.914	0.685	0.548	0.392	0.274	0.183	0.137	0.0914	0.0685	0.0548
124	0.901	0.676	0.541	0.386	0.27	0.18	0.135	0.0901	0.0676	0.0541
125	0.889	0.667	0.533	0.381	0.267	0.178	0.133	0.0889	0.0667	0.0533
126	0.877	0.658	0.526	0.376	0.263	0.175	0.132	0.0877	0.0658	0.0526
127	0.865	0.649	0.519	0.371	0.26	0.173	0.13	0.0865	0.0649	0.0519
128	0.854	0.641	0.513	0.366	0.256	0.171	0.128	0.0854	0.0641	0.0513
129	0.844	0.633	0.506	0.362	0.253	0.169	0.127	0.0844	0.0633	0.0506
130	0.833	0.625	0.5	0.357	0.25	0.167	0.125	0.0833	0.0625	0.05
131	0.823	0.617	0.494	0.353	0.247	0.165	0.123	0.0823	0.0617	0.0494
132	0.814	0.61	0.488	0.349	0.244	0.163	0.122	0.0814	0.061	0.0488

Your Name - June 2018

133	0.804	0.603	0.483	0.345	0.241	0.161	0.121	0.0804	0.0603	0.0483
134	0.795	0.596	0.477	0.341	0.239	0.159	0.119	0.0795	0.0596	0.0477
135	0.787	0.59	0.472	0.337	0.236	0.157	0.118	0.0787	0.059	0.0472
136	0.778	0.584	0.467	0.333	0.233	0.156	0.117	0.0778	0.0584	0.0467
137	0.77	0.578	0.462	0.33	0.231	0.154	0.116	0.077	0.0578	0.0462
138	0.762	0.572	0.457	0.327	0.229	0.152	0.114	0.0762	0.0572	0.0457
139	0.755	0.566	0.453	0.323	0.226	0.151	0.113	0.0755	0.0566	0.0453
140	0.747	0.561	0.448	0.32	0.224	0.149	0.112	0.0747	0.0561	0.0448
141	0.74	0.555	0.444	0.317	0.222	0.148	0.111	0.074	0.0555	0.0444
142	0.734	0.55	0.44	0.314	0.22	0.147	0.11	0.0734	0.055	0.044
143	0.727	0.545	0.436	0.312	0.218	0.145	0.109	0.0727	0.0545	0.0436
144	0.721	0.541	0.433	0.309	0.216	0.144	0.108	0.0721	0.0541	0.0433
145	0.715	0.536	0.429	0.306	0.214	0.143	0.107	0.0715	0.0536	0.0429
146	0.709	0.532	0.426	0.304	0.213	0.142	0.106	0.0709	0.0532	0.0426
147	0.704	0.528	0.422	0.302	0.211	0.141	0.106	0.0704	0.0528	0.0422
148	0.698	0.524	0.419	0.299	0.209	0.14	0.105	0.0698	0.0524	0.0419
149	0.693	0.52	0.416	0.297	0.208	0.139	0.104	0.0693	0.052	0.0416
150	0.688	0.516	0.413	0.295	0.206	0.138	0.103	0.0688	0.0516	0.0413
151	0.683	0.513	0.41	0.293	0.205	0.137	0.103	0.0683	0.0513	0.041
152	0.679	0.509	0.407	0.291	0.204	0.136	0.102	0.0679	0.0509	0.0407
153	0.675	0.506	0.405	0.289	0.202	0.135	0.101	0.0675	0.0506	0.0405
154	0.67	0.503	0.402	0.287	0.201	0.134	0.101	0.067	0.0503	0.0402
155	0.667	0.5	0.4	0.286	0.2	0.133	0.1	0.0667	0.05	0.04
156	0.663	0.497	0.398	0.284	0.199	0.133	0.0994	0.0663	0.0497	0.0398
157	0.659	0.494	0.395	0.282	0.198	0.132	0.0989	0.0659	0.0494	0.0395
158	0.656	0.492	0.393	0.281	0.197	0.131	0.0984	0.0656	0.0492	0.0393
159	0.652	0.489	0.391	0.28	0.196	0.13	0.0979	0.0652	0.0489	0.0391
160	0.649	0.487	0.39	0.278	0.195	0.13	0.0974	0.0649	0.0487	0.039
161	0.646	0.485	0.388	0.277	0.194	0.129	0.097	0.0646	0.0485	0.0388
162	0.644	0.483	0.386	0.276	0.193	0.129	0.0966	0.0644	0.0483	0.0386

163	0.641	0.481	0.385	0.275	0.192	0.128	0.0962	0.0641	0.0481	0.0385
164	0.639	0.479	0.383	0.274	0.192	0.128	0.0958	0.0639	0.0479	0.0383
165	0.636	0.477	0.382	0.273	0.191	0.127	0.0955	0.0636	0.0477	0.0382
166	0.634	0.476	0.381	0.272	0.19	0.127	0.0951	0.0634	0.0476	0.0381
167	0.632	0.474	0.379	0.271	0.19	0.126	0.0949	0.0632	0.0474	0.0379
168	0.631	0.473	0.378	0.27	0.189	0.126	0.0946	0.0631	0.0473	0.0378
169	0.629	0.472	0.377	0.27	0.189	0.126	0.0943	0.0629	0.0472	0.0377
170	0.627	0.471	0.376	0.269	0.188	0.125	0.0941	0.0627	0.0471	0.0376
171	0.626	0.47	0.376	0.268	0.188	0.125	0.0939	0.0626	0.047	0.0376
172	0.625	0.469	0.375	0.268	0.187	0.125	0.0937	0.0625	0.0469	0.0375
173	0.624	0.468	0.374	0.267	0.187	0.125	0.0936	0.0624	0.0468	0.0374
174	0.623	0.467	0.374	0.267	0.187	0.125	0.0934	0.0623	0.0467	0.0374
175	0.622	0.467	0.373	0.267	0.187	0.124	0.0933	0.0622	0.0467	0.0373
176	0.621	0.466	0.373	0.266	0.186	0.124	0.0932	0.0621	0.0466	0.0373
177	0.621	0.466	0.373	0.266	0.186	0.124	0.0931	0.0621	0.0466	0.0373
178	0.621	0.465	0.372	0.266	0.186	0.124	0.0931	0.0621	0.0465	0.0372
179	0.62	0.465	0.372	0.266	0.186	0.124	0.093	0.062	0.0465	0.0372
180	0.62	0.465	0.372	0.266	0.186	0.124	0.093	0.062	0.0465	0.0372

Table 24 Rotational differential cross sections of electron-furfural scattering in bohr^2. Energy range 70 eV - 1000 eV. Angle in degrees.

θ	70	100	150	200	300	400	500	700	1000
0	1E+10	1.42E+10	2.13E+10	2.84E+10	4.26E+10	5.68E+10	7.1E+10	9.95E+10	1.42E+11
1	1650	1160	770	578	385	289	231	165	116
2	413	289	193	144	96.3	72.2	57.8	41.3	28.9
3	183	128	85.6	64.2	42.8	32.1	25.7	18.3	12.8
4	103	72.3	48.2	36.1	24.1	18.1	14.5	10.3	7.23
5	66.1	46.3	30.8	23.1	15.4	11.6	9.25	6.61	4.63
6	45.9	32.1	21.4	16.1	10.7	8.03	6.43	4.59	3.21

7	33.7	23.6	15.7	11.8	7.87	5.9	4.72	3.37	2.36
8	25.8	18.1	12.1	9.04	6.03	4.52	3.62	2.58	1.81
9	20.4	14.3	9.53	7.15	4.77	3.57	2.86	2.04	1.43
10	16.6	11.6	7.72	5.79	3.86	2.9	2.32	1.66	1.16
11	13.7	9.58	6.39	4.79	3.19	2.39	1.92	1.37	0.958
12	11.5	8.05	5.37	4.03	2.68	2.01	1.61	1.15	0.805
13	9.81	6.87	4.58	3.43	2.29	1.72	1.37	0.981	0.687
14	8.46	5.93	3.95	2.96	1.98	1.48	1.19	0.846	0.593
15	7.38	5.17	3.44	2.58	1.72	1.29	1.03	0.738	0.517
16	6.49	4.54	3.03	2.27	1.51	1.14	0.909	0.649	0.454
17	5.75	4.03	2.69	2.01	1.34	1.01	0.806	0.575	0.403
18	5.14	3.6	2.4	1.8	1.2	0.899	0.719	0.514	0.36
19	4.62	3.23	2.15	1.62	1.08	0.808	0.646	0.462	0.323
20	4.17	2.92	1.95	1.46	0.973	0.73	0.584	0.417	0.292
21	3.79	2.65	1.77	1.32	0.883	0.662	0.53	0.379	0.265
22	3.45	2.42	1.61	1.21	0.806	0.604	0.483	0.345	0.242
23	3.16	2.21	1.48	1.11	0.738	0.554	0.443	0.316	0.221
24	2.91	2.04	1.36	1.02	0.679	0.509	0.407	0.291	0.204
25	2.62	1.84	1.22	0.918	0.612	0.459	0.367	0.262	0.184
26	2.34	1.63	1.09	0.817	0.545	0.409	0.327	0.234	0.163
27	2.09	1.46	0.975	0.731	0.488	0.366	0.293	0.209	0.146
28	1.88	1.31	0.876	0.657	0.438	0.329	0.263	0.188	0.131
29	1.69	1.19	0.79	0.593	0.395	0.296	0.237	0.169	0.119
30	1.53	1.07	0.715	0.537	0.358	0.268	0.215	0.153	0.107
31	1.39	0.975	0.65	0.487	0.325	0.244	0.195	0.139	0.0975
32	1.27	0.889	0.592	0.444	0.296	0.222	0.178	0.127	0.0889
33	1.16	0.812	0.541	0.406	0.271	0.203	0.162	0.116	0.0812
34	1.06	0.745	0.496	0.372	0.248	0.186	0.149	0.106	0.0745
35	0.978	0.684	0.456	0.342	0.228	0.171	0.137	0.0978	0.0684
36	0.901	0.631	0.42	0.315	0.21	0.158	0.126	0.0901	0.0631

37	0.832	0.582	0.388	0.291	0.194	0.146	0.116	0.0832	0.0582
38	0.77	0.539	0.359	0.27	0.18	0.135	0.108	0.077	0.0539
39	0.715	0.5	0.334	0.25	0.167	0.125	0.1	0.0715	0.05
40	0.664	0.465	0.31	0.233	0.155	0.116	0.093	0.0664	0.0465
41	0.619	0.433	0.289	0.217	0.144	0.108	0.0866	0.0619	0.0433
42	0.578	0.404	0.27	0.202	0.135	0.101	0.0809	0.0578	0.0404
43	0.54	0.378	0.252	0.189	0.126	0.0945	0.0756	0.054	0.0378
44	0.506	0.354	0.236	0.177	0.118	0.0885	0.0708	0.0506	0.0354
45	0.474	0.332	0.221	0.166	0.111	0.083	0.0664	0.0474	0.0332
46	0.446	0.312	0.208	0.156	0.104	0.078	0.0624	0.0446	0.0312
47	0.419	0.293	0.196	0.147	0.0978	0.0734	0.0587	0.0419	0.0293
48	0.395	0.277	0.184	0.138	0.0922	0.0691	0.0553	0.0395	0.0277
49	0.373	0.261	0.174	0.13	0.087	0.0652	0.0522	0.0373	0.0261
50	0.352	0.247	0.164	0.123	0.0822	0.0616	0.0493	0.0352	0.0247
51	0.333	0.233	0.155	0.117	0.0777	0.0583	0.0466	0.0333	0.0233
52	0.316	0.221	0.147	0.11	0.0736	0.0552	0.0442	0.0316	0.0221
53	0.299	0.209	0.14	0.105	0.0698	0.0524	0.0419	0.0299	0.0209
54	0.284	0.199	0.133	0.0994	0.0663	0.0497	0.0398	0.0284	0.0199
55	0.27	0.189	0.126	0.0945	0.063	0.0472	0.0378	0.027	0.0189
56	0.257	0.18	0.12	0.0899	0.0599	0.045	0.036	0.0257	0.018
57	0.245	0.171	0.114	0.0856	0.0571	0.0428	0.0343	0.0245	0.0171
58	0.233	0.163	0.109	0.0816	0.0544	0.0408	0.0327	0.0233	0.0163
59	0.223	0.156	0.104	0.0779	0.0519	0.039	0.0312	0.0223	0.0156
60	0.213	0.149	0.0992	0.0744	0.0496	0.0372	0.0298	0.0213	0.0149
61	0.203	0.142	0.0949	0.0712	0.0474	0.0356	0.0285	0.0203	0.0142
62	0.195	0.136	0.0908	0.0681	0.0454	0.034	0.0272	0.0195	0.0136
63	0.186	0.13	0.087	0.0652	0.0435	0.0326	0.0261	0.0186	0.013
64	0.179	0.125	0.0834	0.0625	0.0417	0.0313	0.025	0.0179	0.0125
65	0.171	0.12	0.08	0.06	0.04	0.03	0.024	0.0171	0.012
66	0.165	0.115	0.0768	0.0576	0.0384	0.0288	0.023	0.0165	0.0115

67	0.158	0.111	0.0738	0.0553	0.0369	0.0277	0.0221	0.0158	0.0111
68	0.152	0.106	0.0709	0.0532	0.0355	0.0266	0.0213	0.0152	0.0106
69	0.146	0.102	0.0683	0.0512	0.0341	0.0256	0.0205	0.0146	0.0102
70	0.141	0.0986	0.0657	0.0493	0.0329	0.0247	0.0197	0.0141	0.00986
71	0.136	0.095	0.0633	0.0475	0.0317	0.0238	0.019	0.0136	0.0095
72	0.131	0.0916	0.0611	0.0458	0.0305	0.0229	0.0183	0.0131	0.00916
73	0.126	0.0884	0.0589	0.0442	0.0295	0.0221	0.0177	0.0126	0.00884
74	0.122	0.0854	0.0569	0.0427	0.0285	0.0213	0.0171	0.0122	0.00854
75	0.118	0.0825	0.055	0.0412	0.0275	0.0206	0.0165	0.0118	0.00825
76	0.114	0.0797	0.0532	0.0399	0.0266	0.0199	0.0159	0.0114	0.00797
77	0.11	0.0771	0.0514	0.0386	0.0257	0.0193	0.0154	0.011	0.00771
78	0.107	0.0747	0.0498	0.0373	0.0249	0.0187	0.0149	0.0107	0.00747
79	0.103	0.0723	0.0482	0.0362	0.0241	0.0181	0.0145	0.0103	0.00723
80	0.1	0.0701	0.0467	0.035	0.0234	0.0175	0.014	0.01	0.00701
81	0.097	0.0679	0.0453	0.034	0.0226	0.017	0.0136	0.0097	0.00679
82	0.0941	0.0659	0.0439	0.0329	0.022	0.0165	0.0132	0.00941	0.00659
83	0.0914	0.064	0.0426	0.032	0.0213	0.016	0.0128	0.00914	0.0064
84	0.0887	0.0621	0.0414	0.0311	0.0207	0.0155	0.0124	0.00887	0.00621
85	0.0862	0.0603	0.0402	0.0302	0.0201	0.0151	0.0121	0.00862	0.00603
86	0.0838	0.0587	0.0391	0.0293	0.0196	0.0147	0.0117	0.00838	0.00587
87	0.0815	0.057	0.038	0.0285	0.019	0.0143	0.0114	0.00815	0.0057
88	0.0793	0.0555	0.037	0.0278	0.0185	0.0139	0.0111	0.00793	0.00555
89	0.0772	0.054	0.036	0.027	0.018	0.0135	0.0108	0.00772	0.0054
90	0.0752	0.0526	0.0351	0.0263	0.0175	0.0132	0.0105	0.00752	0.00526
91	0.0733	0.0513	0.0342	0.0256	0.0171	0.0128	0.0103	0.00733	0.00513
92	0.0714	0.05	0.0333	0.025	0.0167	0.0125	0.01	0.00714	0.005
93	0.0696	0.0488	0.0325	0.0244	0.0163	0.0122	0.00975	0.00696	0.00488
94	0.068	0.0476	0.0317	0.0238	0.0159	0.0119	0.00951	0.0068	0.00476
95	0.0663	0.0464	0.031	0.0232	0.0155	0.0116	0.00929	0.00663	0.00464
96	0.0648	0.0453	0.0302	0.0227	0.0151	0.0113	0.00907	0.00648	0.00453

97	0.0633	0.0443	0.0295	0.0221	0.0148	0.0111	0.00886	0.00633	0.00443
98	0.0618	0.0433	0.0289	0.0216	0.0144	0.0108	0.00866	0.00618	0.00433
99	0.0605	0.0423	0.0282	0.0212	0.0141	0.0106	0.00846	0.00605	0.00423
100	0.0591	0.0414	0.0276	0.0207	0.0138	0.0103	0.00828	0.00591	0.00414
101	0.0579	0.0405	0.027	0.0203	0.0135	0.0101	0.0081	0.00579	0.00405
102	0.0566	0.0396	0.0264	0.0198	0.0132	0.00991	0.00793	0.00566	0.00396
103	0.0555	0.0388	0.0259	0.0194	0.0129	0.0097	0.00776	0.00555	0.00388
104	0.0543	0.038	0.0254	0.019	0.0127	0.00951	0.00761	0.00543	0.0038
105	0.0532	0.0373	0.0248	0.0186	0.0124	0.00932	0.00745	0.00532	0.00373
106	0.0522	0.0365	0.0244	0.0183	0.0122	0.00913	0.00731	0.00522	0.00365
107	0.0512	0.0358	0.0239	0.0179	0.0119	0.00896	0.00716	0.00512	0.00358
108	0.0502	0.0351	0.0234	0.0176	0.0117	0.00879	0.00703	0.00502	0.00351
109	0.0493	0.0345	0.023	0.0172	0.0115	0.00862	0.0069	0.00493	0.00345
110	0.0484	0.0339	0.0226	0.0169	0.0113	0.00846	0.00677	0.00484	0.00339
111	0.0475	0.0332	0.0222	0.0166	0.0111	0.00831	0.00665	0.00475	0.00332
112	0.0467	0.0327	0.0218	0.0163	0.0109	0.00816	0.00653	0.00467	0.00327
113	0.0458	0.0321	0.0214	0.016	0.0107	0.00802	0.00642	0.00458	0.00321
114	0.0451	0.0315	0.021	0.0158	0.0105	0.00789	0.00631	0.00451	0.00315
115	0.0443	0.031	0.0207	0.0155	0.0103	0.00775	0.0062	0.00443	0.0031
116	0.0436	0.0305	0.0203	0.0153	0.0102	0.00763	0.0061	0.00436	0.00305
117	0.0429	0.03	0.02	0.015	0.01	0.0075	0.006	0.00429	0.003
118	0.0422	0.0295	0.0197	0.0148	0.00985	0.00739	0.00591	0.00422	0.00295
119	0.0416	0.0291	0.0194	0.0145	0.0097	0.00727	0.00582	0.00416	0.00291
120	0.0409	0.0286	0.0191	0.0143	0.00955	0.00716	0.00573	0.00409	0.00286
121	0.0403	0.0282	0.0188	0.0141	0.00941	0.00706	0.00564	0.00403	0.00282
122	0.0397	0.0278	0.0185	0.0139	0.00927	0.00695	0.00556	0.00397	0.00278
123	0.0392	0.0274	0.0183	0.0137	0.00914	0.00685	0.00548	0.00392	0.00274
124	0.0386	0.027	0.018	0.0135	0.00901	0.00676	0.00541	0.00386	0.0027
125	0.0381	0.0267	0.0178	0.0133	0.00889	0.00667	0.00533	0.00381	0.00267
126	0.0376	0.0263	0.0175	0.0132	0.00877	0.00658	0.00526	0.00376	0.00263

127	0.0371	0.026	0.0173	0.013	0.00865	0.00649	0.00519	0.00371	0.0026
128	0.0366	0.0256	0.0171	0.0128	0.00854	0.00641	0.00513	0.00366	0.00256
129	0.0362	0.0253	0.0169	0.0127	0.00844	0.00633	0.00506	0.00362	0.00253
130	0.0357	0.025	0.0167	0.0125	0.00833	0.00625	0.005	0.00357	0.0025
131	0.0353	0.0247	0.0165	0.0123	0.00823	0.00617	0.00494	0.00353	0.00247
132	0.0349	0.0244	0.0163	0.0122	0.00814	0.0061	0.00488	0.00349	0.00244
133	0.0345	0.0241	0.0161	0.0121	0.00804	0.00603	0.00483	0.00345	0.00241
134	0.0341	0.0239	0.0159	0.0119	0.00795	0.00596	0.00477	0.00341	0.00239
135	0.0337	0.0236	0.0157	0.0118	0.00787	0.0059	0.00472	0.00337	0.00236
136	0.0333	0.0233	0.0156	0.0117	0.00778	0.00584	0.00467	0.00333	0.00233
137	0.033	0.0231	0.0154	0.0116	0.0077	0.00578	0.00462	0.0033	0.00231
138	0.0327	0.0229	0.0152	0.0114	0.00762	0.00572	0.00457	0.00327	0.00229
139	0.0323	0.0226	0.0151	0.0113	0.00755	0.00566	0.00453	0.00323	0.00226
140	0.032	0.0224	0.0149	0.0112	0.00747	0.00561	0.00448	0.032	0.00224
141	0.0317	0.0222	0.0148	0.0111	0.0074	0.00555	0.00444	0.00317	0.00222
142	0.0314	0.022	0.0147	0.011	0.00734	0.0055	0.0044	0.00314	0.0022
143	0.0312	0.0218	0.0145	0.0109	0.00727	0.00545	0.00436	0.00312	0.00218
144	0.0309	0.0216	0.0144	0.0108	0.00721	0.00541	0.00433	0.00309	0.00216
145	0.0306	0.0214	0.0143	0.0107	0.00715	0.00536	0.00429	0.00306	0.00214
146	0.0304	0.0213	0.0142	0.0106	0.00709	0.00532	0.00426	0.00304	0.00213
147	0.0302	0.0211	0.0141	0.0106	0.00704	0.00528	0.00422	0.00302	0.00211
148	0.0299	0.0209	0.014	0.0105	0.00698	0.00524	0.00419	0.00299	0.00209
149	0.0297	0.0208	0.0139	0.0104	0.00693	0.0052	0.00416	0.00297	0.00208
150	0.0295	0.0206	0.0138	0.0103	0.00688	0.00516	0.00413	0.00295	0.00206
151	0.0293	0.0205	0.0137	0.0103	0.00683	0.00513	0.0041	0.00293	0.00205
152	0.0291	0.0204	0.0136	0.0102	0.00679	0.00509	0.00407	0.00291	0.00204
153	0.0289	0.0202	0.0135	0.0101	0.00675	0.00506	0.00405	0.00289	0.00202
154	0.0287	0.0201	0.0134	0.0101	0.0067	0.00503	0.00402	0.00287	0.00201
155	0.0286	0.02	0.0133	0.01	0.00667	0.005	0.004	0.00286	0.002
156	0.0284	0.0199	0.0133	0.00994	0.00663	0.00497	0.00398	0.00284	0.00199

157	0.0282	0.0198	0.0132	0.00989	0.00659	0.00494	0.00395	0.00282	0.00198
158	0.0281	0.0197	0.0131	0.00984	0.00656	0.00492	0.00393	0.00281	0.00197
159	0.028	0.0196	0.013	0.00979	0.00652	0.00489	0.00391	0.0028	0.00196
160	0.0278	0.0195	0.013	0.00974	0.00649	0.00487	0.0039	0.00278	0.00195
161	0.0277	0.0194	0.0129	0.0097	0.00646	0.00485	0.00388	0.00277	0.00194
162	0.0276	0.0193	0.0129	0.00966	0.00644	0.00483	0.00386	0.00276	0.00193
163	0.0275	0.0192	0.0128	0.00962	0.00641	0.00481	0.00385	0.00275	0.00192
164	0.0274	0.0192	0.0128	0.00958	0.00639	0.00479	0.00383	0.00274	0.00192
165	0.0273	0.0191	0.0127	0.00955	0.00636	0.00477	0.00382	0.00273	0.00191
166	0.0272	0.019	0.0127	0.00951	0.00634	0.00476	0.00381	0.00272	0.0019
167	0.0271	0.019	0.0126	0.00949	0.00632	0.00474	0.00379	0.00271	0.0019
168	0.027	0.0189	0.0126	0.00946	0.00631	0.00473	0.00378	0.0027	0.00189
169	0.027	0.0189	0.0126	0.00943	0.00629	0.00472	0.00377	0.0027	0.00189
170	0.0269	0.0188	0.0125	0.00941	0.00627	0.00471	0.00376	0.00269	0.00188
171	0.0268	0.0188	0.0125	0.00939	0.00626	0.0047	0.00376	0.00268	0.00188
172	0.0268	0.0187	0.0125	0.00937	0.00625	0.00469	0.00375	0.00268	0.00187
173	0.0267	0.0187	0.0125	0.00936	0.00624	0.00468	0.00374	0.00267	0.00187
174	0.0267	0.0187	0.0125	0.00934	0.00623	0.00467	0.00374	0.00267	0.00187
175	0.0267	0.0187	0.0124	0.00933	0.00622	0.00467	0.00373	0.00267	0.00187
176	0.0266	0.0186	0.0124	0.00932	0.00621	0.00466	0.00373	0.00266	0.00186
177	0.0266	0.0186	0.0124	0.00931	0.00621	0.00466	0.00373	0.00266	0.00186
178	0.0266	0.0186	0.0124	0.00931	0.00621	0.00465	0.00372	0.00266	0.00186
179	0.0266	0.0186	0.0124	0.0093	0.0062	0.00465	0.00372	0.00266	0.00186
180	0.0266	0.0186	0.0124	0.0093	0.0062	0.00465	0.00372	0.00266	0.00186

Table 25 Rotational differential cross sections of electron-furfural scattering in bohr^2. Energy range 2000 eV - 10 000 eV. Angle in degrees.

θ	2000	3000	5000	10000	θ	2000	3000	5000	10000
0	2.84E+11	4.26E+11	7.1E+11	1.42E+12	91	0.00256	0.00171	0.00103	0.000513

Your Name - June 2018

1	57.8	38.5	23.1	11.6	92	0.0025	0.00167	0.001	0.0005
2	14.4	9.63	5.78	2.89	93	0.00244	0.00163	0.000975	0.000488
3	6.42	4.28	2.57	1.28	94	0.00238	0.00159	0.000951	0.000476
4	3.61	2.41	1.45	0.723	95	0.00232	0.00155	0.000929	0.000464
5	2.31	1.54	0.925	0.463	96	0.00227	0.00151	0.000907	0.000453
6	1.61	1.07	0.643	0.321	97	0.00221	0.00148	0.000886	0.000443
7	1.18	0.787	0.472	0.236	98	0.00216	0.00144	0.000866	0.000433
8	0.904	0.603	0.362	0.181	99	0.00212	0.00141	0.000846	0.000423
9	0.715	0.477	0.286	0.143	100	0.00207	0.00138	0.000828	0.000414
10	0.579	0.386	0.232	0.116	101	0.00203	0.00135	0.00081	0.000405
11	0.479	0.319	0.192	0.0958	102	0.00198	0.00132	0.000793	0.000396
12	0.403	0.268	0.161	0.0805	103	0.00194	0.00129	0.000776	0.000388
13	0.343	0.229	0.137	0.0687	104	0.0019	0.00127	0.000761	0.00038
14	0.296	0.198	0.119	0.0593	105	0.00186	0.00124	0.000745	0.000373
15	0.258	0.172	0.103	0.0517	106	0.00183	0.00122	0.000731	0.000365
16	0.227	0.151	0.0909	0.0454	107	0.00179	0.00119	0.000716	0.000358
17	0.201	0.134	0.0806	0.0403	108	0.00176	0.00117	0.000703	0.000351
18	0.18	0.12	0.0719	0.036	109	0.00172	0.00115	0.00069	0.000345
19	0.162	0.108	0.0646	0.0323	110	0.00169	0.00113	0.000677	0.000339
20	0.146	0.0973	0.0584	0.0292	111	0.00166	0.00111	0.000665	0.000332
21	0.132	0.0883	0.053	0.0265	112	0.00163	0.00109	0.000653	0.000327
22	0.121	0.0806	0.0483	0.0242	113	0.0016	0.00107	0.000642	0.000321
23	0.111	0.0738	0.0443	0.0221	114	0.00158	0.00105	0.000631	0.000315
24	0.102	0.0679	0.0407	0.0204	115	0.00155	0.00103	0.00062	0.00031
25	0.0918	0.0612	0.0367	0.0184	116	0.00153	0.00102	0.00061	0.000305
26	0.0817	0.0545	0.0327	0.0163	117	0.0015	0.001	0.0006	0.0003
27	0.0731	0.0488	0.0293	0.0146	118	0.00148	0.000985	0.000591	0.000295
28	0.0657	0.0438	0.0263	0.0131	119	0.00145	0.00097	0.000582	0.000291
29	0.0593	0.0395	0.0237	0.0119	120	0.00143	0.000955	0.000573	0.000286
30	0.0537	0.0358	0.0215	0.0107	121	0.00141	0.000941	0.000564	0.000282

31	0.0487	0.0325	0.0195	0.00975	122	0.00139	0.000927	0.000556	0.000278
32	0.0444	0.0296	0.0178	0.00889	123	0.00137	0.000914	0.000548	0.000274
33	0.0406	0.0271	0.0162	0.00812	124	0.00135	0.000901	0.000541	0.00027
34	0.0372	0.0248	0.0149	0.00745	125	0.00133	0.000889	0.000533	0.000267
35	0.0342	0.0228	0.0137	0.00684	126	0.00132	0.000877	0.000526	0.000263
36	0.0315	0.021	0.0126	0.00631	127	0.0013	0.000865	0.000519	0.00026
37	0.0291	0.0194	0.0116	0.00582	128	0.00128	0.000854	0.000513	0.000256
38	0.027	0.018	0.0108	0.00539	129	0.00127	0.000844	0.000506	0.000253
39	0.025	0.0167	0.01	0.005	130	0.00125	0.000833	0.0005	0.00025
40	0.0233	0.0155	0.0093	0.00465	131	0.00123	0.000823	0.000494	0.000247
41	0.0217	0.0144	0.00866	0.00433	132	0.00122	0.000814	0.000488	0.000244
42	0.0202	0.0135	0.00809	0.00404	133	0.00121	0.000804	0.000483	0.000241
43	0.0189	0.0126	0.00756	0.00378	134	0.00119	0.000795	0.000477	0.000239
44	0.0177	0.0118	0.00708	0.00354	135	0.00118	0.000787	0.000472	0.000236
45	0.0166	0.0111	0.00664	0.00332	136	0.00117	0.000778	0.000467	0.000233
46	0.0156	0.0104	0.00624	0.00312	137	0.00116	0.00077	0.000462	0.000231
47	0.0147	0.00978	0.00587	0.00293	138	0.00114	0.000762	0.000457	0.000229
48	0.0138	0.00922	0.00553	0.00277	139	0.00113	0.000755	0.000453	0.000226
49	0.013	0.0087	0.00522	0.00261	140	0.00112	0.000747	0.000448	0.000224
50	0.0123	0.00822	0.00493	0.00247	141	0.00111	0.00074	0.000444	0.000222
51	0.0117	0.00777	0.00466	0.00233	142	0.0011	0.000734	0.00044	0.00022
52	0.011	0.00736	0.00442	0.00221	143	0.00109	0.000727	0.000436	0.000218
53	0.0105	0.00698	0.00419	0.00209	144	0.00108	0.000721	0.000433	0.000216
54	0.00994	0.00663	0.00398	0.00199	145	0.00107	0.000715	0.000429	0.000214
55	0.00945	0.0063	0.00378	0.00189	146	0.00106	0.000709	0.000426	0.000213
56	0.00899	0.00599	0.0036	0.0018	147	0.00106	0.000704	0.000422	0.000211
57	0.00856	0.00571	0.00343	0.00171	148	0.00105	0.000698	0.000419	0.000209
58	0.00816	0.00544	0.00327	0.00163	149	0.00104	0.000693	0.000416	0.000208
59	0.00779	0.00519	0.00312	0.00156	150	0.00103	0.000688	0.000413	0.000206
60	0.00744	0.00496	0.00298	0.00149	151	0.00103	0.000683	0.00041	0.000205

61	0.00712	0.00474	0.00285	0.00142	152	0.00102	0.000679	0.000407	0.000204
62	0.00681	0.00454	0.00272	0.00136	153	0.00101	0.000675	0.000405	0.000202
63	0.00652	0.00435	0.00261	0.0013	154	0.00101	0.00067	0.000402	0.000201
64	0.00625	0.00417	0.0025	0.00125	155	0.001	0.000667	0.0004	0.0002
65	0.006	0.004	0.0024	0.0012	156	0.000994	0.000663	0.000398	0.000199
66	0.00576	0.00384	0.0023	0.00115	157	0.000989	0.000659	0.000395	0.000198
67	0.00553	0.00369	0.00221	0.00111	158	0.000984	0.000656	0.000393	0.000197
68	0.00532	0.00355	0.00213	0.00106	159	0.000979	0.000652	0.000391	0.000196
69	0.00512	0.00341	0.00205	0.00102	160	0.000974	0.000649	0.00039	0.000195
70	0.00493	0.00329	0.00197	0.000986	161	0.00097	0.000646	0.000388	0.000194
71	0.00475	0.00317	0.0019	0.00095	162	0.000966	0.000644	0.000386	0.000193
72	0.00458	0.00305	0.00183	0.000916	163	0.000962	0.000641	0.000385	0.000192
73	0.00442	0.00295	0.00177	0.000884	164	0.000958	0.000639	0.000383	0.000192
74	0.00427	0.00285	0.00171	0.000854	165	0.000955	0.000636	0.000382	0.000191
75	0.00412	0.00275	0.00165	0.000825	166	0.000951	0.000634	0.000381	0.00019
76	0.00399	0.00266	0.00159	0.000797	167	0.000949	0.000632	0.000379	0.00019
77	0.00386	0.00257	0.00154	0.000771	168	0.000946	0.000631	0.000378	0.000189
78	0.00373	0.00249	0.00149	0.000747	169	0.000943	0.000629	0.000377	0.000189
79	0.00362	0.00241	0.00145	0.000723	170	0.000941	0.000627	0.000376	0.000188
80	0.0035	0.00234	0.0014	0.000701	171	0.000939	0.000626	0.000376	0.000188
81	0.0034	0.00226	0.00136	0.000679	172	0.000937	0.000625	0.000375	0.000187
82	0.00329	0.0022	0.00132	0.000659	173	0.000936	0.000624	0.000374	0.000187
83	0.0032	0.00213	0.00128	0.00064	174	0.000934	0.000623	0.000374	0.000187
84	0.00311	0.00207	0.00124	0.000621	175	0.000933	0.000622	0.000373	0.000187
85	0.00302	0.00201	0.00121	0.000603	176	0.000932	0.000621	0.000373	0.000186
86	0.00293	0.00196	0.00117	0.000587	177	0.000931	0.000621	0.000373	0.000186
87	0.00285	0.0019	0.00114	0.00057	178	0.000931	0.000621	0.000372	0.000186
88	0.00278	0.00185	0.00111	0.000555	179	0.00093	0.00062	0.000372	0.000186
89	0.0027	0.0018	0.00108	0.00054	180	0.00093	0.00062	0.000372	0.000186
90	0.00263	0.00175	0.00105	0.000526					